Exploring Electronic Structure of a few Biomolecules and Graphitic Materials

A Thesis

Submitted for the Degree of

DOCTOR OF PHILOSOPHY

in the Faculty of Science

by

Arun Kumar Manna

THEORETICAL SCIENCES UNIT
JAWAHARLAL NEHRU CENTRE FOR ADVANCED SCIENTIFIC RESEARCH
Bangalore – 560 064

SEPTEMBER 2013

To my family

DECLARATION

I hereby declare that the matter embodied in the thesis entitled "**Exploring Electronic Structure of a few Biomolecules and Graphitic Materials**" is the result of investigations carried out by me at the Theoretical Sciences Unit, Jawaharlal Nehru Centre for Advanced Scientific Research, Bangalore, India under the supervision of Prof. Swapan K. Pati and that it has not been submitted elsewhere for the award of any degree or diploma.

In keeping with the general practice in reporting scientific observations, due acknowledgement has been made whenever the work described is based on the findings of other investigators.

Arun Kumar Manna

CERTIFICATE

I hereby certify that the matter embodied in this thesis entitled "**Exploring Electronic Structure of a few Biomolecules and Graphitic Materials**" has been carried out by Mr. Arun Kumar Manna at the Theoretical Sciences Unit, Jawaharlal Nehru Centre for Advanced Scientific Research, Bangalore, India under my supervision and that it has not been submitted elsewhere for the award of any degree or diploma.

Prof. Swapan K. Pati
(Research Supervisor)

Acknowledgements

Well, the much speculated time has finally come to say Thank You to the people in my life who created impact and made my life worthy enough to me.

Almost 5 years coming to an end and standing at this point in life, when I look back, memories after memories I see flashing by. I learnt how to deal with life, how to taste the goodness of life and be a good human being. As the saying goes, 'life goes on', and so does it truly. From being a simple village lad to a grown up man, I came across some wonderful people in my life who influenced my life in many ways than one. I take this special moment in my life to acknowledge them all for being with me and helping me out in several ways.

First and foremost, I want to thank my parents (Maa and Baba). They made me what I am and instilled in me the first lessons of humanity and simplicity. Their indomitable efforts to provide me with whatever I needed and whenever, their continued support and love gave me the strength to materialise their dream. Can't thank enough my sisters (Bon and Didi) too whose support saw me through many hardships. Life is not a bed of roses and their loving hand helped me see through all the troubles. Thank You!

Next, I want to acknowledge my supervisor, Prof. Swapan K. Pati, for his guidance, inspiration and encouragement all these years. Discussions both scientific and also non-academic issues were always welcome. His passion for science instilled in me the urge to do good work. Words are falling short to express my gratitude towards him. I also want to thank Anusooya Ma'am for being so friendly and caring. They together gave us a homely environment, miles away from home. I also want to thank Ma'am for her help in learning referencing style for the thesis. Phew! Without her help, referencing would have been really tough!

I want to thank all my course instructors Prof. Shobhana Narasimhan, Prof. Umesh V. Waghmare, Prof. Balasubramanian Sundaram, Prof. Hemalatha Balaram, Prof. Chandrabhas Narayana, Dr. Vidhyadhiraja N. S., Dr. Subir K. Das, and Prof. Swapan K. Pati for making the concepts lucid and clear.

I am thankful to all my excellent collaborators Prof. C. N. R. Rao, Prof. Prabal K Maiti (IISc), Prof. Anna Painelli (Italy), Prof. Tapas K. Kundu, Dr. Tapas K. Maji, Dr. T. Govindaraju, Dr. Ranjan Datta, Dr. Francesca Terenziani (Italy), Dr. Cristina Sissa (Italy), Dr. Sudipta Dutta, Dr. Dattatray J. Late, Dr. Barun Das, Dr. A. Gomathi, Dr. K. S. Subrahmanyan, Dr. Ganga Periyasamy, Shrinwantu Pal, Debabrata Maity, D. Karthigeyan, H. S. S. Ramakrishna Matte, Biswajit Choudhury, Pralok K Samanta, Anindita Chakraborty, and Somananda Sanyal.

A warm thanks to all my former labmates Dr. Ayan Datta, Dr. S. Lakshmi, Dr. Debrabata Parihari, Dr. Sairam S. Mallajosyula, Dr. Sudipta Dutta, Dr. Tarun K. Mandal, Dr. Sasmita Mohakud, Dr. Elizabeth C. V.,

Dr. Anusuya Kundu, Shrinwantu, Santanu, Wasim, Ershaad, Alex, Rajavarman, Manju, Ranjib, Gautam, Aniket, Rukhsan and Ankita whose company I enjoyed and the wonderful scientific discussions which helped me in my work. Ayan da helped me immensely with his vast knowledge of science and in the basic understanding of my concepts. He was always there whenever I needed his support and still he does. Sudipta da.... well I have not much words to describe the supporting hand he has lend me from the very first day, when I joined here. I learnt many things from him, both in personal and professional life. Will never forget our movie sessions in lab at weekends, early morning football sessions, cooking parties ... in which he always took an active part. No, it wasn't about fun always, as a teacher, as a senior and as an elder brother, I learnt a lot about computation, designing problems, thinking about scientific problems from a different angle from him. Life is all about learning and implementing, and from Sudipta da and Ayan da, I learnt many which I wish to implement in my life. Thanks a lot to my two "Dadas" (elder brothers)!

My present labmates Prakash, Pralok, Dr. Siam, Dr. Ganga, Dr. Meera, Sharma garu, Dibyajyoti, Wasim, Pallavi, Swastika, Somananda, Arkamita, Bradraj and Kavyashree created a wonderful environment and scientific atmosphere in the lab. We have been like a family and the love they bestowed on me is immense. Here, I must mention of my special friend Prakash, my friend since the first day in JNCASR. We joined lab at the same time and a special bonding had developed between us. His support as a friend, his knowledge, his clear concepts in Physics, his humour, helped me in more ways than one. I got a great friend in him, with whom scientific discussions

reached new heights, personal gossips were enjoyable, whose company was fun! I thank them all!

I also want to thank specially Dr. Siam, Dr. Meera, Pralok, Dibyajyoti, Arkamita, Somananda, Bradraj, and Kavyashree who helped me in completing my thesis writing. They did the last minute corrections in each chapter, taking time out of their busy schedule. No word will suffice for Somananda for her extensive help at all moments. Without all of their help, submitting within the deadline would have been a gargantuan job!

Thanks to all POCE, SRPF, and short-term visitors in our lab, especially Deepthi, Anisha and Nabanita for being so friendly.

My heartfelt regards to my teachers from school, from whom I learnt the basics of loving and sharing and the first lessons on being a good natured person. Thank You! My sincere regards also to my teachers in Jadavpur University, who ignited the passion to do research in scientific field. Special mention of my childhood teachers Shanti Sir, Monoranjan Sir, Debranjan Sir and Saikat da must be made for their immense encouragement, inspiration and support.

My stay in JNCASR was made memorable by the presence of my wonderful friends here. They made the 5 year research life span a period of nostalgia for the years to come. Can't remain without mentioning my friends, seniors and juniors here, Suman, Debu, Partha, Prakash Kanoo, Sudip, Arup, Sutapa, Madhura, Sananda, Vishwas, Amit, Gayatri, Mighfar, Sabyasachi, Pranab, Gopal Bhai, Hembram Bhai, Sandy da, Himadri da, Anupama, Arpan, Rana, Ritesh, Sudeshna, Anirban, Koushik, Sisir, Tarak, Sandeep, Satyanarayan, Avinash, Vasudevan, Pramod, Satyaprasad, and Rajdeep for

creating a enjoyable life here, at JNCASR.

"The reason it hurts so much to separate is because our souls are connected." -Nicholas Sparks, The Notebook

Yes, I am experiencing the truth of the words, truly. I am so much connected to all here that saying Fare-thee-well is tough.

My sincere acknowledgement to ALL!

Synopsis

Biomolecules, particularly DNA quadruplexes (Q-DNA), a guanine rich sequence containing four-stranded nucleic acids, are of potential interest in anti-cancer therapy for selective designing of ions and small molecules, which can stabilize the quadruplex structure. In addition, recently, there is great research interest in using Q-DNA in nano-technological applications because of their increased structural stability compared to duplex DNA. Another class of low-dimensional systems, where the carrier (electron and hole) motions are restricted within reduced dimensions, have triggered a great deal of study in both fundamental and applied sciences. Low-dimensional quantum systems have garnered increase attention over the last few decades, fuelled by a constant stream of striking discoveries and by the potential for, and realization of, new state-of-the-art electronic device architectures. Restricting the electron's motion in reduced dimensions ("quantum confinement") leads to many exciting quantum phenomena. The interest in these low dimensional devices stem both from Understanding the quantum nature of the exotic phenomena and the applcations these systems would show and thus is very challenging. Moreover, controlling the electronic and magnetic properties of these materials is desired for their better device applications under

appropriate external perturbations.

In this thesis, structural dynamics, energetics and electronic and optical properties of a class of biomolecules are investigated in detail. Additionally, electronic structures, magnetic properties and quantum transport of a few mesoscopic nanostructures, such as, graphene sheets, graphene nanoribbons and carbon nanotubes, have been studied. Classical molecular dynamics simulations and density functional theory, coupled with non-equilibrium transport formalisms have been used to elucidate their structure-function relationships.

The thesis is divided into the following six chapters.

In the first chapter, a brief introduction to a few molecular systems, which are bio-relevant and different types of base-pairing effects on the formation of various nucleic acid quadruplex structures consisting of G(Guanine)-quartets (G_4), such as DNA (de-oxy ribo nucleic acid), RNA (ribo nucleic acid) and PNA (peptide nucleic acid) quadruplexes (G_4-DNA, G_4-RNA and G_4-PNA), which are found in human genome, is provided. Additionally, a brief description of a few low-dimensional graphitic materials, such as, graphene and carbon nanotubes and their boron nitride analogue: hexagonal boron nitride (h-BN) sheet and their nanoribbons are also provided. Both experimental and existing theoretical overviews of DNA/RNA/PNA quadruplex structures and graphitic materials have also been outlined. Several key factors that regulate and stabilize quadruplex structure in physiological conditions are addressed. In addition, how the electronic structure and magnetic properties of graphitic materials respond to different external perturbation, *e.g.*, defects, doping, substitution, have also been presented in detail.

Overviews to the different computational techniques which are used in subsequent chapters for exploring structure and electronic properties, particularly, molecular dynamics (MD) simulations, used for flexible biomolecules as well as density functional theory (DFT) have also been discussed.

Structural stability, optical and charge transfer properties of different hydrogen bonded nucleobase pairs found both in duplex and quadruplex DNA and variation of their properties in presence of different monovalent and divalent ions are reported in the second chapter. Additionally, the structural dynamics and stability of various DNA, RNA and PNA quadruplex structures in presence of explicit water and ions using MD simulation at T=300 K and 1 atm pressure, are investigated in detail. The structure and optoelectronic properties of porphyrin and different metal-porphyrin intercalated G_4-DNA have also been studied. Using DFT calculations, the electronic, optical and charge transfer properties for all the biomolecules are investigated and discussed in detail. Our results suggest that G_4-PNA is stable in presence of NaCl and KCl salts, as was also found for the G_4-DNA. Interestingly, a new quadruplex structure, G_4A_4-DNA, which consists of consecutive planes of G- and A+ quartets, stabilized through simultaneous binding to cations and anions, respectively, has been proposed. Moreover, our study shows that this quadruplex structure is stable under different salts solution, *e.g.*, LiCl, NaCl and KCl at T=300 K. Also, the present investigation suggests large charge carrier (hole) mobility for G_4-DNA. Additionally, it is shown that the divalent metal ion (Cu^{2+}) can stabilize G_4-DNA and form a ferromagnetic one-dimensional chain along the quadruplex strand direction, which may find potential applications in magnetic storage and memory devices.

Understanding the interactions of different nucleosides and single-stranded DNA with graphene is needed for dispersing hydrophobic graphene in aqueous solution and for the possible applications in DNA sequencing. In the third chapter, the interactions of various nucleosides and their stable quartets, adsorbed on graphene, have been studied using both MD and DFT simulations. The detailed structural and dynamical aspects of various single-stranded DNA (ssDNA) dodecamer interacting with graphene in aqueous solution are explored using MD simulations within NPT (T = 300 K and P = 1 atm) ensemble. The results suggest that, the ssDNA containing purine nucleobases (Adenine (A) and Guanine (G)) strongly interact with graphene in comparison to the pyrimidine nucleobases (Thymine (T) and Cytosine (C)) containing ssDNA. Interestingly, we find that mixed base sequences ssDNA, such as ssd$(AGTC)_3$ considered, show higher binding strength compared to all others. The effects of various competing forces, *e.g.*, hydrogen bonding and π stacking interactions, are discussed in detail. The simulation results provide atomic understanding of recent experimental findings for the formation of different ssDNA architectures observed on graphene surface depending on the nucleotide sequences.

Since the discovery of graphene and h-BN sheets, there is an increasing research interest among both theoreticians and experimentalists for controlling their electronic and magnetic properties for practical electronic applications. Motivated by this, the effects of boron and nitrogen substitution on graphene and graphene nanoribbons have been studied extensively using DFT and discussed in the fourth chapter in detail. The two-dimensional $B_xN_yC_z$ sheet

is considered, where the particular focus has been given towards the formations of various B_xN_y domains in graphene and their energetic behaviours. The changes in electronic and magnetic properties are also addressed for this 2D $B_xN_yC_z$ hybrid graphitic material. Our results suggest various possible tunable electronic states depending on the size and shape of B_xN_y domains hybridized with graphene. Furthermore, the effect of 'B' and 'N' atoms substitution for the 'C' atoms in zigzag graphene nanoribbons is also considered. Along with several possible electronic states, the results suggest robust half-metallic state, where one type of spin channel conduct while the other spin channel remain semiconducting or insulating. For possibility in practical device applications, the spin-polarized electrical transport properties is calculated using Non-equilibrium-Greens-Function (NEGF) method coupled with DFT. The results suggest 100 % spin-polarized currents within small bias windows for these modified graphene nanoribbons.

In the fifth chapter, the effect of various metals, including both transition metals (Fe, Co, Ni) and non-transition metals (Pd, Ag, Pt and Au) and their larger clusters, on graphene and h-BN sheets properties are explored using DFT calculations. The results show a large binding affinity of the porous graphene and h-BN sheets for the adsorbed Fe than their pristine analogues. Moreover, a spin-switching behavior is found for the single-layer graphene and h-BN decorated Fe complexes with the variation in sheet's intriguity and chemistry.

Additionally, bi-layer sandwich complexes of Fe for both the porous graphene and h-BN sheets have been studied, and the results are contrasted to their

pristine bi-layer analogues. An interesting variation of electronic and magnetic states depending on the adsorbed metal type and nature of the sheets are indicated.

Molecular charge transfer effects on graphene and single-walled carbon nanotubes (SWCNTs) electronic structures are studied using DFT methods and presented in sixth chapter. The two classes of organic molecules: electron withdrawing molecules (TCNE and TCNQ) and electron donating molecule (TTF) have been considered for investigating the response of molecular doping on graphene and SWCNTs electronic properties. The presence of surface adsorbed electron acceptors and donors have been found to modulate the carrier types (electron and hole) and carrier densities, because of the molecular charge transfer effects. Additionally, the adsorption of donor/acceptor molecules causes small local structural distortions of these materials. It is found that the electron acceptors have higher binding affinity for these graphitic materials than that of the electron donor molecules because of the greater extent of charge transfer. Moreover, we find that the electron acceptors bind strongly with metallic SWCNT than semiconducting SWCNT, corroborating with the experimental results. The study also suggests that the surface adsorption of selective donor or acceptor molecules on the SWCNTs surface can change the electronic state from metal to semiconductor or vice versa, depending on the nature of adsorbed molecules. In fact, the present study unravels the microscopic understanding of a few experimental observations that were reported recently.

List of Publications

Publications Related to the Thesis Work

1. *Tuning the Electronic Structure of Graphene by Molecular Charge Transfer: A Computational Study*
   Arun K. Manna and Swapan K. Pati,
   Chem. Asian. J. **4**, 855 (2009).

2. *Doping Single-Walled Carbon Nanotubes Through Molecular Charge-Transfer: A Theoretical Study*
   Arun K. Manna and Swapan K. Pati,
   Nanoscale **2**, 1190 (2010).

3. *A study of graphene decorated with metal nanoparticles*
   K. S. Subrahmanyam, **Arun K. Manna**, Swapan K. Pati, and C. N. R. Rao,
   Chem. Phys. Lett. **497**, 70 (2010).

4. *Doping of Graphene: A Computational Study*
   Arun K. Manna and Swapan K. Pati,
   World Scientific Publishing Co. Pte. Ltd. Singapore: **ISBN: 13-978-981-4329-35-4 (Book Chapter)**, 59 (2011)

5. *Tunable Electronic and Magnetic Properties in $B_xN_yC_z$ Nanohybrids: Effect of Domain Segregation*

   Arun K. Manna and Swapan K. Pati,

   J. Phys. Chem. C **115**, 10842 (2011).

6. *Designing Tunable Electronic and Magnetic Properties of Graphene: A Theoretical Perspective*

   Arun K. Manna and Swapan K. Pati,

   Int. J. Mod. Phys. B **26**, 1242003 (2012).

7. *Theoretical Understanding of Single-stranded DNA Assisted Dispersion of Graphene*

   Arun. K. Manna and Swapan K. Pati, J. Mater. Chem. B **1**, 091 (2013).

8. *Effect of Edge States on the Electronic, Magnetic and Transport Properties of BN-Fused Polyacene Zigzag Nanoribbons*

   Arun. K. Manna and Swapan K. Pati, J. Mater. Chem. C **1**, 3439 (2013).

9. *Metal Modified DNA Quadruplex: A Promising Molecular Wire*

   Arun. K. Manna and Swapan K. Pati (submitted, 2013).

10. *Diverse Structures and Electronic Properties of DNA and PNA Quadruplexes: A Computational Study*

    Arun. K. Manna, Prabal K. Maiti and Swapan K. Pati (submitted, 2013).

Other Publications by the Author

11. *The role of H bonding and dipole-dipole interactions on the electrical polarizations and charge mobilities in linear arrays of urea, thiourea and their derivatives*
    Shrinwantu Pal, **Arun K. Manna** and Swapan K. Pati,
    J. Chem. Phys. **129**, 204301 (2008).

12. *Intrinsic Half-Metallicity in Modified Graphene Nanoribbon*
    Sudipta Dutta, **Arun K. Manna** and Swapan K. Pati,
    Phys. Rev. Lett. **102**, 096601 (2009).

13. *Graphene analogues of MoS_2 and WS_2*
    H. S. S. Ramakrishna Matte, A. Gomathi, **Arun K. Manna**, Dattatray J. Late, Ranjan Datta, Swapan K. Pati and C. N. R. Rao,
    Angew. Chem. **49**, 4059 (2010).

14. *Interaction of metal oxide nanoparticles with graphene*
    Barun Das, Biswajit Choudhury, A. Gomathi, **Arun K. Manna**, S. K. Pati and C. N. R. Rao,
    Chem. Phys. Chem. **12**, 937 (2011).

15. *Beyond the Förster formulation for resonance energy transfer: the role of dark states*
    C. Sissa, **A. K. Manna**, F. Terenziani, A. Painelli and S. K. Pati,
    Phys. Chem. Chem. Phys. **13**, 12734 (2011).

16. *Visible-near infrared and fluorescent copper sensors based on julolidine conjugates: selective detection and fluorescence imaging in living cells*

Debabrata Maity, **Arun K. Manna**, D. Karthigeyan, Tapas K. Kundu, Swapan K. Pati and T. Govindaraju,
Chem. A Eur. J. **17**, 11152 (2011).

17. *Computational Studies on Structural and Optical Properties of Single-stranded DNA encapsulated Silver/Gold cluster*
Pralok Kumar Samanta, Ganga Periyasamy, **Arun K. Manna** and Swapan K. Pati,
J. Mater. Chem. **22**, 6774 (2012).

18. *Thieno Analogues of RNA Nucleosides: A Detailed Theoretical Study*
Pralok K Samanta, **Arun K. Manna** and Swapan K. Pati,
J. Phys. Chem. B **116**, 7618 (2012).

19. *Resonance energy transfer between polar charge-transfer dyes: A focus on the limits of the dipolar approximation*
C. Sissa, F. Terenziani, A. Painelli, **A. K. Manna** and S. K. Pati,
Chem. Phys. **404**, 9 (2012).

20. *Structural, Electronic, and Optical Properties of Metallo Base Pairs in Duplex DNA: A Theoretical Insight*
Pralok K. Samanta, **Arun. K. Manna** and Swapan K. Pati,
Chem. Asian. J. **7**, 2718 (2012).

21. *Effect of Imide Functionalization on the Electronic, Optical and Charge Transport Properties of Coronene: A Theoretical Study*
Somananda Sanyal, **Arun K. Manna** and Swapan K. Pati,
J. Phys. Chem. C **117**, 825 (2013).

22. *Computational Studies on Non-covalent Interactions of Carbon and Boron Fullerenes with Graphene*
Arun K. Manna and Swapan K. Pati,
ChemPhysChem **14**, 1844 (2013).

23. *Discrete dinuclear complex to extended 2D compound in a Cu-azido system by controlling coligand stoichiometry: synthesis and magneto-structural correlations*
Anindita Chakraborty and Lingampalli S. Rao, **Arun K. Manna**, Swapan K. Pati, Joan Ribas and Tapas K. Maji,
Dalton Transactions **42**, 10707 (2013).

24. *Stability and Electronic Structure of Carbon Capsules with Superior Gas Storage Properties: A Theoretical Study*
Arun K. Manna and Swapan K. Pati,
Chem. Phys. **DOI: 10.1016/j.chemphys.2013.09.004** (2013).

List of Figures

List of Tables

Contents

Chapter 1

Introduction

Biomolecules are a class of soft-materials, which are considered to be essestial for controlling various physiological functions in all living organisms. Deoxyribonucleic acid (DNA) and Ribonucleic acid (RNA), the most relevant biomolecules, are the polymer of nucleotide, which contains nucleobases and sugar-phosphate backbone. In 1953, Watson and Crick [1] first proposed the DNA double helical structure, which describes the unique base-pairing effects in canonical duplex, DNA. Specific base sequences of duplex nucleic acids stores the genetic informations. Moreover, the nucleic acids also regulate and catalyze various important biological processes. In order to perform these diverse biological functions, nucleic acids, not only form the canonical duplex structures, but it also adopts various non-canonical conformations. In fact, there are various non-cannonical nucleic acid structures, which includes triplexes, hairpin loops, cruciform, poly(dA), duplex (A-motif) junctions, G-quadruplex structures, and many other higher order structures [2–5]. Among all these non-standard nucleic acids structures, G-quadruplexes have drawn

much attention because of their both in vivo and in vitro applications. Many experimental as well as theoretical studies have been devoted to deeply understand their biological functions and possible nanobiotechnological applications [6–12].

Low-dimensional materials are of increasing interest to both theorists and experimentalists alike, owing to their novel properties, which arise from quantum confinement effects [13–19]. Due to the constrained degrees of freedom in reduced length scale, the electronic correlations play the most crucial role, giving rise to many exotic properties that have drawn much research interest in condensed matter and materials science over the decades [20–24]. Recent experimental advancements, like thin film deposition [25–32], mechanically controlled break junction [33–36], scanning tunneling microscopy (STM) [37–40], transmission electron microscopy (TEM) [41–43], atomic force microscopy (AFM) [44–49], angle resolved photo emission spectroscopy (ARPES) [50–54] have opened up a new dimension of fabricating and characterizing the low-dimensional materials. A large number of theories have also been proposed to account for the interesting behavior of materials at the reduced length scale.

In this thesis, we have investigated a class of biomolecules, particularly, DNA quadruplexes and a number of low-dimensional materials and have explored their interesting properties, originating from various interactions.

In this chapter, we give a brief overview of DNA and G_4-DNA quadruplexes and a few low-dimensional materials and various theoretical models and numerical techniques that are used to study their structures and interesting electronic properties. In the next section, we discuss the structure

and various remarkable aspects of duplex and quadruplex DNA. Thereafter, we discuss about light elements based materials in two-dimension and quasi one-dimension. We focus on graphene, hexagonal boron nitride and hybrid boron-carbon-nitrogen (BCN) sheets and their nanoribbon materials. We also briefly address some interesting electronic properties of carbon nanotubes. In section 1.3, we present a brief discussion on various theoretical methods and models used to capture the interesting aspects of biomolecules and low-dimensional materials. Subsequently, we discuss various numerical methodologies which have been adopted in the thesis to study the DNA quadruplexes and the low-dimensional materials. Finally, we provide brief outline of the subsequent chapters that constitute the thesis at the end of this chapter.

1.1 Nucleic Acids: Potential Biomolecules

Nucleic acids are essential biomolecules present in almost all the living organisms. They are the central molecules for regulating transmission, gene expression and conservation of genetic information. The early experimental works by Avery *et al.* [55] and Hershey *et al.* [56] demonstrated the role of DNA as the carrier of genetic information. As already mentioned, Watson and Crick [1] were the pioneer scientists, to discover the DNA double helical structure based on the X-ray fiber diffraction patterns produced by Franklin *et al.* [57] and Wilkins *et al.* [58], together with the chemical evidence of base complementarity proposed by Chargaff [59]. Since the realization of DNA structure, there have been remarkable research interest for understanding

the molecular basis of the various biological functions that are regulated by DNA and investigating the intricate relationship between structure and function.

Nucleic acids are composed of repeatative units of nucleotides, and are also called oligo-nucleotide or poly-nucleotide. Each nucleotide consists of a nitrogeneous base, a sugar, and a phosphate group. The structures of the five nucleosides are shown in Fig.1.1. Note that, Adenosine (A) and Guanosine (G) are purine nucleosides, whereas, Cytosine (C), Thymidine (T) and Uridine (U) are pyrimidine nucleosides. All the nucleosides are found in DNA with the exception for U, which is present only in RNA. Interestingly, nucleic acids form both single-stranded DNA (ssDNA) and canonical double stranded DNA (duplex DNA) as well as many non-standard structures, such as triplex, i-motif, hairpin loops and four stranded structures (quadruplexes) with varying molecular topology. Below, we dicuss the nucleic acids duplex and quadruplex structures in detail.

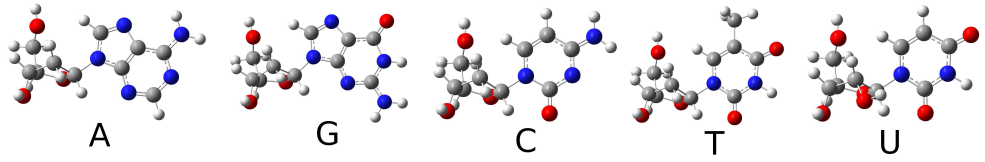

Figure 1.1: Schematic diagrams of five nucleosides (A = Adenosine, G = Guanosine, C = Cytosine, T = Thymidine and U = Uridine). The white, gray, blue and red colours indicate hydrogen (H), carbon (C), nitrogen (N) and oxygen (O) atom, respectively.

1.1.1 Nucleic Acid Duplex

Nucleic acids are the polymer of nucleotides, which carry all the genetic informations through the base-sequences. This constitutes the primary structure of nucleic acid molecules. The polymers of nucleotide consitute single-stranded DNA or RNA (ssDNA or ssRNA) depending on the nature of sugar units present. Although DNA and RNA possesses similar physical properties, the presence of 2′-hydroxy in ribose in RNA and its replacement by 2′-deoxyribose in DNA causes substantial differences in their chemical properties. The 2′-hydroxy group in RNA affects the tertiary structure of RNA in comparison to the DNA structure through the formation of extra hydrogen bonds. This is why the tertiary structure of ssRNA is more stable and commonly found than the tertiary structure of ssDNA. A DNA strand possesses a well defined directionality because of the presence of asymmetric phosphodiester bonds between the phosphate group and third and fifth carbon atoms of adjacent sugar rings. The sugar-phosphate backbone of a ssDNA or ssRNA run from 5′ to 3′ direction, with the 5′-end being attached with a terminal phosphate group and the 3′-end being with the terminal hydroxyl group. A schematic figure of helical shaped ssDNA with Guanine (G) base-sequences (poly-dG_{12}) is shown in Fig.1.2.

The WC (Watson Crick) complementary base-pairing results in the structure of a nucleic acid duplex. In a double stranded DNA or RNA, nucleobase Adenine (A) and Guanine (G) specifically form two and three hydrogen bonds with the complementary bases, Thymine (T in DNA) and Uracil (U in RNA) and Cytosine (C), respectively. On the other hand, in ssDNA or ssRNA,

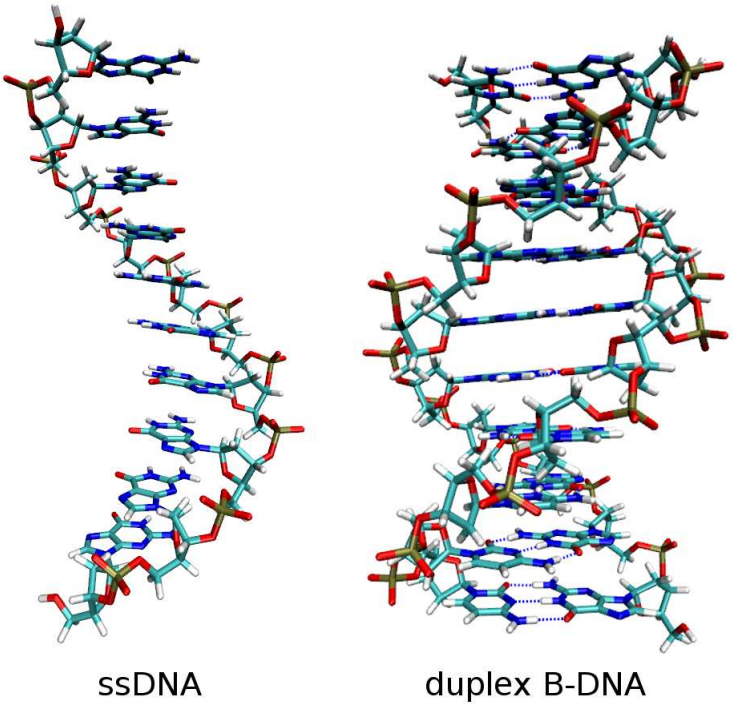

Figure 1.2: Schematic diagrams of single-stranded DNA (ssDNA) and double helical DNA (B-DNA).

intramolecular base pairs between complementary bases determines the secondary structure of the molecule. Note that, all naturally occurring DNAs are double stranded. Moreover, the double stranded DNA structure is regular and uniform because of the similar sizes of A-T and G-C WC base pairs. The A-T base pair has two H-bonds; each nucleobase shares one H-bond donor and one H-bond acceptor, while, G-C base pair has three H-bonds; G forms one H-bond acceptor and two H-bond donor. In the DNA double helix, it is found that the complementary strands run in opposite diections and are aligned anti-parallel to each other. The most common conformation of duplex DNA under physiological conditions is B-DNA (Fig.1.2), which is characterized by 1) an average helical twist of 36^o, 2) the completion of one

Table 1.1: Average structural parameters of three different DNA conformations.

Geometrical Parameters	A-DNA	B-DNA	Z-DNA
Helix type	right-handed	right-handed	left-handed
Repeating unit	1 bp	1 bp	2 bp
Rotation per bp	32.7^o	35.9^o	30^o
No. of bp per turn	11	10.5	12
Rise per bp along axis	2.3 $\mathring{A}$	3.32 $\mathring{A}$	3.8 $\mathring{A}$
Diameter	23 $\mathring{A}$	20 $\mathring{A}$	18 $\mathring{A}$

full helix turn after every 10 base pairs, 3) the helix diameter is found to be approximately 20 $\mathring{A}$ and 4) the helical rise is estimated to be about 3.4 $\mathring{A}$ [60]. However, depending on the environmental conditions, duplex DNA can adopt many other conformations, such as A-DNA and Z-DNA [61]. As already mentioned, the DNA adopts B-conformation, which is a right-handed helical duplex structure under physiological conditions. Under dehydration, DNA is found in A-DNA form in organisms, which is also a right-handed helix, with a shallow, wide minor groove and a narrower, deeper major groove. Contrary to the right-handed helical structures of A- and B-DNA, the Z-DNA is a helf-handed helix and has a structure that repeats every two base pairs. The main structural differences of the three DNA conformations are summarized in Table 1.1 [62, 63].

The stability of duplex DNA and RNA are determined by the H-bonding interactions and π-π-stacking interactions to compensate the destabilization caused by the electrostatic interactions between the negatively charged phosphate groups in two strands. However, the destabilization energy can be minimized by neutralizing the phosphate backbone with the cations, e.g.,

Na^+, K^+ etc. A schematic structure of duplex DNA containing G-C base pairs ($d(GC)_{10}$) is shown in Fig. 1.2.

1.1.2 Nucleic Acid Quadruplex

Apart from the canonical duplex DNA structures, which have been discussed above, there are several non-canonical and polymorphic nucleic acid structures present in organisms, which regulate various catalytic biological processes. These non-standard nucleic acid structures include DNA triplexes, hairpin loops, internal loops, junctions, i-motif and G-rich quadruplexes and many higher order structures [2–5]. Among all these non-canonical DNA structures, G-quadruplexes have received tremendous attention because of their potential function in vivo as well as in vitro applications [9, 10, 64–73]. G-quadruplex is a four-stranded nucleic acid structure with stacked G-quartets (also known as G-tetrads), which are held together via eight Hoogsteen hydrogen bonds. Structural investigation of G-quadruplexes have demonstrated that, the G-rich nucleobase sequences are prone to form these four-stranded structures under appropriate conditions. Moreover, they show various structural polymorphism depending on the base-sequences, loop connectivity and the experimental conditions. G-quadruplex structure can form from four separate single-stranded nucleic acids structures, known as tetramolecular, from two single-strands, called bimolecular, and only from one single-strand, termed as unimolecular [68,74–76]. Moreover, depending on the base-sequences and type of connecting loops, G-quadruplexes can form parallel and anti-parallel structures. Several high resolution crystal structures were

established for both the parallel-and anti-parallel-stranded guanine tetraplex with varying nucleobase sequences from organism [77–79]. The crystal structure of parallel-stranded G-quadruplex was first predicted by Parkinson *et al.* from human telomeric DNA in K^+ solutions [79].

However, the existence and possible structure of G-quartets were first proposed about 50 years ago by Gellert *et al.* [80]. Since then, there have been lot of attempts in exploring the G-quadruplex structures, and understanding their functions both in experiments and in several theoretical studies [81–84]. Among the various polymorphic G-quadruplexes, in particular, a major attention has been given to the G-quadruplex structures formed by human telomeric sequences, which consists of tandem repeats of 5′-TTAGGG-3′, and there is a 3′ overhand of the G-rich strand at the end of the chromosomes [85]. It is known that G-quadruplex DNA inhibits the activity of the enzyme, telomerase, as the enzyme cannot act on the G-quadruplex structure. Therefore, the development of G-quadruplex stabilizing ligands has become an area of immense research interests [10, 66, 86–90]. It was found that, in general, G-quadruplex binding ligands possesses a large aromatic planar surface, which stabilize the quadruplex structure through strong π-π-stacking interactions. To illustrate a few, the porphyrin derivatives, cationic TMPyP4 and Phthalocyanines, have been found to be effective for stabilizing the G-quadruplex structures [91, 92].

The most important unit of a G-quadruplex structure is the nucleobase G-quartet, which is formed by a planar association of four G nucleobases forming eight Hoogsteen hydrogen bonds [93]. A schematic of a G-quartet is shown in Fig. 1.3. As shown in Fig. 1.3, the core of the G-quartet consists

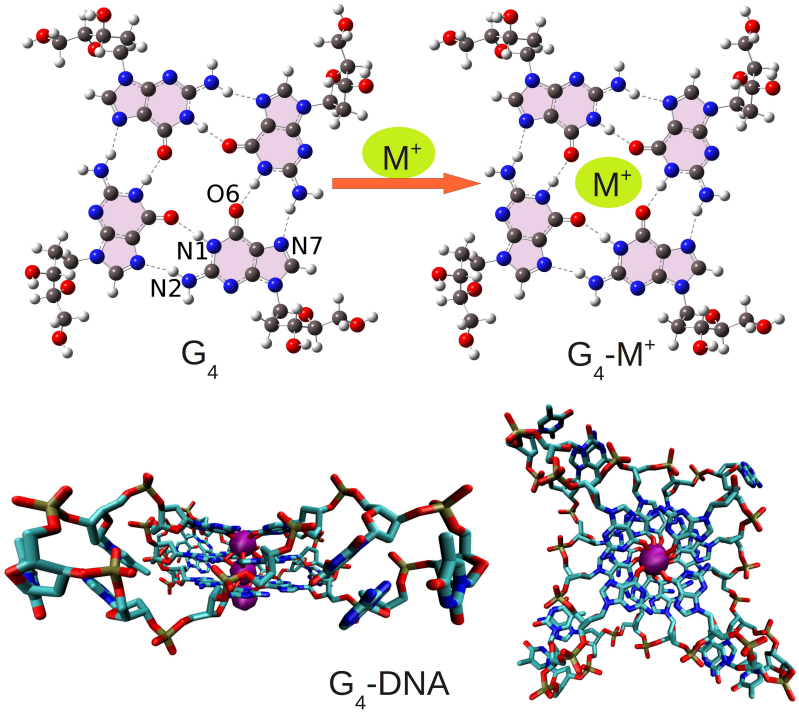

Figure 1.3: Schematic of a G-quartet (G_4) structure stabilized by cation (M^+) and the structure of a K^+ ions stabilized DNA quadruplex (PDB ID: 1KF1). The white, gray, blue, red and purple colours indicate hydrogen (H), carbon (C), nitrogen (N), oxygen (O) and potassium (K) atom, respectively.

of four O6 oxygen atoms pointing towards the center of the G-quartet. Consequently, the centre of the G-quartet is enriched with negative electrostatic potential. Thus, G-quartet can be further stabilized by coordination with cations of suitable sizes, which is schematically shown in Fig. 1.3. In fact, it was shown that the G-quadruplex structures are only stable in presence of monovalent cations, such as Na^+ and K^+ in aqueous solution. It was also demonstrated that the core region of G-quadruplex structure traps monovalent cations with suitable sizes in order to gain the structural stability. The

cations, Na^+ and K^+ were found between the two G-quartets of a quadruplex structure, and thus, the effective coordination number of the cation becomes eight (see Fig. 1.3). G-quadruplex structures are stable under optimal physiological conditions, and the stability of the quadruplex structure is due to the H-bonding interactions within a G-quartet, π-π-stacking interactions between the successive G-quartets plane and the electrostatic interactions induced by coordinated metal ions. It is also clear that the structural stability of G-quadruplexes is greater in comparison to the duplex DNA stability, and hence, a potential candidate for biological applications. In fact, there have been several theoretical demonstrations [94, 95], suggesting their use as the efficient molecular wire because of the enhanced structural stability and larger carrier (hole) mobility along the strand direction.

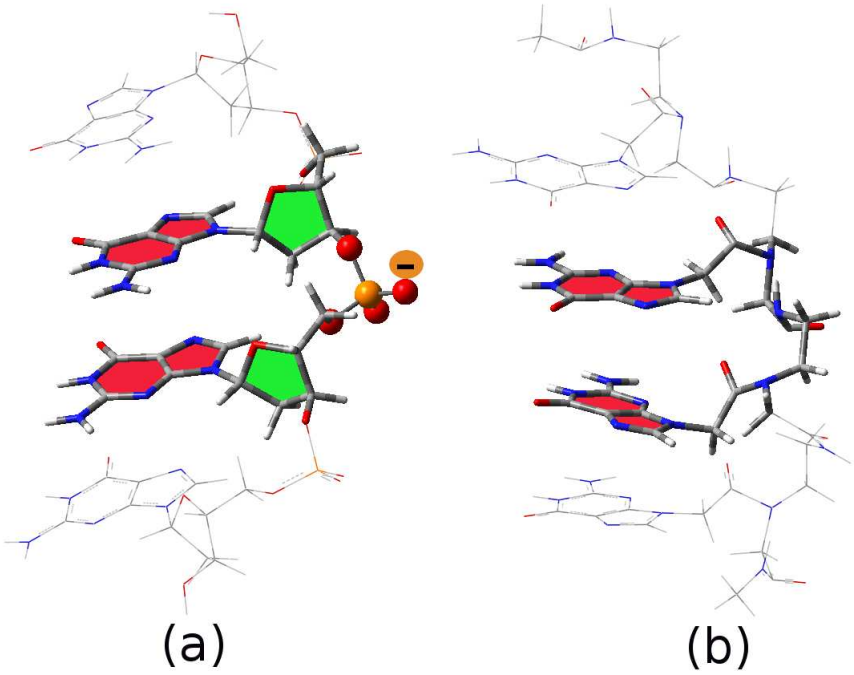

Figure 1.4: Schematic of a ssDNA with negatively charged sugar-phosphate backbone (a) and a ssPNA with neutral peptide backbone (b).

However, there are several experimental reports, which have suggested the formation of G-quadruplex structures from RNA and PNA (peptide nucleic acid) under suitable conditions [96–103]. It is important to note that, unlike DNA, PNA has neutral peptide backbone, as schematically shown in Fig. 1.4. Moreover, there are studies which investigated the hybridization of DNA and PNA to form the many interesting nucleic acid structures [104–106]. In this thesis, we have studied the structure and conformational dynamics of various DNA, RNA and PNA quadruplex structures with and without the presence of monovalent cations (Li^+, Na^+, K^+) using molecular dynamics simulations. Moreover, we have investigated a sets of new quadruplex structures which can simultaneously binds to cations and anions, thus, acting as ion-pair receptor. Additionally, we have studied the electronic structure, optical properties and charge transfer characteristics of a few model DNA quadruplex structures. At the end of the chapter 2, we have discussed the stability of G-quartets in presence of cations other than Li^+, Na^+ and K^+ and also have explored their electronic and optical properties. Finally, we have investigated the structures of porphyrin and metal-porphyrin intercalated G-quadruplexes.

1.2 Graphitic Materials

In the recent years, two-dimensional (2D) materials have gained extensive research attention because of both their interesting basic physics and their possible applications in future generation devices. The sophistications of recent experimental techniques have made possible the fabrication of two-dimensional (2D) materials with one atom to few atom thickness. These

materials have found remarkable device applications in electronics as well as in photo-voltaics [107–118]. The recent experimental findings of graphene enriches the family of 2D materials, opening a new platform of exploring two-dimensional electron gas systems.

Graphene, a one-atom thick layer of sp^2 hybridized carbon atoms extented in 2D lattice, has been proposed as candidate for next generation electronic applications [119]. Materials that are similar to graphene and also materials derived from graphene, are known as graphitic materials. These include, hexagonal boron nitride (h-BN) sheet, quasi-one-dimensional (1D) nanoribbons of graphene and h-BN sheets, quasi-1D carbon nanotubes and zero dimensional (0D) fullerenes. In this introductory chapter, we provide brief literature overview of all these materials one-by-one. Here, we have mainly investigated the structure and various novel aspects of these graphitic materials.

1.2.1 Two-Dimensional Graphene and Hexagonal Boron Nitride Sheets

Although the allotropes of carbon, such as, zero-dimensional fullerenes [120], one-dimensional carbon nanotubes [121–123] and three-dimensional graphite have been known for a long time, their two-dimensional analogue has continued to be in back stage because of the long standing robust theoretical concepts [124–128]. These theories suggest that, due to thermal and quantum fluctuations, the perfect two-dimensional systems in free state would

segregate at finite temperature and thus, would cease to exist. The experimental realization of the two-dimensional carbon crystal continued to be a conjecture until 2004, when graphene was successfully isolated by mechanical exfoliation of highly oriented pyrolytic graphite [129–131]. This technique can provide high quality graphene flakes upto 100 μm in size. Arc-discharge technique has also been employed to obtain graphene flakes with the ease of doping with boron and nitrogen atoms [132]. However, the large graphene flakes are known to form ripples and thus, deviate from planarity in free state to gain stability, validating the pioneering theoretical concepts [133, 134].

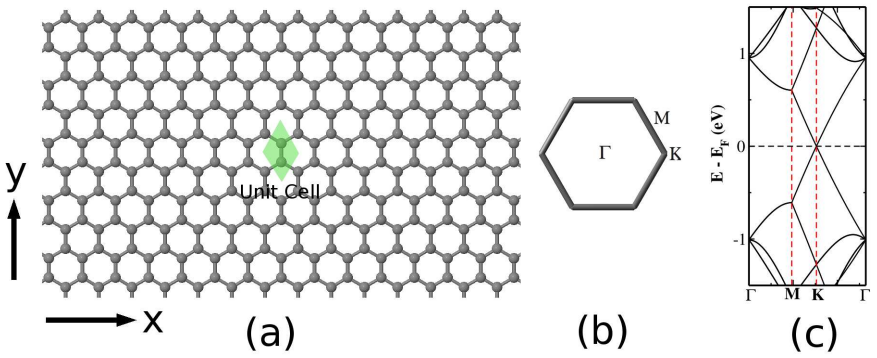

Figure 1.5: The schematic representation of the two-dimensional graphene sheet, periodic along x and y axes, with middle shaded region representing the rhombus unit cell containing two atoms (a). The hexagonal brillouin zone with high symmetric points (Γ, K and M) is also shown in (b). Panel (c) shows the electronic band structure calculated along the lines joining the high symmetric points, with linear bands dispersion close the Fermi level (E_F).

Graphene is a two-dimensional monolayer of carbon atoms tightly packed into a honeycomb lattice as shown in Fig. 1.5a. The carbon atoms form sp^2 hybridized network with three nearest neighbors, each at a distance of $\sim$1.42 Å, leaving one unhybridized half-filled p-orbital, perpendicular to the

graphene plane for every carbon. The rhombus unit cell contains the two atoms from two different sublattices making graphene a bipartite lattice. According to Leib's theorem [135], the electronic spins prefer to align antiferromagnetically within the two sublattice points in a bipartite lattice. Graphene can be considered as the parental compound for all other carbon allotropes of different dimensionalities. The wrapping of graphene, introducing curvature in terms of intervening five membered rings leads to fullerene. Rolling of graphene segments with different boundaries results into carbon nanotubes of varying chiralities. Moreover, three-dimensional graphite can be obtained by stacking the graphene atomic layers stabilized by van der Waals forces.

Since its discovery, graphene systems made possible the understanding of various properties in low-dimension and has opened up new possibilities in electronic device fabrications because of its very high charge carrier mobilities [129–131], long phase coherent lengths and linear energy dispersion at the Dirac point [136] (see Fig. 1.5c). In fact, it has shown a lot of promises for the replacement of silicon based electronic devices. Moreover, the observation of integer quantum Hall effect even up to room temperature [137–153], breakdown of adiabatic Born-Oppenheimer approximation [154], realization of Klein paradox [155–158], possibilities of high T_c superconductivity [159–163], metal free magnetism [164–175], ballistic electronic transport [176–180] etc. have made graphene the ideal candidate material for 21^{st} century research. As a truly two-dimensional nanostructure, graphene has garnered considerable interest, mainly due to its unique electronic and transport properties described by a *massless* Dirac equation [181, 182]. Because of these unique

and diverse properties, A. K. Geim and K. S. Novoselov were jointly awarded the prestigious Nobel Prize in physics in 2010 for their ground breaking experimental work on graphene in 2004 [129].

On the other hand, hexagonal boron nitride (h-BN) sheet, an iso-electronic analogue of graphene, also known as "white graphene", has been successfully materialized by various means [183–189]. Although, both the structures have similar 2D networks, they possess very contrasting electronic and optical properties. Unlike graphene, which is a zero band gap semiconductor, the h-BN sheet is a wide band gap ($\sim$5.9 eV) insulator [190], and is a promising material in optics and opto-electronics [191]. The relatively large ionicities of boron and nitrogen atoms than the carbon atom cause the optical and electronic properties of graphene and h-BN to be substantially different [190, 192]. Note that, graphene is stabilized because of the presence of delocalized π electron, whereas, the h-BN is stabilized by p_π-p_π B$\leftarrow$N charge transfer interactions.

In fact, the diversities in structural and electronic properties with exciting application possibilities have attracted a large community of both the theoretical and experimental groups all over the world to explore the plenty of room in the reduced dimension [181, 193–205].

1.2.2 Quasi One-Dimensional Graphene and Boron Nitride Nanoribbons

The electronic properties of low-dimensional materials are mainly governed by electronic correlations, their size and geometry and consequent boundary conditions. Finite termination of 2D graphene results in quasi one-dimensional ribbon like structures with two different possible edge geometries, namely zigzag and armchair as shown in Fig. 1.6. Accordingly, they are named as zigzag graphene nanoribbons (ZGNRs) and armchair graphene nanoribbons (AGNRs), respectively. They exhibit very different electronic properties arising from their contrasting boundary conditions. Note that, the atoms along a zigzag edge come from the same sublattice, whereas, the atoms from two different sublattices make bonds along the armchair edges.

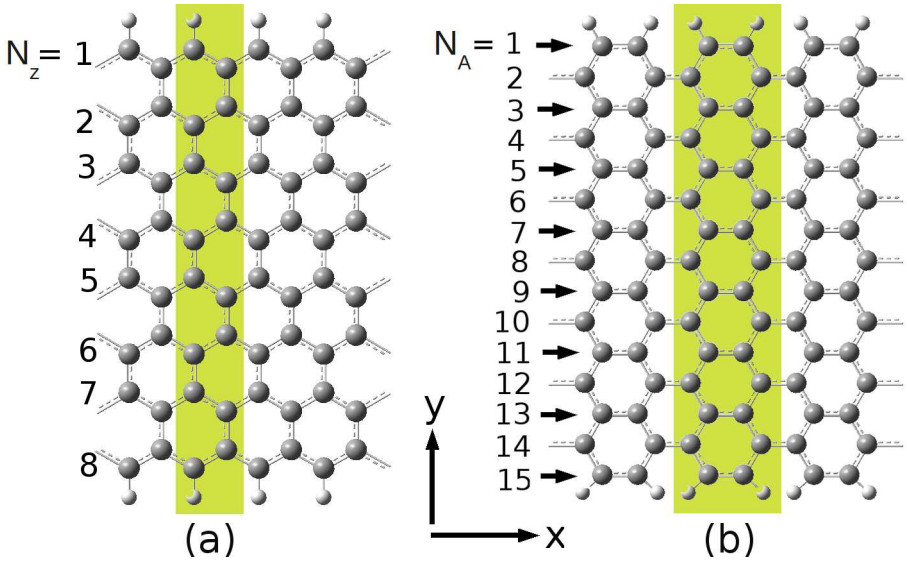

Figure 1.6: Schematic representation of the GNRs. The unit cells of zigzag (a) and armchair (b) graphene nanoribbons (GNRs) is indicated by the shaded regions. The GNRs are periodic along the x axis. The N_Z and N_A indices specify the width of zigzag and armchair GNRs, respectively.

Both the ZGNRs and AGNRs are schematically depicted in Fig. 1.6. As can be seen, the translations of the unitcell (shaded region in Fig. 1.6) along the x axis produce infinite GNRs with zigzag and armchair edges. Note that, although the translation up to infinity results in GNRs in true sense, the finite size systems with very large length/width ratio in principle can be considered as ribbons. These rectangular ribbons resemble traditional "Indian Saree". The width of these GNRs are determined along the cross ribbon direction. As it is evident from Fig. 1.6, the edge atoms in the cross ribbon direction of ZGNRs form armchair structure and hence, the width is determined by counting the number of zigzag chains in cross ribbon width (as shown by N_Z indices) and hence, the ZGNRs are named as N_Z-ZGNRs. In case of AGNRs, the width is determined by the number of atoms along the terminating zigzag edge in the cross ribbon direction, as shown by N_A indices, and named as N_A-AGNRs.

The replacement of all the "C-C" units by iso-electronic "B-N" units in GNRs structures results in quasi one-dimensional boron nitride nanoribbons (BNNRs) with the two edge geometries, namely, zigzag and armchair edges. Accordingly, they are termed as zigzag boron nitride nanoribbons (ZBNNRs) and armchair boron nitride nanoribbons (ABNNRs) with zigzag and armchair edge structures, respectively.

Although, both the GNRs and BNNRs have similar structures, they possess very different electronic properties. The finite termination of GNRs and BNNRs result in valency unsatisfied edge dangling states. These edge states are reactive, and generally, undergo various edge reconstructions. To

stabilize the edge states, the hydrogen passivation is considered to be practical from the energetics points of view. In fact, there are large number of studies [206–214], which have considered the H-passivation in exploring the electronic structure of both the GNRs and BNNRs. The H-passivated ZGNRs show spin-symmetric semiconducting properties for the low-energy antiferromagnetic ground state structure [206], whereas, the corresponding ZBNNRs are wide band gap semiconductors [215, 216]. However, the nonmagnetic state of H-passivated ZGNRs shows metallic properties, and is only a few meV higher in energy compared to its stable antiferromagnetic state, and can be accessible at room temperature [214]. Contrary to the ZGNRs, however, ZBNNRs can be either magnetic or nonmagnetic determined by the details of their edge states [217, 218]. However, the band gap values of all these nanoribbons depend on the ribbon widths. Moreover, similar to the AGNRs, which show semiconducting properties [207], the ABNNRs also display semiconducting behaviors independent of their widths [215,219]. Among all these GNRs and BNNRs, the zigzag edge nanoribbons exhibit interesting electronic and magnetic properties due to their typical edge states. Thus, in this thesis, we have investigated the electronic structure details of the zigzag graphene and boron nitride nanoribbons.

Recent experimental sophistications have made possible the materialization of such systems of varying widths with almost smoothly defined edges. These techniques can be classified into two categories: bottom up and top down approaches. The former follows the strategy of attaching small molecular building blocks to grow giant graphene structures using elegant synthetic chemistry route [220–223]. This approach can provide desired graphene

nanostructures like nanoribbons, nanodiscs etc. with full control over their edge geometries. Most importantly, these structures with smooth edges can be efficiently isolated in single layers and can be used in device fabrications. On the other hand, the top down approach uses diverse methodologies with ease for efficient device integration. Following this approach, the graphene nanoribbons (GNRs) has been achieved by etching the graphene surface with STM (scanning tunneling microscopy) tip applying higher (than required for imaging) constant bias potential with atomic level precision [224]. The epitaxially grown few layer graphene has also been patterned by conventional lithographic techniques to fabricate GNR based devices [225–228]. Thermally activated metallic nanoparticles have also been used for atomically precise etching along crystallographic axes to obtain graphene nanoribbons [229]. It has also been observed recently that, the solution dispersion and sonication of exfoliated graphite results in ultra-smooth edges even for sub 10 nm width GNRs [230, 231]. Note that, all these top down approaches, however, result in irregular edge geometry with some control over the number of only the layers. Very recently one fascinating technique has been emerged by means of unzipping and flattening the carbon nanotubes to obtain smooth edge GNRs [232–236]. Theoretical predictions followed by experiments, have shown that, the epoxydation of carbon-carbon bonds and their subsequent breakage into carbonyl pairs prefers to happen along a line in carbon nanotubes and thus, results in smooth GNR edges [232–234]. GNRs can also be obtained by plasma etching of multi wall carbon nanotubes partly embedded in polymer film. This technique has been used to produce single layer to a few layers GNRs depending on the time period of etching [235].

1.2.3 Hybrid Graphene and Boron Nitride Sheets and Nanoribbons

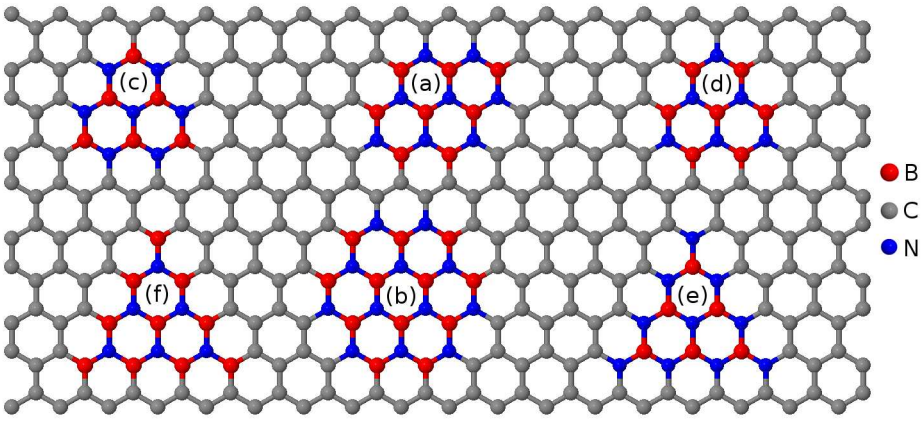

Figure 1.7: The schematic representation of different finite size B_xN_y nanodomains of varieties of shapes, e.g., rhombohedral, R-B_xN_y (a), hexagonal, H-B_xN_y (b) and triangular, T-B_xN_y (c, d, e, f) embedded in graphene.

Recently, there have been tremendous research interests, amongst experimentalists and theoreticians alike, on the hybrid structures of graphene and boron nitride nanoscale materials [237–250]. Since, h-BN has similar bonding architecture as 2D graphene with only a small lattice mismatch, it is possible to realize a hybrid materials of both graphene and h-BN sheets. In fact, it was demonstrated that a hybrid 2D sheet of boron, carbon and nitrogen atoms, known as BCN, is possible to synthesize experimentally with varying constitutional compositions [240, 251–256]. Depending on the compositions, the resulting BCN sheet show a range of electronic and magnetic properties. Using chemical vapour deposition (CVD) method, it was found that, thermodynamically, a domain segragated hybrid BCN sheet is energetically favoured over many possible other nanostructures [237]. A schematic

of various BN quantum dots hybridized with graphene is shown in Fig. 1.7. Following the experimental realization of hybrid BCN structures, there have been several theoretical studies, which have discussed the structure, bonding, electronic and magnetic properties of these 2D hybrid sheets and their quasi-1D nanoribbons in detail [211, 213, 249, 257–259].

1.2.4 Carbon Nanotubes

Carbon nanotubes are quasi-one-dimensional nanoscale carbon materials and can be considered as the rolled graphene sheet. Before the successful isolation of 2D graphene in 2004 by Novoselov *et al.* [260], carbon nanotubes were first discovered in 1991 by Iijima [121] and, since then, have attracted much research interests because of their unique electronic, optical and mechanical properties. Nanotubes can be either of single-wall or multi-walls and, accordingly, termed as single-walled carbon nanotubes (SWCNTs) and multi-walled carbon nanotubes (MWCNTs). Although both the nanotubes show considerable mechanical properties, the SWCNTs have drawn much attention due to their interesting electronic and optical properties. The structure and electronic properties of SWCNTs are uniquely characterized by the (n, m) chiral indices. Depending on the values of 'n' and 'm', nanotubes are of two types: "zigzag" and "armchair", corresponding to (n, 0) and (n, n) chiral indices. In general, (n, 0) SWCNTs are semiconducting, while, (n, n) SWCNTs are metallic. Moreover, a (n, m) SWCNT is considered to be metallic if (n - m) is divisible by 3, and semiconducting otherwise [261, 262].

Although, variation in nanotubes chirality results in different elctronic

properties, there is a great need for tuning their intrinsic electronic structures for practical device applications. In fact, along these lines, there are plenty of research works, demonstrating the modifications of SWCNT's electronic structures. These include, the substitutions of nanotubes carbon atoms by boron and/or nitrogen atoms [263–267], introducing various defects [267–273], and functionalizations [274–283] among many others. All these schemes greatly expand the potential applications areas of SWCNTs. However, note that, complete substitutions of "C-C" units in carbon nanotubes by isoelectronic "B-N" units, produces boron-nitride nanotubes, which are large band gap insulators.

Nanotubes functionalizations are done in two different ways; namely, covalent and non-covalent functionalization approaches. Interestingly, non-covalent functionalizations have potential in controlling tubes physico-chemical properties without introducing significant structural changes in nanotubes. Also, it holds promise for industrial applications. In a part of this thesis, we have discussed the non-covalent functionalizations of different SWCNTs.

In the subsequent section, we will discuss some of the theoretical models and methods, and outline some of the numerical techniques, which can capture the essence of the materials structures and properties, investigated in this thesis.

1.3 Theoretical Models and Methods

In this section, the different theoretical methods that are used to compute various properties are introduced briefly.

Every system consists of a number of nuclei and electrons. For a system with N_e number of electrons and N_n number of nuclei, the total Hamiltonian can be written as:

$$H = -\frac{1}{2m}\sum_{i=1}^{N_e}\nabla_i^2 - \frac{1}{2M}\sum_{I=1}^{N_n}\nabla_I^2 - \sum_{i=1}^{N_e}\sum_{I=1}^{N_n}\frac{Z_I}{|r_i - R_I|} + \sum_{i=1}^{N_e}\sum_{j>i}^{N_e}\frac{1}{|r_i - r_j|} + \sum_{I=1}^{N_n}\sum_{J>I}^{N_n}\frac{Z_I Z_J}{|R_I - R_J|} \quad (1.1)$$

where m and M are the masses of electrons and nuclei, respectively. The Laplacian operators, ∇_i^2 and ∇_I^2 represent the second order differentiation with respect to the coordinates of the i-th electron and the I-th nucleus. Z_I is the atomic number of the nucleus I. r_i and R_I represent the spatial coordinates of i-th electron and I-th nucleus, respectively. The first two terms in the equation 1.1 are the kinetic energy operators of electrons and nuclei, respectively. The third term represents the Coulomb attraction between electrons and nuclei. The fourth and fifth terms represent the Coulomb repulsion between the electrons and between the nuclei, respectively.

1.3.1 Born-Oppenheimer Approximation

To understand the electronic structure, the motion of massive nucleus can be neglected. As a consequence, the nuclear skeleton can be considered to be frozen with respect to the electronic motion. Therefore, the kinetic energy for the nuclei can be neglected and the Coulomb repulsion among the nuclei can be considered as a constant. This approximation is called *Born-Oppenheimer*

approximation which considers the movement of electrons in the static nuclei potential. With this approximation, the Hamiltonian turns out to be:

$$H = -\frac{1}{2m}\sum_{i=1}^{N_e}\nabla_i^2 - \sum_{i=1}^{N_e}\sum_{I=1}^{N_n}\frac{Z_I}{|r_i - R_I|} + \sum_{i=1}^{N_e}\sum_{j>i}^{N_e}\frac{1}{|r_i - r_j|} \tag{1.2}$$

for a fixed nuclear coordinate. In fact, the second term can also be accounted for after solving the electronic Hamiltonian,

$$H_{el} = -\frac{1}{2m}\sum_{i=1}^{N_e}\nabla_i^2 + \sum_{i=1}^{N_e}\sum_{j>i}^{N_e}\frac{1}{|r_i - r_j|} \tag{1.3}$$

since the nuclear coordinates are fixed. However, in case of large molecular vibration, the consideration of nuclear motion becomes unavoidable and Born-Oppenheimer approximation breaks down. The calculation of vibrational and rotational spectroscopy also need explicit consideration of nuclear motion.

1.3.2 Models for Charge Transport

The mechanism of charge transport in organic π-conjugated materials has shown great scientific and technological interests in recent years [284–292]. The key quantity which characterizes the charge transport phenomena is the carrier mobility.

The charge carrier mobility (μ) is defined as the ratio between the drift

velocity of the charge carrier (v) induced by the electric field and the amplitude of the applied electric field (F).

$$\mu = v/F \tag{1.4}$$

In general, the carrier mobility is dictated by the diffusion coefficient (D) since the charge transport follows diffusive mechanism. The carrier mobility is related to the diffusion coefficient via Einstein equation:

$$\mu = \frac{eD}{k_B T} \tag{1.5}$$

The carrier mobility in conjugated organic materials is very low as compared to the inorganic materials although there have been reports on high room temperature mobility of a few tens of $cm^2V^{-1}s^{-1}$ for single organic crystals. However, these carrier mobilities strongly depend upon the chemical structure and preparation of the sample, processing conditions and measurement techniques. Various experimental techniques have been developed to characterize the charge carrier mobilities. The most widely referred approaches are the time of flight (TOF) [293, 294], field effect transistor configuration [295–297], diode configuration [298, 299] and pulse radiolysis time resolved microwave conductivity techniques [300–303], which are elaborately discussed in several literatures [288].

There are two basic models describing charge transport and hence, the

carrier mobility: (i) band model and (ii) hopping model.

Band Model

In general, the charge transport in inorganic semiconductors is described by this band model, where, well defined valence band and conduction bands are formed very strongly. In fact, the charge transport in these materials are mainly realized due to the wave like propagation of charge carriers in their well constructed valence or conduction bands. Thus, the charge carrier mobilities are very large in these inorganic materials. However, the presence of dislocations, and lattice vibrations (phonons) greatly reduces the charge carrier mobility values. This band like transport behavior has successfully been described within the Holstein-Peierls model coupled with first-principles calculations and has widely been investigated [304–306].

However, the major drawback of this model is the overestimation of carrier mobility in case of pure and ordered single crystals. To overcome such limitations and to understand this band like transport behavior in detail, many new as well as modified approaches have been developed in recent years, which explicitly consider the quantum corrections and effect of thermal fluctuations [306–309].

Hopping Model

Unlike inorganic materials, the weak van der Waals and π-π interactions in organic materials result in narrow bands. Additionally, with increase in temperature, the electron-phonon interactions play major role. The formation of narrow bands and enhanced electron-phonon coupling cause the charge

carrier to be localized in polaron like states [287–289, 306]. For this reason, the mean-free path for the scattering of carriers becomes comparable to the order of intermolecular spacing which enforces the charge carriers to hop between adjacent localized states, leading to a process known as thermally activated hopping mechanism. The hopping process is the dominant mechanism of charge transport in organic materials at room temperature, where the rate of hopping in each step can be described by a semi-classical Marcus theory [310–312].

Within the approach, the rate (W) of charge transfer between the pair of molecules (i, j) at a particular temperature (T) is expressed as;

$$W = \frac{2J_{ij}^2}{h}(\frac{\pi^3}{\lambda k_B T})^{\frac{1}{2}} exp(-\frac{\lambda}{4k_B T}) \tag{1.6}$$

where J_{ij} is the coupling matrix element between the pair (i, j) of molecules, λ is the reorganization energy and k_B is the Boltzmann constant. From the above expression, it is clear that the rate of hopping would be high if the reorganization energy is small and the intermolecular coupling is large.

The reorganization energy (λ) is defined as the energy cost by locally charging a single molecule within the molecular crystals during charge transfer process. On the other hand, the charge transfer integral reflecting the interactions strength between the molecular pairs, is defined by the matrix element $J_{ij} = \langle\psi_i|H|\psi_j\rangle$, where H is the electronic Hamiltonian of the system and ψ_i and ψ_j are the wave functions of two charge localized states. In fact, there exist different methods for estimating the charge transfer integrals

(J_{ij}). Two popular and widely simplified methods used in several previous studies [287–292, 313, 314], are based on dimer molecular energy levels splitting, commonly known as Koopmans' theorem [315], and fragment orbital approach [313, 314].

In this thesis, the fragment orbital approach, which considers the spatial overlap between the molecular orbitals, and thereby, provides accurate estimation of the charge transfer integrals, is employed [313, 314]. Within this approach, the dimer molecular levels are expressed as the linear combination of individual monomer molecular levels (fragment orbitals) and the charge transfer integral (J'_{ij}) can be obtained as the off-diagonal elements of the Kohn-Sham Hamiltonian matrix which is expanded from the orbital energies as follows.

$$H_{KS} = SCEC^{-1} \tag{1.7}$$

Hhere S is the intermolecular overlap matrix, C is the molecular orbital coefficient and E are the molecular orbital energies. This procedure allows direct calculations of the charge transfer integrals, including signs, without invoking the assumption of negligible spatial overlap. Further, the generalized charge transfer integral (J'_{ij}) in the orthogonal basis can be calculated using Lowdin transformation which is expressed as

$$J'_{ij} = J_{ij} - \frac{1}{2}S(E_1 + E_2). \tag{1.8}$$

Then, the rate of charge transfer (W) can be computed using the calculated values of J' and λ. Since, the charge transfer phenomena is diffusive in the absence of any external potential, the diffusion coefficient which is related to the hopping rate between pairs of the molecules, can be calculated as

$$D = \frac{1}{2d} \frac{\sum_i r_i^2 W_i^2}{\sum_i W_i} \tag{1.9}$$

where d is the dimensionality, r is the distance between the pairs of molecules considered and W_i is the probability for the charge carrier to a particular ith neighbor, normalized over the total hopping rate ($\sum_i W_i$). At a given temperature, the final drift mobility due to hopping, μ, can then be evaluated from the Einstein relation as mentioned earlier. However, this drift mobility is strongly influenced by many factors, including, molecular packing, impurities, temperature, pressure, external field, carrier density, molecular weight and size.

1.4 Numerical Methods

Exploring materials' properties using different simulation techniques serve not only as tools to aid in the interpretation of experimental data, but to directly complement such data by providing a relationship between the macroscropic behavior observed experimentally and the microscopic properties represented in the model or simulation. Unprecedented developement of

computer hardware and different simulation algorithms in past decades has enabled us to study the systems, ranging from a few atoms to a large number of atoms. In this section, we discuss some of the numerical methods which have been used for simulating bio-molecules and low-dimensional materials in this thesis. Depending on the properties of interest, we use either the electronic structure methods or molecular dynamics (MD) simulations for studying different materials.

1.4.1 Molecular Dynamics Simulations

Accurate prediction of system properties is required to understand the existing materials nature and further designing of new meterials. Modeling of the complex and large systems using the solution of relativistic time-dependent Schrödinger equation is not possible, and only a few atoms can be handled on the ab inito level. However, molecular dynamics (MD) simulation helps to understand the detailed structural and conformational aspects on a realistic and atomic level, within an affordable computational cost. Within MD, ensemble-averaged properties, such as binding energy and relative stability of molecular conformations, are obtained by averaging over representative statistical ensembles of structures.

Solving the Newton's equation of motion [316] for all the nuclei within a system is the basic foundation of MD. In classical MD, the force (F_i) on a atom, i, exerted by other atoms is expressed as:

$$\overrightarrow{F_i} = m_i \frac{\partial^2 \overrightarrow{r_i}}{\partial t^2} \tag{1.10}$$

The vector notations in forces F_i and positions r_i, i.e. in three dimensions the whole system is described by 3N coordinates. The forces on a atom i is calculated as the negative derivative of the potential U, which describes the interactions between the particles and can be written as:

$$\overrightarrow{F_i} = \frac{\partial U}{\partial \overrightarrow{x_i}} \tag{1.11}$$

where, U, the inter-atomic potential, is a function of many degrees of freedom corresponding to all nuclei.

Forcefields

The potential function, U, mentioned above, is defined by the bonded and the non-bonded interactions terms, as given below:

$$U(\overrightarrow{x_1}, \overrightarrow{x_2}, ..., \overrightarrow{x_N}) = U_{bonded} + U_{non-bonded} \tag{1.12}$$

The contribution to the bonded inter-atomic potential is given as:

$$U_{bonded} = \sum_{bonds} K_r(r - r_0)^2 + \sum_{angles} K_\theta(\theta - \theta_0)^2 + \sum_{improper} K_\omega(\omega - \omega_0)^2 + \sum_{dihedrals} K_\phi(1 + \cos(n\phi - \phi_0)) \tag{1.13}$$

where, bonding, angle and improper interactions are described by harmonic

potentials based on Hooke's law, while for the dihedral potential, a periodic function is used.

The non-bonded interactions are decomposed into two parts: electrostatic Coulomb potential, $U_{Coulomb}$ and a combination of van der Waals attractive and Pauli repulsion part. The later part is defined usually by Lennard-Jones (LJ) potential, U_{LJ}. Thus, the non-bonded interactions are expressed as:

$$\begin{aligned} U_{non-bonded} &= U_{Coulomb} + U_{LJ} \\ &= \sum_i \sum_{j>i} \frac{1}{4\pi\epsilon_0\epsilon_r} \frac{q_i q_j}{r_{ij}} + \sum_i \sum_{j>i} 4\epsilon_{ij}((\frac{\sigma_{ij}}{r_{ij}})^{12} - (\frac{\sigma_{ij}}{r_{ij}})^6) \end{aligned} \quad (1.14)$$

where, ϵ_0 and ϵ_r are the dielectric constant in vacuum and the relative dielectric constant of medium (for water, 78), respectively.

As can be seen from Equ. 1.13 and 1.14, conducting the MD sumilations for a given system requires all the constant parameters in hands, which can be estimated using either quantum chemical calculations or, if available, from experimental data. The major drawback of the classical MD simulations is the low transferability of these emperical parameters, that differs from system to system, and may have to be adjusted while dealing with a new system.

Integration Algorithms

Here, we will briefly describe the basic algorithms that involves solving Newton's equation of motion. The usual and most common algorithm implemented in almost all MD packages (AMBER and GROMACS), is the leap-frog algorithm [317], which uses position $\overrightarrow{x}$ at time t and velocities $\overrightarrow{v}$ at

time t - $\frac{1}{2} \triangle t$:

$$\overrightarrow{v}(t + \frac{1}{2} \triangle t) = \overrightarrow{v}(t - \tfrac{1}{2} \triangle t) + \tfrac{F(t)}{m} \triangle t, \tag{1.15}$$

$$\overrightarrow{x}(t + \triangle t) = \overrightarrow{x(t)} + \overrightarrow{v}(t + \tfrac{1}{2} \triangle t) \triangle t \tag{1.16}$$

Combining these two equations leads to:

$$\overrightarrow{x}(t + \triangle t) = 2\overrightarrow{x}(t) - \overrightarrow{x}(t - \triangle t) + \tfrac{F(t)}{m} \triangle t^2, \tag{1.17}$$

and thus, generating MD trajectories are very similar to those produced by the Verlet algorithm [318]. Unlike leap-frog algorithm , the equation of motions integration by the Velocity-Verlet algorithm [319] uses the positions $\overrightarrow{x}$ and velocities $\overrightarrow{v}$ at the same time, t. However, note that, the equation of motions need to be modified for accounting the temperature and pressure coupling as well as the conservation of any structural constraints.

MD simulations without couplings to heat and pressure baths results in so-called NVE ensemble (constant particles, volume and total energy, respectively), also known as the micro-canonical ensemble. Most physical quantities should be estimated from either the NVT ensemble, i.e. the canonical ensemble, in which the temperature is conserved as well, or the NPT (isothermal-isobaric) ensemble, in which both pressure and temperature are conserved. The latter realization appears to be most closely to laboratory conditions. Therefore, thermostat and barometer have to be introduced for representing, temperature and pressure coupling, respectively.

Temperature Coupling

In MD simulations, the temperature of the system is controlled via a thermostat. A weak coupling to an external heat bath can be realized with the Berendsen thermostat [320]. Here, the deviation of the system temperature (T) from a given reference temperature (T_0) is slowly corrected by first order kinetics:

$$\frac{dT}{dt} = \frac{T_0 - T}{\tau} \tag{1.18}$$

τ is the temperature coupling time constant, which can be adapted two different values, for system equilibration (small τ) and MD simulations (large τ). Note that, the temperature deviation decays exponentially with the time constant τ. The temperature of a system containing N particles is directly related to the particle velocity ($\overrightarrow{v}_i$) via kinetic energy E_k:

$$E_k = \frac{3}{2} N k_B T = \sum_i^N \frac{1}{2} m_i \overrightarrow{v}_i^2 \tag{1.19}$$

where, k_B is the Boltzmann constant. Accordingly, T, T_0 and the change in temperature ($\Delta T = T_0 - T$) can be expressed as:

$$T = \frac{1}{3Nk_BT}\sum_{i}^{N} m_i \overrightarrow{v}_i^2,$$

$$T_0 = \frac{\zeta^2}{3Nk_BT}\sum_{i}^{N} m_i \overrightarrow{v}_i^2,$$

$$\Delta T = \frac{1}{3Nk_BT}\sum_{i}^{N} m_i \overrightarrow{v}_i^2(1+\zeta^2) \tag{1.20}$$

where ζ is the velocity scaling factor and can be calculated from the following relation:

$$\zeta = \sqrt{1 + \frac{\Delta t}{\tau}(\frac{T_0 - T}{T})} \tag{1.21}$$

The Berendsen thermostat does not produce a proper canonical ensemble, as it suppresses the kinetic energy fluctuations of the system. However, for a large system, the most of the ensemble properties are not significantly affected.

However, Nosé-Hoover thermostat produces correct canonical ensemble. In Nosé-Hoover method, the ensemble is extended by introducing a thermal reservoir and a friction term in the equation of motion. The friction force is proportional to the product of each particle's velocity and friction parameter ξ. Now, the equation of motion for each particle is:

$$\overrightarrow{F_i} = m_i\frac{\partial^2 \overrightarrow{r_i}}{\partial t^2} + m_i\xi\frac{\partial \overrightarrow{r}}{\partial t} \tag{1.22}$$

and the equation of motion for the bath parameter ξ is:

$$\frac{d\xi}{dt} = \frac{1}{Q}(T - T_0) \tag{1.23}$$

where Q determines the strength of the coupling to the heat bath. Note that, both temperature coupling methods are implemented in GROMACS [321] and AMBER [322] MD codes.

Pressure Coupling

Similar to the temperature coupling, the system can be coupled to a pressure bath by rescaling the coordinates of the particles and the dimensions of the simulation box. Again Berendsen [320] provided an algorithm which relaxes the pressure, p, of a system to a given reference pressure, p_0, by first-order kinetics:

$$\frac{dp}{dt} = \frac{1}{\tau_p}(p_0 - p) \tag{1.24}$$

However, this procedures of the Berendsen Thermostat does not generate the correct NPT ensemble, although it yields simulations with the correct average pressure. More realiable NPT ensemble can be produced with the Parinello-Rhaman approach [323], which is very similar to the Nosé-Hoover thermostat. However, the weak coupling Berendsen thermostat has been used for all constant pressure MD simulations.

Constraint Algorithm

For large and complex systems, it is sometimes not affordable, may not be even necessary to propagate all degrees of freedom in the system. Therefore, constraints can be applied in the simulation, which keep e.g. bonds, angles, etc. at their predefined values. There are two major algorithms which can account for constraints, the SHAKE algorithm [324] and the LINCS algorithm [325]. The SHAKE is used for MD simulations of biomolecules using AMBER code, described in chapter 2, while the LINCS algorithm is used in chapter 3 for constraining all hydrogen bonds.

Periodic Boundary Conditions and Long Range Electrostatics

Periodic boundary conditions (PBC) is used to avoid the edge effects in the simulations of finite systems. In PBC, atoms that leave a box, enter the adjacent box on the opposite side, thus, the number of particles is always conserved. In this thesis, all simulations are carried out using rectangular boxes.

In general, a cut-off is used for the non-bonded LJ interactions, sinces it decays very fast with the distance as $\frac{1}{r^6}$. But, for the Coulomb interactions, the potential falls of with the distance as $\frac{1}{r}$. Thus, a cut-off for the longe-range Coulomb interactions is not suitable. With PBC, the electrostatic energy of a system with N particles and their periodic images is described as:

$$V_{Coulomb} = \frac{1}{8\pi\epsilon_0\epsilon_r} \sum_{n_x} \sum_{n_y} \sum_{n_z{}^*} \sum_{i}^{N} \sum_{j}^{N} \frac{q_i q_j}{r_{ij,\overrightarrow{n}}} \tag{1.25}$$

where the box vectors $\overrightarrow{n} = (n_x, n_y, nz)$ and $\mathrm{r}_{ij,\overrightarrow{n}}$ is the real distance. Note,

the "*" indicates that, the terms with $i = j$ are discarded if $\overrightarrow{n} = \overrightarrow{0}$. However, the above sum converges very slowly. Ewald [326] introduced the idea of subdividing the slowly-converging sum into two fast-converging sums plus a constant term:

$$V_{Coulomb} = V_{Coulomb}^{direct} + V_{Coulomb}^{reciprocal} + V_{Coulomb}^{0} \tag{1.26}$$

Here the reciprocal sum is computationally much expensive, and hardly affordable for the large systems [327]. However, the particle-mesh Ewald (PME) method [328, 329], greatly improves the difficulty of calculating the reciprocal term, and thereby, widely used for the treatment of long-range electrostatic interactions in MD simulations.

1.4.2 Quantum Chemical Calculations

Since the simulation based on classical molecular dynamics does not take into account explicitly the electronic degrees of freedom, they can not be used to study the chemical reactions involving the formation of new bonds or breading of the existing bonds. The electron consideration requires the quantum mechanical description of the system, which leads to the developements of quantum chemical calculations. Using quantum chemical calculations, it is possible to determine the ground state electronic structure and various properties associated with it for both the molecular as well as extended class of systems. The molecular wave functions obtained from quantum chemical calculations can be used to study a range of physiochemical properties, such as, dipole and higher multipole moments, polarizability, vibrational spectra,

NMR (Nuclear Magnetic Resonance), etc with a great accuracy, and often comparable with the experimental results.

In quantum mechanics, each particle is described by a wave function Ψ (r, t), where, Ψ*Ψ gives the probability of finding the particle at position r and time t. The total energy operator of a system is represented by a Hamiltonian H, whose expectation value provides the total energy of the system. The time-independent Schrodinger equation is as follows:

$$H\Psi = E\Psi \tag{1.27}$$

In practice, the wave functions of an interacting many electron systems is not known a priori. To solve the Schrödinger equations, one starts with the initial guess wave functions, which is usually considered to be as the linear combination of the basis functions. However, solving Schrödinger equation for many electron wave funtions becomes very difficult and often impossible for moderate to a larger system sizes. To this end, the density functional theory (DFT) has emerged an alternative choice to solve many electron problems, where, the Hamiltonian for many electron system is mapped onto a single particle Hamiltonian. Therefore, the DFT approach reduces the complexity of the problem to a great extent.

1.4.3 Density Functional Theory

The many body numerical methods can not be adopted for very large scale simulations due to the huge dimension of basis space. In this context, *ab-initio* density functional theory (DFT) has been proved to be highly efficient

and successful, which maps the electronic correlations within one electron formalism. This has been widely used to study the materials with satisfactory agreement with the experimental observations.

Within DFT, the Hamiltonian of an N electron system in the external field, $V_{ext}(r)$, including the field induced by the nuclei is given by,

$$H = -\frac{1}{2}\sum_{i=1}^{N} {\nabla_i}^2 + \frac{1}{2}\sum_{i\neq j}\frac{1}{|r_i - r_j|} + V_{ext} \tag{1.28}$$

The strength of DFT is based on the fact that the ground state electronic wave function, $\Psi_0(r_1, r_2, ..., r_N)$ can be entirely described only by its electron density $\rho_0(r)$, as stated by the Hohenberg-Kohn theorem [330, 331]. It is based on a variational principle stating that the ground state electronic density minimizes the energy functional.

- The external potential, V_{ext} is uniquely determined by the corresponding ground state electronic density. It can be stated in other way as well: the external potential, V_{ext} determines exactly the electron density $\rho(r)$. Furthermore, the ground state expectation value of any observable is a unique functional of the ground state electron density.

- The variational principle is also valid for the electron density. The total energy is minimal for the ground state density, $\rho_0(r)$, of the system.

The Schrödinger equation can now be reformulated in terms of the density, ρ:

$$E[\rho] = \hat{F}[\rho] + \int dr V_{ext}(r)\rho(r) \tag{1.29}$$

$\hat{F}$ is a universal functional of ρ and the ground state density is found by minimizing the functional, $E[\rho]$ with respect to ρ. DFT would in principle be exact if the functional were known exactly. This is, however, not the case. To tackle this, Kohn and Sham separated $\hat{F}$ into three distinct parts as follows [330, 331]:

$$E[\rho(r)] = T_s[\rho(r)] + \frac{1}{2}\int \frac{\rho(r)\rho(r')}{|r_i - r_i'|} dr dr' + E_{xc}[\rho(r)] + \int \rho(r) V_{ext}(r) dr \tag{1.30}$$

The kinetic energy term and the exchange-correlation functional are not solvable in this form. The former can, however, be calculated if the electron density $\rho(r)$ is built up from wave functions $\Psi_i(r)$ which are then used to calculate the kinetic energy, T_s:

$$T_s[\rho(r)] = \frac{1}{2}\sum_{i=1}^{N} \int \Psi_i^*(r)\nabla^2\Psi_i(r) dr \tag{1.31}$$

Kohn and Sham proposed a coupled set of differential equations, known as the Kohn-Sham equations:

$$[\nabla^2 + V_H + V_{xc} + V_{ext}]\Psi_i(r) = \epsilon_i \Psi_i(r) \tag{1.32}$$

where V_H is the Hartree potential, V_{xc} is the exchange-correlation term, V_{ext}

is the external potential and $\Psi_i(r)$ are the Kohn-Sham orbitals. These equations are then solved iteratively until self consistency is attained. From equation 1.32, the exchange correlation potential, V_{xc} follows as:

$$V_{xc} = \frac{\delta E_{xc}[\rho(r)]}{\delta \rho(r)} \tag{1.33}$$

This potential, since not known exactly, has to be approximated.

- **Local Density Approximation (LDA)** [332]: The first approximation to the exchange-correlation energy functional, $E_{xc}[\rho(r)]$, was the Local Density Approximation (LDA), defined as:

$$E_{xc}^{LDA} = \int d^3 r \epsilon_{xc}(\rho(r)).\rho(r) \tag{1.34}$$

  where $\epsilon_{xc}(\rho(r))$ is the exchange and correlation energy per electron of the homogeneous electron gas with density $\rho(r)$. It assumes that the electronic density is a smooth function in space. Any region of space can then be locally seen as a homogeneous electron gas of density, $\rho(r)$. The total exchange-correlation energy is then the sum over all electrons in every region of space of the local exchange-correlation energy.

- **Generalized Gradient Approximation (GGA)**: These approximations are extensions and improvements of the LDA functional to inhomogeneous systems. In GGA approach, the local exchange-correlation energy depends not only on the local charge densities but also on their gradients. There are basically three types of GGA:

- *Ab-initio*: These functionals are based on exact results, asymptotics etc. The exchange and correlation parts are treated independently. These are typically PBE (Perdew-Burke-Ernzerhof) [333, 334] or PW91 (Perdew-Wang 1991) [335, 336].
- Atom based GGA: These also include some exact results but functional parameters are fitted on close-shell atom properties. Exchange and correlations are again treated separately. Examples include, Becke's GGA for exchange [337] and Lee Yang and Parr (LYP) functional for correlation [338].
- Empirical: In this formalism, the exchange and correlations are considered as a whole. Functional parameters are determined by fitting on a set of atomic and molecular properties. Common example are the HCTH (Hamprecht-Cohen-Tozer-Handy) functionals [339, 340].

For solving the Kohn-Sham equations, one expands the one-particle wave functions in a basis $g_j(r)$:

$$\Psi_i(r) = \sum_{j=1}^{N_b} C_{i,j} g_j(r) \tag{1.35}$$

where $C_{i,j}$ are the coefficients of expansion and N_b is the size of the basis. Thus, the Kohn-Sham equations become one-particle matrix equations and we have to diagonalize the one particle Hamiltonian matrix to get the eigen values and eigen vectors. The Kohn-Sham equation is solved self-consistently because the Hamiltonian depends on the density, which in turn is calculated

from the wave functions, which is what we are solving for. Therefore, we start with some guess for the density and keep improving the density and potential in successive iterations till self-consistency is achieved.

Pseudopotentials and Numerical Orbitals

Generally it is assumed that, the core electrons are rather unaffected by changes in their chemical environment. A pseudopotential, (V_{PP}) is an effective external potential experienced by valence electrons in an atom when all the core electrons of the atom are frozen. It is obtained by constructing smoother wave functions wherein the oscillations of the valence wave function in the core region are removed [341–344]. The pseudo wave function and the all electron wave function match each other beyond a particular value of radial distance which is chosen to be outside the last node in the all electron wave function; this is called the cutoff radius r_c. If we can use the same pseudopotential to describe different chemical environments then the pseudopotential is said to be transferable. A good pseudopotential needs to fulfill the following conditions:

- The lowest pseudo wave function generated by the pseudopotential should not contain any nodes.
- The normalized atomic radial pseudo wave function with an angular momentum l should be equal to the normalized radial all electron (AE) wave function outside a given cut-off radius r_c (Fig. 1.8):

$$R_i^{PP}(r) = R_i^{AE}(r) \; (r > r_c) \tag{1.36}$$

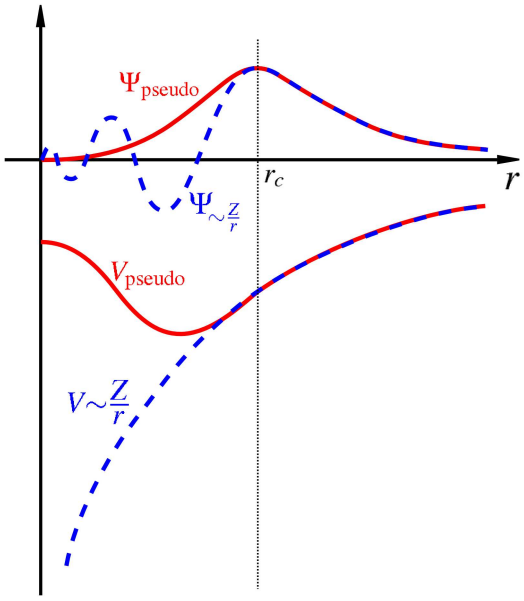

Figure 1.8: Comparison of a wave function in the Coulomb potential of the nucleus (blue) to the one in the pseudopotential (red). The real and the pseudo wave function and potentials match above a certain cutoff radius r_c.

- Norm conservation: The charge inside of r_c has to be the same for both wave functions,

$$\int_0^{r_c} |R_i^{PP}(r)|^2 r^2 dr = \int_0^{r_c} |R_i^{AE}(r)|^2 r^2 dr \tag{1.37}$$

- The eigenvalues of both wave functions should be the same.

Many packages have been developed in the last few decades implementing the self-consistent calculations for electronic structure using Hartree-Fock, post Hartree-Fock and DFT methods. Some of these packages which have been used to study nanomaterials are Gaussian [345], General Atomic and Molecular Electronic Structure System (GAMESS) [346] and Amsterdam Density Functional (ADF) [347, 348] etc. However, since these packages use the localized all orbital basis functions, one cannot handle larger systems using these packages. To this end, a combination of numerical orbitals and pseudopotentials make an ideal choice for studying large systems. This combination of numerical orbitals and norm-conserving pseudopotentials has been implemented in the Spanish Initiative for Electronic Simulations with Thousands of Atoms (SIESTA) package [349, 350], making it an ideal choice for studying realistic systems. However, for plane augmented wave basis approximations, one may adopt PWScf or Viena Ab-initio Simulations Packages (VASP) [351–354].

1.5 Outline of Thesis

As mentioned above, the increasing research interests on DNA quadruplexes is because of their anti-cancer therapeutic activity and plausible nanotechnological applications. In addition, the low-dimensional materials exhibit many interesting properties, arising from a host of interactions. The recent experimental sophistications have made possible the understanding of structural morphology of many complex biomolecules as well as many unique phenomena observed in the reduced length scale. In this thesis, we have discussed the structures and electronic properties of some biosystems, particularly, the DNA quadruplex structures and a class of interesting two-dimensional, such as graphene, h-BN and hybrid BCN sheets, and their quasi one-dimensional nanoribbons materials.

In the second chapter, we have discussed the structural stability and electronic properties of different nucleobase pairs, including WC and Hoogsteen base-pairs found in various forms of DNA. We have also discussed the structures of various DNA and PNA quadruplexes and analyzed their structural stability in presence of different monovalent cations under physiological conditions, *i.e.*, temperature (T = 300 K), pressure (P = 1 atm) and aqueous (solvent = water) medium using extensive MD simulations. Here, we have proposed a stable DNA quadruplex structure which contains four-strands of ssd$(AG)_n$. This structure simultaneously binds with cations and anions in its core channel. Further, we have investigated their electronic, optical and charge transfer properties for possible applications in opto-electronic devices.

In the third chapter, we have studied the interactions of different nucleobases, nucleobase quartets and various ssDNA with graphene using MD simulations at room temperature and atmospheric pressure in aqueous medium. Our results show that various ssDNA form different networks on 2D graphene, which strongly depends on the chemical nature of nucleobases and base-sequences in ssDNA.

We have investigated the electronic and magnetic properties of 2D hybridized graphene and h-BN sheets ($B_xN_yC_z$-hybrid) using density functional theory calculations and these are discussed in fourth chapter in detail. Our study predicts different electronic states, which includes metal, half-metal and semiconductor, depending on the shapes and sizes of embedded B_xN_y nanodomains. The electronic structure and electrical transport behaviours of quasi one-dimensional boron and nitrogen substituted zigzag nanoribbons (ZBNCNRs) have also been studied using *ab initio* density functional theory and non-equilibrium Greens function formalism. Our study shows new inroads to achieve metallic, semiconducting and half-metallic properties in these zigzag edge nanoribbons. The possibilities of metal free magnetism in these hybrid materials, originating from the different zigzag edge types, are also predicted in these ZBNCNRs.

In the fifth chapter, we have discussed the changes in electronic and magnetic properties of 2D graphene and h-BN sheets decorated with different metals and metal clusters using density functional theory. We have also investigated the electronic structures of porous graphene and h-BN sheets and examined how the electronic properties are susceptible to the presence of

magnetic impurity. The results show that magnetic ordering found in pristine sheets changes in its porous analogues. Furthermore, our study also predicts tunable electronic band gaps and strong binding affinities of these porous sheets for the magnetic impurities, and suggests possible applications in removing any magnetic contaminants from solutions. Additionally, we have performed *ab-initio* density functional calculations to investigate the molecular charge transfer effects on the electronic properties of 2D graphene and quasi-1D single-walled carbon nanotubes (SWCNT) in the final chapter. Our results have shown that the electron acceptor molecules interact strongly with these graphitic materials than the electron donor molecules because of the differences in charge transfer. The study also show significant changes in SWCNT's electronic structure, including metal to semiconductor and semiconductor to metallic transition depending on the nature of the adsorbed molecules.

Chapter 2

Structures of Nucleic Acids G-quadruplexes and their Electronic Properties*

2.1 Introduction

As discussed in chapter 1, G-rich nucleobase sequences form DNA quadruplex (G_4-DNA) structures in presence of suitable monovalent ions. These G_4-DNA quadruplexes can adopt various polymorphic structures and are characterized by different molecularity, topology and strand orientation, which depends on the base sequences and experimental conditions. These include unimolecular, bimolecular and tetramolecular quadruplex structures [76]. In uni-, bi-, and tetra-molecular G-quadruplexes, each nucleic acid strand provides one,

*Work reported in this chapter is submitted for publication as: (a) Arun K. Manna and Swapan K. Pati (2013); (b) Arun K. Manna, Prabal K. Maiti and Swapan K. Pati (2013)

two and four G residues to form the planar nucleobase quartet, which is held together by Hoogsteen H-bonding interactions. G_4-DNA forming nucleobase sequences are found at the chromosomal ends and in transcriptional regularity regions in several oncogenes, some promoter regions and ribosomal DNA [355, 356]. Although, G-quadruplex structures are mainly formed from nucleic acids DNAs, the quadruplex structure can also form from other nucleic acids, such as RNA, PNA, etc. PNA G-quadruplex (G_4-PNA) has neutral peptide backbones in contrast to the negatively charged sugar-phosphate backbones in DNA. However, the peptide backbone is more flexible in comparison to the DNA sugar-phosphate backbone. Therefore, it possesses lesser structural rigidity than G_4-DNA. Designing of ions or ligands that stabilize the long-strand of G_4-DNA and G_4-PNA or any other quadruplex structures may find potential applications in nanoelectronics. However, along these lines, there are several theoretical studies already been reported [357–361], which discussed the electronic properties of G_4-DNA.

In this chapter, we have investigated the detailed structural conformations of various parallel-stranded G-quadruplexes in aqueous medium with and without the presence of monovalent cations (Li^+, Na^+, K^+) using MD simulations at temperature, T = 300 K and pressure, P = 1 atm (atmosphere). Based on structural analysis of MD simulated structures, we examine the relative stability of short G-rich $d(TG_4T)_4$ DNA and $r(UG_4U)_4$ RNA quadruplexes and compared their structural stability. Moreover, the structures of long G_4-DNA and PNA quadruplexes have been explored with/without the presence of cations. We have discussed the role of these monovalent cations

for stabilizing the four-stranded quadruplex structures and compared our results with the reported data from previous studies. We have also investigated the electronic and optical properties of G_4-DNA/PNA modeled tetramers (four G_4-stacks) constructed from the MD averaged structures in presence of explicit water and ions in details. Additionally, we have calculated the charge transfer integrals for all possible hopping pathways and estimated the carrier (electron and hole) mobilities.

Interestingly, we have proposed new sets of parallel-stranded quadruplex structures of DNA and PNA, containing consecutive repeats of G and A nucleobases, and thus, making alternating G_4- and A_4-quartets, which are stacked together via π-π-stacking interactions. This quadruplex can simultaneously bind to both the monovalent cations (Li^+, Na^+, K^+)) and anions (e.g. Cl^-), suggesting a potential ion-pair receptor material. Our results have shown that the DNA quadruplex structures consisting of repeating units of G_4- and A_4-quartets (G_4A_4-DNA) are stable in presence of MCl (M = Li^+, Na^+, K^+), where G_4 binds to M and A_4 binds to Cl^-, creating a MCl dimer line along the quadruplex long axis. It is also found that the quadruplex structures of PNA corresponding to the G_4A_4-DNA are not stable even in presence of MCl.

Further, we have investigated the structure, energetics and electronic properties of G_4-DNA monomers and π-stacked dimers in presence of cations, other than Li^+, Na^+ and K^+. We have considered Cu^{2+}, Ag^+ and Au^+ cations for the present study. Note that, all these ions are toxic for any biological systems, and can not be used to stabilize the G-quadruplex structure in vivo. However, the G-quadruplex structure can be used as a substrate

material for selective detection of these toxic metal ions from some environments. Moreover, as well be discussed in details in this chapter, the Cu^{2+} stabilized G-quadruplexes may act as an effective molecular wire, where, the magnetic ions, here, Cu^{2+}, coupled ferromagnetically.

Moreover, there have been increasing interests in designing G-quadruplex stabilizing ligands, in particular, large number of studies have shown that, the polycyclic porphyrin derivatives can be used to stabilize G-quadruplex structures [91]. At the end of this chapter, we have also studied the G-quadruplex structures stabilized by porphyrin ($PorH_2$) and various metal-porphyrin (M-Por) derivatives. Additionally, we have analyzed the electronic and optical absorption properties in details for their possible applications as optoelectronic devices.

2.2 Computational Methods

To understand the dynamics and minimum energy structures of various G-quadruplex (DNA, RNA and PNA), we have performed classical MD simulations of these biomolecules under physiological conditions (T = 300 K and P = 1 atm) in aqueous solution. The MD simulations are performed for 6 ns within NPT ensemble using AMBER package [322] and AMBER force fields [362]. Based on the available crystal structures, first, we have considered the two parallel-stranded G-quadruplex structures of nucleic acids, DNA and RNA with $d(TG_4T)$ and $r(UG_4U)$ single-stranded base sequences, respectively. Additionally, we have also considered the two parallel-stranded G-quadruplex of DNA and PNA with 16 G nucleobases in a single-strand

($ssdG_{16}$). All initial quadruplex structures are built using xleap module of AMBER package. To study the stable position and the role of the core-ions within the G-quadruplex channels on their structural stability, we have chosen three different monovalent ions, namely, Li^+, Na^+ and K^+, which are placed in the G-quartet's plane for the initial conformations. All DNA quadruplexes are charge-neutralized by adding an appropriate number of additional counter-ions, like, Li^+ or Na^+ or K^+ based on the type of core-ions. Then, the systems are immersed in a periodic box of TIP3P water molecules extending up to 15 $\mathring{A}$ from the solute in each direction. The whole system is, then, energy optimized using 1000 steps minimization without any geometry constraint in order to remove the possible bad contacts that might be present in the initial geometries. The systems are, then, temperature equilibrated at T = 300 K for 300 ps using a constant pressure dynamics without any structural restraint imposed on the solute. Finally, we have carried out a 6 ns long MD simulations using isothermic-isobaric (NPT) ensemble. Langevin dynamics and Langevin piston algorithm are used to maintain the temperature at 300 K and 1 atm of pressure. The Particle Mesh Ewald (PME) method for calculating the long-range electrostatic interactions is used with a cutoff of 12 $\mathring{A}$. The constraint algorithm, SHAKE, is applied to constrain all the bonds containing hydrogen atoms. A time step of 2 fs is used to integrate the equations of motion using leaf-frog method. The program, Visual Molecular Dynamics (VMD) is used to visualize and create all the MD simulated structures.

For the electronic structure calculations, we have used first-principles approach based on DFT. The DFT calculations are performed using a set of

quantum chemistry codes, Gaussian09 [345] suit of programs with different levels of theories for the geometry optimizations and calculations of the optical absorptions of comparatively smaller size molecular systems, ADF codes [347, 348] for single-point charge transfer integral calculations, and SIESTA code [349, 350] for the electronic and optical properties calculations of relatively larger systems have been considered in this chapter.

2.3 Results and Discussion

2.3.1 Energetics and optical properties of nucleic acids base pairs

It is known that, the two ssDNA/ssRNA within a nucleic acids duplex structure, are bound together via Watson-Crick (WC) H-bonded base pairs, while, Hoogsteen H-bonding interactions play an important role in forming nucleic acids quadruplex structures. In this section, the structures and energetics of various nucleic acid base pairs are discussed using quantum chemical calculations. We have considered both WC and Hoogsteen H-bonded base pairs in the present study.

WC base pairs

First, we discuss the stability and electronic structure of WC nucleobase pairs, A-T and G-C, and compare the results with the existing literature data. We have chosen the two nucleosides base pairs, A-T and G-C, which contain both the sugar and nitrogeneous bases. We have fully relaxed the

geometries of these WC base pairs in gas-phase (without solvent) using dispersion corrected ωB97XD exchange and correlation functional and 6-31+g(d,p) as the basis sets for all the atoms, employing Gaussian09 software code [345]. The ωB97XD functional has been shown to be appropriate for accounting the weak interactions, such as, H-bonding and van der Waals interactions [363–365]. DFT optimized geometries of A-T and G-C base pairs are shown in Fig. 2.1. To understand the stability of these WC base pairs, we have calculated the binding energy (E_b) and formation energy (E_f), which are defined as follows:

$$E_b = E_{A-T/G-C} - E_{A/G} - E_{T/C} \tag{2.1}$$

$$E_f = E_{A-T/G-C} - E'_{A/G} - E'_{T/C} \tag{2.2}$$

where, $E_{A-T/G-C}$ represents the total optimized energy of either A-T or G-C base pair. $E_{A/G}$ and $E_{T/C}$ denote the total energy of A or G and T or C in their optimized WC base pair conformation. And, $E'_{A/G}$ and $E'_{T/C}$ indicates the total optimized energy of individual nucleoside. Accordingly, it is expected that the formation energy would have higher value than binding energy as it takes into account the deformation energy of individual nucleoside.

All structural parameters and energies are provided in Table 2.1. Our results show that, the WC G-C base pair has larger binding strength in comparison to the A-T base pair, because of the presence of three H-bonds in G-C, when, compared to the two H-bonds in A-T. This result agrees well

Table 2.1: Binding and formation energies of WC base pairs, calculated using DFT within ωB97XD/6-31+g(d,p) level. The low-energy absorption peak positions (λ) are also indicated with the corresponding oscillator strength value in bracket.

WC pair	E_b (kcal mol^{-1})	E_f (kcal mol^{-1})	λ (nm)
A-T	-17.88	-15.92	258.34 (0.23) and 254.22 (0.16)
G-C	-34.67	-33.51	258.34 (0.22)

with the previous theoretical and experimental findings [366–369].

Next, we have investigated the extent of charge transfer integrals for both the electron and hole, calculated using fragment molecular orbital approach, as implemented in ADF code [347, 348]. We have considered dispersion corrected PBE exchange and correlation flavor of GGA functional and a double ζ basis sets with triple polarization for all the atoms. Our result shows that the effective electron transfer integral is larger than the hole transfer integral for both the WC base pairs. The effective charge transfer integrals for electron and hole between the two complementary nueclobases in WC pairs are found to be 0.0428 eV and 0.0230 eV for A-T, and 0.0376 eV and 0.0184 eV for G-C, respectively. The larger extent of electron transfer integral than hole transfer integral found in WC base pairs, is due to the charge transfer interactions between the H-bonded nucleobases.

To understand the effects of the H-bonding interactions on the optical properties, we have calculated the optical absorption of the two H-bonded WC base pairs as well as for the individual nucleosides using time-dependent density functional theory (TDDFT), employing B3LYP/6-31+G(d,p) level of theory. We calculate excitation energies and corresponding oscillator

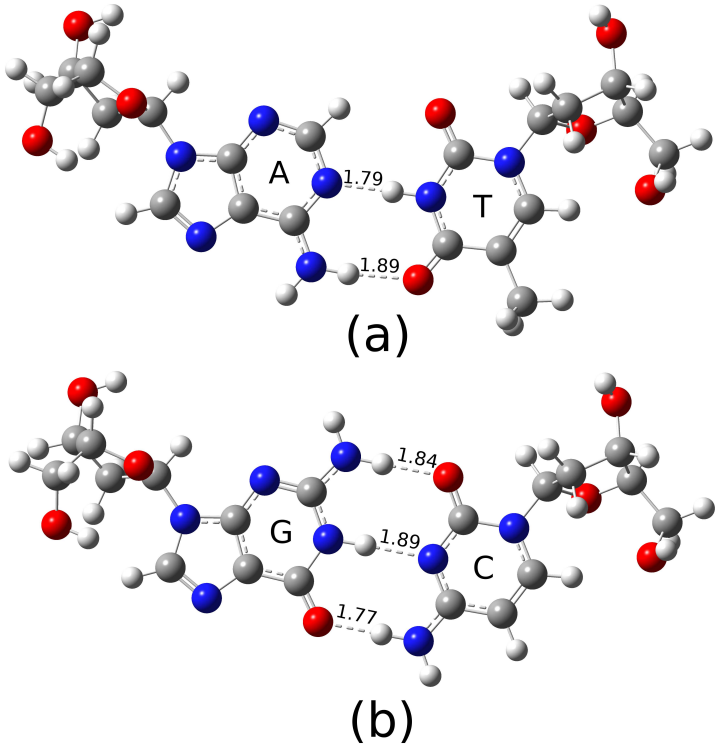

Figure 2.1: Optimized geometries for the WC A-T (a) and G-C (b) base pairs. Important H-bonds distances are indicated in $\mathring{A}$. The white, gray, blue and red colours indicate hydrogen, carbon, nitrogen and oxygen atom, respectively.

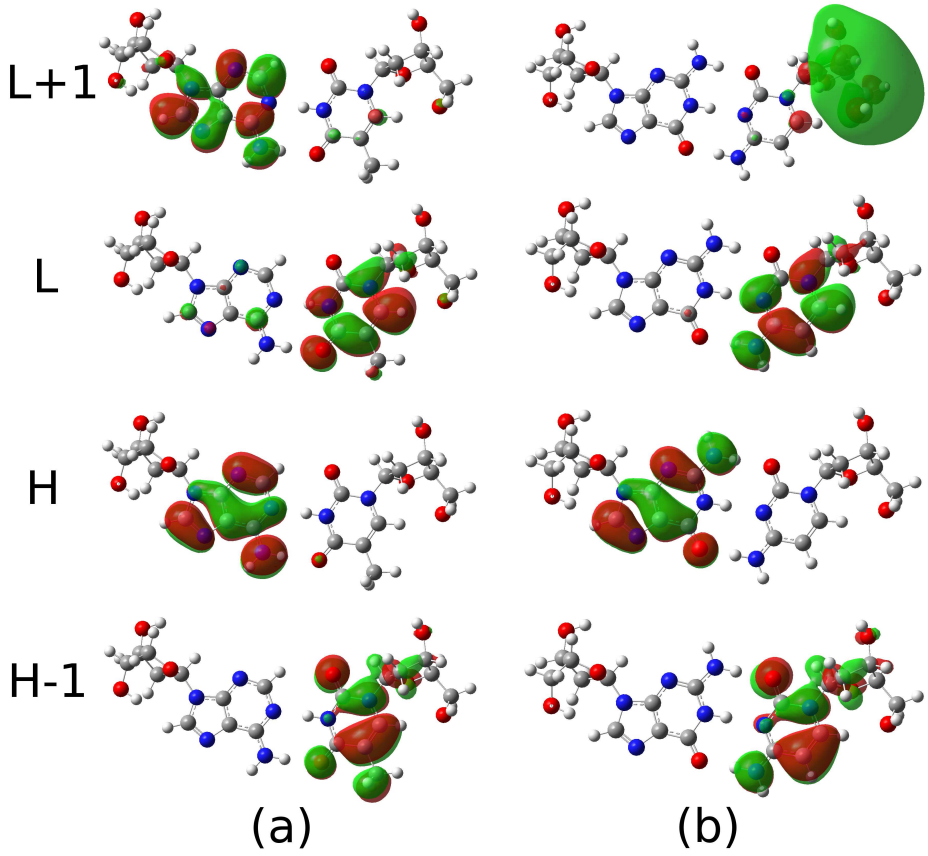

Figure 2.2: The relevant FMOs (H-1, H, L and L+1) for the low-energy absorption peaks for the WC A-T (a) and G-C (b) base pairs. H and L indicate the highest occupied molecular orbital (HOMO) and lowest unoccupied molecular orbital (LUMO), respectively.

strengths for the first 10 low-energy excited states. The low-energy optical absorption peaks calculated for the isolated A, G, C and T nucleosides, are found to be at ∼249.05 nm, ∼256.50 nm, ∼266.94 nm and ∼206.44 nm, respectively. These results are similar to what have been reported previously [363, 370, 371]. Interestingly, we find that the H-bonding interactions in WC base pairs shift the low-energy absorption peak to slightly lower energy. The two low-energy transitions found for A-T base pair are at ∼258.34 nm and ∼254.22 nm, which correspond to the electronic excitations from the occupied to unoccupied orbitals of T and A, respectively (see Fig. 2.2). On the other hand, we find only one intense transition at ∼258.34 nm, solely originating from C's HOMO-1 to C's LUMO orbital in G-C base pair (see Fig. 2.2). The detailed molecular orbitals analysis have shown that, there is no cross-electronic transition, i.e., transitions occuring from a specific nucleobase's occupied orbital in WC base pairs to the complementary nucleobase's virtual/unoccupied orbital. This means that the low-energy excitation is mainly due to the electronic excitations occuring within the same nucleobase present in a WC base pair. Moreover, we have found that, the nature of the relevant nucleoside's orbitals involved in optical transitions are of π (occupied) and π^* (unoccupied) orbitals types. The present findings are in good agreement with previous studies [363, 370, 371].

Note that, the hybrid B3LYP exchange and correlation functional employed here, does not provide the quantitative estimate of the charge transfer (CT) excitations energies because of its poor description of long-range exchange potential. The functional always trends to underestimate the CT excitations energies. In fact, there are some energy functionals, which are

designed for accurately describing the long-range asymptotic behavior of the CT excitations. To name a few, these include CAM-B3LYP, ω-B97XD, and range-separated hybrid (RSH) functionals, such as BNL (Baer, Neuhauser, and Livshits) and ω-PBE [372–374]. The RSH functionals require satisfaction of Koopmans$'$ theorem by optimizing a system specific range-separation parameter. These RSH functionals have been shown successful for investigating CT processes and designed to produce accurate electronic and optical gaps. However, the low-energy excitations found in A-T and G-C base pairs considered here, are of localized type, and thus, we believe the energetics predicted using B3LYP functional are reasonably accurate for the present study.

Hoogsteen base pairs

In this section, we discuss the structure and electronic properties of Hoogsteen H-bonded G_4, i.e., G-quartet using DFT calculations. G-quartet was previously studied in a number of theoretical works [375–379]. It was shown that, in absence of any cations, the G_4 can be found with the two minimum energy structures, where, the H-bonding interactions between the G nucleobases are mediated through either bifurcated or Hoogsteen H-bonds. In the present study, we have considered only the Hoogsteen H-bonded G-quartet structure consisting of G nucleosides for the comparison with its cation-chelated G-quartet structure. Note that, all the previous studies have considered methylated G nucleobase, while, the present study consider the presence of sugar units in the G residues (G-nucleoside) in forming the G-quartet structures. Also, it is clear from the optimized structure of G_4 that,

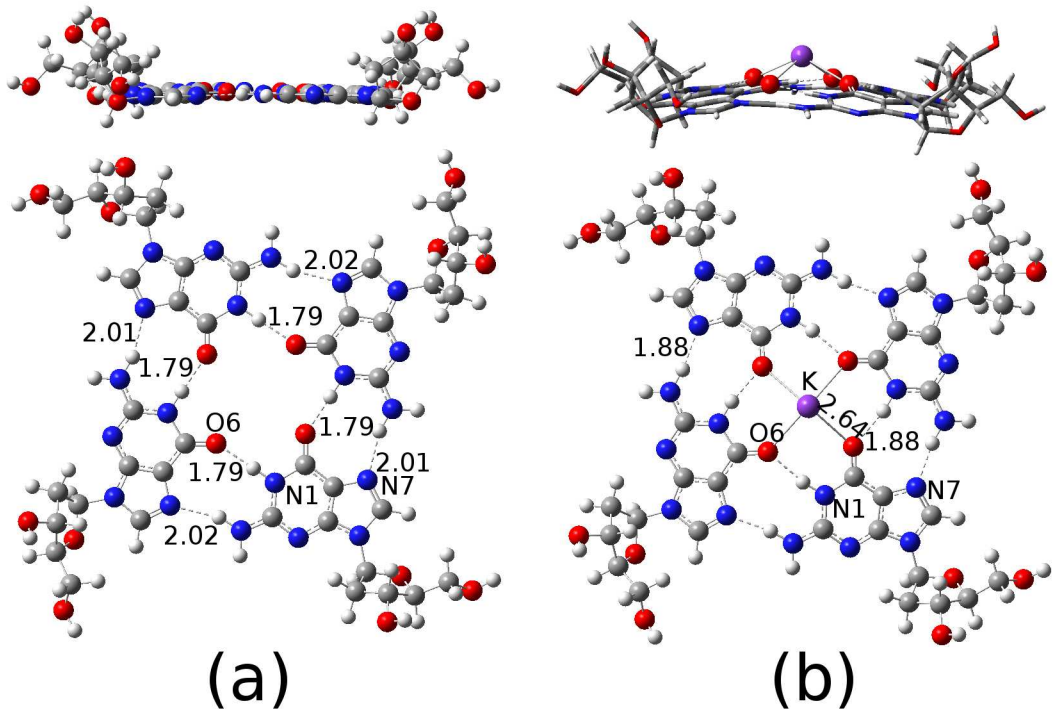

Figure 2.3: DFT optimized structures of G-quartet without (a) and with (b) the coordinated K^+ ion. All the relevant bond distances are indicated in $\mathring{A}$. The white, gray, blue, red and purple colours indicate hydrogen, carbon, nitrogen, oxygen and potassium atom, respectively.

all the carbonyl O6 atoms point towards the center of the G-quartet core, and thus, creating a more electron rich region, which, may be coordinated with cations, such as, Li^+, Na^+, K^+ ions. In fact, it was shown that, the stability of a G-quartet can be increased by incorporating monovalent cations, and the stability order while considering solvation energy follows as: $Li^+ < Na^+ < K^+$. For an understanding of detailed structures and electronic properties, we have considered the G_4 nucleoside quartet in presence/absence of coordinated K^+ ion. The optimized structures of bare and K^+ coordinated G-quartets within ωB97XD/6-31+g(d,p) level of theory are shown in Fig. 2.3.

Structural analysis reveals that, each G O6 atom forms shorter and

stronger H-bond with the N1-H group of the adjacent G, while, the N7 atom forms relatively longer and weaker H-bond with the exocyclic -NH_2 group of neighbouring G residue. Moreover, the C=O bond lengths elongate slightly due to the formation of H-bonds. The calculated distances for the identical bonds are found to be almost same in G_4 (see Fig. 2.3). Moreover, the optimized geometry of G-quartet is found planar and highly symmetric. However, the K^+ coordinations changes the bond distances that are found in bare G_4. The increase in bond distances is found due to the K^+ coordination to the G_4 structure. The distance between the G O6 and K^+ is $\sim$2.64 $\mathring{A}$. Moreover, all identical bond distances are found to be same in G_4-K^+. As shown in Fig. 2.3, the K^+ is displaced from the G-quartet's plane and positioned at $\sim$1.06 $\mathring{A}$ above the plane of four O6 atoms. However, the geometry of G_4-K^+ remains symmetric.

To understand the strength of H-bonding interactions in G-quartet, we calculate the binding energy (E_b) due to the presence of H-bonds using the below-mentioned relation. Additionally, we have also calculated the formation energy (E_f) to examine the propensity of G-quartet formation from their isolated G nucleosides. Both the energy terms are defined as:

$$E_b = E_{G_4} - E_{G^1} - E_{G^2} - E_{G^3} - E_{G^4} \quad (2.3)$$

$$E_f = E_{G_4} - 4 * E_G \quad (2.4)$$

where, E_{G_4} and E_G are the total optimized energies of G_4 and G, respectively.

E_{G^i} (i = 1-4) is the energy of the G unit in the relaxed structure of the G-quartet. All results are given in Table 2.2.

As can be seen from the Table 2.2, the magnitude of the binding and formation energies are large, indicating their gas-phase formation. However, the magnitude of binding energy is higher by ∼10 kcal mol^{-1} than the formation energy. This is due to the lack of energetics involved for the structural deformation of the G-units while forming the stable G-quartet. Further, to understand how the H-bonding interactions assist the formation of stable G-quartet, we have performed energy decomposition analysis (EDA) by considering step-wise formation of the G_4 from their constitutional G-units. Additionally, we define an energetic term, which takes into account any synergetic effects, present if any, due to the H-bonding interactions between the G-nucleobases in G_4. For this, we calculate all the pair-wise interactions (total 6 pairs: 4 direct Hoogsteen H-bonded and 2 diagonal) present in a G-quartet and subsequently, subtracted from the total interactions energy (here, E_b) calculated for the G_4 unit and term it as E_{syn}. Our results show that, the interactions energy between two G nucleobase is -14.71 kcal mol^{-1}. The addition of third G unit to the existing G_2 unit changes the interactions energy by -20.50 kcal mol^{-1}, while, the inclusion of fourth G to the G_3 causes -40.08 kcal mol^{-1} change to the interactions energy, which is significantly larger than the previous energy change. This is because, the addition of third G makes only a single pair of H-bonds, whereas, the fourth G creates two pairs of H-bonds, thus, causing higher changes in interactions energy. Moreover, the E_{syn} calculated for the G-quartet is found to be -16.40 kcal mol^{-1}, which is significantly large and may be partially accounted for

the resonance assisted H-bonding interactions and partly, due to the covalent nature of these Hoogsteen H-bonded base pairs. In fact, this has been demonstrated in a recent study [366].

As already have been mentioned, the core of the G-quartet has negative electrostatic potential region, which can be coordinated with cations in order to gain extra stability via electrostatic interactions. To this end, we have chosen K^+ ion for coordinating to the central core of G_4 and analyze the structural stability. We have used ωB97XD/6-31+g(d,p) level of theory for the structural optimizations and the energetics calculations. Our results show that, the coordinated K^+ ion does not lie on the plane of G_4 unit, but, eventually, it finds stable position at 1.8 $\mathring{A}$ above the plane of four G O6 atoms. This is fully consistent with the previous theoretical and experimental findings, which have shown that the channel K^+ ions situate between the two G-quartet planes. As given in Table 2.2, we find that, there is significant enhancement for both the binding and formation energy values calculated for G_4-K^+ than ion-free G_4. The E_b and E_f calculated for the G_4-K^+ are found to be -171.36 kcal mol^{-1} and -134.48 kcal mol^{-1}, respectively. The energetic enhancement is due to the presence of strong electrostatic stabilization by the corodinated K^+ ion. The contribution from the H-bonding and electrostatic interactions to the total binding energy is found to be -83.48 kcal mol^{-1} and -87.88 kcal mol^{-1}, respectively. We have also calculated the synergy in H-bonding interactions for G_4-K^+ using the method discussed above. We find almost similar synergetic effects for the G_4-K^+ unit as found for the G_4 (see Table 2.2). The difference in E_{syn} is only 1.6 kcal mol^{-1} with the smaller negative value obtained for the K^+ coordinated G_4.

Table 2.2: Energetics of Hoogsteen base pairs G_4 and G_4-K^+. E_b, E_f and E_{syn} correspond to the binding energy, formation energy and the synergy in the binding energy, respectively.

Quartet	E_b (kcal mol^{-1})	E_f (kcal mol^{-1})	E_{syn} (kcal mol^{-1})
G_4	-79.29	-69.59	-16.40
G_4-K^+	-171.36	-134.48	-14.79

Note that, so far, the energetics have been discussed based on the DFT results, and the effects of solvent (water) and temperature are not considered. To examine whether the K^+ coordinated G_4 would be stable in presence of explicit water and thermal effects, we have carried out short atomistic classical MD simulation on a G_4-K^+ using GROMACS code, adopting AMBER03 force fields. We have used TIP3P water model and the simulation was run for 300 ps using NPT ensemble at temperature, T = 300 K and pressure, P = 1 atm. Our simulation results show that G-quartet is stable in presence of explicit water and K^+ ion. Only the difference between the DFT and MD results, is in the structural aspects. We have found that, the G-quartet structure is devoid of planar shape because of the presence of G and water intermolecular interactions as well as thermal effects.

Now, we focus on the extent of charge transfer integrals for both the electron and hole, calculated using fragment molecular orbital approach, as implemented in ADF code [347,348]. We have considered dispersion corrected PBE exchange and correlation functional and a double ζ basis sets with triple polarization for all the atoms. Our result shows that the effective hole transfer integral is larger than the electron transfer integral in G_4. The effective charge transfer integrals for electron and hole between two neighbouring G

units are found to be 0.0086 eV and 0.0181 eV, respectively, which are small in comparison to the hopping integrals found for the WC A-T and G-C base pairs. The greater extent of hole transfer integral than electron transfer integral, is due to the large HOMO overlap between the consecutive G units present in G-quartet.

Next, we have investigated the optical absorption properties of G-quartet in its free form as well as in K^+ coordinated structure using TDDFT method. Our study shows that, in G_4, there are almost two degenerate electronic transitions at about ∼265.53 nm and ∼265.45 nm, which are of $\pi \rightarrow \pi^*$ types. After chelation with K^+ ion, both the degenerate transitions are shifted slightly (∼13 nm) to the lower energy region. The two low-energy transitions are found at ∼278.21 nm and ∼278.33 nm for the G_4-K^+. The detailed orbital analysis reveals that the orbital's nature corresponding to these transitions remain unchnaged, i.e., $\pi \rightarrow \pi^*$ types. The occupied and unoccupied molecular orbitals involved in the two low-energy degenarate transitions found for G_4 and G_4-K^+ are shown in Fig. 2.4. As can be seen, the electron excitations from HOMO-1 and HOMO-2 to LUMO+4 is responsible for the two low-energy peaks in G_4's optical absorption, while, the electronic transitions from HOMO-1 and HOMO-2 to LUMO mainly responsible for the degenerate peaks for the G_4-K^+. Note that, the HOMO-1 and HOMO-2 orbitals for both the G_4 and G_4-K^+, are almost degenerate, and show similar spatial distribution (see Fig. 2.4). The FMOs picture suggests the CT behavior of the low-energy excitations. However, all the low-energy optical excitations found in these systems involve the electronic transitions from the G π molecular orbitals to the π^* orbitals (see Fig. 2.4). Here, we again mention that,

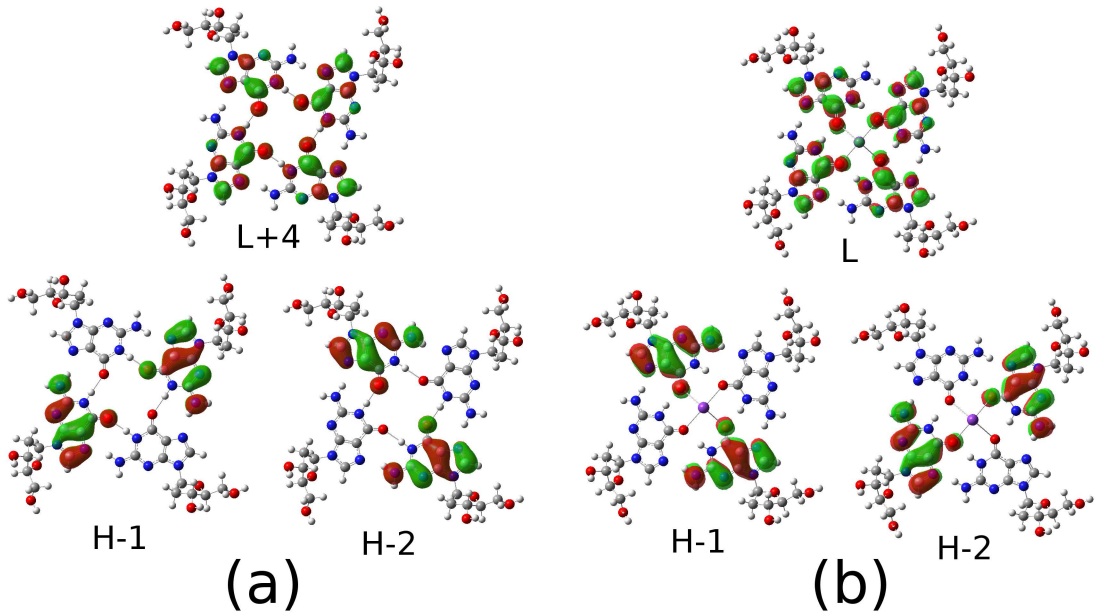

Figure 2.4: FMO diagrams of G-quartet in absence (a) and presence (b) of coordinated K^+ ion. The FMOs in top and bottom panels show the unoccupied and occupied molecular orbitals. H and L denote the highest occupied molecular orbital (HOMO) and lowest unoccupied molecular orbital (LUMO), respectively.

the energetics of CT excitations are poorly described by hybrid B3LYP functional. However, the CT energetics could be improved by the usage of RSH functionals.

2.3.2 Simulations of G-quadruplex Structures

In this section, the structures and conformational dynamics of various G-rich four-stranded DNA, RNA and PNA quadruplex structures are explored and discussed in details. Results obtained both for the short DNA, RNA (6 quartets) and long G_4-DNA and G_4-PNA (16 G-quartets) are presented. The role of various alkali metal ions for stabilizing these quadruplex structures

are also discussed.

Structures of $d(TG_4T)_4$ and $r(UG_4U)_4$ Quadruplexes

Here, we discuss the strutures of parallel four-stranded $d(TG_4T)_4$ DNA and $r(UG_4U)_4$ RNA as obtained from 6.3 ns MD simulation in explcit water in absence and in presence of monovalent alkali ions (Li^+, Na^+, K^+) at temperaturre T = 300 K and pressure P = 1 atm. The difference between the two structures is in their sugar backbone part and terminal quartet units. The $d(TG_4T)_4$ has deoxyribose sugar in the backbones, while, $(UG_4U)_4$ has ribose sugar in its backbone. Moreover, the former quardruplex is capped with a thymine (T_4) quartet unit, whereas, the $(UG_4U)_4$ quadruplex structure is terminated with uridine (U_4) quartet. We have analyzed the root mean square deviation (RMSD) of G-residues in quadruplexes and different average structural parameters for understanding their structure and stability. Results obtained from MD simulation are compared with the structural data as available for the corresponing crystal structures with PDB (Protein Data Bank) database, ID 244D and 1J8G, reported in literature [77, 97].

The time evolution of RMSD for the $d(TG_4T)_4$ and $r(UG_4U)_4$ quadruplex DNA and RNA considering only the G-residues is shown in Fig. 2.5 and Fig. 2.6. Note that, the reference structure for the RMSD calculation is chosen as the initial structures for the corresponding production MD run.

As shown in Fig. 2.5 and Fig. 2.6, the RMSD calculated for the quadruplex structures without the central core ions are considerally larger than those where the central ions are present. This indicates the importance of core ions for the stability of the quadruplex structures. In fact, the structure without

core ions for both DNA and RNA quadruplexes are very much flexible, and no regular quadruplex helical sturtures would be stable. The large RMSD values, range up to 2.65 $\mathring{A}$ and 2.20 $\mathring{A}$ for the $d(TG_4T)_4$ and $r(UG_4U)_4$ quadruplex structures, respectively, without central ions indicate that, the short G-rich quadruplexes are not stable and can not be formed in aqueous medium, fully consistent with the reported experimental findings and previous simulation studies, which were failed to build the short stable G-quadruplex sturtures in absence of monovalent central cations [380–382]. However, the RMSD values suggest that the short RNA quadruplex $r(UG_4U)_4$ is relatively more rigid compared to the $d(TG_4T)_4$ DNA quadruplex. This may be because of the difference in backbone geometry with the two different quadruplex structures. The Na^+ ions coordinated $d(TG_4T)_4$ quadruplex structure seems to be more stable among others, as the calculated RMSD values are rather smooth and vary from only 1.40 to 1.90 $\mathring{A}$. However, as indicative from the RMSD diagrams, the structure with K^+ coordination show comparable stability with the quadruplex structure with Na^+ channel ions. On the other hand, we have found that, the Li^+, Na^+ and K^+ ions stabilized RNA quadruplex $r(UG_4U)_4$ structures show 0.50 $\mathring{A}$, 0.70 $\mathring{A}$ and 0.90 $\mathring{A}$ RMSD deviations, which emphasize that the structural stability follows the order of $Li^+ > Na^+ > K^+$. It is interesting to note that the all the $r(UG_4U)_4$ quadruplexes with/without central metal ions show comparatively less RMSD than the $d(TG_4T)_4$ structures, sugggesting that the short RNA quadruplex is more stable than the DNA quadruplexes.

The structures of both types of quadruplexes after 6 ns MD simulation are shown in Fig. 2.5 and Fig. 2.6. As can be seen, the quadruplex structure

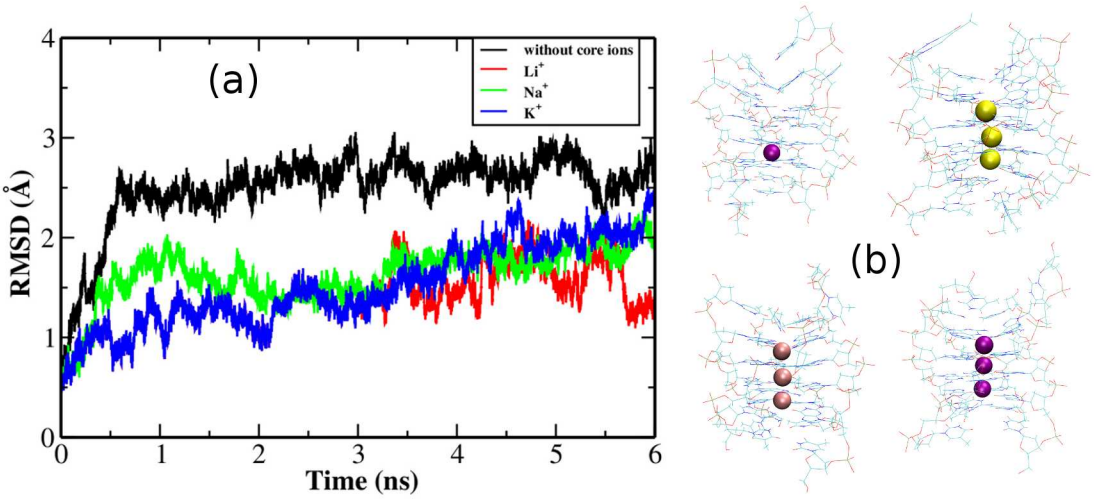

Figure 2.5: (a) RMSD for the MD simulation of $d(TG_4T)_4$ with/without various monovalent ions. (b) MD simulated structures after 6 ns MD run. Yellow, pink and purple colored spheres indicate Li^+, Na^+ and K^+, respectively.

without the channel core ions are destabilized due to the large base pairs and backbone fluctuations without the stabilizing monovalent ions. The parallel G-quadruplex structures are destroyed due to the significant structural change. Also, note that, the 3′ end of each quadruplex structure is very much flexible than the 5′ end. Interestingly, we have found that one K^+ ion enters through the 5′ end of both the quadruplex sturtures from the solution within the simulation time considered here. Note that, the simulated systems contained K^+ ions, which was needed to neutralize the whole system. This finding supports that, the formation of the quadruplex structure indeed requires the stabilizing cations. However, the results reported in a previous study [95] does not highlight the observation of ions entering from the solution to the G-quadruplex core to gain the structural stability. However, the presence of initial core ions significantly stabilizes both the DNA

and RNA quadruplex structures. Obviously, there is significant differences concerning the position of ions within the G-quadruplex. Note that, the Li^+ finds centre of the G-quartet plane as the stable position, while, both Na^+ and K^+ are positioned in between two G-quartets. This is mainly because of the different sizes of the ions. However, the position of the stabilizing core ions is very much dynamic within the G-quadruplex channel. The different preferences for the position of channel ions are in good accordance with the previous simulation study [95]. One important observation can be drawn from the MD simulated structure of $d(TG_4T)_4$ and $r(UG_4U)_4$ is that, the former quadruplex has three coordinated metal ions, whereas, five, four and three metal ions are coordinated within the RNA quadruplex channels for the Li^+, Na^+ and K^+ ion, respectively. This is completely consistent with the RMSD calculations discussed above, which altogether, suggest that, the order of quadruplex structural stability follows as: $Li^+ > Na^+ > K^+$. Moreover, for the $r(UG_4U)_4$ quadruplex, the $5'$ terminal U-quartet terminates its structure in comparison to the $5'$ T-quartet in $d(TG_4T)_4$ quadruplex structure.

We have also analized some structural parameters and results are given in Table 2.3 for both the quadruplex structures studied. For a comparison, we have also provided the corresponding values for the available crystal structures 244d and 1J8G for the DNA and RNA quadruplexes, respectively.

As given in Table 2.3, the average distance between the two guanine quartets, measured as the avearge distances between the two consecutive guanine O6 atoms of the middle two G-quartets, ranges between 3.31 to 4.12 $\mathring{A}$ with the largest value obtained for $d(TG_4T)_4$ without the channel core ions. On the other hand, the G-G stacking distance is found to be ranging between

Table 2.3: Various structural parameters of $d(TG_4T)_4$ and $r(UG_4U)_4$. r_{i-j} is the average distance between i^{th} and j^{th} unit in a system. All distances are given in $\mathring{A}$.

Quadruplex	r_{G-G}	r_{O6-O6}	r_{M+-M+}	r_{O6-M+}
244d	-	4.55	-	2.55
$d(TG_4T)_4$ without core ions	4.12 ± 0.13	6.26 ± 0.13	-	-
$d(TG_4T)_4$ with Li^+	3.31 ± 0.08	4.12 ± 0.10	3.85 ± 0.12	2.68 ± 0.10
$d(TG_4T)_4$ with Na^+	3.39 ± 0.07	4.03 ± 0.09	3.60 ± 0.06	2.62 ± 0.08
$d(TG_4T)_4$ with K^+	3.33 ± 0.07	4.09 ± 0.09	3.80 ± 0.11	2.66 ± 0.09
1J8G	-	-	-	-
$r(UG_4U)_4$ without core ions	3.61 ± 0.09	5.99 ± 0.07	-	-
$r(UG_4U)_4$ with Li^+	3.25 ± 0.06	3.93 ± 0.04	3.21 ± 0.04	2.52 ± 0.06
$r(UG_4U)_4$ with Na^+	3.28 ± 0.06	4.00 ± 0.05	3.22 ± 0.04	2.58 ± 0.07
$r(UG_4U)_4$ with K^+	3.66 ± 0.07	4.23 ± 0.04	3.47 ± 0.04	2.69 ± 0.04

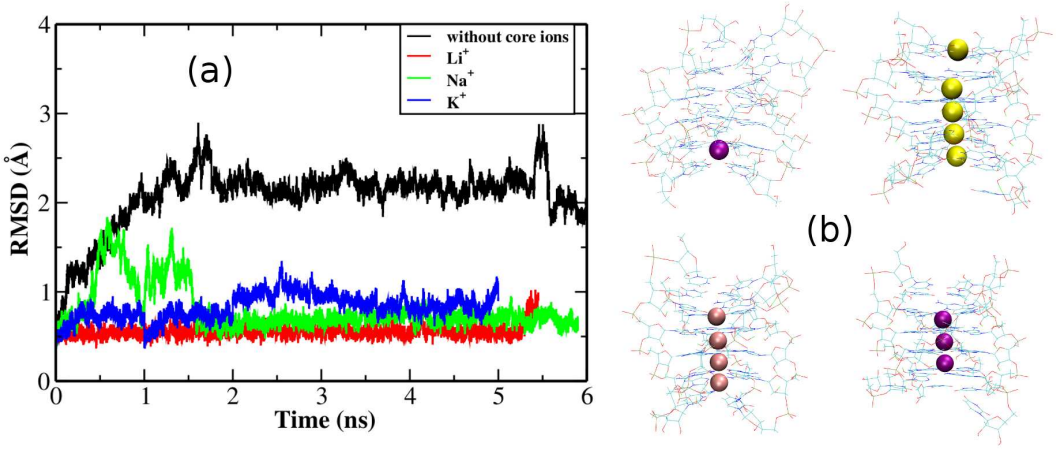

Figure 2.6: (a) RMSD for the MD simulations of $r(UG_4U)_4$ with/without the core channels ions and (b) MD simulated structures after 6 ns simulation run. Yellow, pink and purple colored spheres indicate Li^+, Na^+ and K^+, respectively.

3.24 $\mathring{A}$ to 3.66 $\mathring{A}$ for the r$(UG_4U)_4$ quadruplex studied. Moreover, the average distance between the two metal ions in a quadruplex structure is within 3.21-3.84 $\mathring{A}$. However, the large separation between the two middle ions is found for the d$(TG_4T)_4$ than r$(UG_4U)_4$, and this is well consistent with the larger distances between the two G-quartets for the d$(TG_4T)_4$ quadruplex structure. We have also calculated the average distances between the two diagonal guanine O6 atoms and the distance between the guanine O6 and metal ion for the middle G–quartets. Our results have shown that the O6-O6 distance is large for the quadruplex structures without the core ions, while, the distance is within 3.92 $\mathring{A}$ and 4.23 $\mathring{A}$ depending on the DNA/RNA quadruplex with different channel metal ions. Moreover, the calculated distance between O6 and metal ion indicates that, the RNA quadruplex is rigid in comparison to the DNA quadruplex, studied here. This also agrees well with the RMSD findings, which suuggest that short RNA quadruplex is more stable than DNA quadruplex. The increased structural stability is due to the presence of $2'$ hydroxyl (-OH) group present in ribose sugar of RNA, which makes several intramolecular H-bonding interactions with the polar atoms/groups (N and O) of base, sugar and phosphate backbone. These intra-molecular H-bonding interactions supress the hydration of RNA quadruplex regions by the solvent water molecules. As a result, the RNA quadruplex show greater structural stability than DNA quadruplex. These findings are in good agreement with the results from experimental and simulation studies reported recently [96].

To summarize whatever has been discussed so far, our results from the MD simulation have demonstrated that the short r$(UG_4U)_4$ RNA quadruplex structure is more stable than the d$(TG_4T)_4$ DNA quadruplex structure

in presence of different monovalent cations. The results presented in this section, particularly for the DNA quadruplex structure, are in good agreement with the results reported in earlier studies [95, 380, 381].

Structures of G_4-DNA and G_4-PNA quadruplexes

In the above section, we have discussed the structures of short DNA/RNA quadruplexes. In this section, we have investigated the structures and conformational dynamics of long G_4-DNA/PNA quadruplexes with and without the presence of channel core ions, using MD simulations at temperature, T = 300 K and pressure, P = 1 atm in aqueous medium. We have considered 16 stack of G-quartets, approximately 56 $\mathring{A}$ long along the quadruplex axis, in absence/presence of monovalent core cations (Li^+, Na^+, K^+). For G_4-DNA, we have added additional ions to neutralize the charge on the DNA sugar-phosphate backbone. After initial temperature equilibration for about 300 ps, we have carried out the simulation for 6 ns in presence of explicit TIP3P water molecules. The snapshots of MD simulated structures after 6 ns production run are shown in Fig. 2.7 and Fig. 2.9. The avearge structural parameters are provided in Table 2.4.

As can be seen from Fig. 2.7, the quadruplex structures are stable within the 6 ns simulation time in absence/presence of the channel core ions. However, the presence of channel core ions increases the quadruplex stability. Note that, the channel ions are alligned along the quadruplex long axis, where, the Li^+ ions are positioned at the plane of the G-quartets, while, the Na^+ and K^+ ions stabilize between the two G-quartets. The Na^+ and K^+ ions are bipyramidally coordinated by eight carbonyl oxygen atoms from the two

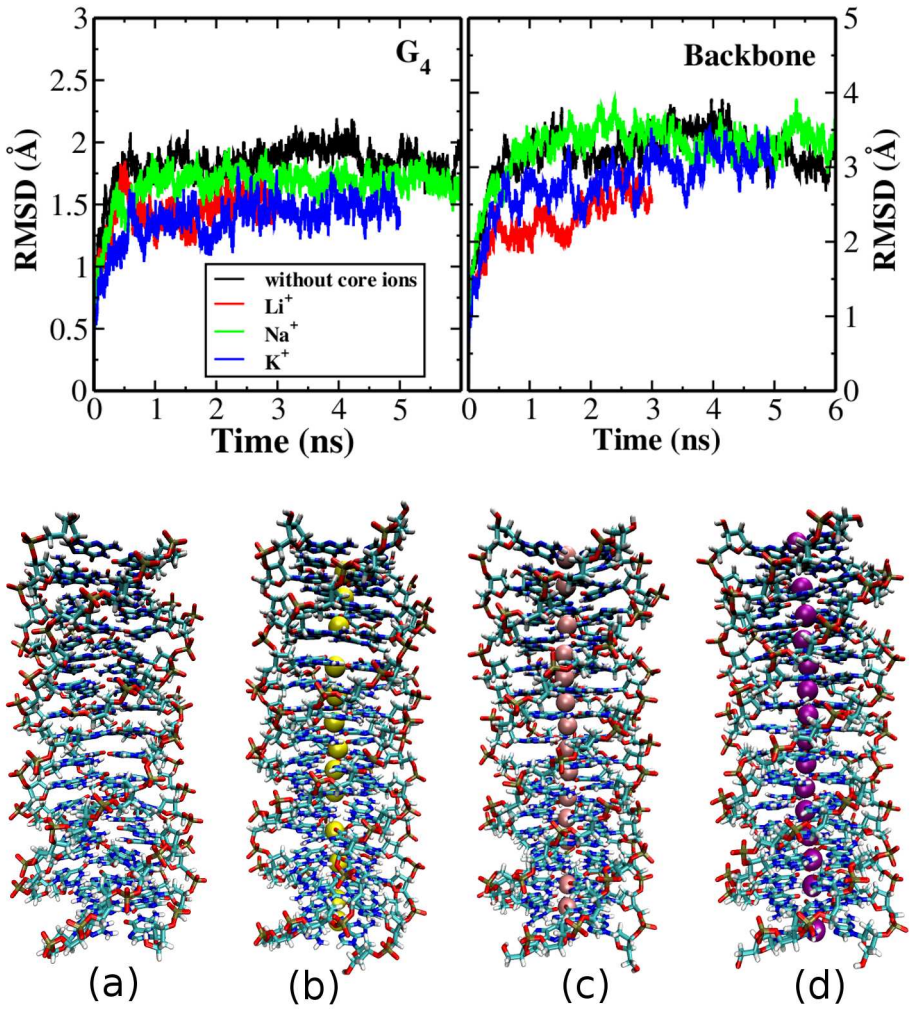

Figure 2.7: RMSD and the simulated structures of G_4-DNA after 6 ns MD run. (a), (b), (c), (d) represent the quadruplex structure without the core ions in K^+ solution and in presence of Li^+, Na^+ and K^+ ions, respectively.

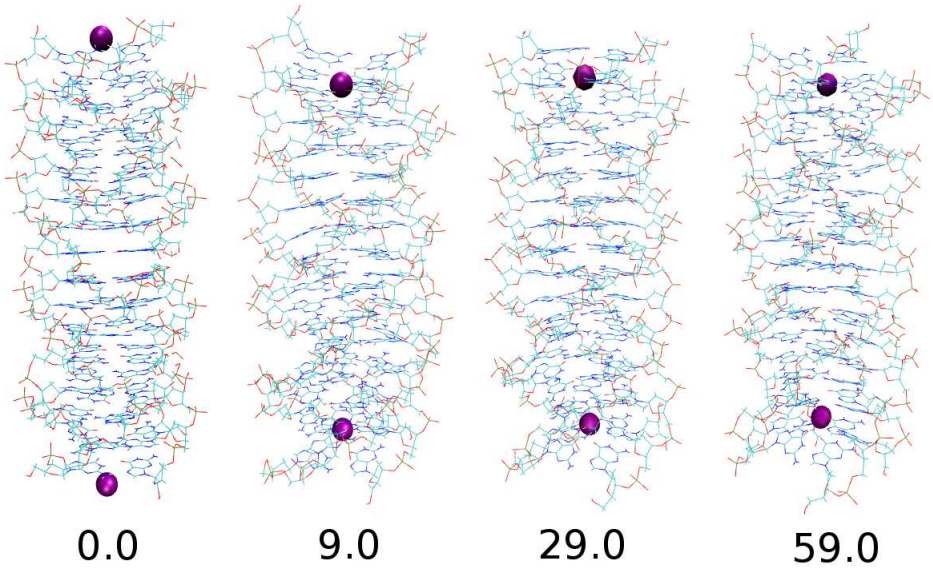

Figure 2.8: The snapshots of G_4-DNA in K^+ solution without the core ions at different simulation time. The MD simulation time is in ns.

consecutive G-quartets. This preferred position for the core ions are in accordance with the simulation done with short DNA and RNA quadruplexes discussed above. Interestingly, it is to be noted that, the long 16 stacks G_4-DNA is stable without the presence of any channel core ions, which were shown to be required to build stable quadruplex structure in aqueous medium. In fact, the simulation performed on short $d(TG_4T)_4$ as discussed above, does not yield stable quadruplex structure in absence of coordinated core ions, and this was also predicted by previous studies [380, 381]. The structural stability of long G_4-DNA arises because of the enhanced π-π stacking interactions. In fact, it was demonstrated by both experiments and simulation study that, the long G_4-DNA can be stable without the precence of channel monovalent cations [95, 383, 384].

To enlighten the fact that the 16 stacks long G_4-DNA is indeed stable

without the presence of core ions, we have performed a long MD simulation in K^+ solution for about 60 ns. The snapshots at different time of MD simulation, namely, at 9 ns, 29 ns and 59 ns, along with the initial structure are shown in Fig. 2.8. Our simulation results show that, after 7.3 ns simulation time, the $5'$ and $3'$ ends of G_4-stacks bind with two K^+ ions from the solution. Note that, in the initial geometry, the two K^+ ions were at very close to the quadruplex $5'$ and $3'$ ends. These two K^+ ions enter into the quadruplex channel because of the large initial fluctuations in the Hoogsteen base pairs at the quadruplex's ends. Subsequently, the ions are stabilized at the end stacks of G-quartets (see in Fig. 2.8). However, we have not observed any penetration of the ions through the grooves regions of the quadruplex structure. Further, after sufficiently long, 60 ns simulation time, no substantial changes in the coordinated K^+ ions position is found in the present study. This is clear from the two snapshots taken at 29 and 59 ns of simulation. This suggests that, the long G_4-DNA structure is stable without the presence of channel ions within the middle G-quartets, while, they are indeed needed for the stability of the end G-quartets stacks. Note that, the end G-quartets are relatively flexible than the middle G-quartets. This is because, the end G-quartets possess only one side π-stacking interactions and are directly exposed to the solvent water and hence, encounter strong solute-solvent interactions. Consequently, the ions within the end G-quartets stacks are required to maintain the stability of the quadruplex structure.

Next, to understand the dynamical behaviors of the quadruplex structure, we have calculated the RMSD for G bases as well as for the DNA sugar-phosphate backbones. The RMSD results are shown in Fig. 2.7. Note

Table 2.4: Various structural parameters of G_4-DNA and G_4-PNA. r_{i-j} is the average distance between i^{th} and j^{th} unit in a system. All distances are given in $\mathring{A}$
.

Quadruplex	r_{G-G}	r_{O6-O6}	$r_{M^+-M^+}$	r_{O6-M^+}
G_4-DNA without core ions	3.49 ± 0.08	6.14 ± 0.06	-	-
G_4-DNA with Li^+	3.33 ± 0.07	4.56 ± 0.06	3.61 ± 0.05	2.48 ± 0.06
G_4-DNA with Na^+	3.41 ± 0.07	4.19 ± 0.06	3.41 ± 0.04	2.63 ± 0.09
G_4-DNA with K^+	3.56 ± 0.07	4.23 ± 0.04	3.53 ± 0.03	2.79 ± 0.05
G_4-PNA without ions	4.32 ± 0.12	5.59 ± 0.08	-	-
G_4-PNA without core ions	4.06 ± 0.10	5.54 ± 0.08	-	-
G_4-PNA with Li^+	3.68 ± 0.08	4.08 ± 0.06	3.98 ± 0.08	2.09 ± 0.14
G_4-PNA with Na^+	3.65 ± 0.09	4.02 ± 0.06	3.55 ± 0.05	2.58 ± 0.08
G_4-PNA with K^+	3.66 ± 0.07	4.16 ± 0.03	3.57 ± 0.03	2.64 ± 0.04

that, the RMSD calculations are carried out with respect to the structure used for the production MD run. It is clear from the Fig. 2.7 that, the RMSD of the backbone atoms are large than the RMSD calculated for the G nucleobases, suggesting more rigid G-quartets within the quadruplex structure. From both the G and backbone RMSD values obtained for the first nanosecond simulation, it is found that there is a jump in RMSD, emphasizing the relaxation from the initial model structure. However, all RMSD values calculated over the last 2 ns MD simulation time are constant with minimum deviations. Our results have shown that the G_4's RMSD for the quadruplex structure without the coordinated channel ions display large RMSD deviation of $\sim$1.8 $\mathring{A}$ with considerable fluctuations. This is because of the significant fluctuations in the $5'$ and $3'$ end G-quartets. In fact, the quadruplex structure is deformed towards its ends, as also observed for the short DNA and RNA quadruplexes already discussed above. However, the presence of the

monovalent cations within the G-quadruplex channel significantly reduces the RMSD values. The RMSD values range within ∼1.40 $\mathring{A}$ to ∼1.65 $\mathring{A}$ depending on the coordinated ion types. The small deviation is observed for the K^+ ions coordinated G-quadruplex among others, with ∼1.4 $\mathring{A}$ and ∼3.0 $\mathring{A}$ RMSD values of G_4 and backbones, respectively. This suggests the higher structural stability of G-quadruplex with the coordinated K^+ channel ions.

For further structural analysis and the validation of stable G-quadruplex structure, additionally, we have calculated some structural parameters averaged over the simulation time. These include, (1) the distance between the two G-quartets (r_{G-G}) as measured by the separation between the two carbonyl O6 atoms from the two consecutive G-quartets, (2) the distance between the two O6 atoms positioned diagonally (r_{O6-O6}) within a G-quartet, (3) the separation between the two consecutive channel metal ions ($r_{M^+-M^+}$), and (4) the distance between the O6 atom of G and the nearby metal ions (r_{O6-M^+}). All these structural parameters are provided in Table 2.4. As can be seen, the average distance between the two G-quartets range within ∼3.33 - ∼3.56 $\mathring{A}$, depending on the core ions types, suggesting the effective π-π stacking interactions, which give the quadruplex stability. Note that, the typical π-π stacking distance in a duplex B-DNA is ∼3.4 $\mathring{A}$. The average separation between the two O6 atoms of diagonally positioned two G residues is within ∼4.19 $\mathring{A}$ and ∼6.14 $\mathring{A}$, with the large value obtained for the G-quadruplex structure without the coordinated core ions. This suggests that the presence of coordinated ions hold the G residues together through electrostatic interactions, and thereby results in small diagonal distances. Moreover, it is found that, the difference between two diagonal distance is small for the

metal ions coordinated G-quadruplex structure than that found for the structure without the channel ions. This indicates that, the G-quadruplex with coordinated channel ions are more structured and quite regular compared to the structure without the core ions. Additionally, the average separation between the two consecutive metal ions within the quadruplex channel range between $\sim$3.41 $\mathring{A}$ and $\sim$3.61 $\mathring{A}$, with the large value obtained for the Li^+ coordinated G-quadruplex, suggesting their greater mobility through the quadruplex helical channel. Further, the distance between the O6 atom of G residue and the nearby metal ions is within $\sim$2.48 $\mathring{A}$ and $\sim$2.79 $\mathring{A}$, with small deviations. The large value is found for the K^+ coordinated structure, which is fully consistent with its larger size among others ions. All these findings suggest the increased structural rigidity of G-quadruplex structures with the coordinated channel ions with the higher stability predicted for the K^+ coordinated G-quadruplex DNA.

So far, we have seen that, the stable G-quadruplex DNA can form in solution in presence of monovalent cations. Although, the formation of stable G-quadruplex DNA structure is important for various biological functions, it has limited applications in nanoelectronics because of the presence of negatively charged sugar-phosphate backbone. However, there exist several experimental studies, which have demonstrated the duplex, triplex, and quadruplex stabilities with varying backbone chemistry. In this regard, the structure of PNA (peptide nucleic acid) quadruplex has drawn much attention among several other higher order structures due to the expected large structural stability. A tetrameric PNA quadruplex was shown to form intermolecular four-standed structure, which exhibits similar structural stability

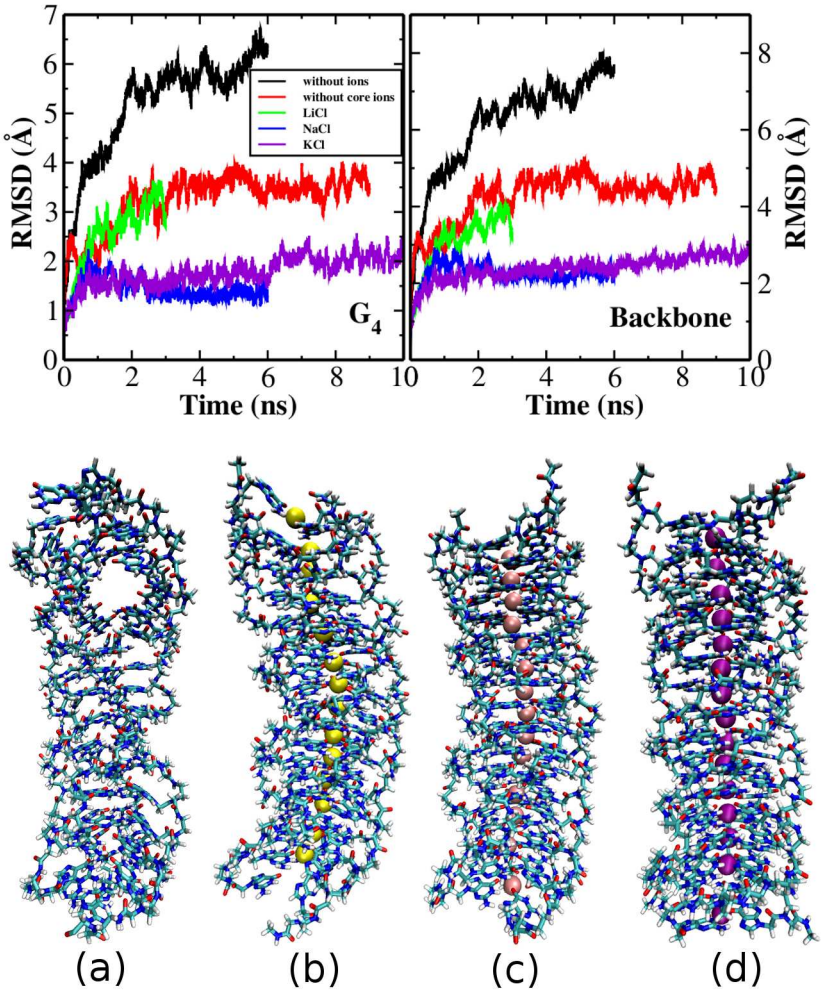

Figure 2.9: RMSD and the simulated structures of G_4-PNA after 6 ns MD run. (a), (b), (c), (d) represent the quadruplex structure without any ions and in presence of Li^+, Na^+ and K^+ ions, respectively.

as the DNA quadruplex [101]. It was also demonstrated experimentally, a G-rich sequences can form dimeric and tetrameric quadruplex structures with PNA backbones [100].

PNA is considered as the synthetic analogue of DNA, which has neutral peptide backbones in contrast to the negatively charged sugar-phosphate backbones in DNA. To model the G_4-PNA structure, we have considered the G_4-DNA as the starting structure, and subsequently, replaced the sugar-phosphate backbone by the peptide backbone using the xleap module of AMBER package [322]. The parameters for the ssPNA with G base sequences is taken from a previous study [385]. We have considered 16 G-quartets stacked G_4-PNA, as was modeled for the G_4-DNA with/without the presence of channel core ions in explicit TIP3P water molecules within a rectangular simulation box. Since the core cations containing PNA quadruplex structure has neutral peptide backbone, we have additionally added Cl^- ions to neutralize the charge of the whole system. We have chosen Cl^- salts of Li^+, Na^+ and K^+ ions for the present simulation study. The MD simulation is carried out for 6 ns using NPT ensemble after initial thermalization at temperature, T = 300 K. The simulated structures obtained after 6 ns production MD run are shown in Fig. 2.12. Similar simulation protocols have been used as was employed for the MD simulation of G_4-DNA quadruplexes. Additionally, we have also shown the time evolution of RMSD diagrams calculated for the G base and peptide backbone in the same figure.

As can be seen from Fig. 2.9, the quadruplex structures without the salts are completely destroyed within 6 ns simulation time. The quadruplex structure is maintained in the presence of salts, where, the monovalent cations

are present within the helical channel. However, the structure with Li^+ ions within the quadruplex channel is significantly distorted, whereas, the Na^+ and K^+ ions coordinated G_4-PNA preserved their parallel four-stranded structures. Moreover, the position of the cations is found to be identical as was observed for the G_4-DNA quadruplex structure. The Li^+ ions occupy the G-quartet plane, while, the Na^+ and K^+ find stable position at the middle of the two G-quartets, making an effective coordination number eight.

To further investigate dynamical aspects of G_4-PNA structures, we have calculated the RMSD for both the G-quartet as well as peptide backbone, and presented them in Fig. 2.12. As can be seen, the RMSD values for the G-quartet and backbones, are significantly high for the G_4-PNA quadruplex without salts, without the presence of core ions in KCl solution and for the Li^+ coordinated quadruplex structures. This suggests that, the G_4-PNA quadruplex can not form stable structures without any salts as well as in LiCl solution. This is due to the large conformational fluctuations in more flexible peptide backbones than the comparatively rigid DNA sugar-phosphate backbones. However, we have found that, the presence of Na^+ and K^+ ions coordinated within the PNA quadruplex channel greatly reduce the RMSD values for both the G residues as well as for the backbones. This results suggest that, the stable G_4-PNA quadruplex can only form in presence of Na^+ and K^+ salts solution.

Further, to understand the structural rigidity in details, we have computed a few time averaged parameters from the MD simulated snapshots for the G_4-PNA in presence/absence of stabilizing core ions. The results are given in Table 2.4. The average G-G stacking distance is found to be

within 3.65-4.32 $\mathring{A}$ with the high value obtained for the quadruplex structure without the presence of salts. The presence of Li^+, Na^+ and K^+ core ions results in almost indential G-G stacking distance (see Table 2.4). Note that, the stacking distance is slightly larger in comparison to that found for the G_4-DNA quadruplex structure, reflecting relatively weaker π-π stacking interactions. The O6-O6 distance between the two G residues situated diagonally range between $\sim$4.02 $\mathring{A}$ and $\sim$5.59 $\mathring{A}$, with the large value obtained for the G_4-PNA without the channel core ions. The difference between the two diagonal distances is significant for the structure without the core ions, indicating the destruction of the four-stranded quadruplex structure in absence of the channel ions. Furthermore, the average distance between the two metal ions are within $\sim$3.55 $\mathring{A}$ and $\sim$3.98 $\mathring{A}$. These values are comparatively larger than the values found for corresponding G_4-DNA quadruplexes. This is consistent with the higher G-G stacking distance found for the G_4-PNA than G_4-DNA. All these results suggest that, the parallel four-stranded G_4-PNA can form stable quadruplex structure in Na^+ and K^+ solution, in accordance with the experimental findings [100, 101].

Structures of G_4A_4-DNA and G_4A_4-PNA quadruplexes

Up to now, we have discussed the structure and dynamical nature of the four-stranded DNA and PNA quadruplexes, containing ploy(G) nucleobase sequences using MD simulations. Note that, G and A are purine nucleobase, which possess large π-surface available for base-base stacking interactions. Since G can form stable quartet through Hoogsteen H-bonding interactions, it is anticipated that four A nucleobases may form A-quartet structure similar

to G_4, in presence of suitable ions. In fact, there are both experimental works and theoretical demonstration for the existence of stable A-A H-bonding interactions and A-quartet formation [386–388].

We first analyze the structure and energetics of A-quartets using DFT calculations, employing dispersion corrected ωB97XD exchange and correlation functional with 6-31+g(d,p) basis sets for all atoms, as implemented in Gaussian09 [345]. Our results have shown that the structure of A_4 is energetically feasible and stabilized through the H-bonding interactions. The formation energy of A-quartet is found to be -60.0 kcal mol^{-1}. Unlike planar structure of G-quartet, the optimized structure of A-quartet does not show planarity and rather, a bowl shaped structure is formed (see Fig. 2.10). A more careful structural analysis of the optimized A-quartet reveal that the four amino ($-NH_2$) groups point towards the centre of the A-quartet. The core amino hydrogens possess partial positive charges, and can form H-bonding interactions with anions, such as Cl^-. To confirm this, we have done the geometry optimization of Cl^- bound A-quartet using the same level of theory. The optimized structures of both the A-quartet and A-quartet coordinated with Cl^- anion, are shown in Fig. 2.10. Upon chelation with Cl^-, the formation energy of the A-quartet enhances by $\sim$20.00 kcal mol^{-1} due the extra stability gained through electrostatic interactions. However, the optimized structure still lacks the planarity and retain the bowl shaped geometry. We anticipate that the structure can form planar geometry by the π-π stacking interactions with the neighbouring nucleobase quartets in a quadruplex structure. However, it is clear that, the stability of the K^+ coordinated G-quartet is much higher compared to the A-quartet coordinated with Cl^- ion.

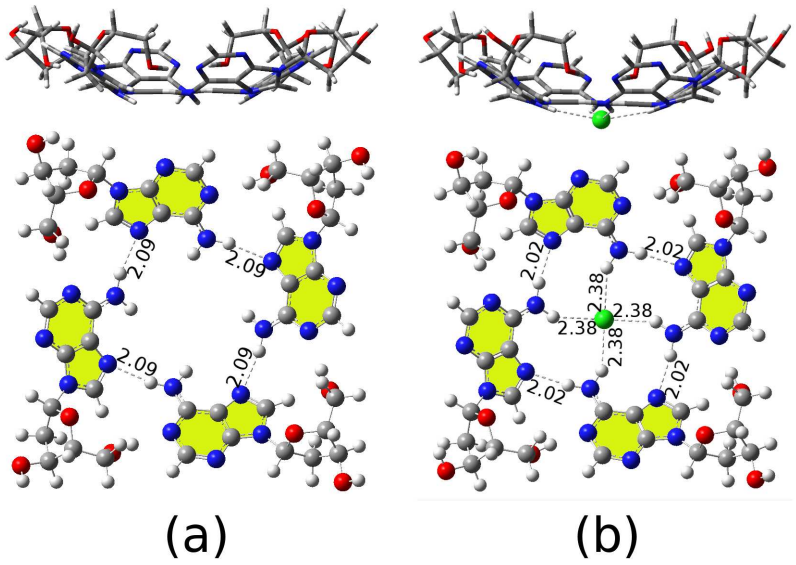

Figure 2.10: DFT optimized structures of A-quartet with (a) and without (b) coordinated Cl^- ion. Important H-bond distances are indicated in $\mathring{A}$. The white, gray, blue, red and green colours indicate hydrogen (H), carbon (C), nitrogen (N), oxygen (O) and chlorine (Cl) atom, respectively.

Next, we have proposed a tetrameric parallel-stranded quadruplex structure (G_4A_4-DNA) constructed from the ssDNA sequences containing alternating repeats of G and A nucleobases, where, the G-quartet is stabilized by cations and A-quartet coordinates with anions, creating a one dimensional channel of MCl (M = Li^+, Na^+ and K^+). We have carried out the 9 ns long MD simulation using the same protocols that are used for the above simulation studies in presence of explicit TIP3P water molecules. We have performed the simulation both in absence and in presence of core channel MCl ions to explore the effects satls on the structure and dynamical behaviors of these quadruplexes. The MD simulated snapshots after 9 ns production run are shown in Fig. 2.11.

As can be seen, the simulated structures maintain their four-stranded

Table 2.5: Various structural parameters of G_4A_4-DNA. r_{i-j} is the average distance between i^{th} and j^{th} unit in a system. All distances are given in $\mathring{A}$.

G_4A_4-DNA	r_{G-A}	r_{O6-O6}	r_{N6-N6}	$r_{M^+-Cl^-}$	r_{O6-M^+}	r_{N6-Cl^-}
no core ions	5.52 ± 0.09	5.00 ± 0.09	5.76 ± 0.04	-	-	-
with Li^+	5.17 ± 0.05	4.40 ± 0.04	8.87 ± 0.02	2.74 ± 0.04	2.37 ± 0.05	3.33 ± 0.03
with Na^+	4.48 ± 0.09	4.40 ± 0.04	6.94 ± 0.03	2.72 ± 0.04	2.39 ± 0.04	3.32 ± 0.06
with K^+	6.09 ± 0.14	5.19 ± 0.15	6.54 ± 0.05	2.72 ± 0.03	2.51 ± 0.24	3.37 ± 0.07

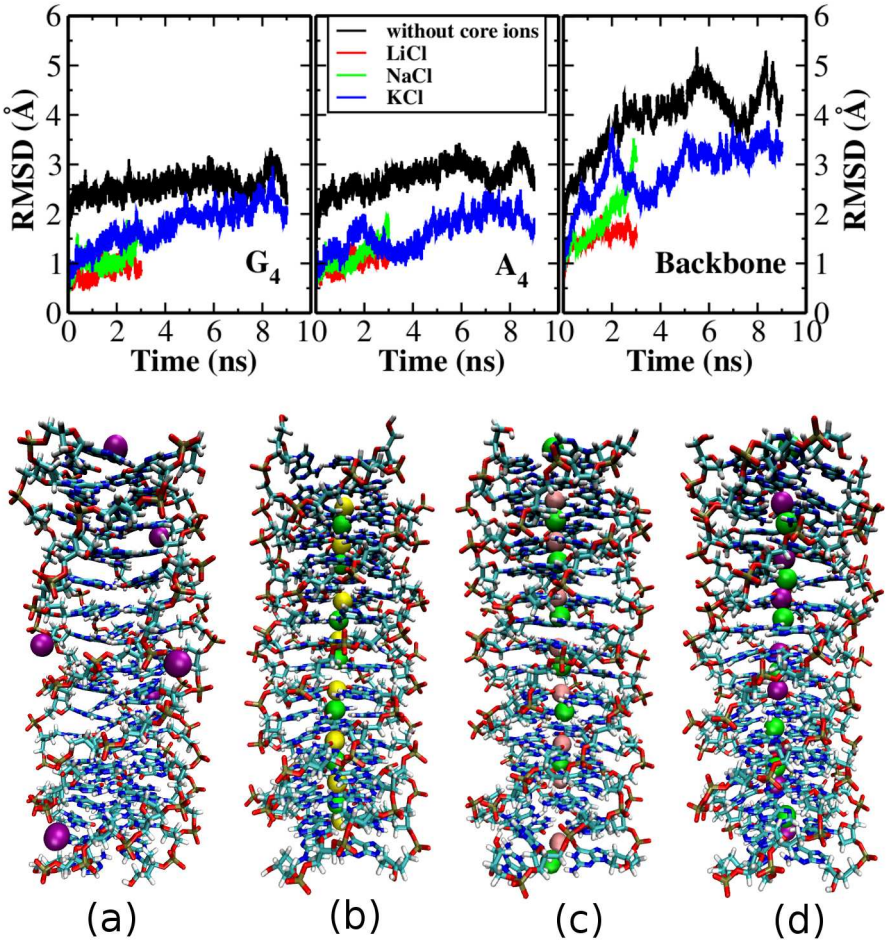

Figure 2.11: RMSD and the simulated structures of G_4A_4-DNA after 9 ns MD run. (a), (b), (c), (d) represent the quadruplex structure without core ions in aqueous solution of K^+ and in presence of LiCl, NaCl and KCl ions, respectively.

geometry with/without the presence of channel core ions. However, there are a few K^+ ions near to the quadruplex structure, in particular, occupying the groove regions as well as at the proximity of endgroup quartets, for the G_4A_4-DNA without the initial channel core ions. It is also clear that, the position of the Cl^- ions is at center of the A-quartet plane, whereas, the cations occupy at/nearby the center of the G-quartet plane. This is different from the DNA/PNA quadruplex structure formed in presence of the Na^+ and K^+ ions, where, the ions find stable position between the two G-quartets plane. This is because, the presence of cations only within the G-quadruplex channel causes the electrostatic repulsion, while, the the presence of cations and anions alternatively, results in electrostatic attraction, which causes the cations to be slightly off-centered from the middle of the G-quartets stack.

Next, we have performed the RMSD calculations of base, both G and A individually, and backbone atoms for all the G_4A_4-DNA quadruplexes studied here. The time evolution of RMSD values are shown in Fig. 2.11. As can be seen from the RMSD plots, the backbone atoms RMSD is large (1.5-4.5 $\mathring{A}$) compared to that of the nucleobases (0.7-3.0 $\mathring{A}$) present within the quadruplex. However, the RMSD values obtained for the G-quartet is small than the RMSD values found for the A-quartet. This suggests the greater stability of G-quartet than A-quartet, corroborating with our DFT results. Also, note that, within the 3 ns simulation time, the base RMSD values for the LiCl stabilized G_4A_4-DNA is smaller in comparison to the quadruplex structures coordinated with others salts (NaCl and KCl). The higher stability of LiCl coordinated quadruplex structure can be attributed to the greater electrostatic stabilization because of the smaller size of the Li^+ ion

among others ions. Moreover, being a small cation, Li^+ is found stabilizing at the planar core position of the G-quartet. However, our MD results have shown that, all G_4A_4-DNA quadruplexes can be formed with/without the presence of the channel MCl satls.

To examine the effects of various salts on the dynamical behaviors of the quadruplex structure, we have calculated some structural parameters averaged over the simulation time. For this, we have estimated (1) the distance between the G and A plane (r_{G-A}), (2) the diagonal O6-O6 for G_4 and the diagonal N6-N6 for A_4 (r_{O6-O6} and r_{N6-N6}), (3) the distance between the M^+ and Cl^- ($r_{M^+-Cl^-}$), (4) the separation between the M^+ and O6 atom of G (r_{O6-M^+}) and (5) the distance between the N6 of A and Cl^- (r_{N6-Cl^-}). All the results are given in Table 2.5.

As given in table 2.5, the average separation between the G- and A-quartet, as calculated by the shortest distance between the G O6 and A N6 atoms in the consecutive quartets, is found to be within $\sim$4.48 $\mathring{A}$ and $\sim$6.09 $\mathring{A}$. The small stacking distances are found for the LiCl and NaCl coordinated G_4A_4-DNA quadruplex structure. Moreover, the diagonal O6-O6 distance within a G-quartet is $\sim$4.40 $\mathring{A}$ for the quadruplex structures stabilized by both LiCl and NaCl salts. The distance between two diagonal N6 atoms in a A-quartet varies from 5.76 $\mathring{A}$ to $\sim$8.87 $\mathring{A}$, indicating greater structural fluctuations for the A-quartet in comparison to the G-quartet within the quadruplex structure. The average distance between the M^+ and Cl^- is found to be $\sim$2.74 $\mathring{A}$ for LiCl and $\sim$2.72 $\mathring{A}$ for both NaCl and KCl coordinated G_4A_4-DNA. However, the avearge separation between the G O6 atom and M^+ varies from $\sim$2.37 $\mathring{A}$ to $\sim$2.51 $\mathring{A}$ with increasing order as the ionic

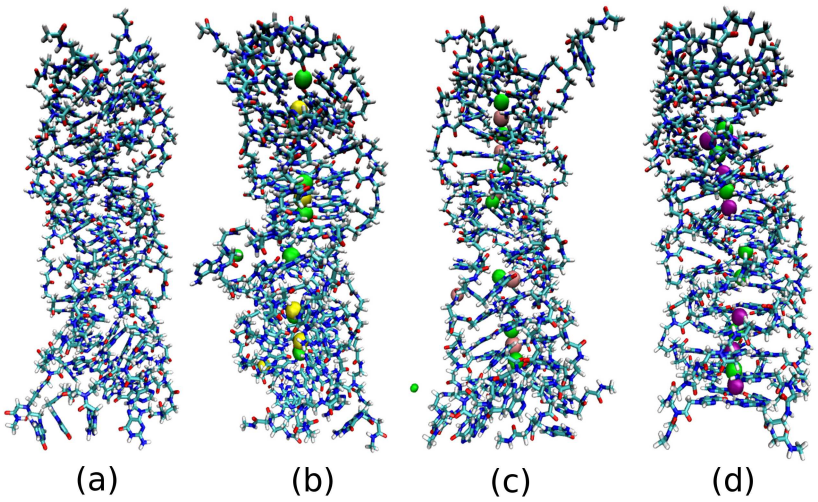

Figure 2.12: The simulated structures of G_4A_4-PNA after 6 ns MD run. (a), (b), (c), (d) represent the quadruplex structure without ions and in presence of LiCl, NaCl and KCl ions, respectively.

radius of the cation increases. The distance between the A N6 atom and Cl^- is within ∼3.32 $\mathring{A}$ and ∼3.37 $\mathring{A}$ for all the G_4A_4-DNA quadruplex structures. Based on the structural and RMSD analysis, we conclude that the the G_4A_4-DNA quadruplexes can form in absence of any central salts, and the structural stability increases by coordinating with the chloride salts of monovalent cations. Our results also suggest that, the proposed quadruplex sturcture can be used to trap both the cations and anions simultaneously.

Additionally, we have also investigated the possibility of forming G_4A_4 quadruplex structure with the peptide nucleic acid (PNA) backbone using MD simulation for 6 ns in aqueous medium with/without the presence of channel salts. All the simulations were carried in the same manner as discussed earlier. The simulated snapshots of G_4A_4-PNA structures are shown in Fig. 2.12. As can be seen, the parallel four-stranded quadruplex sturctures

are completely destroyed after 6 ns MD simulations irrespective of the presence of coordinated MCl salts (M = Li^+, Na^+ and K^+). This is because of the presence of more flexible PNA backbone as well as less stable A-quartet units within the quadruplex channel. The results suggest that, the formation of parallel tetrameric G_4A_4-PNA quadruplexes are not feasible in aqueous solution at temperature, T = 300 K and pressure, P = 1 atm, as considered in the present study.

Electronic structures of G_4-DNA, G_4-PNA and G_4A_4-DNA

In the previous sections, we have discussed the structures of various G-quadruplexes and the importance of coordinated monovalent metal ions using MD simulations. However, it would be interestingly to study the electronic structure of these quadruplexes for understanding the various quantum effects, which might play important role on these soft-condensed biological materials properties. To this end, we have used DFT study to analyze the electronic and optical properties of the systems, considered from the energy minimized average MD simulated structures. We have considered four consecutive stacks for the DNA and PNA quadruplexes in presence of coordinated channels ions as well as a few surrounding water molecules for the single-point DFT calculations. To neutralize the systems, we have considered the presence of appropriate number of K^+ or Cl^- ions at nearby positions of quadruplex structure as found from the MD simulations. All model systems considered for the DFT calculations are shown in Fig. 2.13. The DFT calculations are performed using SIESTA code [349,350], employing generalized gradient approximation (GGA) in the Perdew-Burke-Ernzerhof (PBE)

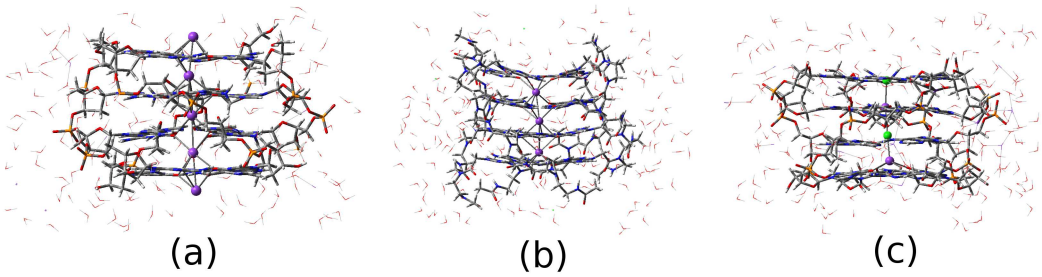

Figure 2.13: Model structures for the DFT study. (a), (b) and (c) represent the four stacks quadruplex structure of G_4-DNA, G_4-PNA and G_4A_4-DNA coordinated with K^+ ions and KCl salts, respectively.

form [389] as exchange and correlation and double ζ polarized (DZP) basis sets for the valence electrons of all atoms. The interaction between ionic cores and valence electrons is described by norm conserving pseudopotentials [390] in the fully non-local Kleinman-Bylander form [391].

To investigate the optical properties, we have calculated the optical conductivity of these model quadruplex systems in presence of unpolarized light propagating along the quadruplex strand direction using Kubo formalism as implemented in SIESTA DFT package [349, 350]. Note that, the optical conductivity calculated here, does not consider scissor corrections. The conductivity profiles for the quadruplex sturctures are shown in Fig. 2.14 (top panel). The onset of optical conductivity occurs at/above ∼3.0 eV for the DNA systems, and the peak positions depend on the nucleobase sequences. However, the G-rich DNA show optical conductivity at 3.0 eV light energy. This occurs because of the $\pi \rightarrow \pi^*$ orbital transitions. In Fig. 2.14, the intense peaks in conductivity profiles at/above ∼3.0 eV is due to the electronic excitations from G π orbitals to G π^* orbitals. Additionally, a few low-energy peaks ($<$ 3.0 eV) appear in the optical conductivity profiles for

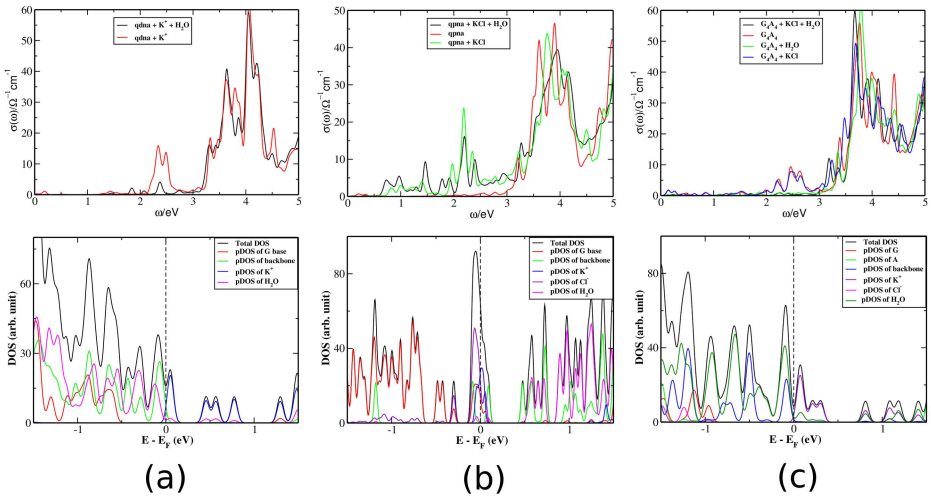

Figure 2.14: Optical conductivity profiles (upper panels) and electronic density of states (DOS) (lower panels) of G_4-DNA (a), G_4-PNA (b) and G_4A_4-DNA (c).

the quadruplexes studied here. To understand the origin of these low-energy peaks, we have considered analyzing the energy level diagrams in terms of partial density of states (DOS) as well as the highest occupied molecular orbital (HOMO) and lowest unoccupied molecular orbital (LUMO) for these systems. The DOS of all three quadruplexes are shown in Fig. 2.14.

As can be seen, the HOMO is mainly distributed on negatively charged sugar-phosphate backbone, while, the LUMO is localized on the nearby K^+ ions surrounded by water molecules in G_4-DNA. In case of G_4-PNA, the HOMO and LUMO orbitals are mainly localized on surrounding Cl^- and on coordinated K^+ ions, respectively. However, a significant contribution to the LUMO also comes from the G nucleobases. For the G_4A_4-DNA, the orbital's contribution to the HOMO comes from the sugar-phosphate backbone and nearby water molecules, whereas, the LUMO is mainly distributed over surrounding K^+ ions and the nearby water molecules. The orbital analysis

suggests that, the low-frequency peaks in the optical conductivity profiles may arise from the electronic transition from the occupied orbitals of backbone atoms and nearby water molecules to the unoccupied K^+ orbitals for the DNA quadruplexes. Also, the transition from Cl^- occupied orbitals to K^+ unoccupied orbitals is most likely to be responsible for the low-frequency conductivity peaks found in G_4-PNA quadruplex. It is also found that, the presence of surrounding water molecules highly suppresses the conductivity strength. This is because the presence of water molecules strongly stabilizes both the backbone and K^+ orbitals, and the water coordination shells block the possibility of low-energy electronic transition from the DNA backbone orbitals to the K^+ unoccupied orbitals. However, for the G_4-PNA quadruplex, which does not have negatively charged sugar-phosphate backbone, the possible low-energy transitions occur because of the presence of K^+ and Cl^- ions. Therefore, the surrounding water molecules do not show any influence in changing the conductivity peak's intensity.

Next, we have studied the charge transfer properties of the G_4-DNA quadruplex sturctures using DFT. Note that, the G_4-DNA is structurally more rigid than any double-stranded DNA. Moreover, it possesses a large number of G_4 units stacked together along the long quadruplex helical axis by π-π stacking interactions. Becasue of the presnece of more poralizable G nucleobase and its low ionization energy, it is expected that G_4-DNA would serve as efficient molecular wire for hole conduction. Here, we have calculated charge (electron and hole) transfer integrals between the G nucleobases, which create the paussible charge transport channels within the G_4-DNA quadruplex. We have considered four consecutive G-quartets stacks without

Table 2.6: Effective charge transfer integrals (J_{eff} in eV) between the possible hopping channels in a G_4-DNA. R_{ij} is the center of mass distance between i^{th} and j^{th} unit the system. All distances are given in $\mathring{A}$.

R_{ij}	J^{h}_{eff}	J^{elec}_{eff}	μ^h ($cm^2V^{-1}s^{-1}$)	μ^e ($cm^2V^{-1}s^{-1}$)
3.66	0.0432	0.1312	1.7502	0.0139
6.00	0.0256	0.0392	-	-
6.51	0.0210	0.0499	-	-
6.57	0.0229	0.0101	-	-
8.68	0.0005	0.0001	-	-
9.39	0.0003	0.0002	-	-
9.65	0.0001	0.0003	-	-

the central ions connected through the H-passivated DNA sugar-phosphate backbone. We have used the fragment molecular orbitals (FMOs) approach, as implemented in ADF software code, for calculating the charge transfer integrals. We have used GGA/PBE exchange and correlation with dispersion interactions and TZ2P basis sets for all atoms. All the effective transfer integrals (J_{eff}) as function of distances for both the electron and hole are provided in Table 2.6.

As given in Table 2.6, for the short inter-nucleobase distance, the effective electron transfer integral is found significantly large than the hole transfer integral. However, the transfer integrals for electron and hole are almost similar for large distances. Moreover, the reorganization energy for hole injection is found to be small in comparison to that calculated for the electron injection in G. This suggests that, the creation of a hole is much easier than the electronic injection for the G nucleobase. The comparable hole transfer integral together with small hole reorganization suggest that, the G_4-DNA containing G nucleobases may give rise to high hole mobility. To examine

this speculation, we have calculated the charge carrier mobilities for both the electron and hole using the semi-classical Marcus hopping mechanism. Our results suggest that, the hole mobility is significantly high ($\mu^h = 1.75$ cm^{2}V^{-1} s^{-1}) than the mobility estimated for the electrons ($\mu^e = 0.014$ cm^{2}V^{-1}s^{-1}) at room temperature. We conclude that, the G-rich G_4-DNA may be a potential candidate meterials for hole transport. Here, it is important to note that, the calculations of the carrier mobilities do not include various key controlling factors, namely, fluctuations in base-pair level, molecular vibrations and solvation effects, etc. Thus, the mobility values calculated here, are only to be considered in a qualitative manner.

2.3.3 Stability and electronic structure of G_4-DNA in presence of Cu^{+2}, Ag^+ and Au^+

In the previous sections, so far investigated, we have discussed the structures and electronic properties of the G-quartet and G_4-DNA/PNA quadruplexes. We have shown that the presence of monovalent ions is necessary for the stability of G-quadruplex structures, at least, for the short oligonucleotides. However, it would be really interesting to examine the effect of other ions for stabilizing the G-quadruplex structures. In this section, we have studied the stability of G_4-DNA structure within single- and di-nucleosides level (i.e., one and two G_4-stacks) in presence of divalent ion, Cu^{2+} and monovalent ions, Ag^+ and Au^+, using DFT calculations. Note that, the G_4-Cu^{2+} is magnetic

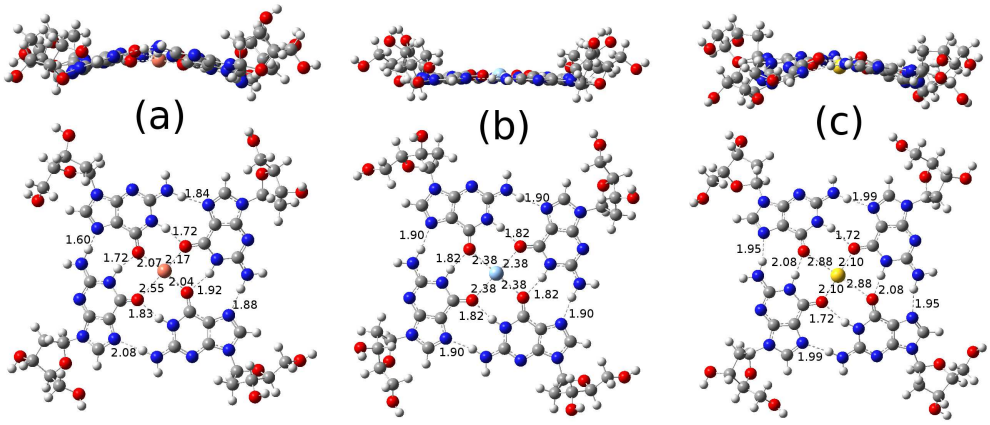

Figure 2.15: DFT optimized structures of G-quartets in presence of Cu^{+2} (a), Ag^{+} (b) and Au^{+} (c). Important distances are indicated in $\mathring{A}$.

as it possesses the spin-$\frac{1}{2}$ Cu^{2+}. Consequently, we have performed the spin-unrestricted DFT calculations for the G_4-Cu^{2+} complex, while, the spin-restricted calculations are carried out for the G_4-Ag^{+} and G_4-Au^{+}. Moreover, it is important to note that, these ions are toxic to the human cells, and can not be used to stabilize the G-quadruplex structure in vivo biological systems. However, the diverse polymorphic structures of G-quadruplex may be used to trap these toxic ions from the solutions contaminated with these ions.

For the geometry optimization, we have considered ωB97XD functional and 6-31+g(d,p) basis sets for the atoms except the metal ions, for which, we have considered the effective core potential basis set, LANL2DZ for Cu and Ag, while, LANL2MB for Au. The DFT calculations are performed using Gaussian09 suit of programs [345]. The DFT optimized structures of G-quartets coordinated with Cu^2+, Ag^{+} and Au^{+} ions are shown in Fig. 2.15.

The binding energy (E_b) and formation energy (E_f) have been calculated using the methods already discussed for analyzing the energetics of these

Table 2.7: Binding energy (E_b) and formation energy (E_f) of G-quartets in presence of Cu^{2+}, Ag^+ and Au^+

G-quartet	E_b (kcal mol^{-1})	E_f (kcal mol^{-1})	E_b^H (kcal mol^{-1})	$E_b^{Elec.}$ (kcal mol^{-1})
G_4-Cu^{2+}	-531.79	-469.05	-91.59	-440.20
G_4-Ag^+	-220.89	-173.10	-94.47	-126.41
G_4-Au^+	-228.82	-166.37	-78.42	150.40

complexes. Additionally, we have also quantified the contribution of the electrostatic ($E_b^{Elec.}$) and the H-bonding (E_b^H) interactions to the total binding energy (E_b) for the detailed analysis. The results are provided in Table 2.7.

As shown in Fig. 2.15, the structure of G-quartet with coordinated Ag^+ ion, is highly symmetric and planar than the G_4 structures with Cu^{2+} and Au^+ ions. The Cu^{2+} coordinated G_4 shows higher binding and formation strength in comparison to the others two complexes (see Table 2.7). The strong electrostatic interactions due to the double (2+) positive charges on Cu and the greater extent of orbital interactions because of the presence of more diffused d-orbitals, result in the higher stability of the G_4-Cu^{2+}. The G_4 with Au^+ is found to be slightly more stable (8 kcal mol^{-1}) than the G_4-Ag^+ complex. This is because of the presence of higher energy atomic orbitals in Au. However, the H-bonding interactions are found to be large (-94.47 kcal mol^{-1}) for the G_4-Ag^+ than the others two complexes. This is due to the formation of planar and more symmetric G-quartet structure, which forms the stable H-bonds.

Since the Cu^{2+} system is magnetic, it would be really interestingly to look

at the nature of magnetic ordering along the G-quadruplex helical channel. To examine this, we have considered the two G_4-stacks with coordinated Cu^{2+} ions, and fully optimized the structures with two different spin-configurations, namely, ferromagnetic and antiferromagnetic spin coupling between the magnetic Cu^{2+} centers, using SIESTA code, within GGA/PBE level. Our results show that, the ferromagnetic spin ordering is only stable by $\sim$3 meV than the antiferromagnetic spin allignment between the two Cu^{2+} centers. This suggests that, there is no such stable spin allignment between the magnetic centers, and hence, the system would behave as a paramagnet at room temperature ($\sim$26 meV). However, a few studies have demonstrated that, the ligands, such as water or hydroxyl or oxo groups, bridged between the magnetic centers induces weak/strong ferromagnetic coupling due to the geometry specific orbital interaction [369, 392]. To understand the effect of water coordination between the two Cu^{+} centers, we have chosen three water molecules coordinated to the Cu^{2+} centers, making the Cu^{2+} coordination environment to an octahedral. The fully optimized geometry of water coordinated G_4-Cu^{2+} dimer obtained within the same level of calculations is shown in Fig. 2.16.

Our results have shown that, the minimum energy structure is a high-spin state, where, the spins on the Cu^{2+} centers, are alligned parallel to each other, i.e., leading to the ferromagnetic interactions. The high-spin ferromagnetic state is stable by $\sim$195 meV than the low-spin antiferromagnetic state. The five degenarate d-orbitals are splitted into two sets of orbitals (t_{2g} and e_g) because of the presence of octahedral ligand fields. Moreover, an unsymmetrical filling of e_g orbitals ($d_{x^2-y^2}$ and d_{z^2}) induces further splitting of the e_g

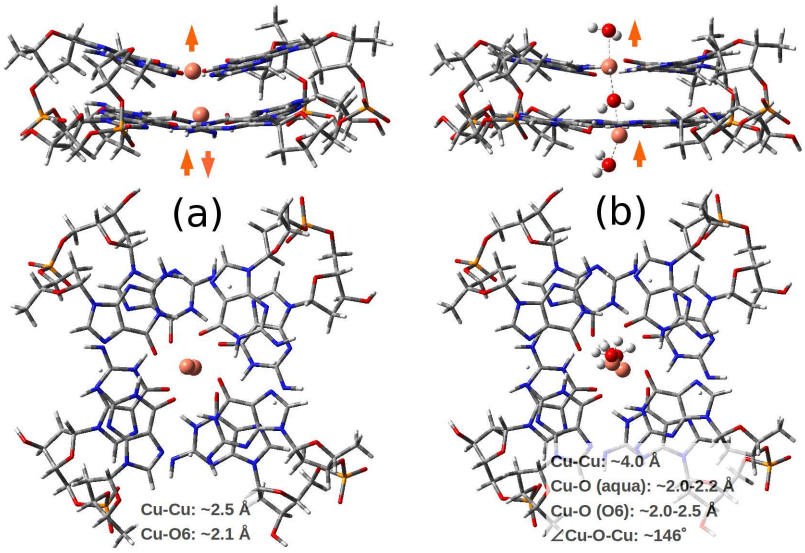

Figure 2.16: DFT optimized structure of G_4 dimer in presence of Cu^{+2} ions without (a) and with (b) the coordinated aqua ligands. The up and down arrows indicate the spin configurations on the Cu atoms. Important structural parameters are also indicated.

orbitals to remove the degenaracy. This is commonly known as Jahn-Teller effect. Due to this, the unpaired electrons on Cu atoms situate on the d_z^2 orbitals, which are coupled through ferromagnetic interactions via aqua bridge. Note that, the unpaired electrons were placed on the Cu $d_{x^2-y^2}$ orbital for the complex without bridged water molecules. The optimized structure in high-spin state, as shown in Fig. 2.16, shows that, the distance between the two Cu^{2+} centers is $\sim$4.0 $\mathring{A}$, which is large than the value ($\sim$2.5 $\mathring{A}$) found for the Cu^{2+}-complex without coordinated water molecules. This is due to the presence of water molecules between the two G-quartets. Moreover, the planarity of G-quartets is greatly enhanced because of the presence of coordinated water molecules. Our results have demonstrated that, the bridging

of water molecules between the Cu^{2+} centers within the G-quadruplex structure stabilize the high-spin ferromagnetic state, which may be useful for the spintronic and memory device applications.

2.3.4 Energetics and optical properties of porphyrin intercalated G_4-DNA dimers

So far, we have discussed the stability and electronic properties of G-quadruplexes stabilized by various monovalent and divalent cations using different theoretical techniques. However, it was also possible to stabiliize the G-quadruplex sturtures by appropriate organic molecules. In fact, as already mentioned, there is large number of G-quadruplex stabilizing ligands reported in literature. Among all of these, the importance of porphyrin derivatives have drawn much attention for anti-cancer therapeutic treatments in medicine, because, it stabilizes the G-quadruplex structure [91]. Thus, it is really important to understand the molecular basis of porphyrin stabilized G-quadruplex structure and their electronic properties.

In this section, we have provided the mechanistic understanding of porphyrin intercalated G-quadruplex formation, based on theoretical studies. In a previous study, using MD simulation, Rosa Di Felice and coworkers have shown the stability of G-quadruplex structure by intercalating a porphyrin derivative without the channel cations [393]. Here, we have considered the two G_4 stacks, *i.e.*, dinucleotide G-quadruplex (G_4-DNA dimer), intercalated with free base porphyrin ($PorH_2$) and a few metal-porphyrin (M-Por) derivatives. We have chosen the most common Mg-porphyrin (Mg-Por) and the two

other magnetic porphyrins; namely, Fe-porphyrin (Fe-Por) and Cu-porphyrin (Cu-Por), where, the two core acidic imino protons (-NH) are replaced by these divalent metal ions. Note that, these metal porphyrin are synthetically available and studied extensively both in theories and experiments. To neutralize the systems, we have considered the hydrogen passivation of the negatively charged phosphate groups, which essentially mimic the acidic conditions. Note that, the hydrogen passivation was successfully emmployed in several previous studies concerning the modeling of duplex DNA [394–398]. All DFT optimized geometries within GGA/PBE level using SIESTA code, are shown in Fig. 2.17.

From the relaxed geometries, it is clear that, the stacking distance between the two G-quartets increase significantly in presence of the encapsulated porphyrin moiety for all the complexes. Note that, the equilibrium distance between the two G-quartets in the optimized structure of G_4-DNA dimer is $\sim$2.99 $\mathring{A}$, which is slightly smaller in comparison to the average stacking distance $\sim$3.4 $\mathring{A}$ found for the long G_4-DNA quadruplex. However, in presence of porphyrin/metal-porphyrin between the two G-quartets, the distance (R_{G-G}) increases to $\sim$6.38-6.53 $\mathring{A}$ depending on the intercalated porphyrin types (see in Table 2.8). In fact, the size expansion is possible due to the presence of flexible DNA sugar-phosphate backbone, and was also found in previous study [393]. This results in volume expansion along the quadruplex helical axis due to the large repulsive electronic interactions between the G-quartet and porphyrin π electron surfaces. The large unfavourable π-π electronic interactions is compensated by the strong hydrogen bonding interactions. To understand the stability of these complexes, we have defined

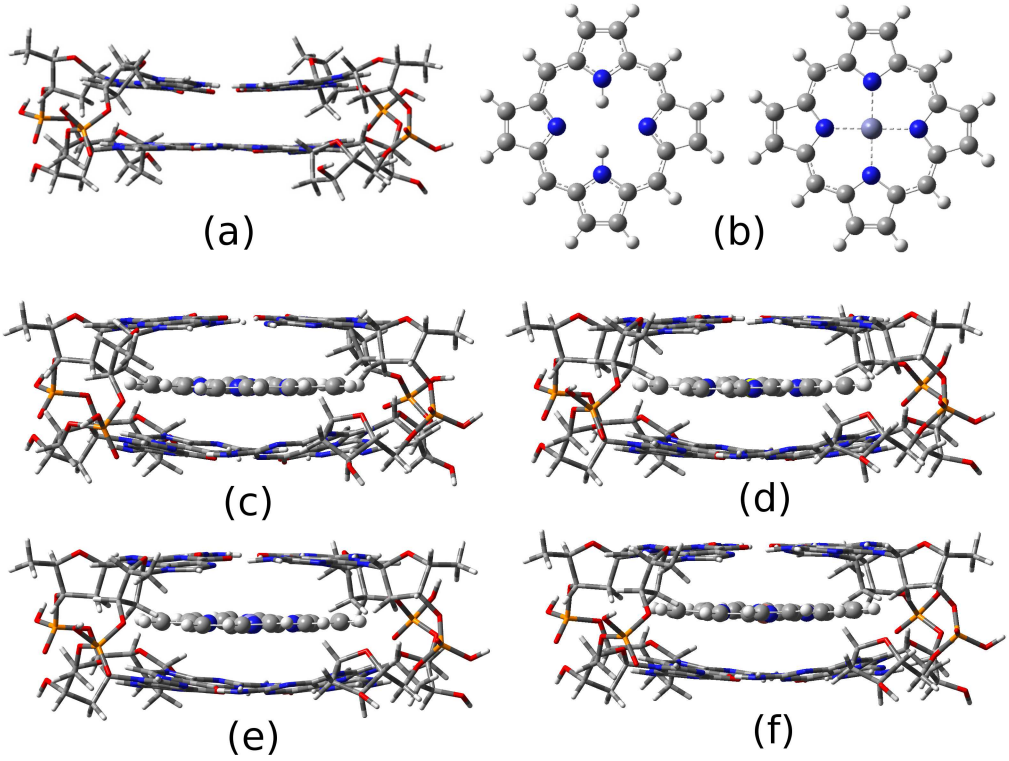

Figure 2.17: DFT optimized structures of G-quartet dimer (a), free base porphyrin and Zn-porphyrin (b), free base porphyrin (c), Mg-porphyrin (d), Fe-porphyrin (e) and Cu-porphyrin (d) intercalated G-quartet dimers.

binding energy (E_b), which is calculated as:

$$E_b = E(G_4 - DNA - (PorH_2/PorM)) - \sum_{i=1}^{4} E(G_4 - DNA) - E(PorH_2/PorM) \quad (2.5)$$

where E(G_4-DNA-($PorH_2$/PorM)) is the total energy of the optimized complex and E(G_4 and E($PorH_2$/PorM; M = Mg^{2+}, Fe^{2+}, Cu^{2+}) are the single-point energy of the G_4-DNA dimer and $PorH_2$/PorM, calculated at their optimized geometry of their corresponding complex structure. Further, to quantify the contribution of π interactions and H-bonding interactions to the overall binding energy (E_b) of these complexes, we have decomposed the binding energy into mainly two intractions: π electronic interactions and the H-bonding interactions. All the energetics terms are provided in Table 2.8. As can be seen, the binding energy range between ∼-158.42 kcal mol^{-1} and ∼-164.42 kcal mol^{-1} for the complexes studied. Note that, the difference in binding energy is only ∼6 kcal mol^{-1}, suggesting similar energetic behaviors for all the porphyrin-G_4-DNA complexes. However, the favourable binding energies for all the complexes is mainly due to the strong H-bonding interactions between the G nucleases forming G-quartets. Interestingly, the PorFe and PorCu possess magnetic moments of 2 and 1 μ_B in their complexed structures. This suggests that, the formation of long G_4 wire encapsulated with these two metal porphyrin would result in quasi-one-dimensional magnetic chains, which may find applications in memory devices.

Additionally, we have investigated the optical absorption properties for the G_4-DNA encapsulated with $PorH_2$ complex, using TDDFT methods, as

Table 2.8: Binding energy (E_b) and equilibrium stacking distances of free base porphyrin and metal porphyrin intercalated G_4-DNA dimer.

Systems	E_b (kcal mol^{-1})	E_b^{π} (kcal mol^{-1})	E_b^{H} (kcal mol^{-1})	R_{G-G} ($\AA$)	μ_B
G_4-DNA-PorH2	-164.42	38.28	-202.70	6.53	0.00
G_4-DNA-PorMg	-163.95	35.05	-199.00	6.39	0.00
G_4-DNA-PorFe	-158.42	33.90	-192.32	6.38	2.00
G_4-DNA-PorCu	-162.11	37.82	-199.93	6.36	1.00

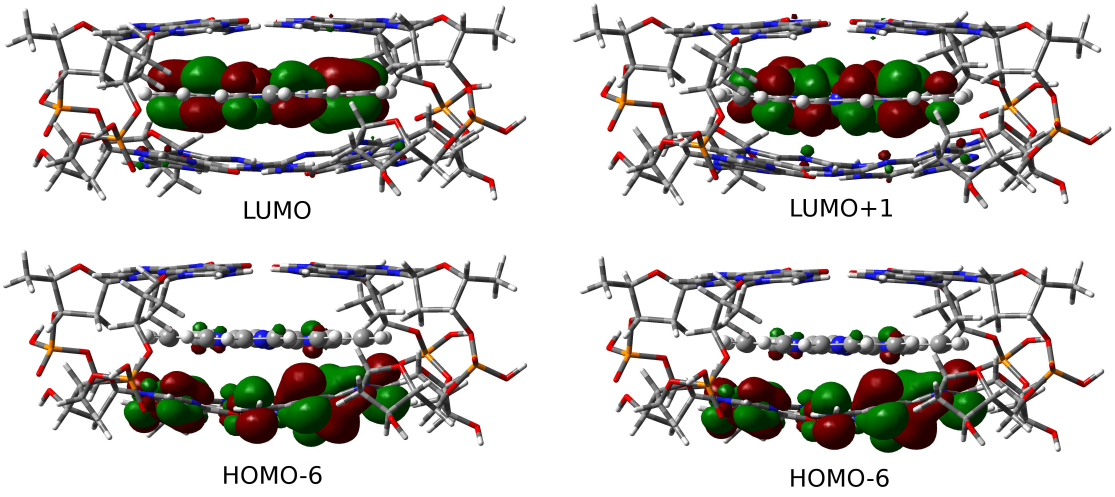

Figure 2.18: The FMOs relevant to the low-energy excitations for free base porphyrin ($PorH_2$) intercalated G-quartets dimers. HOMO and LUMO are the highest occupied molecular orbital and lowest unoccupied molecular orbital, respectively. The two low-energy transitions involve the electron promotions from HOMO-6 to LUMO (∼409.39 nm) and LUMO+1 (∼408.24 nm).

implemented in Gaussian09 code [345]. Our results have demonstrated that, there are two low energy peaks, at ∼409.39 nm and ∼408.24 nm, in the optical absorption spectrum. Also, note that, the electronic absorption spectra calculated for the isolated G-quartet and free base porphyrin ($PorH_2$) have shown that, the low-energy electronic transitions appear at comparatively higher energy. The first intense abosrption peaks appear at ∼265 nm for the G_4, whereas, the four low-energy peaks are obtained for the $PorH_2$. The positions of these peaks are at ∼369.10 nm, ∼348.88 nm, ∼326.88 nm and ∼318.09 nm. Note that, all these transitions involve electron promotions from π to π^* orbitals. To understand the origin of the low-energy absorption peaks found for the $PorH_2$ intercalated G_4-DNA dimer, we have analyzed the frontier molecular orbitals (FMOs), that are mainly involved in these transitions in details. We find that, the intense low-energy peaks arise due to the charge (electron) transfer transitions from G_4 π orbitals to porphyrin π^* orbitals (see Fig. 2.18). We conclude that, the porphyrin intercalted G_4-DNA may find applications in optical devices.

2.4 Conclusions

In conclusion, we have studied the structural stabilities and conformational dynamics of various G-rich DNA, RNA and PNA quadruplexes with and without the presence of stabilizing monovalent cations using MD simulations in aqueous solution at ambient conditions (T = 300 K and P = 1 atm). Our results have demonstrated the importance of different alkali cations for stabilizing the G-quadruplex structures investigated in this chapter. Our

results have shown that, the stability increases with increase in size of monovalent cations and the order follows as $Li^+ < Na^+ < K^+$. We have shown that, the $r(UG_4U)_4$ RNA quadruplex is more stable in comparison to the $d(TG_4T)_4$ DNA quadruplex, which agrees well with the experimental results. The greater stability of $r(UG_4U)_4$ quadruplex is due to the presence of $2'$ hydroxyl group (-OH), which form several extra intra-molecular H-bonds with the polar oxygen groups, and thereby, reducing the hydration from solvent water molecules. The present investigations also demonstrate that, similar to the DNA quadruplexes, the four-stranded PNA quadruplex can also be stable in aqueous medium in presence of the suitable cations. Additionally, we have proposed a potential four-stranded quadruplex sturture, which contains the consecutive repeating units of G- and A-quartets along the quadruplex channels. This quadruplex structure binds simultaneouly caions and anions in its G-quartet and A-quartet plane, respectively. Therefore, this structure may have applications for selective detection of both the cations and anions simultaneously. We have also analyzed the low-energy optical conductivity diagrams of these quadruplexes. We have found that there are peaks in the low-frequency regions of optical conductivity profiles orginating because of the presence of nearby ions and water molecules. Interestingly, we have found larger hole carrier mobility for the G-quadruplexes studied here. Further, we have also investigated the possibility of stabilizing G-quadruplex structures using Cu^{+2}, Ag^+ and Au^+ ions. Our results have predicted that the Cu^{+2} ions could be aligned ferromagnetically along the G-quadruplex channel. Additionally, we have also discussed the stability and electronic properties of porphyrin and metal-porphyrin intercalated G-quadruplexes.

The optical absorption have revealed that, there is change transfer transitions from G π orbitals to porphyrin π^* orbitals, which causes large red-shift in the low-energy absorption peaks. Overall, our detailed simulation studies have shown the diversity in G-quadruplex structures, and their stability and electronic properties. We believe that the present investigation would help to understand not only the microscopic structural details of these biologically interesting molecules, it would also stimulate their applications in opto-electronic and electronic devices.

Chapter 3

Understanding the Interactions of Nucleosides and Nucleic Acids with Graphene*

3.1 Introduction

Applications of carbon based nanomaterials, such as two-dimensional (2D) graphene, one-dimensional (1D) carbon nanotubes and zero-dimensional (0D) fullerenes, as molecular diagnostics, biosensors, DNA sequencing and biochip and in bio-medical treatments are of increasing interest among researchers since past few years [399, 400]. Carbon nanostructures can be broadly functionalized and their low-dimensional electronic properties are sensitive to

*Work reported in this chapter is published in: Arun K. Manna and Swapan K. Pati, *J. Mater. Chem. B* **1**, 091 (2013)

molecular adsorption. Graphene, a sp^2 hybridized 2D hexagonal nanocarbon crystal, is considered as promising nanoscale building blocks of new generation applications, for example, a substrate material for dispersion of polymer, nanoparticles, and delivering essential drug molecules to the cells, etc [401–403]. Recent reports also highlight its potential device application in nanoelectronics because of its remarkable mechanical, electrical and thermal properties [260, 404–406].

Dispersion of carbon nanostructures using DNA or any biopolymer has significant impact in isolating these structures from their mixtures. Furthermore, rapid, selective, and cost-effective analysis of biomolecules is important in clinical diagnostics, DNA sequencing and various treatment processes. Significant advancement has been made in this direction employing-carbon based nanostructures, such as, carbon nanotubes [407–409] carbon nanodots [410, 411] and carbon nanofibers [412]. Recently, Tan *et al*. have proposed to use ssDNA and carbon nanotube for the homogenous detection of biomolecules [413,414]. Both experimental and simulation works predict that the single walled carbon nanotubes could be completely wrapped by ssDNA molecules through noncovalent interactions, and thus, providing a route to separate out nanotubes with different chiralities [415–439]. Moreover, carbon nanotubes can act as protector of DNA strands during cellular delivery [440]. Much attention has been given to the dispersion and solubilisation of carbon nanotubes using various ssDNA oligonucleotides. However, there is hardly any report on interactions of ssDNA with 2D graphene. Recent experiment by Saliha *et al*. [441] have demonstrated that there exist two competing π-stacking interactions: base-base -stacking and base-graphene -stacking, when

ssDNA is added in graphene solution. A crossover between these two competing interactions results in two distinct ssDNA pattern formations, small spherical particles and elongated networks, onto graphene surface. A molecular simulation study by Zhao [442] explores various self-assembly structures of duplex DNA onto the graphene and carbon nanotube surfaces, highlighting the importance of π-stacking interactions between the nucleotides and nanostructure surfaces in aqueous environments. This study considers double stranded DNA, which is comparatively more rigid than ssDNA. A more flexible oligomer, such as ssDNA, would be better candidate for the dispersion of 2D graphene in solution. As mentioned above, the experiment by Saliha et al. involves the usage of the ssDNA oligonucleotide in contact with graphene and found two distinct pattern formations. Although, the work qualitatively explains the underline reason behind two distinct self-assembly pattern, it does not unravel the microscopic origin of the observation. Moreover, it does not consider what would be the role of base sequences on the formation of self-assembly nanostructures on graphene. Indeed, it is a really challenging task to probe them by experiment due to the experimental complexity. In this regard, molecular simulations can provide useful insight to rationalize the experimental findings by analysing the microscopic details. To our knowledge, there is no such study, which considers the effects of various base sequences and explicit usage of environmental conditions on the patterning of ssDNA self-assembled nanostructures on graphene.

In this chapter, we have investigated the interactions of various nucleosides, nucleoside quartets and single-stranded DNA with graphene using classical molecular dynamics simulations and *ab initio* study. This chapter

is divided into two main parts: (1) stability of different nucleoside quartets on graphene surface and (2) interactiions of various ssDNA with graphene. We have used classical molecular dynamics simulations to explore the structural diversities and energetics of various nucleoside quartets and a number of ssDNA hybridized with graphene in aqueous environments. For a detailed analysis, we first consider the single nucleoside (A, G, C and T) and nucleoside quartets (G_4, A_4, T_4 and U_4) interacting with graphene, and then, focus on the formation of various oligonucleotide assembled on graphene surface. We consider four different homologous dodecamer ssDNA oligonucleotides of varying base sequences; namely ssA_{12}, ssT_{12}, ssG_{12} and ssC_{12}, on graphene surface. We also consider a 12 base pairs ssDNA which consist of a consecutive repeats of A-G-T-C, i.e. $ss(AGTC)_3$. We find that all the ssDNA oligonucleotides loose its helical shape and strongly hybridize with graphene through π-π stacking interactions between nucleobase and graphene surface. The interaction order among different ssDNA with graphene follows the extent of base-graphene-π stacking interactions. Additionally, we have also calculated and analysed the electronic structure of nucleoside quartets and graphene composites, and ssDNA adsorbed graphene hybrids using density functional theory.

3.2 Computational Methods

For the MD simulations of individual nucleosides and the nucleoside quartets interactions with graphene, we have considered a two-dimensional neutral single-layer graphene sheet within a periodic box of dimensions 3.41 $\times$

3.20 × 3.00 nm^3 in aqueous solutions, while, a mono-layer graphene sheet of sufficiently large dimensions 10.22 × 10.23 × 50 nm^3 has been considered for understanding the interactions of various ssDNA with graphene, at 300 K temperature and 1 atmospheric (atm) pressure in aqueous solution. We have considered five different nucleosides (A, G, C, T, U) and four nucleoside quartets (A_4, G_4, T_4 and U_4) in the first part of the present study. To obtain the microscopic picture of the ssDNA specificity towards the graphene sheet, simulations are performed by considering $ssdA_{12}$, $ssdG_{12}$, $ssdC_{12}$, $ssdT_{12}$, and a mixture of nucleobase sequences, $ssd(AGTC)_3$ of discrete strands, which are modeled from duplex B-DNA using NAB [443] (Nucleic Acid Builder) module of Amber 11 Tools Package [444]. The AMBER99 force fields [362] are used to model ssDNA. The graphene carbon atoms are modeled as uncharged Lennard-Jones particles (using C sp^2 parameters from the AMBER99 force field) as reported in the literature for the study of graphene and single-walled carbon nanotubes [432, 445–448]. The negatively charged backbones of ssDNA are neutralized using Na^+ counter ions. The total number of Na^+ ions needed to neutralize each of the ssDNA systems is 11. The transferable intermolecular potential three point (TIP3P) model [449] is considered for solvent water. All the MD simulations are performed using GROMACS simulations package [450] with an initial water box of dimensions as mentioned above. The initial configuration for the hybrid systems are considered by keeping the ssDNA at ∼4.0 $\mathring{A}$ distance away from the graphene plane. The high energy contacts between the atoms in the initial conformations of graphene, ssDNA and the hybrid systems are removed by minimizing the energy of each system using steepest decent integration method. Following that, MD

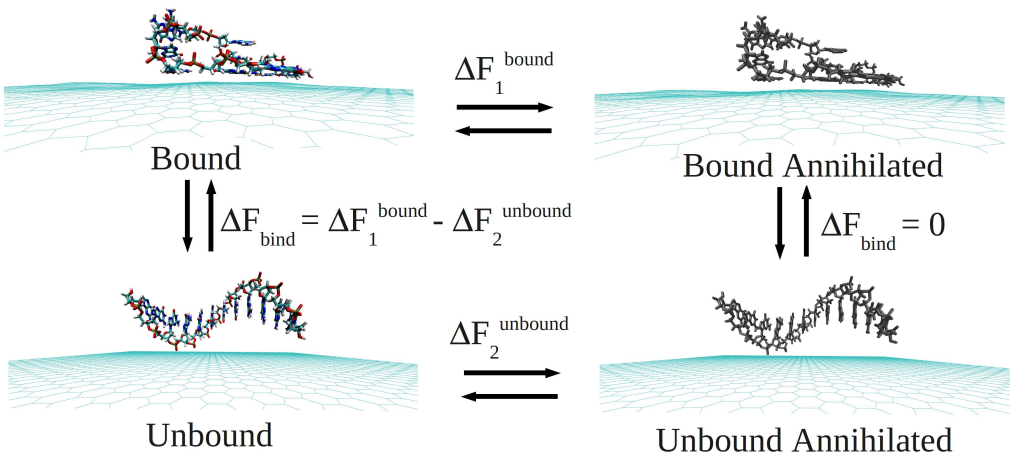

Figure 3.1: The schematic of thermodynamic cycle used for the free energy calculations. All systems contain explicit water molecules and counter ions, which are not shown for the better clarity of the figure.

simulations are performed using leap-frog algorithm for integrating Newtons equation of motion for 30 ns at constant temperature (300 K) and pressure (1 bar). Long-range electrostatic interactions are calculated with the Particle Mesh Ewald (PME) method [328] . In order to get clear picture about the dynamical assembly formation of ssDNA, the position of all graphene atoms are allowed to relax throughout the MD simulations. The time step for the MD simulation is 1.5 fs (femtosecond) and the atomic coordinates are recorded at every 7.5 ps (picosecond) for trajectory analysis. Analysis and visualization of MD trajectories are performed with VMD software [451].

Thermodynamics Integration (TI) [452] method, as implemented in GROMACS code, is employed to compute the binding free energies between the ssDNA and graphene by introducing various coupling parameters (λ) in the Hamiltonian (H). Following previous studies [453,454], the binding free energies, Δ F_{bind}, are calculated by considering a thermodynamics cycle as shown

in Fig 3.1. Δ F$_{bind}$ is defined as the free energy difference between the bound and unbound states.

$$\Delta F_{bind} = \Delta F_1^{bound} - \Delta F_2^{unbound} \tag{3.1}$$

where, ΔF_1^{bound} and $\Delta F_2^{unbound}$ are defined as the change in free energy to create and annihilate ssDNA in the bound and unbound states, respectively. To compute the ΔF, vdW interactions are annihilated or created using λ values of 0.00, 0.25, 0.50, 0.75 and 1.00. Soft-core LJ (Lennard Jones) potentials are employed with soft-core parameter $\alpha = 0.5$ and λ power, p = 1. At each λ value, $(\frac{\partial H}{\partial \lambda})$ is extracted from the 30 ns long simulation trajectory. To understand the electronic behaviours of various ssDNA adsorbed graphene composites, we have calculated the electronic structure using density functional theory (DFT) calculations as implemented in SIESTA [349,350], which uses numerical atomic orbital basis sets. We consider norm-conserving pseudopotentials in the fully nonlocal Kleinman-Bylander form [391], and a real space mesh size of 300 Ry energy cut-off employing Γ point calculations for all the modeled systems within the DFT calculations. We have performed non spin-polarized calculations within generalized gradient approximation (GGA) considering Perdew-Burke-Ernzerhof (PBE) [389] exchange and correlation functional using double ζ polarized (DZP) basis sets for all the atomic valence electrons. We consider each hybrid system within a box of dimensions $90 \times 90 \times 60$ $\mathring{A}^3$ to ensure the negligible interactions between the periodic images.

3.3 Results and Discussions

The structures and energetics of various nucleosides, their quartets and different ssDNA oligonucleotides interacting with graphene are discussed here. The discussions have been divided into two major parts. First, we have addressed the results obtained from the nucleosides and nucleoside quartets interactions with 2D graphene. Next, we have discussed the structures, conformations and energetic behaviours of various ssDNA interacting with graphene in aqueous solution.

3.3.1 Interactions of various nucleosides and nucleoside quartets with graphene

Understanding the structural basis and different binding modes of various nitrogeneous nucleosides with graphene is crucial to examine the detailed structures of the complicated DNA polymer as will be discussed below while adsorbing on graphene surface. In this section, we have discussed the interactions of various nucleosides and nucleoside quartets with graphene in presence of explicit TIP3P water molecules using MD simulations at T = 300 K and P= 1 atm.

Nucleosides adsorption on graphene

In order to understand the formation of various nucleoside quartets on 2D graphene and the interactions strength of different ssDNA poly-nucleotides with graphene, it is important to quantify the binding affinity of different nucleosides with graphene in aqueous environments at room temperature.

Previous DFT studies have shown that, G binds strongly with graphene, while A, C, and T have similar binding strength, which is lower than G [455]. However, other studies have shown that the nucleobase binding affinity goes as: G > A > T > C [456,457], which is expected from their chemical nature. Note that, the reported values of binding affinities for different nucleobases are calculated based on mainly gas-phase DFT calculations, where, only the work by Varghese *et al*. consider the solvation effects, by implicitly taking into account the dielectric continuum of water. However, in the presence of explicit water molecules, two competing forces are simultaneously present: base-graphene π-stacking interaction and nucleobase solvation by the water molecules. To our knowledge, there are no such studies examining the effect of explicit water molecules in estimating the binding free energy of individual nucelobase with graphene. Here, we have considered calculating the binding free energy of various nucleosides interacting with graphene in aqueous medium using the TI method as described previously. To model the nucleoside-graphene system, we choose each of individual nucleoside initially placed at $\sim$4.0 $\mathring{A}$ distance apart from a rectangular periodic graphene, containing 416 C atoms, where the plane of the nucleoside is aligned parallel to the graphene surface. From a 15 ns MD simulation, we have found that C and T pyrimidine nucleosides bind strongly to the graphene, whereas the purine nucleosides, A and G, show relatively lesser binding affinity. The calculated binding free energy of different nucleosides are -4.17 kcal mol^{-1} for A, -5.77 kcal mol^{-1} for G, -9.00 kcal mol^{-1} for C and -6.65 kcal mol^{-1} for T, and the binding sequence follows the order: C > T > G > A (see Table 3.1). Note that, the binding free energy order does not agree with the previously

Table 3.1: Binding free energies of various nuclosides and nucleosides quartets with graphene.

Nucleosides	F_b (kcal mol^{-1})	Quartets	F_b (kcal mol^{-1})
G	-5.77	G_4	-17.41
A	-4.17	A_4	-16.03
C	-9.00	N/A	-
T	-6.65	T_4	-16.19
U	-8.84	U_4	-13.61

reported results. However, the lesser extent of binding free energy found for T than C is due to the presence of an additional bulky methyl group in T nucleoside, which causes structural destabilization while adsorbing on graphene surface. This is well consistent with the experimental results [458] reporting higher binding energy for poly-thymidine than poly-cytosine oligonucleotide. It is interesting to note that, larger the number of polar sites available in nucleoside, greater is the extent of solvation free energy, and consequently, results in lower binding affinity of the nucleoside for the graphene. Thus, the observed discrepancy in predicting the order of binding strength is mainly because of the nucleoside solvation effects by the explicit water molecules, and partly may also be due to the presence of thermal and dynamical fluctuations during the simulation, which were not taken into account in previous studies [456, 457]. It is worth to mention here that, the binding free energy order found from our simulation considering only the single nucleosides, may vary depending on the environmental conditions as well as on the number of nucleosides present in the simulation.

Nucleoside quartets on graphene

Here, we present the results obtained from the four nucleoside quartets (G_4, A_4, T_4 and U_4) adsorptions on graphene in aqueous solution using MD simulations. The starting geometries of all the quartets are modeled from previously reported structures [97, 98, 459–462], and are shown in Fig. 3.2. Now, it is known that, the nucleosides quartets stability is greatly enhanced by the coordination of monovalent cations. Moreover, it is also known that, the K^+ is best suited for the quartet stability, in particular, for the stability of G_4 quartet. Consequently, we have considered one K^+ initially placed above the center of all the quartet's core, which is enriched with negative electron density, with the only exception for A_4, for which, we have considered a Cl^- ions coordinated to its central positive electron density rich region. Note that, in order to neutralize the whole system, each system contains one K^+ and one Cl^- ions. The nucleoside quartets are placed at $\sim$4.0 $\mathring{A}$ above the graphene plane for all the graphene-quartet systems. After initial temperature equilibration at T = 300 K, the simulations are carried out for about 15 ns at P = 1 atm, within NPT ensemble, using AMBER MD code. All the final geometries of graphene-quartets composites after 15 ns MD simulations run, are shown in Fig. 3.3.

As can be seen, the quartets structures on graphene in aqueous medium after 15 ns NPT run, show different extent of structural distortions from their starting planar geometries, depending on the chemical nature of the quartets. Our results have shown that, only G_4 maintains the stable planar quartet geometry on 2D graphene surface. All others quartets are significantly distorted

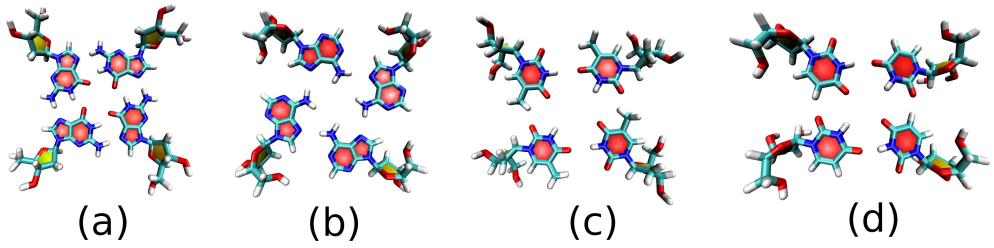

Figure 3.2: Initial structures of all four quartets. (a), (b), (c) and (d) represent the structure of G_4, A_4, T_4 and U_4 nucleoside quartet, respectively.

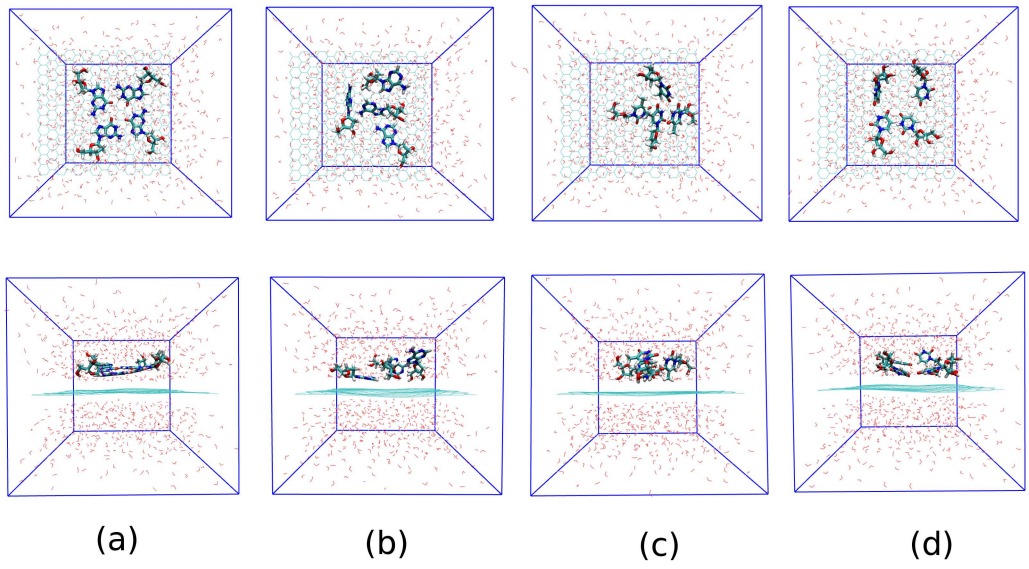

Figure 3.3: Structures of MD simulated nucleoside quartets on graphene in presence of explicit water molecules. (a), (b), (c) and (d) represent the structures of G_4, A_4, T_4 and U_4 on graphene after 15 ns NPT simulations.

and completely lost their initial planar geometries. The nucleosides present in these quartets are preferred to form base-base π stacks. To understand the different stacking conformations, we have looked at various forces, which are acting on the nucleosides (over graphene) in explicit water medium. In fact, their exist three competing forces simultaneously acting on each nucleosides. Firstly, the interactions of nucleoside with graphene via π-π stacking interactions, which depend on the available π surface area on nucleosides. Obviously, the purine nucleosides would have large π stacking interactions with the graphene surface due to the presence of the two ring structures. Secondly, the π-π stacking and H-bonding interactions between the nucleosides. The nucleoside-nucleoside H-bonding interactions stabilize the planar quartet's geometry, while, the π-π stacking favours the stacking of nucleosides on top of each other. The strength of π-π interactions again directly related to the available π surface area in a nucloside. Third, the solvation of individual nucleosides through the H-bonding interactions with the solvent water molecules. This depends on the number of polar sites available for the water coordinations. We note that, the number of available polar sites for making H-bonding interactions with solvent water molecules present in each nucelobase is 7, 6, 4 and 4 for G, A, T and U, respectively. Consequently, the solvation strength is expected to be more for the purine (G, A) nucleosides than for the pyrimidine (T, U) nucleosides.

To quantify the binding strength of these nucleosides quartets, we have calculated the binding free energy for each system using TI methods, as discussed above. The binding free energy values are provided in Table 3.1. As can be seen, the G_4 forms stable quartets with the greater extent of

negative binding free energy (-17.41 kcal mol^{-1}) among others. The higher negative binding free energy of graphene-G_4 complex is due to the larger number of base-graphene π stacks. The binding free energy strength follows the order as $G_4 > T_4 > A_4 > U_4$. However, the difference in binding free energy is only $\sim$0.16 kcal mol^{-1} between the A_4 and T_4 quartets with the graphene.

So far, we have discussed the results mainly on structures and energetics obtained from the classical MD simulations. As already stated, the classical MD does not include the electronic degrees of freedom, which needs to be explicitly treated for calculating any reliable physical and chemical properties. To investigate the electronic structures, we have used DFT as implemented in SIESTA code [349, 350], within GGA/PBE as well as vdW density functional calculations. The vdW-DFT explictly take into account the dispersion interactions, which are important for predicting the structure and accurate energetics for these surface adsorbed nucleosides quartets on graphene systems. We have considered a periodic super cell of single-layer graphene containing 288 C atoms with the quartets placed at 3.5 $\mathring{A}$ aboove the graphene plane. The quartets are modeled as similar to those used for the MD simulations, without the sugar moiety, which is replaced by the methyl groups. The separation of a quartet from its mirror image in the next cell in graphene plane directions (xy-plane) is kept more than 15 $\mathring{A}$, which ensures negligible interactions between the periodic images. Also, the distance between the two graphene layers in the perpendicular directions to the graphene surface is $\sim$40 $\mathring{A}$. This also suggest, the negligible interactions between the periodic images in the direction normal to the graphene plane.

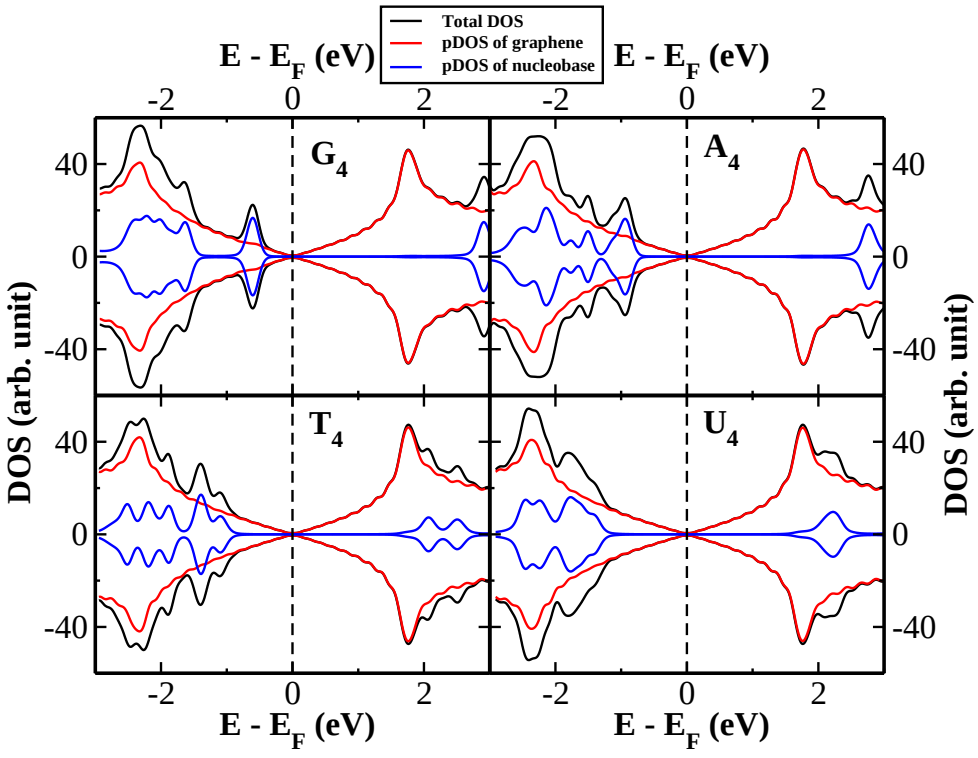

Figure 3.4: Electronic density of states (DOS) and projected density of states (pDOS) for G_4 (a), A_4 (b), T_4 (c) and U_4 (d) adsorbed on graphene.

The adsorption energy calculated for the quartets adsorbed on graphene follows the similar trend even found by the density functional theory calculations. However, the vdW-DFT results slightly small adsorption energy as compared to the GGA-PBE functional. The equilibrium distances between the planes of quartet and graphene is found to be ∼3.0-3.5 $\AA$. Our analysis has also shown that, there is negligible charge transfer between the graphene and adsorbed nucleobase quartets. This is consistent with the previous study considering the single nucleobase adsorption onto graphene surface [457].

To understand the electronic structures of these graphene-quartet composities, we have calculated the electronic density of states (DOS) as well as

projected density of states (pDOS) and provided in Fig. 3.4. It is clear that, the graphene electronic structure does not change by the presence of these nucleobase quartets. The characteristic Dirac cone picture, as found in pristine graphene, is preserved for these graphene-quartets complexes. However, there appears some localized electronic states below the Fermi level, which mainly come from the adsorbed quartet's electronic states. The positions of these localized states are at ∼0.60, ∼0.93, ∼1.09 and ∼1.41 eV below the charge neutrality point (Dirac point). Interestingly, the positions of these localized states exactly corresponds to the inonization energy of individual nucleobases. The present findings suggest that, 2D graphene can be used for sensing applications of biomolecules with different nucleobase sequences. Moreover, since the low-energy electronic properties does not alter upon the nucleobase adsorptions, the same graphene sheet would be useful for recycling processes for many other applications after the desorption of surface adsorbed molecules.

3.3.2 Interactions of various single-stranded DNA with graphene

To understand the assembly phenomena of various ssDNA on graphene surface in aqueous media, we need to understand the two distinctive processes: the process of ssDNA solvation and subsequently, the adsorption of different ssDNA on graphene. Consequently, we have studied and analyzed the results stepwise of these two different processes.

First, we look at the solvation processes of all ssDNA considered in the

present study at physiological conditions, i.e., 300 K temperature and 1 atm pressure using a NPT ensemble. For this, we consider all five individual ssDNA (ssdA_{12}, ssdG_{12}, ssdC_{12}, ssdT_{12} and ssd$(AGTC)_3$) in presence of explicit TIP3P water molecules and Na^+ counter ions in a simulation box of dimensions $70 \times 70 \times 70$ $\mathring{A}^3$. We find that all the ssDNA interact with the solvent water molecules through strong hydrogen bonding interactions, which is characterised by H-bonds involving a H-bond donor and acceptor distance of 0.25 - 0.30 nm and 165 - 175° angle of ∠donor-H-acceptor. The strength of H-bonding interactions varies with the number of H bonds formed in the solution, which, in turn, depend on the nature of various ssDNA. Note that, all the ssDNA in gaseous phase maintains their helical S shape as the counter part of duplex DNA, because of the stabilization gains through inter-base π-π stacking interactions. However, in aqueous medium, there is a competition between this inter-base π-π stacking interactions and H- bonding interactions between the ssDNA and solvent water molecules. In fact, we find that the H-bonding interactions try to destroy ssDNAs helical structure and consequently, solubilize them in aqueous medium. Note that, unlike duplex B-DNA, the ssDNA is very flexible in bond torsional angles at least within the dinucleotide levels as well as within the sugar-phosphate backbone levels.

In fact, the solvation energy should be lower in comparison to the energy require to destroy π-π stacking interactions and bond torsional rotations along the DNA sugar-phosphate backbone. In the process of various ssDNA solvation, the number of inter-base π-π stacking interactions decreases, while the intra-molecular (within ssDNA) and inter-molecular (between ssDNA and water) H-bonding interactions increases. Therefore, we consider looking

Table 3.2: The average number of H-bonds (within 3.5 $\AA$ distance between the H-bond donor and H-bond acceptor) within ssDNA and between the ssDNA and water molecules over the 30 ns long MD simulation. E_{int} represents the average interaction energy between various ssDNA and water over 30 ns MD simulation.

Systems	Average number of H-bonds within ssDNA	Average number of H-bonds between ssDNA and water	E_{int} (kcal mol^{-1}) between ssDNA and water
$ssdA_{12}$	0.24	134.40	-122.73
$ssdG_{12}$	0.14	150.47	-140.03
$ssdC_{12}$	2.26	131.91	-124.09
$ssdT_{12}$	0.67	123.87	-123.25
$ssd(AGTC)_3$	0.88	134.10	-126.45
Graphene@$ssdA_{12}$	1.80	123.94	-105.82
Graphene@$ssdG_{12}$	2.57	141.60	-124.25
Graphene@$ssdC_{12}$	2.80	120.44	-110.06
Graphene@$ssdT_12$	2.35	107.03	-101.53
Graphene@$ssd(AGTC)_3$	1.46	125.53	-114.60

at the average number of each type of H-bonds over the 30 ns simulation times. We also focus on the interaction energy between the ssDNA and water molecules in order to quantify the solvation strength of various ssDNA in aqueous solution. We find that $ssdG_{12}$ forms larger number of H-bonds (little above 150 as given in Table 1) with the water molecules, and consequently, results in greater solvation energy (140.03 kcal mol^{-1}) among all the ssDNA. The average number of H-bonds for both $ssdA_{12}$ and $ssd(AGTC)_3$ is about 134, while the H-bonds number is about 131 and 123 for $ssdC_{12}$ and $ssdT_{12}$, respectively (see Table 1). We note that, the number of H-bonding sites available to solvent water molecules present in each nucelobase is 7, 6, 5 and 4 for G, A, C and T, respectively. As a result of that, the ssdG12, $ssdA_{12}$ and $ssd(AGTC)_3$ show large number of H-bonds formation with solvent water in comparison to other ssDNA, and thereby, resulting in higher interaction strengthwith water (higher negatiive interaction energy). Moreover, as given in Table 3.1, the average number of H-bonds between various ssDNA with water follows the same order as the average number of H-bonding sites present in each poly-nucleotide. The greater extent of solvation energy found for $ssdG_{12}$ and $ssd(AGTC)_3$ compared to other ssDNA, may also be accounted for the presence of large average surface area exposed to the solvent water molecules. However, we find almost similar interaction energies for the $ssdA_{12}$, $ssdC_{12}$ and $ssdT_{12}$, and relatively moderate interaction energy for mixed sequence, $ssd(AGTC)_3$. Also note that, the average number of H-bonds within the various ssDNA is less than 1 with the exception found for $ssdC_{12}$, for which the number is found to be 2, indicating its greater extent of intra-molecular folding compared to others. Overall, our analysis shows

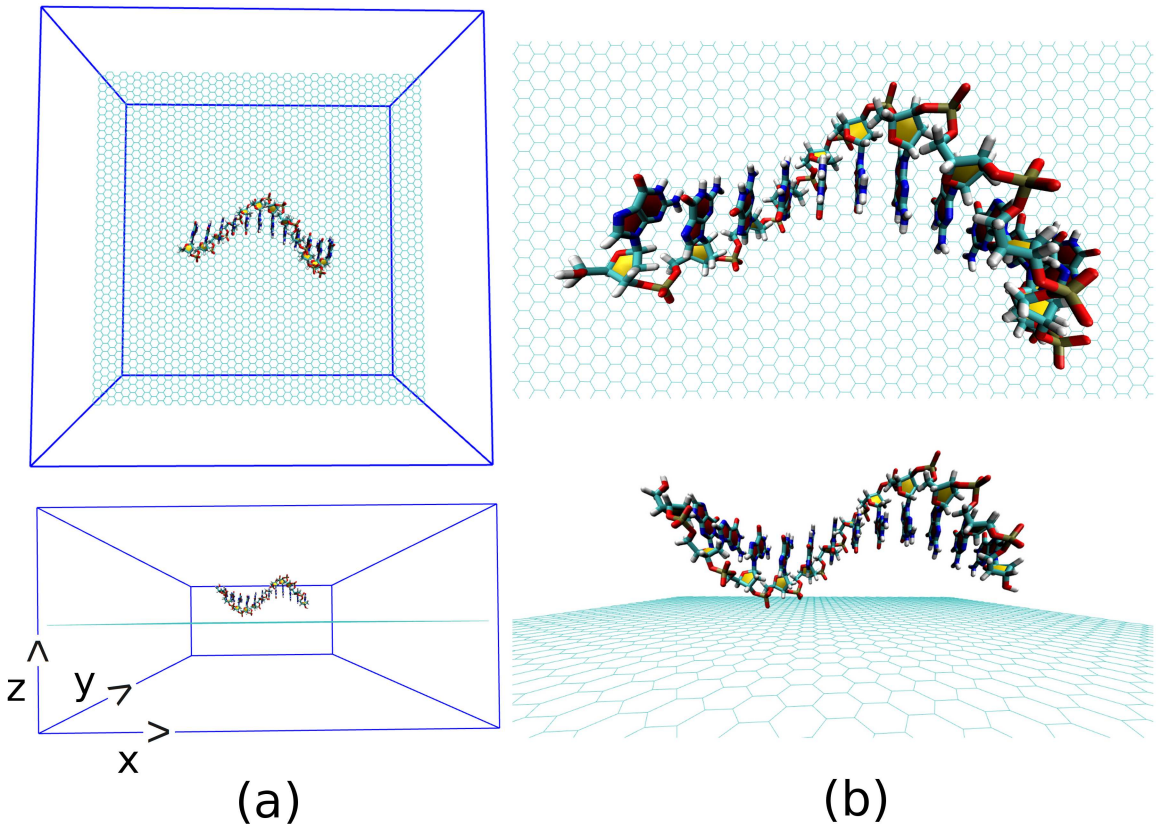

Figure 3.5: The schematic of initial simulation system for a representative system: Graphene@ssdG_{12} (Explicit water molecules and counter ions are not shown for better figure quality.)

that both the nucleobase π-π stacking interactions within each ssDNAand H-bonding interactions between the ssDNA and solvent water molecules have to be overcome for the stable composite formation with graphene.

Now, before we begin analysing the assembly processes of various ssDNA onto graphene surface, we first look at the stability of monolayer and AB stacked bi-layer graphene in presence of explicit water solvent at T = 300 K and P = 1 atm, in order to validate the reliability of empirical force field used in the present study. Moreover, although, pristine graphene is hydrophobic

in nature, it is important to study the interaction between the solvent water molecules and graphene surface to understand the detailed atomic picture of graphene dispersion by various ssDNA. Note that, each single-layer of the graphene model contains 4032 C atoms, and for the initial configuration of bi-layer graphene, we choose the inter-layer separation of 3.4 $\mathring{A}$, and no water molecules in between the graphene layers. In the MD simulation, we have not considered any geometric constraint and allowed all the graphene carbon atoms to relax during the simulations. Our simulation results show that the graphene layer remains stable at the simulation conditions, and there is no penetration of solvent water molecules within the layers for the bi-layer graphene. We find that the average interlayer separation for the bi-layer graphene varies from 3.3 to 3.6 $\mathring{A}$ over the simulation time. The average interaction energy between two layers is found to be -1.21 kcal mol^{-1} per layer C atoms. Additionally, the binding free energy is found to be 0.04 kcal mol^{-1} per layer C atoms. However, we find a significant corrugation of graphitic layer during the simulation. This is because of the long-range fluctuation at finite temperature, which is fully consistent with the Mermin-Wagner theorem [463] and with the intrinsic rippling observed in graphene [464]. Our simulations results on mono and bi-layer graphene clearly demonstrate the reliability of the empirical force field employed in the present study.

Next, we investigate the detailed atomistic picture of assembly phenomena of various ssDNA onto graphene surface with the progress of simulation time up to a total time of 30 ns. Note that, the hybrid simulation is a complex process and needs systematic study in order to understand the details of the interaction mechanism. In the initial model structure, we consider

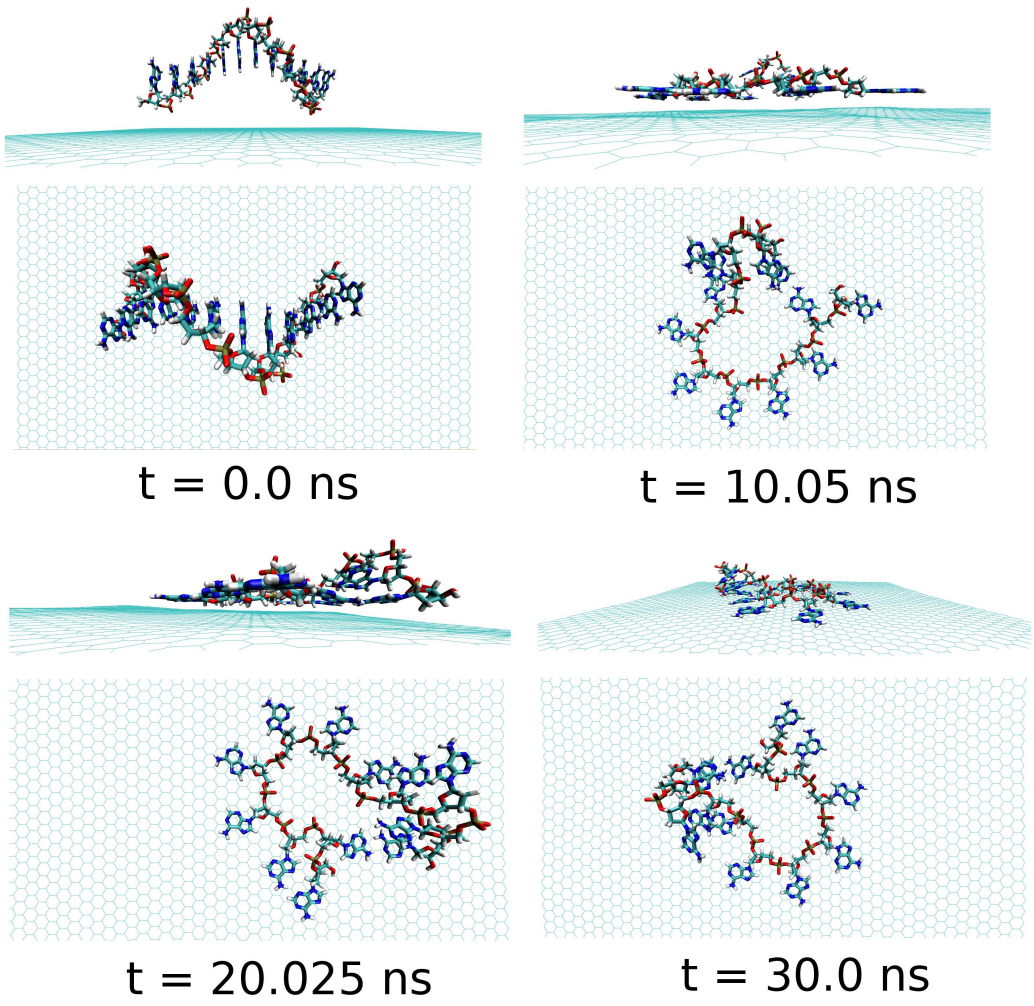

Figure 3.6: The simulation structures at various time interval for Graphene@ssdA$_{12}$. The water molecules and ions are not shown for better quality of the figure.

the ssDNA and graphene hybrid, where the helical axis of ssDNA is placed parallel to the graphene surface, and maintaining an initial distance of about 4.0 $\mathring{A}$ from the plane of the graphene surface. The initial geometrical orientation of ssDNA with respect to the graphene would provide the details understanding of adsorption mechanism of various ssDNA during the course of MD simulations. The schematic of a simulation set up is depicted in Fig. 2. As has already been mentioned, we have considered five sets of individual simulation with varying the base sequences of ssDNA. To this end, we choose two pure purine polynucleotides, namely, ssdA_{12} and ssdG_{12}, and two pyrimidine polynucleotides, namely, ssdC_{12} and ssdT_{12}. Additionally, we also consider a DNA polynucleotide of AGTC consecutive base-sequences, i.e. ssd$(AGTC)_3$, where the two terminal nucleobases (A and C) are of different type. Note that, all the polynucleotides are modeled from their corresponding duplex B-DNA structure of dodecamer size (i.e., polymer of 12 nucleotides). Consequently, each of the model ssDNA contains 12 nucleobase of varying sequences. Here, we discuss the assembly processes of various ssDNA on graphene surface over 30 ns simulation time step-wise. We would also analyse the results at 10, 20, 30 ns simulation time in details.

First, we analyse the results obtained for the ssdA_{12} adsorption onto graphene surface in aqueous solution. The configurations of graphene@ssdA_{12} hybrid at different simulation time are shown in Fig. 3.6. Our simulation results show that within a time period of 10 ns, most of the A nucleobases formed stable π-stacks with the flat graphene surface. After 10 ns MD simulation, we find 9 number of A nucleobase formed stable π-stacked onto

Table 3.3: Average interaction energy (E_{int}) per nucleotide between the ssDNA and graphene, and binding free energy (ΔF_{bind}) per nucleotide for all graphene@ssDNA systems together with the number of base-graphene and base-base stacks at different simulation times.

Systems	F_{int} (kcal mol^{-1})	F_{bind} (kcal mol^{-1})	No. of base-graphene π stacks	No. of base-base π stacks
Graphene@ssdA_{12}	-19.34	-4.56	9 (10 ns), 9 (20 ns), 9 (30 ns)	3 (10 ns), 3 (20 ns), 3 (30 ns)
Graphene@ssdG_{12}	-13.02	-4.14	4 (10 ns), 6 (20 ns), 6 (30 ns)	7 (10 ns), 6 (20 ns), 5 (30 ns)
Graphene@ssdC_{12}	-10.86	-3.57	4 (10 ns), 7 (20 ns), 7 (30 ns)	4 (10 ns), 3 (20 ns), 2 (30 ns)
Graphene@ssdT_{12}	-15.84	-2.18	7 (10 ns), 8 (20 ns), 8 (30 ns)	3 (10 ns), 3 (20 ns), 3 (30 ns)
Graphene@ssd$(AGTC)_3$	-20.84	-5.92	11 (10 ns), 10 (20 ns), 11 (20 ns)	1 (10 ns), 1 (20 ns), 1 (30 ns)

graphene surface, while 3 A nucleobase still maintain their intra-base π-stacks within the ssdA_{12}. Further progress in simulation time neither change the ssdA_{12} conformations adsorbed onto graphene nor altered the number of base-graphene and base-base π-stacks, as given in Table 3.3. This clearly indicates that the hybrid system has attained its stable conformation. Moreover, the calculated interaction energy between the ssdA_{12} and graphene does not show significant changes after the 5 ns simulation time, as shown in Fig. S1, suggesting that the stable assembly has been formed within this period of MD simulation. Also, the root mean square deviation (RMSD) of ssdA_{12} with respect to the final energy minimized structure also suggests the formation of stable graphene@ssdA_{12} hybrid (See Fig. 3.7). The average interaction energy and binding free energy per nucleotide between ssdA_{12} and graphene is calculated to be -19.34 kcal mol^{-1} and -4.56 kcal mol^{-1}, respectively.

We also find that the average number of H-bonds between the ssdA_{12} and solvent water molecules has been reduced to 123 from 134, and thereby,

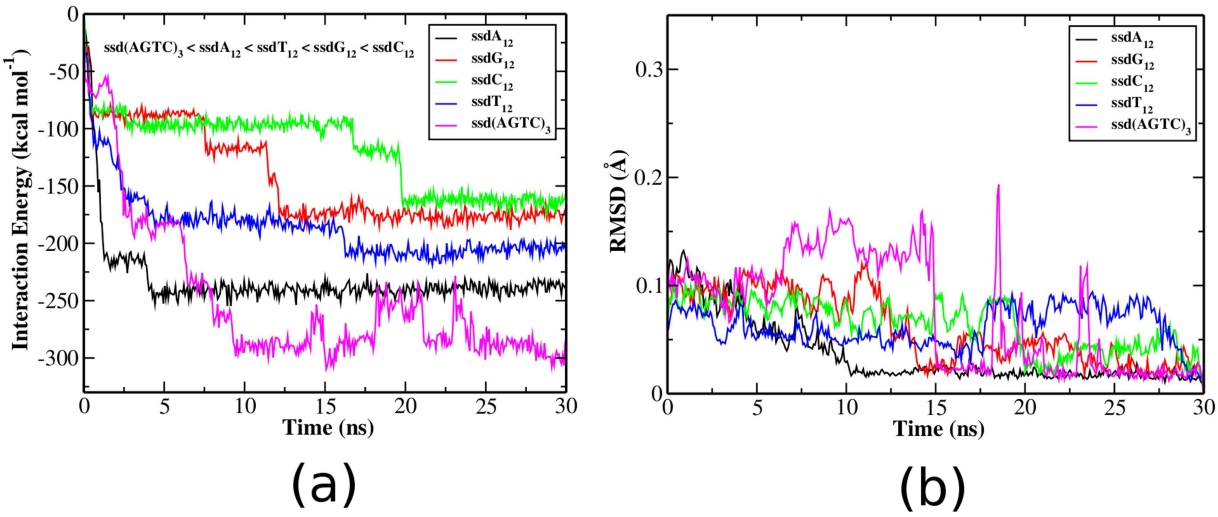

Figure 3.7: The interaction energy (E_{int}) and RMSD of the graphene@ssDNA systems with the progress in simulation time.

increase in the H-bonding interaction energy (increase in the negative interaction strength) in comparison to the free $ssdA_{12}$ in aqueous environment (see Table 3.1). However, there is a small increment in the number of intramolecular H-bonds, which indicate the structural coiling behaviour as also found over the progress of simulation time. A detailed structural analysis reveal that the 2nd A nucleobase from 5′ end forms stable H-bonds with the 1st A nucleobase from 3′ end of the adsorbed $ssdA_{12}$, resulting in a coiled structure. Also note that, this H-bonded A-A nucleobase pair form stable π-stack on the graphene surface.

Now, we discuss and analyse the dynamical adsorption process of $ssdG_{12}$ polynucleotide onto graphene surface in aqueous solution at T = 300 K and P = 1 atm. The details of the structural changes during the progress of simulation are shown in Fig. 3.8. We find that the $ssdG_{12}$ forms stable composite with graphene after 20 ns of MD simulation, as indicative from the RMSD

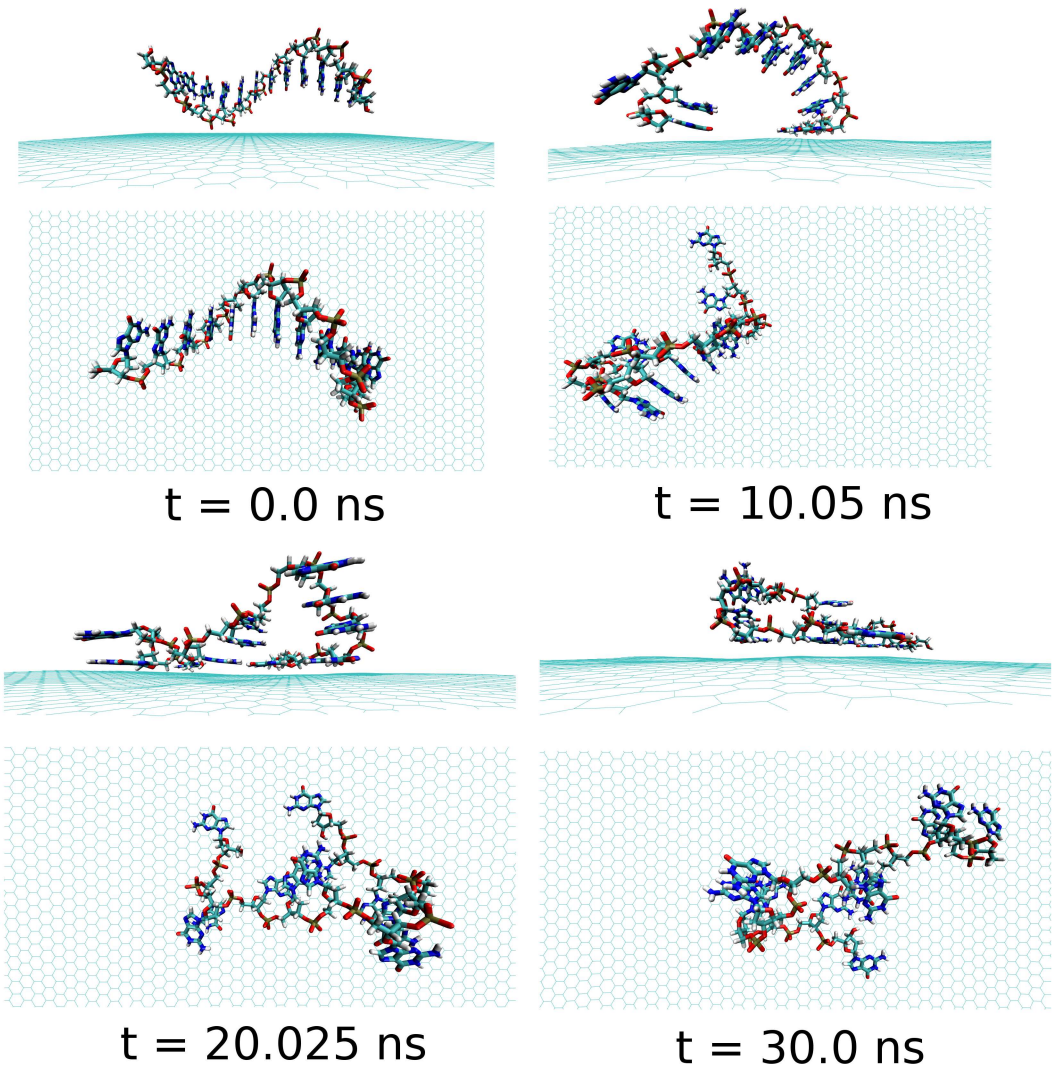

Figure 3.8: The simulation structures at various time interval for Graphene@ssdG$_{12}$. The water molecules and ions are not shown for better quality of the figure.

and average interaction energy diagrams calculated over the simulation time. Our results show that at 10 ns simulation time, the number of nucleobase-graphene π-stack is 4, whereas the number of base-base π-stack is 7. With the progress in simulation time, the number of base-graphene -stack is increased to 6, and the number of base-base π-stack is decreased to 5 after 30 ns simulation. This clearly indicates the greater binding affinity of $ssdG_{12}$ with respect to the prolonged simulation time. However, we find stable trajectory over 30 ns simulation time. The calculated interaction energy between $ssdG_{12}$ and graphene, and binding free energy per nucleotide are found to be -13.02 kcal mol^{-1} and -4.14 kcal mol^{-1}, respectively. Note that, both the interaction and binding free energy are comparatively higher than the values obtained for $ssdA_{12}$ adsorption on graphene. This demonstrates the greater extent of adsorption propensity of $ssdA_{12}$ on graphene surface than $ssdG_{12}$. The higher interaction and binding free energy obtained for $ssdG_{12}$ adsorption on graphene than $ssdA_{12}$ can be accounted for the less number of base-graphene π-stacking interactions for the former composite compared to the later one. The adsorption process significantly reduces the average number of H-bonds between the $ssdG_{12}$ and water molecules, which results in higher solvent-ssDNA interaction energy than in graphene free $ssdG_{12}$ in aqueous solution. We also find a small average number (2.5) of intra-molecular H-bonds within $ssdG_{12}$ when adsorbed onto graphene surface. A closer look at the simulated structure after 20 ns shows that the two G nucleobases, between 4^{th} adenine from $5'$ end and 2^{nd} adenine from $3'$ end, form stable intra-molecular H-bonds on graphene surface. Note that, both the purine base sequence containing ssDNA ($ssdA_{12}$ and $ssdG_{12}$) form stable and planar intra-molecular

H-bonds, and consequently, increases the average number of H-bonds within ssDNA, as given in Table 3.1. These analyses prove that the helical shape of $ssdG_{12}$ is completely destroyed upon adsorption on graphene, forming a folded conformation onto the graphene flat surface.

Next, we have examined the adsorption processes of the pyrimidine base sequence containing two ssDNA polynucleotides, namely $ssdC_{12}$ and $ssdT_{12}$, on the 2D flat surface of graphene in aqueous medium. As shown in Fig 3.7, the small fluctuation in interaction energy between the ssDNA and graphene, and the measured RMSD over the simulation time indicate that, both the ssDNA form stable hybrid with graphene within the 30 ns simulation time. The MD snapshots at different simulation times of these two pyrimidine nucleobases containing ssDNA adsorption on graphene are shown in Fig 3.9 and Fig. 3.10. The graphene-ssDNA interaction energy (binding free energy) estimated for $ssdC_{12}$ and $ssdT_{12}$ are found to be -10.86 kcal mol^{-1} (-3.57 kcal mol^{-1}) and -15.48 kcal mol^{-1} (-2.18 kcal mol^{-1}), respectively. The higher interaction strength found for $ssdT_{12}$ is due the presence of larger number of nucleobase-graphene π-stacking interactions compared to $ssdC_{12}$ adsorption. Additionally, the presence of 5 H-bonding modes for C nucelobase than only 4 H-bonding modes in T encompasses a larger number of H-bonding interactions with solvent water molecules for the former nucleobase, and hence, reducing the extent of graphene-ssDNA interactions. In fact, as expected we find larger extent of both interaction energy and binding free energy for these two pyrimidine nucleobase ssDNA polynucleotide ($ssdC_{12}$ and $ssdT_{12}$) as compared to the purine base sequence containing $ssdA_{12}$ and $ssdG_{12}$ polynucleotide. This is because of the presence of larger π-surface

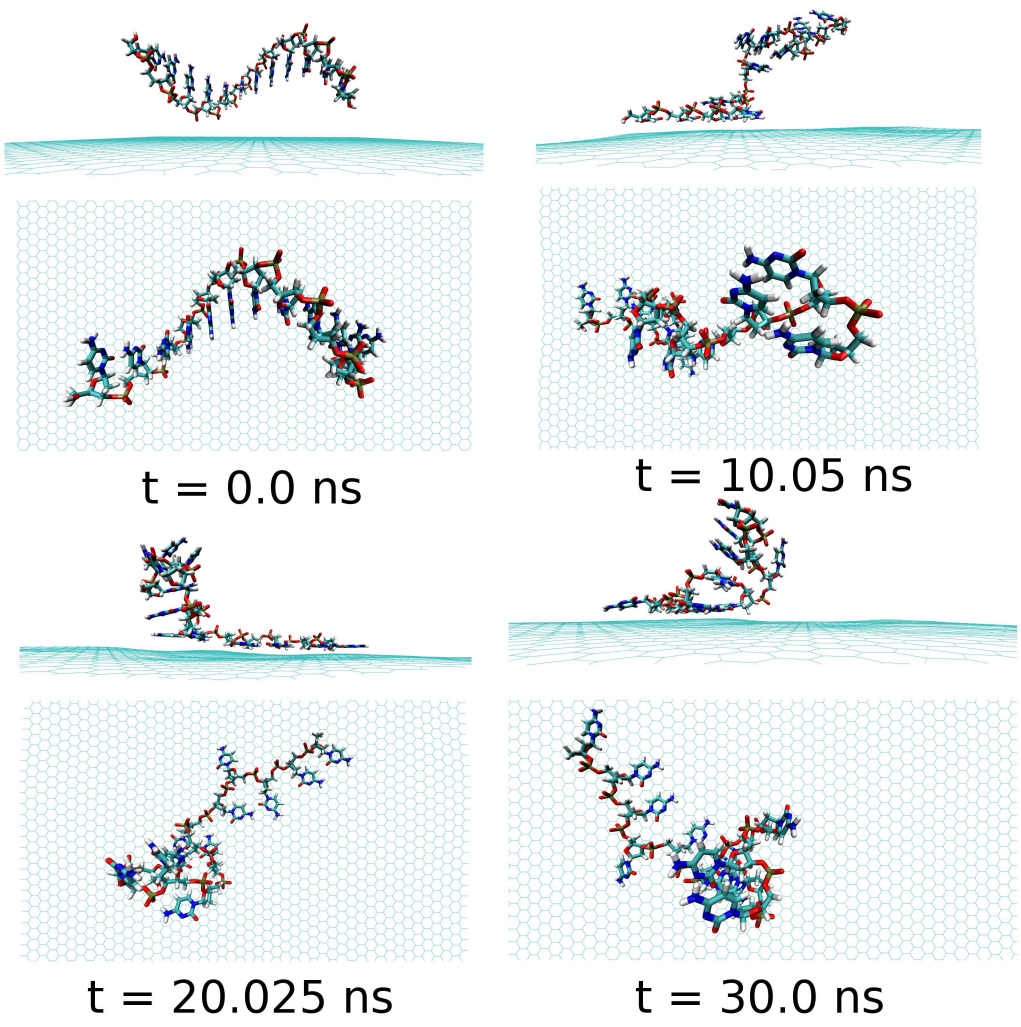

Figure 3.9: The simulation structures at various time interval for Graphene@ssdC_{12}. The water molecules and ions are not shown for better quality of the figure.

(two-rings) in purine nucleobase, which results in greater π-stacking interactions with graphene π-surface than what is expected in single-ring containing pyrimidine nucleobases. Moreover, it is known that the strength of nucleobase interaction with graphene goes as: G > A > T > C [456, 457], which in turn follows their hydrophobicity order [465]. The order of the binding strength found in our study is well consistent with the individual base-graphene binding strength, at least with respect to the purine and pyrimidine base-sequences. Moreover, our simulation results are consistent with the previous results obtained for nucleobase interactions with single-walled carbon nanotube [453]. Also, as can be seen from Table 3.1, both the ssDNA form a small number of intra-molecular H-bonds, suggesting their intra-molecular folding behaviours.

At this point, it is important to investigate the effect of a mixed base sequence to compare and contrast the binding strength, and explore their dynamical conformational changes during the simulation process. To achieve this, we choose a ssDNA consisting of a consecutive repeat of AGTC base sequence forming ssd$(AGTC)_3$ polynucleotide. Note that, this particular ssDNA contains two different terminal nucelobases, i.e., A and C at the $5'$ and $3'$ end of ssDNA, respectively. The calculated graphene-ssDNA interaction energy as well as RMSD (see in Fig 3.7) show a large conformational fluctuations of ssd$(AGTC)_3$ with the progress in simulation time. This is due to the presence of hetero base sequences in the ssDNA considered here. It is also to be noted that after 25 ns of simulation, both the fluctuations become almost constant reaching equilibrated values with time.

As also can be seen from the Fig. 3.11 and Table 3.3, almost all the

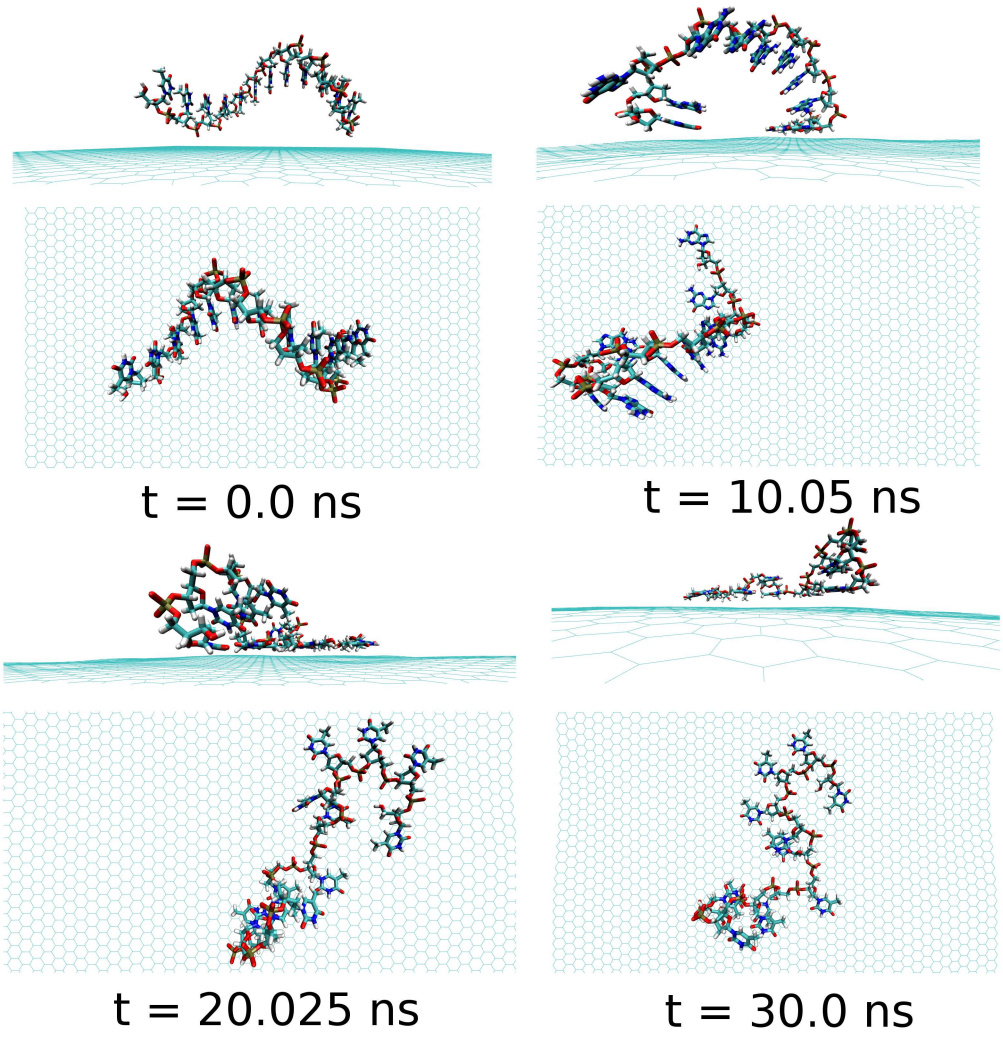

Figure 3.10: The simulation structures at various time interval for Graphene@ssdT_{12}. The water molecules and ions are not shown for better quality of the figure.

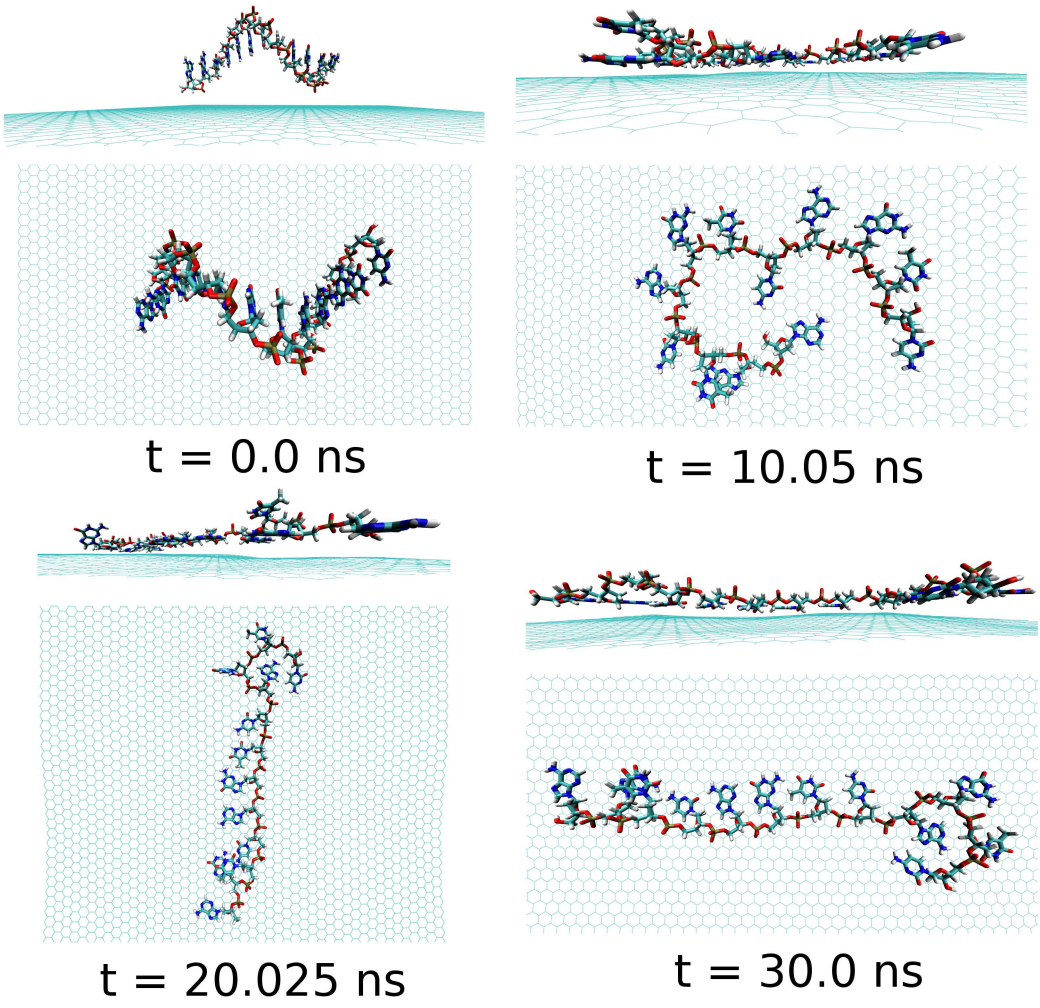

Figure 3.11: The simulation structures at various time interval for Graphene@ssd(AGTC)$_3$. The water molecules and ions are not shown for better quality of the figure.

nucleobase form stable π-stack with the graphene surface. During the 30 ns simulation time, the number of nucleobase-graphene π-stack changes from 11 (10 ns) to 10 (20 ns), which is further changed to 11 at 30 ns, whereas the number of base-base π-stacks remains at the constant value of 1. We find that at 10 ns simulation, the ssd$(AGTC)_3$ form a stable adsorbed π-stacked structure, where 11 nucleobases are strongly adsorbed onto graphene surface, forming a circular flat structure. Further increase in simulation time causes an elongated structure onto the graphene surface which does not alter with the progress of simulation time. The detailed structural changes during the progress of simulation are shown in Fig. 3.11. The calculated interaction energy and binding free energy are found to be -20.84 kcal mol^{-1} and -5.92 kcal mol^{-1}, respectively. We find the greater extent of binding strength for ssd$(AGTC)_3$ adsorption on graphene surface in comparison to the other hybrids. This can be accounted for the larger number of nucleobase-graphene π-stacking interactions. Moreover, due to the adsorption onto graphene, the average number of H-bonds with the solvent water molecules is significantly reduced compared to the free ssDNA solvation, which gives rise to lesser extent of solvation strength by the water molecules. However, we find a small average number of intra-molecular H-bonds (1.5) than in any other graphene-ssDNA hybrid, supporting its solely -stacking stabilized elongated network formation on graphene surface.

To further investigate the electronic structure of ssDNA adsorbed graphene composites, we consider studying these composites within DFT calculations.

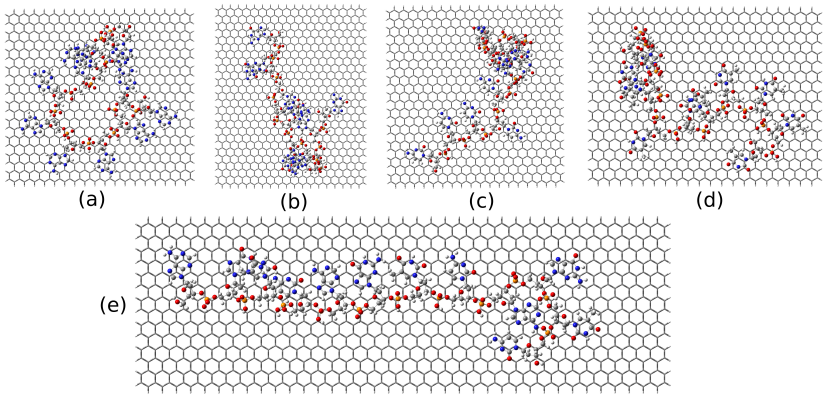

Figure 3.12: The model structures considerd for the DFT study. (a), (b), (c), (d), and (e) represent the structure of ssdA_{12}, ssdG_{12}, ssdC_{12}, ssdT_{12} and ssd$(AGTC)_3$ adsorbed onto hydrogen terminated graphene flake, respectively.

To this end, we model these systems from the final equilibrated structures obtained from MD simulation of individual composite followed by energy minimization using the steepest descent method. We consider the ssDNA with rectangular graphene fragment, whose edges are terminated with the hydrogen atoms for the dangling bonds. We model these molecular hybrid systems in vacuum, that is, we do not take into account of any environmental effects. Moreover, we choose adding hydrogen atoms to the negatively charged phosphate groups to neutralize the system following previous works [394,466]. The total number of atoms present in these model systems are as follow: 1456 for graphene@ssdA_{12}, 1210 for graphene@ssdG_{12}, 1264 forgraphene@ssdC_{12}, 1208 for graphene@ssdT_{12}, and 1543 for the graphene@ssd$(AGTC)_3$. We only consider optimizing the position of the added hydrogen atoms present in each composite using DFT. All the partially optimized structures of model systems are shown in Fig. 3.12.

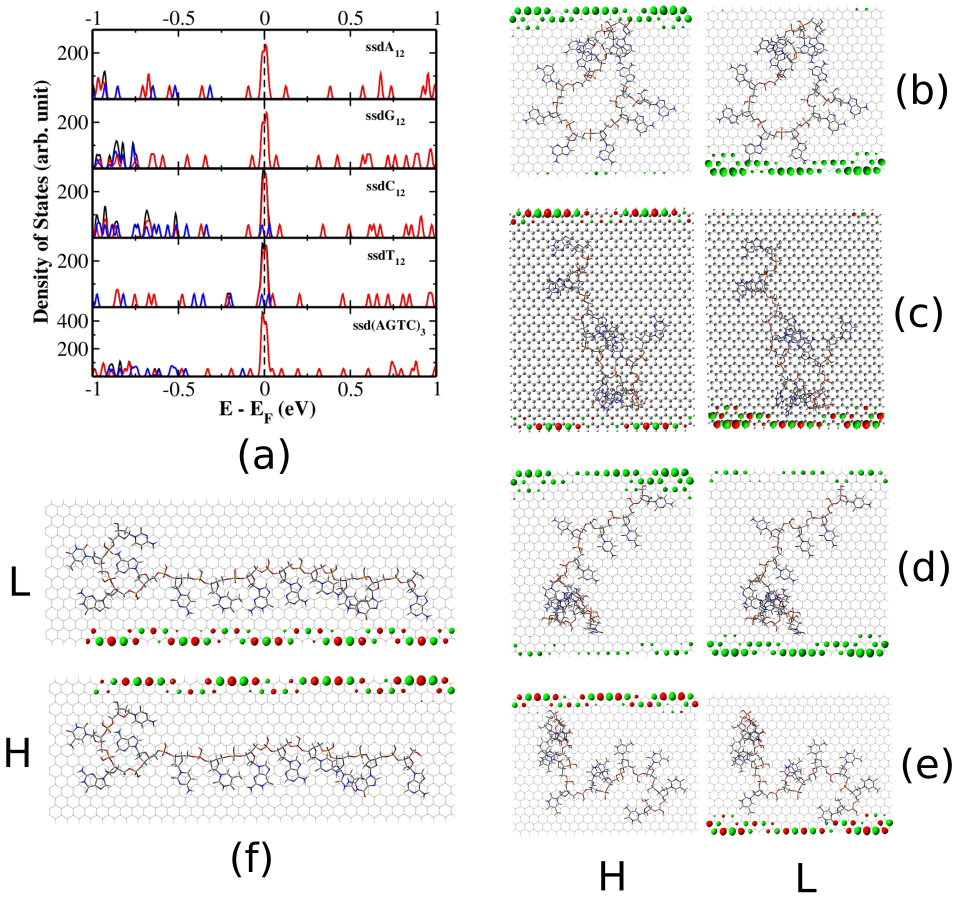

Figure 3.13: The electronic density of states (DOS) (a), and the HOMO (H) and LUMO (L) molecular orbitals for the ssdA$_{12}$ (b), ssdG$_{12}$ (c), ssdC$_{12}$ (d), ssdT$_{12}$ (e) and ssd(AGTC)$_3$ (f) adsorbed hydrogen terminated graphene flake, respectively.

First, we consider discussing the DFT computed interaction energy between graphene and various ssDNA in their folded conformations. To accomplish this, we calculate interaction energy by subtracting the energy of graphene and ssDNA components from the total energy of the respective hybrid composite. The calculated values per nucleobase are -9.21, -15.66, -16.45, -18.73 and -13.02 kcal mol_{-1} for $ssdA_{12}$, $ssdG_{12}$, $ssdC_{12}$, $ssdT_{12}$, and $ssd(AGTC)_3$, respectively. The predicted interaction strength follow as: $ssdT_{12} > ssdC_{12} > ssdG_{12} > ssd(AGTC)_3 > ssdA_{12}$. Note that, the DFT computed trend in interaction energy does not follow either the interaction energy or binding free energy trend estimated from 30 ns MD simulation.This may be due to the lack of any environmental effects considered in DFT calculations. Moreover, we do not find any interfacial charge-transfer between graphene and various ssDNA, suggesting the importance of non-covalent van der Waals and π-π stacking interaction for stabilization of these nano-biocomposites. Furthermore, we also consider calculating the electronic density of states (DOS) together with the projected density of states (pDOS) of individual components, and the distribution of highest occupied molecular orbital (HOMO) and lowest unoccupied molecular orbital (LUMO) for analysing the electronic structure of these model composites in details.We present the electronic DOS and pDOS in Fig. 3.13(a). We find the significant electronic states at the Fermi energy for all ssDNA-graphene hybrids.The pDOS analysis reveals that the major contribution to the DOS at Fermi energy mainly comes from the graphene component of these composites. However, a small contribution to the total DOS also comes from the ssDNA component, in particular, from π-stacked nucleobases, for the $ssdC_{12}$ and $ssdT_{12}$

adsorbed graphene complexes. This is also clear from their small HOMO-LUMO gap values: 44 and 38 meV for ssdC_{12} and ssdT_{12}, respectively, in their free wrapped conformations. The orbital contributions from ssDNA to the DOS for other systems occur at relatively lower in energy. We also find that all the bio-composites show very small HOMO-LUMO electronic gap values, indicating their near-conducting behaviours. The calculated gap values for ssdA_{12}, ssdG_{12}, ssdC_{12}, ssdT_{12}, and ssd$(AGTC)_3$ adsorbed graphene hybrids are 3, 10, 1, 2, 5 meV, respectively, which are very small in comparison to the thermal energy at room temperature ($\sim$26 meV). In fact, we find that these calculated small gap values resemble the HOMO-LUMO gap values of their rectangular graphene fragments. Our analysis also shows that these small gap values arise mainly because of the presence of graphene zigzag edge states, which is consistent with the HOMO and LUMO frontier molecular orbital diagrams as shown in Fig. 3.13. We find that these two molecular orbitals are mainly localized on the zigzag carbon edges of all the graphene fragments considered. However, in an infinite graphene sheet, there are no edge states. Here, edge passivation by hydrogen atoms causes partially occupied edge states at the Fermi level, resulting in metallic behaviour, which needs to be excluded for mimicking infinite graphene sheet. Furthermore, the 2D graphene surface becomes corrugated by the ssDNA adsorption. Thus, it is anticipated that the ssDNA adsorbed infinite graphene hybrid would act as small gap semiconductor.

3.4 Conclusions

In conclusion, we have shown that the biologically important various ssDNA oligonucleotides can serve as efficient dispersing agents for graphene in aqueous medium, using all atom MD simulation at room temperature and 1 atm pressure. Our simulation results show that when ssDNA is added to the aqueous solution of graphene, there exist three simultaneous competing forces: first, the base-base π-π stacking interactions within ssDNA (favour the native ssDNA helical shape), second, H-bonding interactions with solvent water molecules (helps in solubilization process of ssDNA), and third, the base-graphene π-π stacking interactions (assist ssDNA adsorption on graphene). Results obtained for various ssDNA oligonucleotides interaction with graphene show that the binding free energy order goes as: ssd$(AGTC)_3$ $<$ ssdA_{12} $<$ ssdG_{12} $<$ ssdC_{12} $<$ ssdT_{12}, indicating the importance of both π-π stacking as well as H-bonding interactions. Interestingly, we have found that, the interactions follow the same trend as obtained for single nucleoside interaction with graphene in aqueous solution. This clearly demonstrates that the nature of nucleobase, not the sugar phosphate backbone, together with the number of base-graphene π-stacks, are the key determining factors while solubilizing graphene with different ssDNA in aqueous solution. We also found two distinctive ssDNA assemblies, namely coiling and elongated network structures, on to graphene surface resulting from two competing forces acting on ssDNA in graphene solution. Moreover, our results suggest that the hetero-base sequences containing ssDNA, such as, ssd$(AGTC)_3$, is the most suitable candidate within the ssDNA considered here, compared

to any other ssDNA while dispersing graphene like materials in aqueous solution. Additionally, we have also studied detailed electronic structures of these ssDNA-graphene composites, highlighting their conduction properties. We believe that our results certainly would help in understanding the detailed underlined mechanisms for the ssDNA assisted graphene dispersion in aqueous solution.

Chapter 4

Electronic Structure of Boron and Nitrogen Substituted Graphene and Graphene Nanoribbons*

*Work reported in this chapter is published in: (a) Arun K. Manna and Swapan K. Pati, *J. Phys. Chem. C* **115**, 10842 (2011); (b) Arun K. Manna and Swapan K. Pati, *Int. J. Mod. Phys. B* **22**, 1242003 (2012); (c) Arun K. Manna and Swapan K. Pati, *J. Mater. Chem. C* **1**, 3439 (2013)

4.1 Introduction

Nano-carbons, like graphene, carbon nanotube, fullerene and their derivatives, have been of potential research interest in recent years for their novel low-dimensional intriguing structural, electronic and magnetic properties [260, 261, 467–474]. Because of its versatile and unique properties, graphene, a strictly two-dimensional (2D) mono-layer of carbon atoms tightly packed into a honeycomb lattice [194,406], has become an ideal candidate for application in the next generation electronic devices [260, 475–478]. Interestingly, it is a strictly zero band gap semiconductor, also known as semi-metal, possessing linear dispersive bands at the Fermi level forming perfect Dirac cone [406]. Contrastingly, its boron-nitrogen analogue, 2D hexagonal BN (h-BN) sheet, is a large band gap insulator with flat bands [185, 190, 191, 479–481]. Presence of controlled way of transition from insulators through semiconductors to conductors, among all the nano- structured materials, 2D graphene and h-BN sheet with completely contrasting electronic and magnetic properties, are of practical interest in nano-science and nano-technology.

Electronic as well as magnetic properties of low-dimensional materials are mainly governed by their size, geometrical shape and the carrier types and concentrations. The *massless* Dirac Fermions present in graphene results in very high carrier mobilities arising from complete delocalization of π electrons, whereas the carriers mobility of h-BN sheet is very poor due to charge-transfer induced electron localization on B and N atoms. Moreover, it has been shown that electron or hole mobility can be controlled by tuning external electric field in graphene based field effect devices [260]. Furthermore, the

utilization of spin components in graphene based electronic devices depends on the extent of spin polarization [482–485]. In this respect, half-metallic materials are potentially demanding which show zero band gap for electrons with one spin orientation and insulating or semiconducting band gap for the other spin orientation [486–489]. In fact, appropriate controlling and/or tuning of the electronic and magnetic properties of graphene has numerous applications in fabrication of advanced electronic devices. The electro-chemical doping [490] and chemical modifications [491, 492] have been considered the two viable routes for controlling the carrier type and concentration. In fact, the molecular doping induced charge transfer offers a leading approach in tuning of carrier types and its concentrations without invoking significant structural changes in graphene [491–497]. In addition, the replacement of graphene C atoms by B or N atoms would result in a desired and tunable carrier type and its density. Only recently, the B and N substituted nano-carbons, known as BCN analogue, has been realized experimentally [238, 251, 252, 498–502], and has been extensively studied theoretically exploring their novel properties [251, 254, 503–513]. Note that, the BCN analogue of graphene so far studied, mainly consist of irregular distribution of B and N atoms which results in more energy cost and a few studies only involve domain wise phase segregation [252, 254, 257, 499, 504]. More recently, an innovative experimental realization of domain segregated BCN analogue of graphene has been materialized, in which one region is rich with C (graphene), while other one is enriched with B_xN_y nano-domains [237, 514]. This BCN hybrids are considered as hybridized boron nitride and graphene domains. More interestingly, the band gap nano-engineering in graphene as well as in h-BN sheet is of

potentially demanding and more desirable for fabricating advanced devices. There have been several attempts to fulfil this goal in the literature. Along these lines, the realization of energy band gap in graphene by defects engineering, introducing lattice strain, and by the presence of external dopant as well as chemical functionalizations have been explored both theoretically and experimentally [515–519]. Moreover, the breaking of A-B sublattice symmetry in graphene by local structural distortion can result in band gap opening. This has been achieved by surface adsorption of various organic molecules and with nanoparticle adsorbates [493, 517]. In fact, it has been shown that a tunable band gap can be realized in graphene by the controlled adsorption of water molecules [520]. Additionally, the presence of nano-holes in graphene, known as nano-porous graphene or graphene anti-dots [521–526], has also been shown to be effective in semiconductor applications with tunable band gaps. The presence of nano-holes in graphene creates a potential barrier for its carrier mobilities, giving rise to the band gap opening. However, most often, the presence of nano-holes in graphene does not provide suitable structural framework for realistic applications, and therefore remain a challenging issue to be achieved practically. In contrast to this, one can build a nano-hybrid by filling these nano-pores of graphene with suitable semiconducting or insulating nano-domain materials which have similar sp^2 hybridized hexagonal lattice architecture, as present in graphene. This can be accomplished by utilizing nano-domains of h-BN with varying shapes and sizes. In fact, nano-patching of graphene, a zero band gap material, with its h-BN analogue, a large band gap insulator, can produce a hybrid ($B_xN_yC_z$) nanomaterials with tunable band gap values. Interestingly, this has recently

been demonstrated by chemical vapor deposition technique by Ajayan and co-workers [237]. The experimental achievements in synthesizing domain segregated $B_xN_yC_z$ nano-hybrids motivate us to pursue the present study in details which holds good promises for next generation device applications.

In the first part of this chapter, we have discussed the results obtained from a detailed, systematic and comprehensive analysis of the changes in structural as well as in electronic and magnetic properties of B_xN_y (with variation in x and y (integers) values) modified 2D graphene, using first-principles DFT calculations. Here, we have considered a mixture of three elements packed into a 2D honeycomb lattice. Since boron is a Lewis acid, it has strong affinity for nitrogen resulting in strong B-N bonds. In fact, the bonding energy of 'C-C' and 'B-N' bonds are comparatively higher than that of other hetero bonds (C-B and C-N) present in the hybrid system. Consequently, the hybrid systems will be domain segregated into two different regions; one with graphene C rich domain and other with B_xN_y enriched domain to gain thermodynamic stability. Presumably, we have considered a few representative regular shaped B_xN_y nano-domains in graphene. We have chosen a hexagonal (H-B_xN_y), two rhombohedral (R_a-B_xN_y and R_b-B_xN_y), and two triangular (T_a-B_xN_y and T_b-B_xN_y) shaped nano-domains in graphene with varying sizes. Different B_xN_y nano-domains under study are shown in Fig. 4.1.

Our results have shown that all the nano-hybrids are thermodynamically feasible to synthesize and have intermediate structural stability in between that of pristine graphene and h-BN sheet. We found that a major variety

of electronic and magnetic properties emerges as a result of B_xN_y nano-domain within graphene, depending on their shapes and sizes. We also found that it is possible to engineer the band gap of the $B_xN_yC_z$ nano-hybrids by simply varying the domain sizes. Interestingly, the T-B_xN_y nano-domains of varying shapes and sizes hybridized with graphene, result in metallic, semiconducting as well as half-metallic electronic states with full control over its spin components.

Additionally, we have also presented a detailed discussions on the quasi-1D hybridized zigzag graphene and boron nitride nanoribbons structures in the later part of this chapter. Moreover, the BN-fused zigzag polyacene nanoribbons, synthesized recently [248], have also been studied in great detail. Particularly, the electronic structures and the electircal transport properties are investigated for these nanoribbons, and their possible devices applications are also addressed. In fact, the study offers the potential for designing advanced electronic and magnetic devices.

4.2 Computational Methods

The first-principles calculations are carried out using the linear combination of atomic orbital density-functional theory (DFT) methods implemented in the SIESTA package [349, 350]. The generalized gradient approximation (GGA) in the Perdew-Burke-Ernzerhof (PBE) form [389] and double ζ polarized (DZP) basis set are chosen for the spin-polarized DFT calculations. The interaction between ionic cores and valence electrons is described by norm conserving pseudopotentials [390] in the fully non-local Kleinman-Bylander

form [391]. The pseudopotentials are constructed from 3, 4, and 5 valence electrons for the B, C and N atoms, respectively. A reasonable mesh cutoff of 400 Ry for the grid integration is utilized to represent the charge density. For full relaxation of all systems, we have sampled the Brilliouin zone by $5 \times 5 \times 1$ k-points using the Monkhorst-Pack scheme, whereas, for electronic properties calculations, the Brilliouin zone is sampled by $10 \times 10 \times 1$ k-points. We have also performed the geometry optimization for a $B_xN_yC_z$ nano-hybrid considering $7 \times 7 \times 1$ k-points, and found that there is a very small (less than meV order) change in total energy. Thus, we restrict ourselves for geometry optimization with $5 \times 5 \times 1$ k-points for all systems studied. The optimal atomic positions are determined until the magnitude of the forces acting on all atoms is less than 0.04 eVÅ^{-1}. GGA approximation takes into account the semi-local exchange correlations which have significant impact on low-dimensional spin systems like graphene and carbon nanotubes. Periodic boundary conditions and a supercell approximation are used to model different shapes and sizes of B_xN_y nano-domains patched with 2D graphene. The 8×8 supercell ($19.7 \times 19.7 \times 20$ in Å) containing 128 atoms of graphene is used for the electronic structure calculations. The vacuum separation of 20 Å between two layers is found to be sufficient to ensure the energy convergence. Within the calculation methods, the estimated lattice constants of graphene and h-BN sheet are 2.48 Å and 2.51 Å, respectively, which correspond to a C-C and B-N bond lengths of 1.43 Åand 1.45 Å, respectively. These values are close to the experimental values (2.46 Å for graphene and 2.50 Å for h-BN sheet) found at low temperature [527].

For the calculations on nanoribbons structures, the Monkhorst-Pack K

sampling grid is set to 70 points in the periodic direction. The conjugate gradient method is used for geometry optimization until the force acting on each atom is less than 0.04 $eV\mathring{A}^{-1}$. A large vacuum separation of $30\mathring{A}$ is used to suppress spurious interactions between the images in the non-periodic directions.

Our spin transport calculations are based on the non-equilibrium Greens function formalism (NEGF) as implemented in the TRANSIESTA package [528], extended to spin-polarised systems. However, here, we have considered both the zero bias limit as well as finite bias electron transmission and focused on electron transmission close to the Fermi energy. We have also calculated the I-V characteristics for the selective zigzag boron-nitrogen-carbon nanoribbons (ZBNCNRs), as will be discussed in the following sections, for its possible applications in electronic devices. The transmission is obtained from the following expression:

$$T(E) = Tr\left[\Gamma_L(E)G(E)\Gamma_R(E)G^{\dagger}(E)\right] \tag{4.1}$$

where, the Green's function, G(E) is calculated from the Hamiltonian and self-energies of the central region. $\Gamma_\alpha(E)$ is the imaginary part of the self-energies (times two) of the left and right electrodes ($\alpha = L, R$). The spin-polarized current, I (V_b) at a bias-voltage, V_b, is calculated using Landauer-Buttiker formula:

$$I(V_b) = (e/h)\int_{\mu_L}^{\mu_R}\left[f\left(E,\mu_L\right) - f\left(E,\mu_R\right)\right]T\left(E,V_b\right)dE \tag{4.2}$$

where, the $\mu_L = E_F - V_b/2$ and $\mu_L = E_F + V_b/2$, are the chemical potential for

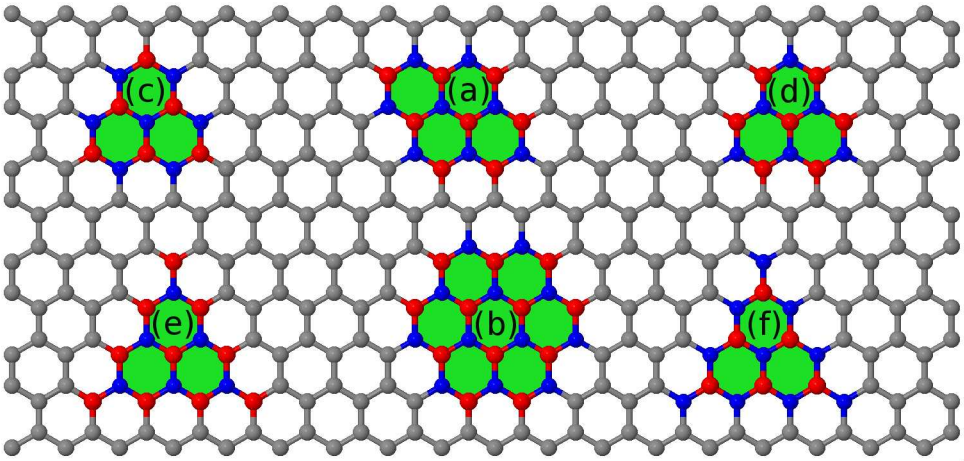

Figure 4.1: Schematic diagram of various B_xN_y nano-domains presence in graphene which includes rhombohedral R-B_xN_y (a), hexagonal H-B_xN_y (b) and triangular T_a-B_xN_y (c, d) and T_b-B_xN_y (e, f) nano-domains. The gray, blue and red colour atoms correspond to carbon, nitrogen and oxygen, respectively.

the left and right electrode, respectively. E_F and V_b are the Fermi energy and applied source-drain bias voltage, respectively. Note that, here T is a function of both energy (E) and bias voltage (V_b) as the bias voltage is included while calculating the Hamiltonian and thereafter the Green's function, G(E, V_b).

4.3 Results and Discussions

4.3.1 $B_xN_yC_z$: Hybrid of graphene and h-BN sheets

First we focus on the relative thermodynamic stability of these modified graphene nano-hybrids as a function of the embedded B_xN_y domain shapes and sizes. In fact, the thermodynamic stability of these modified hybrids strongly rely on the geometry of the nano-domains and their concentrations.

The structural stability and thermodynamic feasibility of a nano-hybrid depend on the extent of cohesive and formation energy, respectively. Thus, we calculate the cohesive energy (E_{coh}) of all the nano-hybrids using the equation (4.3). We also have calculated the formation energy (E_{for}) using equation (4.4), following a zero temperature approach customarily used to determine the relative energy cost for the formation of hybrid $B_xN_yC_z$ mixtures from their pristine analogues [529–533]. Note that, within this approach, the formation energies of the pristine graphene and pristine h-BN sheet are equal to zero, and thereby provides us a reference frame for comparing with other nano-hybrids:

$$E_{coh} = [E_{tot} - \sum_i N_i * E_i]/N(i = C, B, N) \tag{4.3}$$

$$E_{for} = [E_{tot} - \sum_i n_i * \mu_i]/N(i = CC, BN, C, B, N) \tag{4.4}$$

where E_{coh} and E_f are the cohesive and formation energy per atom of the ground state of B_xN_y modified graphene nano-hybrid, respectively, while E_{tot} and E_i represent total energy of a nano-hybrid and of individual element present within the same supercell, respectively. The N_i and n_i are the number of i^{th} species present in $B_xN_yC_z$ for E_{coh} and E_f energy calculation, respectively, while N is the total number of atoms present in a supercell (*i.e.*, N = 128). The μ_i is the suitable chemical potential of the i^{th} species. Additionally, depending on the atomic reservoir employed in synthesizing $B_xN_yC_z$ nano-hybrids, we can have either a nitrogen- or a boron-rich environment. The chemical potential for C, C-C and B-N can be obtained straightforwardly

from the corresponding infinite sheet calculation. However, to obtain μ_B and μ_N, we use the following thermodynamic constraint: $\mu_{B-N} = \mu_B + \mu_N$. Consequently, μ_B is obtained for boron- rich environment by considering μ_N to be α-phase of solid nitrogen (μ_N = -270.22 eV). Similarly, μ_N is obtained for nitrogen-rich environment by considering μ_B to be metallic α-B phase (μ_B = -77.23 eV). The details of this approach can be found elsewhere [529–533].

As is well known, higher the cohesive and formation energy, higher is the structural stability and greater is the thermodynamic feasibility of the nano-hybrids formation. In fact, as shown in Table 4.1, we find that all the B_xN_y substituted graphene hybrids have intermediate cohesive energy in between that of pristine graphene (-8.65 eV/atom) and h-BN sheet (-7.79 eV/atom). Consequently, it should have in between structural stability. However, with increasing concentration of embedded B_xN_y nano-domain belonging to a specific shaped nano-domains, the cohesive energy decreases and tends to attain the value of pristine h-BN sheet. Moreover, for the non-stoichiometric hybrids where there is a difference between number of B and N atoms (*e.g.*; T-B_xN_y substituted graphene hybrids), we find more negative E_{coh} for B-rich $B_xN_yC_z$ in comparison to the N-rich one. This can be understood as follows. For B-rich nano-hybrids, B being a strong Lewis acid, induces charge transfer driven extra cohesivity between the graphitic border C atoms and B atoms from the substituted B_xN_y domains, and hence results in relatively larger E_{coh}, compared to N-rich nano-domains.

Furthermore, as shown in Table 4.1, the relative formation energy slightly decreases (*i.e.* more +ve values) with increase in the size of B_xN_y nano-domains present in graphene irrespective of their shapes. This is because of

the more interfacial energy cost arising from larger perimeter of embedded nano-domains as we move towards bigger nano-domain sizes. Interestingly, we find that the extent of E_{for} is smaller for R-B_xN_y (Fig. 4.1a, b), H-B_xN_y (Fig. 4.1c), and T_a-B_xN_y (Fig. 4.1d) patched graphene compared to other nano-patching. This can be understood as follows. For a ternary alloy containing 3 elemental species C, B, and N in a 2D honeycomb lattice, the systems always try to maximize the number of 'C-C' and 'B-N' bonds and correspondingly, try to avoid the bonds between C and B, as well as between C and N, to gain the thermodynamic stability. Consequently, the more regular shaped B_xN_y hybridized graphene systems would have more thermodynamic stability compared to any other nano-hybrids. In fact, among all regular shaped B_xN_y substituted graphene, the above three systems have smaller interfacial energy, and show relatively smaller extent of formation energy (*i.e.* less positive E_{for} values). Moreover, we find relatively less E_{for} for H-B_xN_y substituted graphene, because of the smaller interfacial energy arising due to their less perimeter among others. This is also expected as the system has stable six member borazine unit in place of stable benzene ring. Interestingly, we find that the N-terminated B_xN_y patched graphene nano-hybrids have greater extent of E_{for} in comparison to the presence of B-terminated B_xN_y nano-domains. This also can be accounted as follows. For the $B_xN_yC_z$ hybrids consisting of B-terminated nano-domains, there is an extra energy cost arising from the interfacial charge transfer between B and C atoms in comparison to the presence of N-terminated nano-domains in graphene. This is well consistent with the results reported in earlier studies, showing the preference for forming the N-terminated edge structures [532].

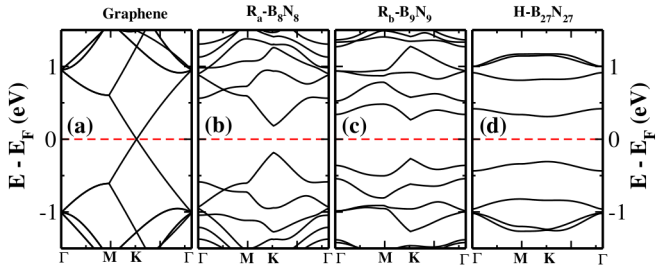

Figure 4.2: Electronic band structures of (a) pristine graphene, and (b) R_a-B_8N_8, (c) R_b-B_9N_9, (d) H-$B_{27}N_{27}$ substituted graphene nano-hybrids. The energy is scaled with respect to the Fermi energy (E_F).

Note that, the relative difference in F_{for} is very small for various $B_xN_yC_z$ nano-hybrids. However, we believe that all the B_xN_y substituted graphene systems proposed in the present study would be thermodynamically feasible to synthesize under suitable experimental growth conditions, as has already been demonstrated [237].

A summary of the results for the optimized structures for all nano-hybrids are provided in Table 4.1.

To understand the effect of various shaped B_xN_y nano-domains within graphene on electronic structure, we plot band diagrams in Fig. 4.2. We first focus on nano-hybrids which are iso-electronic (*i.e.*, possessing same number of electrons) with their parental compounds, namely R_a-B_xN_y, R_b-B_xN_y, and H-B_xN_y nano-domains. The graphene-R-B_xN_y/H-B_xN_y hybrids can be considered as a 2D mixture of C, B, and N, where some of the 'C-C' bonds are substituted by 'B-N' bonds. In both cases, the number of B and N atoms present in the domains are exactly equal, and thereby imposing no extra charge carriers into the systems. As can be seen from Fig. 4.2(a), the

Table 4.1: The cohesive energy (E_{coh}), formation energy (E_{for}), and band gap (E_g) for B_xN_y substituted graphene systems.

Nano-domains	E_{coh} (eV/atom)	E_{for} (eV/atom)	E_g (eV)
R_a-B_8N_8	-8.50	0.04	0.29
R_a-$B_{15}N_{15}$	-8.38	0.06	0.48
R_a-$B_{24}N_{24}$	-8.24	0.08	0.76
R_a-$B_{35}N_{35}$	-8.08	0.10	0.80
R_b-B_4N_4	-8.54	0.05	0.19
R_b-B_9N_9	-8.47	0.06	0.32
R_b-$B_{16}N_{16}$	-8.35	0.08	0.39
R_b-$B_{25}N_{25}$	-8.21	0.10	0.48
R_b-$B_{36}N_{36}$	-8.05	0.11	0.85
H-B_3N_3	-8.58	0.03	0.12
H-$B_{12}N_{12}$	-8.43	0.05	0.38
H-$B_{27}N_{27}$	-8.20	0.08	0.62
T_a-B_7N_6	-8.52	0.06	0.00
T_a-B_6N_7	-8.51	0.05	0.00
T_a-$B_{12}N_{10}$	-8.45	0.09	0.00
T_a-$B_{10}N_{12}$	-8.43	0.08	0.00
T_a-$B_{25}N_{21}$	-8.26	0.15	0.00
T_a-$B_{21}N_{25}$	-8.22	0.13	0.00
T_b-B_6N_3	-8.55	0.09	-
T_b-B_3N_6	-8.52	0.08	-
T_b-$B_{10}N_6$	-8.49	0.12	-
T_b-B_6N_{10}	-8.45	0.10	-
T_b-$B_{15}N_{10}$	-8.41	0.15	-
T_b-$B_{10}N_{15}$	-8.37	0.13	-
T_b-$B_{28}N_{21}$	-8.23	0.21	-
T_b-$B_{21}N_{28}$	-8.16	0.18	-
T_b-$B_{36}N_{28}$	-8.11	0.24	-
T_b-$B_{28}N_{36}$	-8.03	0.22	-

graphene band structure shows a perfect Dirac cone picture which arises due to the meeting of valence band maxima and conduction band minima at the Brillouin zone high symmetric K-point. Interestingly, the Fermi level lies exactly in between valence and conduction bands, leading to a zero band gap semiconductor, also known as semi-metallic graphene. Also can be seen from Fig. 4.2(b,c,d), the graphene nano-hybrids containing R_a-B_8N_8, R_b-B_9N_9, and H-$B_{12}N_{12}$ domains show semiconducting band gaps with gap value varying with the B_xN_y concentrations (see Table 4.1). In fact, the band gap increases with increase in nano-domain concentrations in accordance with the experimental findings [237]. This can be understood as we move to a hybrid system with higher insulating domain concentration where the intrinsic carriers feel a large potential barrier for its ballistic transport as observed in pure graphene [534]. The similar trend in band gaps variation with B_xN_y nano-domain concentrations for these three different shaped B_xN_y nano-domains present in graphene make us to conjecture that the band gap variation is not shape dependent, rather depends solely on the size or concentration of the B_xN_y nano-domains. We also find that the band structures around the Dirac point are significantly affected by the B_xN_y substitution in graphene. The linear dispersion of bands at K-point in graphene slowly disappear with increase in B_xN_y concentrations, and almost localized flat bands characteristic of pure h-BN sheet appear at higher concentration of B_xN_y nano-domains (see Fig. 4.2). However, the Fermi level is placed exactly in between the valence and conduction bands, as there is no predominating charges (either electrons or holes) in these hybrid systems. These systems can be considered as nano-hybrids where the 'C-C' pairs are replaced by their iso-electronic

analogue 'B-N' pairs and thereby, inducing no extra charge. Interestingly, as shown in the Fig. 4.2, the valence and conduction bands are symmetric with respect to the Fermi energy, due to the electron-hole symmetry.

For pure 2D graphene, spin-polarized DOS vanishes exactly at Fermi level due to the presence of *massless* Dirac fermions and thereby there is no net spin-polarization in the system. The calculated DOS together with its projections on individual species (pDOS) for various graphene-B_xN_y nano-hybrids clearly show that the accessible electronic states near the Fermi energy mainly arise from the border C atoms (C atoms those are bonded to B and N atoms) and to some extent C atoms of bulk graphene. With the increase in the B_xN_y concentrations, the contributions from the B and N atoms become significant along with the C contributions. Furthermore, the extent of contribution to the valence and conduction bands energy states are greater from B and N atoms, respectively. Interestingly, we also find that all the systems are stable in nonmagnetic ground states. An extensive analysis of band structure and DOS predict the carriers spin symmetries for all the systems resulting in a nonmagnetic ground electronic state where all sites bear zero spin moment.

We now focus on the changes in electronic and magnetic properties of graphene hybridized with triangular shaped (T-B_xN_y) nano-domains. Depending on the triangular geometry, the domain can be classified in two categories, namely, T_a-B_xN_y and T_b-B_xN_y (see Fig.1d, 1e). In each category, there exists two possibilities of edge termination of the embedded nano-domains. The edge can be terminated either by B or N atoms, and depending on the termination, the system might have excess of holes or electrons, respectively. Consequently, the patching of T-B_xN_y nano-domains with graphene

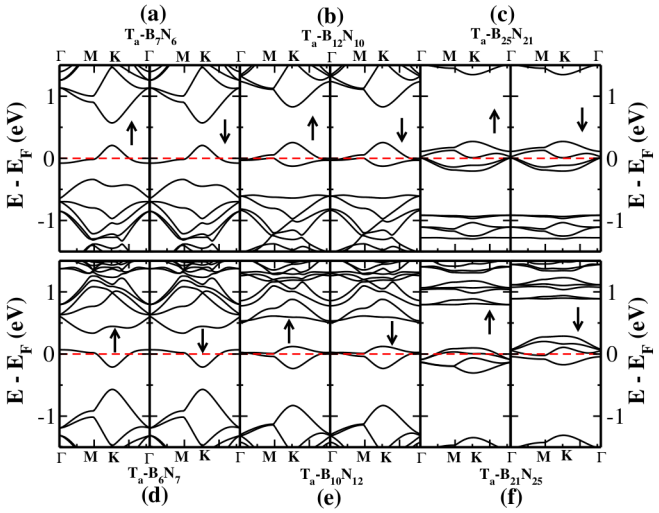

Figure 4.3: Electronic band structures of T_a-B_xN_y substituted graphene nano-hybrids with varying domain sizes. The pair (a, d), (b, e), and (c, f) are the complementary nano-domains patched with graphene systems. The energy is scaled with respect to the Fermi energy (E_F).

results in intrinsically either hole or electron doped systems. In Fig. 4.3, we present the electronic band structures of T_a-B_xN_y substituted graphene with increasing nano-domain sizes for both B and N terminated nano-domains in the top and bottom panel, respectively. We find that all graphene-T_a-B_xN_y hybrids are stabilized in metallic ground states. The metallicity arises due to the presence of mid-gap states in between valence and conduction bands aligning with the Fermi level. These mid-gap states originate due to the imbalance in A-B sublattices within $B_xN_yC_z$ hybrid. The number of such mid-gap states are equal to the difference in the sublattice imbalance [535]. The existence of these mid-gap states at or near the Fermi energy leads to various exotic electronic ground states. Interestingly, we find one, two, and four mid-gap states, according to the difference between number of B and N atoms present in nano-domains with increasing sizes (see Fig. 4.3). We also

analyze the wave functions at different high symmetric k-points in details to understand microscopically the origin of such states. From an analysis of wave functions, we find that the propensity of the atomic orbital contributions to these mid-gap state wave functions do mainly come from the border graphene C atoms, in particular from their p_z-orbitals. Increasing sizes of T_a-B_xN_y domains give rise to a significant contribution from the p_z-orbitals of both B and N atoms. Furthermore, an analysis of electronic DOS as well as pDOS reveal that the major contribution to the electronic conducting states at the Fermi level arises from graphene C atoms with small contribution from B and N atoms. The presence of spin symmetry between the majority and minority spin channels induces zero spin-polarization for systems with smaller B_xN_y. Interestingly, we also find that the valence and conduction bands in band diagrams (see Fig. 4.3) of the electron rich systems (T_a-B_xN_y with x $<$ y) are changed to an inverted structure for hole rich systems (T_a-B_xN_y with x $>$ y). This is because of the presence of electron-hole symmetry between these complementary nano-hybrids.

We now consider a pair of nano-domains making the system iso-electronic (for example, if we consider the pair T_a-$B_{12}N_{10}$ (Fig. 4.3b) and T_a-$B_{10}N_{12}$ (Fig. 4.3e) with equal number of holes and electrons, respectively) to study the effect on the electronic structure. Although, the individual nano-domains hybridized with graphene show perfectly metallic electronic ground states, the pair of complementary nano-domains simultaneously hybridized with graphene possessing no extra charge give rise to a semiconducting electronic structure. Note that, the supercell containing complementary nano-domains patched with graphene does not have any imbalance in A-B sublattice, and

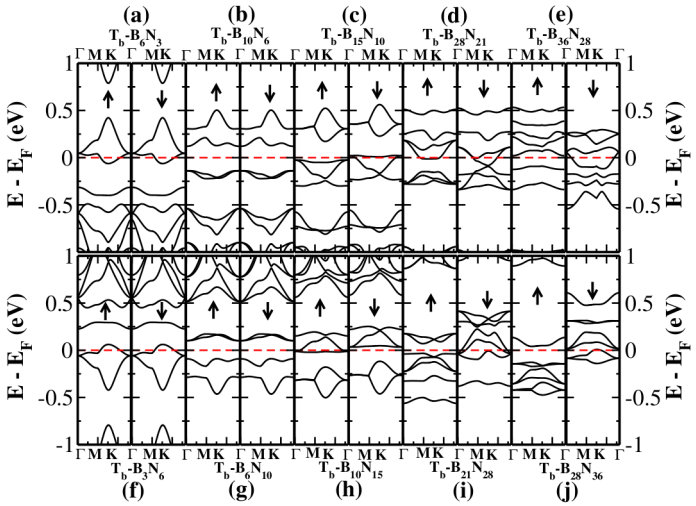

Figure 4.4: Electronic band structures of T_b-B_xN_y substituted graphene nano-hybrids with varying substituents concentrations. The pair (a, f), (b, g), (c, h), (d, i), and (e, j) are the complementary nano-domains present in graphene systems. The energy is scaled with respect to the Fermi energy (E_F).

hence, does not provide any mid-gap states at Fermi energy for metallicity. Here the situation is exactly similar to the case of R_a-B_xN_y nano-domain hybridized with graphene, as discussed earlier.

To analyze the effect of T_b-B_xN_y nano-domain sizes on electronic structure, we have considered a few representative T_b-B_xN_y nano-domains with increasing size in graphene supercell. The (x,y) pairs include (6,3), (10,6), (15,10), (28,21), and (36,28) for B-terminated nano-domains, and in case of N-termination, the pairs include (3,6), (6,10), (10,15), (21,28), and (28,36) for various sizes of nano-domains. In Fig. 4.4, we plot the electronic band diagrams for B- (upper panel) and N-terminated (lower panel) nano-domains patched with graphene. Interestingly, we find that the nano-hybrids can

have a tunable electronic ground states, metallic ↔ semiconducting ↔ half-metallic, with simply varying the sizes of embedded nano-domains. Note that, all these systems have mid-gap electronic states in between valence and conduction bands arising due to the imbalance in A-B sublattice as mentioned above. As shown in Fig. 4.4, we find that the complementary pair T_b-B_6N_3 (Fig. 4.4a) and T_b-B_3N_6 (Fig. 4.4f) hybridizing with graphene show a perfectly conducting ground state as one of the mid-gap states crosses the Fermi energy, whereas the hybridization of T_b-$B_{10}N_6$ (Fig. 4.4b) and T_b-B_6N_{10} (Fig. 4.4g) nano-domains with graphene leads to a semiconducting band structure as none of these mid-gap states cross the Fermi level. Interestingly, with increasing T_b-B_xN_y domain sizes, we also find a metallic and a half-metallic band structure; *i.e.*, one of the spin channel has semiconducting band gap whereas, the other spin channel is available for electronic conduction. From an analysis of wave functions, we find that the mid-gap states near the Fermi energy mainly originate from $2p_z$-orbitals of C atoms directly bonded to the B and N atoms (*i.e.*, border C atoms). However, with increasing nano-domain sizes, the contribution arising from $2p_z$-orbitals of B and N atoms become more significant.

For a better understanding of individual species contribution to the total DOS at and near the Fermi energy, we plot the DOS together with pDOS in top panel of Fig. 4.5 for the representative nano-domains, T_b-$B_{36}N_{28}$ and T_b-$B_{28}N_{36}$ patched graphene, respectively. It is clear from the Fig. 4.5 that the former hybrid is a metal whereas, the later one stabilizes as a half-metal. As also can be seen from Fig. 4.5 (top panel: (a) and (b)), the DOS at and

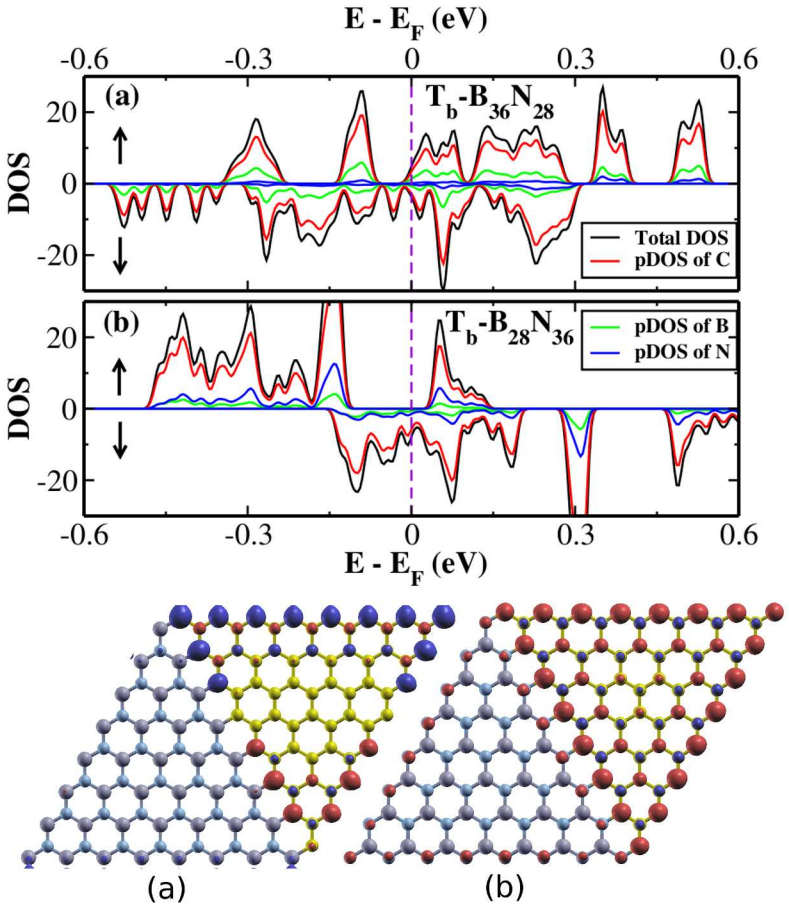

Figure 4.5: Electronic total density of states (DOS) and projected density of states (pDOS) of (a) T_b-$B_{36}N_{28}$ and (b) T_b-$B_{28}N_{36}$ substituted graphene nano-hybrids with their spin-density (↑-spin - ↓-spin) distribution. The energy is scaled with respect to the Fermi energy (E_F).

near the Fermi energy mainly comes from border C atoms with lesser contribution from B and N atoms. Moreover, a significant contribution from B and N atoms arises for larger domain sizes with greater contribution from B and N atoms for the B- and N-terminated nano-domains, respectively. Here, we should point out that the nano-hybrids consisting of T_b-$B_{36}N_{28}$ and T_b-$B_{28}N_{36}$ nano-domains, exhibit significant structural overlap between the adjacent nano-domains in the supercell, and can be considered as a patchwork of triangular h-BN and graphitic nano-domains. However, the calculated energy cost for these nano-hybrids are within $\sim$ 4-6 kcal/mol with respect to their pristine analogues, and thereby, showing the possibilities for their experimental realization under suitable growth conditions. Furthermore, asymmetry in bands dispersion (see Fig. 4.4) for two different spin channels near the Fermi level causes difference in occupation number for two spin channels and hence, leads to the magnetic ground states. Also the presence of mid-gap electronic states with partial occupancy give rise to the net magnetic moment in these nano-hybrids. Note that, the graphene- T_b-B_6N_3/-T_b-$B_{10}N_6$ nano-hybrids as well as its N-terminated counter analogue show nonmagnetic ground states as bands for both majority and minority spin channels are symmetrically dispersed with respect to the Fermi level. However, we find magnetic states for larger T_b-B_xN_y domain sizes patched with graphene which contain greater number of either electrons or holes. More interestingly, we find that the intrinsic magnetic moments do mainly originate from the graphene border C atoms directly bonded to the B and N atoms (see bottom panel in Fig. 4.5) and can be accounted for the redistribution of charges among Kohn-Sham orbitals induced by the interfacial charge transfer between C and B as well as

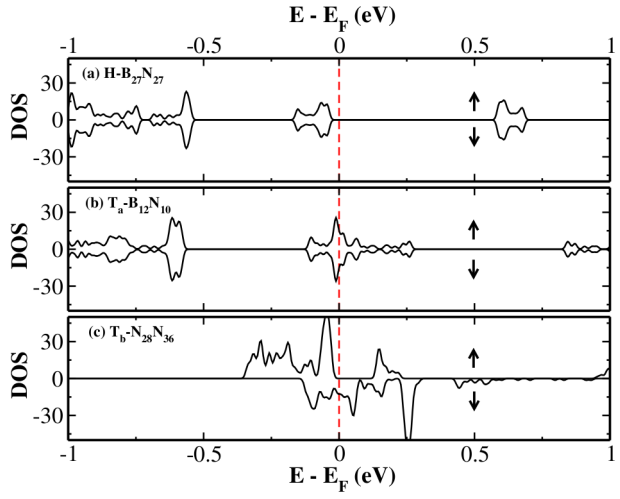

Figure 4.6: Electronic density of states (DOS) of (a) H-$B_{27}N_{27}$, (b) T_a-$B_{12}N_{10}$, and (c) T_b-$B_{28}N_{36}$ substituted graphene nano-hybrids. The energy is scaled with respect to the Fermi energy (E_F).

between C and N atoms, as expected from their electronegativity differences together with Lewis acid character of B atoms.

To verify the consistency of observed semiconducting, metallic, and half-metallic behaviors of various B_xN_y nano-domains substituted graphene, we have also performed the calculations within an extended plane augmented wave [536] basis sets, as implemented in the DFT code, VASP [537–539]. In Fig. 4.6, we plot the total DOS for a H-$B_{27}N_{27}$ (Fig. 4.6a), T_a-$B_{12}N_{10}$ (Fig. 4.6b), and T_b-$B_{28}N_{36}$ (Fig. 4.6c) nano-domains patched graphene systems. Interestingly, we find qualitatively similar behaviours, *i.e.*, semiconducting, metallic, and half -metallic electronic structure, respectively, for these nano-domains patched graphene as found with localized basis sets using SIESTA, highlighting the robustness of our predicted results.

4.3.2 Hybrid Zigzag Graphene and BN nanoribbons

In the previous section, we have discussed the electronic structures of hybridized graphene and h-BN sheets in detail, and particularly, have examined the impact of different shapes and sizes of embedded BN domains on electronic and magnetic properties of the 2D $B_xN_yC_z$ hybrids. It would be really fascinating to investigate their nanoribbons properties too. Given the rapid progresses in synthesizing the hybrid of graphene and h-BN sheets [237], it is highly expected that such quasi-1D materials would be realized experimentally. Interestingly, it was shown that, the zigzag edge nanoribbons structures are of promising electronic and spintronic materials due to the existence of the peculier edge states. Note that, H-passivated zigzag graphene nanoribbons (ZGNRs) and zigzag boron nitride nanoribbons (ZBNNRs) in their ground states, show semiconducting properties with varying band gaps depending on the ribbons widths.

Here, we have studied the electronic structures of the hybridized zigzag graphene and zigzag boron nitride nanoribbons structures (ZBNCNRs) using first-principles DFT methods. We have mainly considered two different ZBNCNRs: (1) the nanoribbons with the terminating polyacene chains and the zigzag boron nitride chains at the middle, termed as ZGNR-BN, and (2) the ZBNCNRs with the polyborazene chains at the edges and the zigzag C-C chains at the middle, named as ZBNNR-CC. We have considered these two nanoribbons structures with two different widths, namely, 8-ZBNCNR, containing 8 zigzag chains and 12-ZBNCNR with 12 zigzag chains. Here, we have discussed the results based on the 8-ZBNCNRs. However, the results

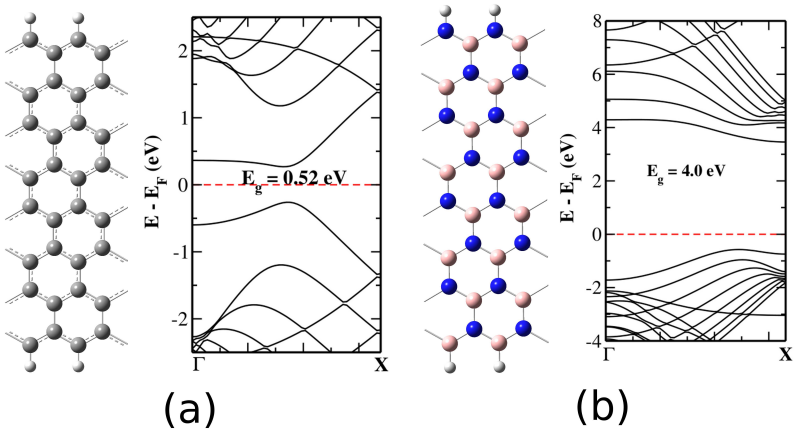

Figure 4.7: The optimized geometry and the spin-polarized electronic band structures of H-passivated pristine 8-ZGNR (a) and 8-ZBNNR.

obtained for the 12-ZBNCNR remain unchnaged. The calculations have revealed that, the two ZBNCNRs with the polyacene or polyborazene chains at the two zigzag edges exhibit robust half-metallic behaviors.

First, we will present the results obtained for the H-passivated zigzag graphene (8-ZGNR) and boron nitride nanoribbons (8-ZBNNR) structures for the comparisons and validations with the existing literature results. Our results have shown that, the 8-ZGNR stabilizes in antiferromagnetic (AFM) state, while, its BN analogue, *i.e.*, 8-ZBNNR is nonmagnetic. Moreover, 8-ZGNR is a spin-symmetric semiconductor, with the band gap of 0.52 eV, whereas, 8-ZBNNR shows a semiconducting gap of 4.0 eV (see Fig. 4.7). These results agree well with the previous findings [219, 540]. It is also important to note that, the 8-ZGNR is predicted to exhibit half-metallicity under the applications of an external cross-ribbon electric field using both the LDA and GGA flavors of DFT [540, 541].

Now, we will discuss on the electronic structures of hybridized ZGNRs

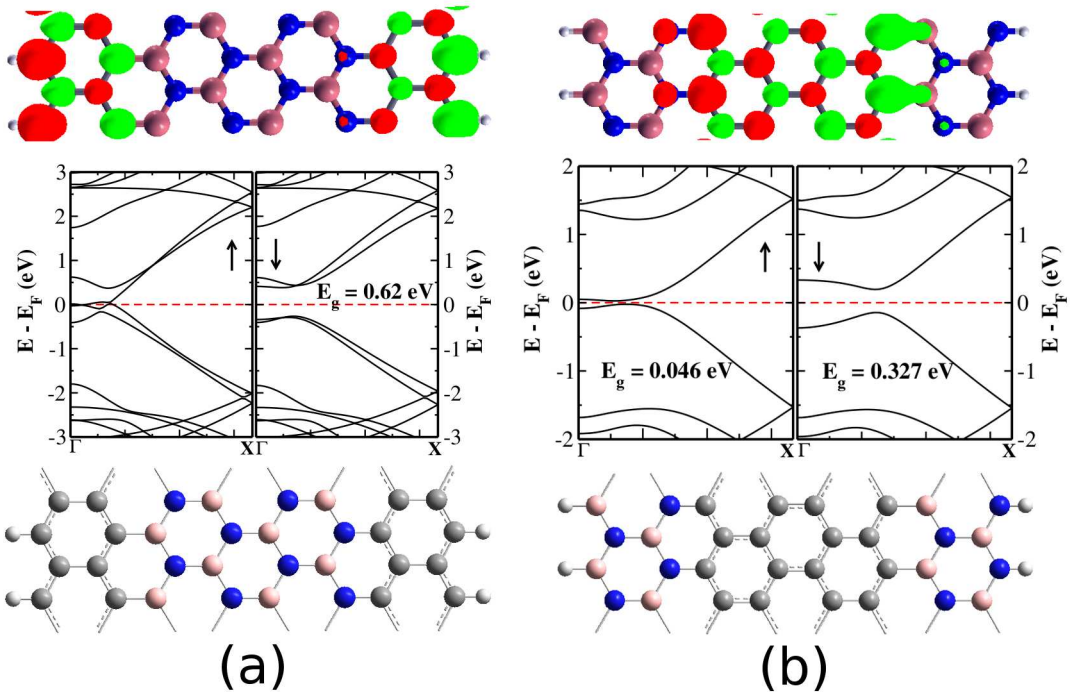

Figure 4.8: The optimized geometry (bottom panel) and the spin-polarized electronic band structures (moddle panel) and spin-density distribution (top panel) of 8-ZGNR-BN (a) and of 8-ZBNNR-CC nanoribbons.

and ZBNNRs considered in the present study. We have calculated the spin-polarized electronic band structures of the two systems (8-ZGNR-BN and 8-ZBNNR-CC), and have shown in Fig. 4.8. Both the nanoribbons structures are stabilized in AFM ground states, as was also found for the pristine 8-ZGNR. The spins at the same edge are coupled ferromagnetically, while, the spins at the two different edges interact antiferromagnetically. Interestingly, for the 8-ZGNR-BN nanoribbons, we have found that, the majority spin channel is conducting, while, there is a semiconducting gap for the minority spin channels. This suggests that, the ZGNR nanoribbon with the middle zigzag C-C chains replaced by the B-N chains is a 100% spin selective conductor, *i.e.*, a half-metal. This half-metallicity originates from the two different interfaces of the two zigzag carbon edges. The presence of middle zigzag B-N chains in 8-ZGNR-BN nanoribbon causes the edge C atoms of the terminating polyacene units, face two different chemical potentail from "B" and "N" atoms of the embedded middle B-N chains. This induces interfacial charge transfer in the C-B and C-N hetero chemical bonds becuase of the difference in electronegativity values of these chemical species. As a result, this causes the different chemical potential at the C atoms of the two zigzag edges, which, in turn, creates an internal electric field gradient across the nanoribbon width direction. This internal electric field induces half-metallicity in these hybrid nanoribbon structures. Note that, an external electric field is required to break the spin symmetry between the zigzag edge C atoms in a pristine ZGNRs, which exhibits half-metallicity under the presence of an external electirc field.

On the other hand, the electronic band structures calculated for the zigzag

graphene nanoribbon with the terminating polyborazene chains (8-ZBNNR-CC) at the two edges, show a spin-polarized semiconducting behavior (see Fig. 4.8). The band gaps for the majority and minority spin channels are ∼0.05 eV and ∼0.33 eV, respectively. Note that, these gap values are more than the room temperature energy (∼0.026 eV), which suggests their applications in semiconducting devices. Also, note that, in this nanoribbon structure, the edge C atoms of middle zigzag C-C chains embedded in ZBNNR, also face two different hetero chemical species (B and N) from the terminating polyborazene units. This causes interfacial charge transfer induced chemical potential differences at the two zigzag edged C atoms, which, creates an internal electric field gradient across the ribbons width, as was also found for the 8-ZGNR-BN. This field helps to close the band gap in one kind of (majority) spin channels. However, the induced internal electric field strength is comparatively small than the field found for the 8-ZGNR-BN nanoribbon. Thus, the generated electric field is not sufficient to close the majority spin channels gap, and hence, the 8-ZBNNR-CC remains as semiconductor. Further, we have found that, the electrons are partially localized on the zigzag edge C atoms, and possess a finite spin-density (see Fig. 4.8). The pDOS analysis reveal that, the electronic states at/near to the Fermi energy (E_F) mainly arise from these zigzag edged C atoms. We have verified our findings using a plane-wave basis sets and projected-augmented wave pseudopotentials with the PBE exchange and correlation functional, as implemneted in DFT code, VASP [537–539]. Moreover, we have also tested the results using the larger width nanoribbons structures, considering 12 zigzag chains, 12-ZGNR-BN and 12-ZBNNR-CC, and found the similar results.

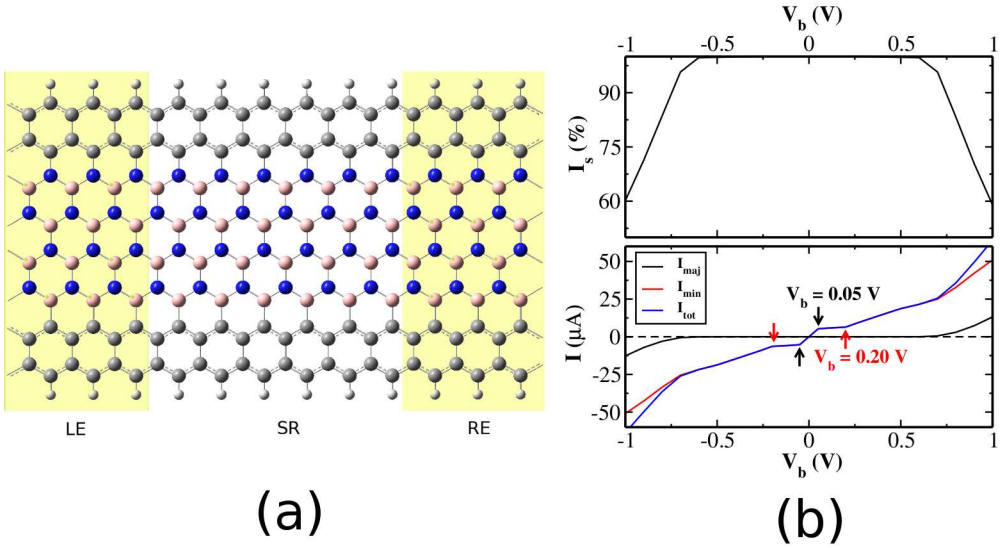

Figure 4.9: Schematic representation of a two-probe electrical device (a) and the spin-polarized currents (I) at different bias voltages (V_b) along with the extent of spinpolarization (I_s) for 8-ZGNR-BN.

Since, the 8-ZGNR-BN considered here exhibits intrinsic spins selective electronic conduction properties, it would be highly desired to investigate the electrical transport properties of the nanoribbon structure at finite bias voltages for the practical devices applications. For this, we have designed a two-probe electronic device made from this 8-ZGNR-BN, where, the nanoribbon structure (scattering region) is seamlessly connected with the two electrodes, namely, left and right electrodes, as shown in Fig. 4.9. We have calculated the electronic transmission functions at different bias voltages (V_b) using the DFT implementation of Greens' function methods discussed in computational methods section. Moreover, we have also calculated the current-voltage (I-V_b) characteristics for this electronic set up using Landauer-Buttiker formula. The spin-polarized I-V_b curves are shown in Fig. 4.9 along with the

extent of spin polarization (I_s), which is calculated using the following relation:

$$I_s = \frac{I_{min} - I_{maj}}{I_{min} + I_{maj}} \tag{4.5}$$

where, I_{min} and I_{maj} represent minority and majority spin-currents, respectively. As shown in Fig. 4.9, the minority spin channel shows conducting behaviors for all the bias voltages (V_b), while, the majority spin channels exhibit non-conducting nature up to the bias voltage, $V_b = \pm$ 0.52 V. As also can be seen, the I-V_b characteristics show a linear Ohmic conductive behavior for the minority spin channels within the small bias voltages, $V_b = \pm$0.055 V. After this bias voltages, the current carried by the minority spin channels remains almost constant with increase in the bias voltages, up to, $V_b = \pm$0.20 V. Further increase in the bias voltage, causes increase in the minority spin current. Note that, this behavior is found symmetric with respect to the source-drain bias voltages (V_b). Interestingly, we have found 100% spin polarized currents, as indicative from the I_s diagram, shown in Fig. 4.9. This suggests that, the electrical device made up of 8-ZGNR-BN performs a strong spins filtering effects. However, in this point, it is important to note that, the similar electric device constructed from pristine 8-ZGNR does not show any spins filtering properties within a source-drain bias voltages, $V_b = \pm$ 0.50 V. However, there is a small spin polarized current found after this bias voltage. The present demonstrations have shown that, the zigzag edge graphene nanoribbons with middle zigzag B-N chains and the edge terminating polyacene chains, shows intrinsic half-metallic behavior, and may be used

in practical device fabrications, operating at finite source-drain bias voltages, for achieving 100% spin polarized currents.

4.3.3 BN-Fused Zigzag Polyacene Nanoribbons

As ZGNRs and ZBNNRs show interesting and promising properties unlike their armchair analogues, in this work, we present a detailed theoretical study on hybrid zigzag BNC nanoribbons (ZBNCNRs), where the cross ribbon polyacene units are connected to each other by the B-N linker, which is isoelectronic to a C-C unit. Previous studies on 2D BNC sheets have shown that the hybrid with maximum number of C-C and B-N bonds are most stable compared to any other structure with different bond types (e.g.; B-B, N-N, C-B and C-N). These results together with the experimentally synthesized BN-fused polycyclic aromatics [248] were utilized to choose the present nanoribbons that would be practical as well as of interest. We consider five different sets of ZNBCNR structures with varying proportions of boron, carbon and nitrogen atoms having different kinds of B-N chain edge terminations: (1) the BN-fused polycyclic nanoribbon structures with boron atoms at both edges, (2) the nanoribbon structures with nitrogen atoms at both edges, (3) the nanoribbons with boron atoms at one edge and nitrogen atoms at the other edge, (4) the nanoribbon structures with hydrogen passivated boron and nitrogen atoms at opposite edges, and (5) the ZBNCNRs with hydrogen passivated carbon atoms at both the edges, as shown in Fig. 4.10. For each of the systems above, we repeat the calculations for different nanoribbon widths, n-ZBNCNR (n is the number of zigzag chains: $n = 6$, 10, 12). We

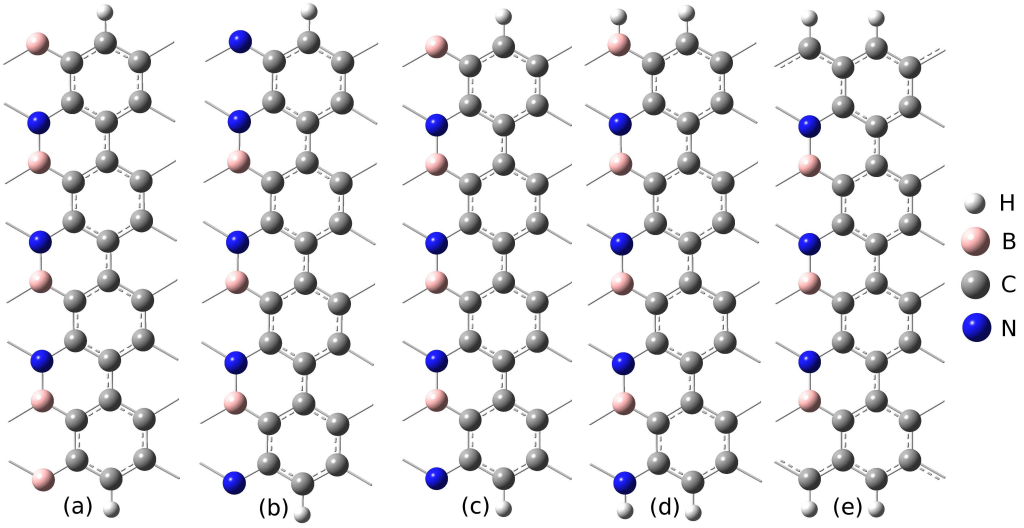

Figure 4.10: The optimized geometries of the 8-ZBNCNRs structures. (a), (b), (c), (d) and (e) represent $C_{pass}B_{bare}$, $C_{pass}N_{bare}$, $C_{pass}(BN)_{bare}$, $C_{pass}(BN)_{pass}$ and $C_{pass}C_{pass}$, respectively.

also study the effect of external electric fields and calculate current-voltage (I-V) characteristics for the selective ZBNCNRs to evaluate their possible applications in nanoscale devices.

Before we discuss the structural, electronic and magnetic properties in details, we first perform the calculations on 2D graphene and h-BN sheet in order to verify the accuracy of our calculation methods used in the present study. Within the calculations, the lattice constants of graphene and h-BN sheets are found to be 2.48 $\mathring{A}$ and 2.51 $\mathring{A}$, respectively, which correspond to C-C and B-N bond lengths of 1.43 $\mathring{A}$ and 1.45 $\mathring{A}$. These calculated values are close to the experimental values (2.46 $\mathring{A}$ for graphene and 2.50 $\mathring{A}$ for the h-BN sheet) found at low temperature and also agree well with the results from previous theoretical studies.

First, we focus on the relative thermodynamic stability of these ZBNC-NRs with different edge states. In fact, the thermodynamic stability of these modified BNC hybrids strongly depends on the concentrations of substitutional species and the bonding pattern among various elements present in each of the structures. The structural stability and thermodynamic feasibility of a BNC-hybrid depend on the extent of cohesive and formation energy, respectively. For calculating the cohesive (E_{coh}) and formation energy (E_{for}, the equations (4.3 and 4.4) would be modified as given below:

$$E_{coh} = \left[E_{coh} - \sum M_i * E_i\right] /M \qquad (i = H, B, C, N) \tag{4.6}$$

$$E_{for} = \left[E_{coh} - \sum m_i * \mu_i\right] /M \qquad (i = CC, BN, CH, BHNH, B, C, N) \tag{4.7}$$

where, E_{coh} and E_{for} are the cohesive and formation energy per atom of the ground state of ZBNCNRs, respectively, while E_{tot} and E_i represent total energy of a ZBNCNR and of individual element present within the same supercell, respectively. The M_i and m_i are the total number and mole fraction of i^{th} species present in ZBNCNRs for E_{coh} and E_{for} energy calculations, respectively, while M is the total number of atoms present in a supercell (i.e., $M = 34$ (without H-passivation) and 36 (with H-passivation)). μ_i is the suitable chemical potential of the i^{th} species. Additionally, depending on the atomic reservoir employed in synthesizing ZBNCNRs hybrids, we can have either nitrogen- or a boron-rich environment. The chemical potential for C, C-C and B-N can be obtained straightforwardly from the corresponding infinite sheet systems. However, to obtain μ_B and μ_N, we use the following

thermodynamic constraint: $\mu_{B-N} = \mu_B + \mu_N$. Consequently, μ_B is obtained for boron-rich environment by considering μ_N from the α-phase of solid nitrogen ($\mu_N = -270.22$eV). Similarly, μ_N is obtained for nitrogen-rich environment by considering μ_B from the metallic α-B phase ($\mu_B = -77.23$ eV). The chemical potential for CH and BHNH units are calculated by considering the stable benzene and its iso-electronic borazene analogues, respectively. The details of this approach can be found elsewhere [247–249, 349, 389, 542]. A summary of the results for the optimized structures of all ZBNCNRs-hybrids are provided in Table 4.2.

As has already been discussed, higher the cohesive and formation energy, higher is the structural stability and greater is the thermodynamic feasibility of the ZBNCNRs formation. In fact, as shown in Table 4.2, we find that all the modified graphene nanoribbons have intermediate cohesive energy in between that of H-passivated pristine 8-ZGNR (-7.92 eV/atom) and 8-ZBNNR (-7.18 eV/atom). Consequently, it would be of intermediate structural and mechanical stability. The larger E_{coh} for pure 8-ZGNR is because of the greater number of C-C bonds, whereas the larger number of B-N bonds in pure 8-ZBNNR causes lesser extent of E_{coh}. This is also because ZGNRs are stabilized by strong covalent bonds, whereas, the presence of ionic bonds stabilizes the ZBNNRs. As can be seen from Table 4.2, the nanoribbon structure with larger number of C-C bonds has greater extent of E_{coh} among others, mainly because of strong C-C covalent bonding energy. Also, note that, all the BNC-nanoribbons have 3 B-N and 27 C-C bonds except for the structure (e) which contains 29 C-C bonds, resulting in moderate cohesive energy. Note that, all the bare edge ZBNCNRs ((a), (b), (c) in Fig. 4.2) possess

Table 4.2: Formation (E_{for}) and cohesive (C_{coh}) energies per atom for each of the 8-ZBNCNRs structures, as shown in Fig. 4.10, along with their pristine analogue; 8-ZGNR and 8-ZBNNR. The number of C-C, B-N, C-B and C-N are also indicated.

Structure	No. of C-C bonds	No. of B-N bonds	No. of C-B bonds	No. of C-N bonds	E_{coh} (eV)	E_{for} (eV)
8-ZGNR	38	0	0	0	-7.92	0.03
(a)	27	3	5	3	-7.68	0.52
(b)	27	3	3	5	-7.69	0.41
(c)	27	3	4	4	-7.69	0.47
(d)	27	3	4	4	-7.51	0.23
(e)	29	3	3	3	-7.60	0.20
8-ZBNNR	0	38	0	0	-7.15	0.01

similar amount of E_{coh} and hence, should exhibit similar structural rigidity. We also find that the H-passivation increases cohesive energy compared to bare edge structures due to terminal changes in bonding energy.

The extent of increment in E_{coh} is larger for structure (d) where both the edge B and N atoms are passivated with H atoms which are more likely to be stable in their three coordinated bare form. Furthermore, we also consider calculating the formation energy (E_{for}) of all the ZBNCNRs, related to their pristine 2D sheet structures using equation (4.7), and present them in Table 4.2. As given in Table 4.2, the lowest formation energy is found for both pristine 8-ZGNR and 8-ZBNNR in comparison to their hybrid-BNC analogues. All the calculated E_{for} values are slightly higher in energy, indicating small energy cost of formation than their pristine analogues, which can be achieved under suitable experimental growth conditions, as was recently reported [248]. As also can be seen from the Table 4.2, structure (b), in which both the edges are terminated with N atoms shows relatively low E_{for} value (0.41 eV/atom) among all the structures with bare edges, which

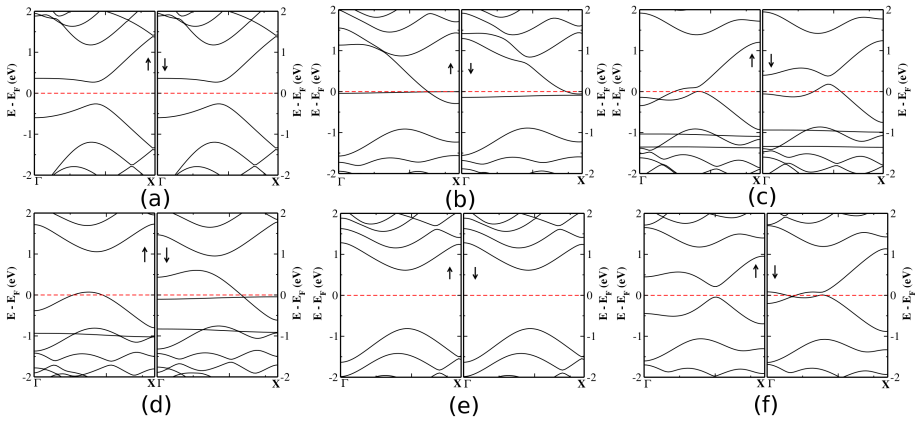

Figure 4.11: Spin-polarized electronic band structures for the different 8-ZBNCNRs. (a), (b), (c), (d), (e) and (f) represent band structures for the H-passivated pure, both sides B-edges, both sides N-edges, both B- and N-edges, H-passivated both B- and N-edges, and H-passivated C-edges 8-ZBNCNRs, respectively. The Fermi level is set to zero.

indicates that the N edges ZBNCNRs are most stable and hence, show preference for formation, as was also found in earlier studies [249,532]. Moreover, the H-passivated ZBNCNRs show lesser extent of formation energy with the lower E_{for} value obtained for structure (e), suggesting its greater thermodynamic formation feasibility among others. Note that, H-passivation of edge dangling bonds reduces the chemical potential of edge atoms, and thereby increases the extent of their formation from respective precursors.

Next, we analyze the electronic structure and magnetic properties of the ZBNCNRs considered. The pristine ZGNRs and its B and N substituted zigzag edged BNC-nanoribbons were found to be anti-ferromagnetic (AFM) because of their localized edge states, and the calculated energy difference between the AFM state and non-magnetic state is found to be only a few meV. Consequently, we consider a number of 8-ZBNCNRs with various spin configurations at the edges to find out the lowest energy spin states by performing

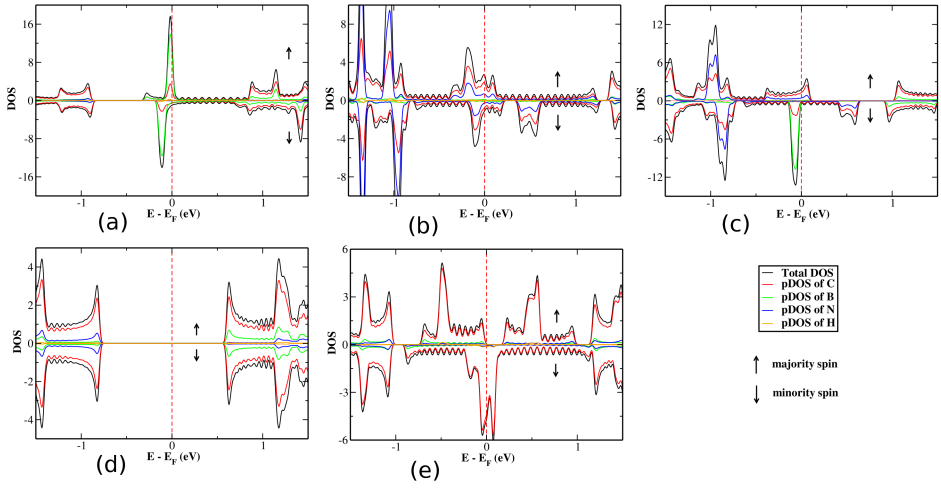

Figure 4.12: Spin-polarized density of states (DOS) for various 8-ZBNCNRs with different edge geometries. Individual DOS diagram corresponds to the nanoribbon structure, as shown in Fig. 4.10. The Fermi level is set to zero.

spin-polarized DFT calculations. Our results show that all the nanoribbons are stabilized in AFM ground state except for the case of H-passivated B and N edged ZBNCNR (structure (d) in Fig. 4.10), which is stabilized in a non-magnetic state. We find that the spins along the same edge are arranged ferromagnetically while they are coupled anti-ferromagnetically across the two different edges, as was found for pristine ZGNRs [206]. It is also to be noted that the AFM states are only stabler than FM or non-magnetic state by a marginal energy difference, of the order of a few meV, which could be overcome by thermal energy at room temperature.

To understand and compare the electronic structure of these B and N substituted 8-ZBNCNRs, we calculate the electronic band diagrams of each nanoribbon structure along with their pristine analogue, 8-ZGNR, and plot them in Fig. 4.11. As shown in Fig. 4.11a,the H-passivated pristine 8-ZGNR

is a direct band-gap semiconductor with the gap value found to be ∼0.52 eV and shows spin degeneracy between the opposite spins for all bands, which compare fairly well with the earlier reported results [206]. Our results also show that all the bare edge 8-ZBNCNRs are metallic, and the conducting behavior arises because of the edge states. However, the H-passivated B and N edge 8-ZNBCNR (structure (d) in Fig. 4.10) exhibits spin degenerate semiconducting behavior bearing a gap of 1.4 eV. Interestingly, we find half-metallic state for H-passivated C-edged 8-ZBNCNR, with the semiconducting channel for one type of spin configuration and conducting channel for the other spin configuration. In order to understand the origin of these different electronic states, we analyze the density of states (DOS) and projected density of states (pDOS), as shown in Fig. 4.12. Additionally, we have also calculated local density of states (LDOS) near to the Fermi energy (E_F) for all the 8-ZNBCNRs, which is shown in top panel of Fig. 4.13. As shown in Fig. 4.12 (a) and (b), we find that the ZBNCNRs with both edges terminated with either bare B or N atoms or both B and N, the electronic states at and close to Fermi energy (E_F) mainly originates from the edge B or N atoms together with the contribution arising from the H-passivated edge C atoms. This is also clear from the LDOS diagrams, as given in Fig. 4.13 (a), (b) and (c), for these three structures, where, the conducting states at/near to the E_F are mainly arising from the edge atoms. For the semiconducting H-passivated B and N edged 8-ZBNCNR (structure (d) in Fig. 4.10), the states close to the E_F originate primarily from the edge C atoms with small contribution from the neighboring C atoms.

Additionally, the top of the valence band and bottom of the conduction

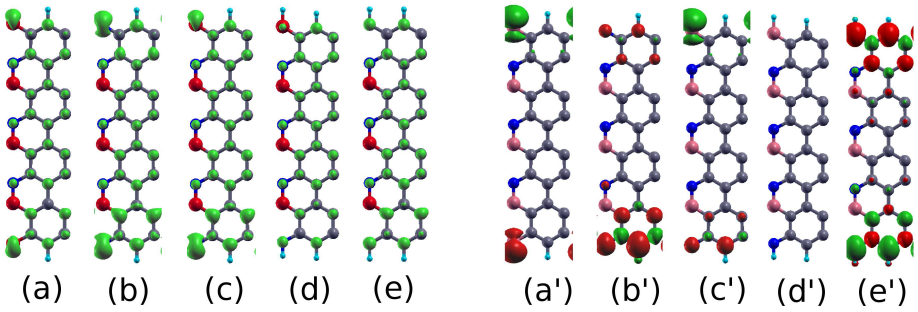

Figure 4.13: Local density of states (left panel) at/near to the Fermi energy and spin density (right panel) of various 8-ZBNCNRs. (a/a′), (b/b′), (c/c′), (d/d′) and (e/e′) correspond to the structure in Fig 4.10

band consist of states localized on B and N edge atoms, respectively, together with major contribution from the edge C atoms. However, for the half-metallic H-passivated C-edged 8-ZBNCNR, pDOS and LDOS analysis reveal that the electronic states at the E_F for minority spin channel and the states closer to the E_F for the majority spin channel mainly arise from edge C atoms along with small contribution from the border atoms.

In order to understand the microscopic origin of intrinsic half-metallicity found in H-passivated C-edged 8-ZBNCNR, we find that there is a charge transfer induced chemical potential differences between the two edge atoms which generates an internal electric field across the ribbon edges. This induced electric field causes the half-metallicity for this 8-ZBNCNR. Here, it is worth to mention that the half-metallic behavior of the pristine ZGNR was only found under a certain external electric field depending on the ribbon width [206].

To examine the width dependency of various ZBNCNRs on their low-energy properties, we have also considered calculating the electronic band structure of nanoribbon with varying widths. For this, we consider three

different nanoribbon widths; namely, 6-ZBNCNR, 10-ZBNCNR, and 12-ZBNCNR and compare and contrast their results with the 8-ZBNCNR. Our results show that all the ZBNCNRs with varying widths preserve both their electronic and magnetic states as obtained for 8-ZBNCNRs, with the only exception found for the H-passivated C-edged ZBNCNR, which shows different electronic states depending on their ribbon widths. All the electronic band diagrams for different widths H-passivated C-edged ZBNCNRs are shown in Fig. 4.14. We find that 6 and 8-ZBNCNRs exhibit half-metallic behavior, while the larger widths ZBNCNRs (10 and 12 zigzag) show metallic character. This can be rationalized as follows: for the smaller width nanoribbons, the induced internal electric field is strong enough to give rise to half-metallic properties, whereas, larger widths ribbons have lesser field density as it decays with the distance, which could induce half-metallicity. However, the edge states become significant which causes metallic behaviors for the larger sized H-passivated C-edged ZBNCNRs.

Since the H-passivated C-edged ZBNCNRs exhibit a range of conduction properties, including metallicity and half-metallicity depending on the ribbon widths, it would be interesting to study the effect of an external electric field on the ribbons electronic properties. Here, we consider applying electric filed in the range of -0.25 $V/\mathring{A}$ to 0.25 $V/\mathring{A}$ on half-metallic 8-ZBNCNRs found at zero electric field. Positive and negative values of electric fields indicate the direction of applied cross-ribbon fields. Since the applied electric field would likely to change the electronic states at and/or near to the E_F, we look at the DOS under different external electric field strengths. The 2D contour plot of the DOS as the function of energy and applied electric field is shown in

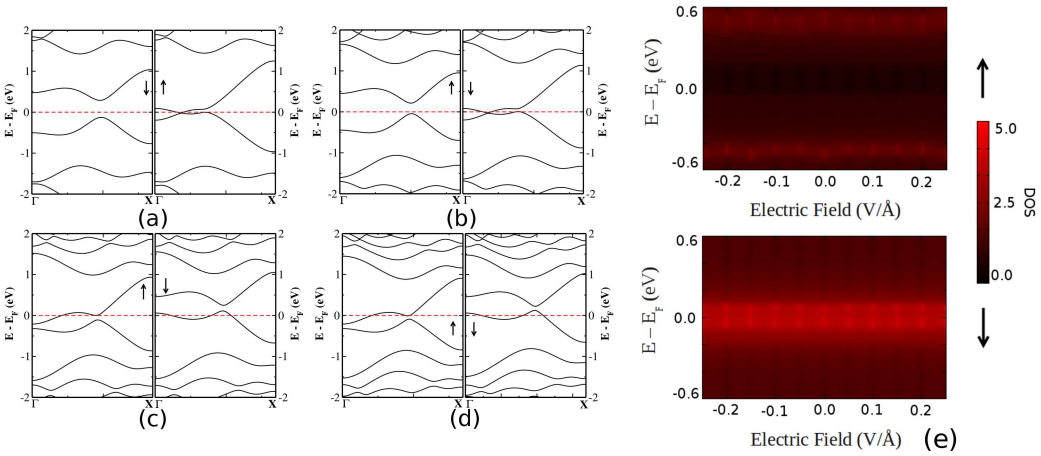

Figure 4.14: Spin-polarized electronic band structures for C-edge H-passivated ZBNCNRs with varying width. (a), (b), (c) and (d) correspond to the band structures of 6-ZBNCNR, 8-ZBNCNR, 10-ZBNCNR and 12-ZBNCNR, respectively. The Fermi level is set to zero. Panel (e) shows the contour plot of the density of states (DOS) as a function of energy, scaled with respect to the Fermi energy, for the insulating (top panel) and conducting (bottom panel) spin channels.

Fig. 4.14 (e). As can be seen from Fig. 4.14 (e), the H-passivated C-edged 8-ZBNCNR maintains its zero field semiconducting gap for the majority spins channel and conducting states for the minority spins channel, when subjected to external electric field of strength 0.25 $V/\mathring{A}$ in any direction. We find that the applied electric field does not alter the zero field half-metallic properties, indicating its robust nature against the external field. We conclude that the intrinsic half-metallic behavior is sustained over a range of applied electric field, suggesting possible application in spintronic devices which functions at finite electric field.

Thus, we have found various interesting results on the H-passivated C-edged ZBNCNRs, which exhibit metallic as well as half-metallic behaviors, depending on the ribbon widths. We have already discussed the results

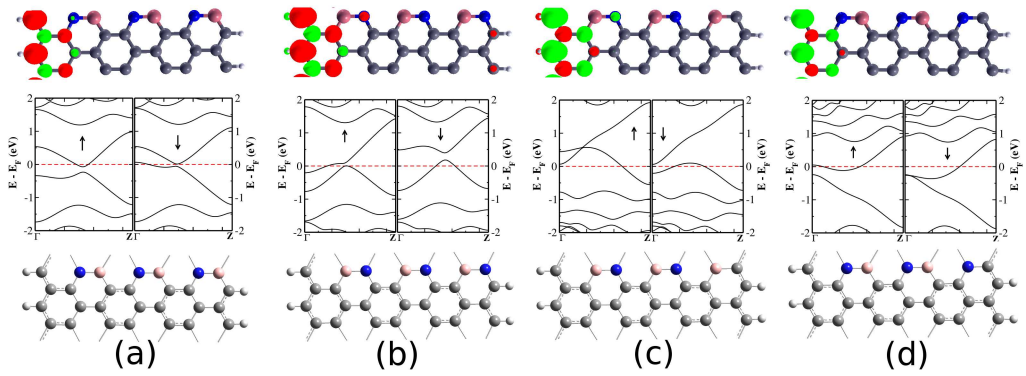

Figure 4.15: The optimized geometry (bottom panel), spin-polarized electronic band structures (middle panel), and spin density (top panel) for H-passivated C-edge 7-ZBNCNRs with different B-N substitutions. (a), (b), (c) and (d) correspond to the different 7-ZBNCNRs, with isoelectronic (a) and (b) to the unsubstituted 7-ZGNR, and hole doped (c) and electronic doped (d) 7-ZBNCNRs. The Fermi level is set to zero.

considering the ZBNCNRs consisting of even number of zigzag chains with different widths (6, 8, 10 and 12 zigzag chains). However, it is really important to examine the nanoribbons properties with odd number of zigzag chains along the width. Thus, we have also considered a few representative ZBNCNRs structures consisting of 7 zigzag chains, *i.e.* 7-ZBNCNRs, with the different B-N substitutions. As shown in Fig. 4.15, we have chosen four 7-ZBNCNRs: structures in (a) and (b) are isoelectronic to the unsubstituted 7-ZGNR, while, (c) and (d) represent the two possible doped systems, hole and electron doped, respectively, because of the presence of excess B and N atoms in (c) and (d) respectively. Note that, all 7-ZBNCNRs structures possess H-passivated C-edges, which are found to be stable compared to any other bare edge nanoribbon structures. Similar to the ZBNCNRs with even number of zigzag chains, all the 7-ZBNCNRs show antiferromagnetic ground state. The electronic band structure calculations have shown that,

all 7-ZBNCNRs show metallic properties, irrespective of the different B-N substitutions (see Fig. 4.15). Moreover, the electronic spins are found to be mainly localized on one of the zigzag edges. The localized spins shows strong preferrence for the H-passivated zigzag C-edge, which does not face direct bonding interactions with the hetero atoms (B and N), and thereby is less perturbed. The calculations have also revealed that, the electronic states at the Fermi energy mainly arise from C atoms of this weakly perturbed zigzag C-edge atoms in 7-ZBNCNRs. The wavefunctions calculated at the Γ-point, show non-symmetric nature close to the Fermi energy, as similar to the asymmetric spin-density distributions. We have attributed this to the symmetry breaking of the ZBNCNRs containing odd number of zigzag chains, while, the nanoribbon structures with even number of zigzag chains show symmetric wavefunctions.

In order to explore the possibility of practical electronic device applications, we study the electronic transport properties of all the 8-ZBNCNRs considered with different edge states. We use Non-Equilibrium Greens Function (NEGF) formalism coupled with DFT to study the transport properties, employing two-probe systems: central scattering region (SR) which is confined between semi-infinite left and right electrodes (LE and RE), as shown in Fig. 4.16 (a). The SR contains three primitive unit cells with a total length of $\sim 15\mathring{A}$. In Fig. 4.16, we present all the spin-polarized transmission functions calculated for all the 8-ZBNCNRs, at zero applied bias voltage ($V_b = 0.0$). To verify and compare, we also calculate the zero-bias spin resolved transmission functions for H-passivated pristine 8-ZGNR and present them in Fig. 4.16 (b). The calculated zero-bias transmission functions (T(E))

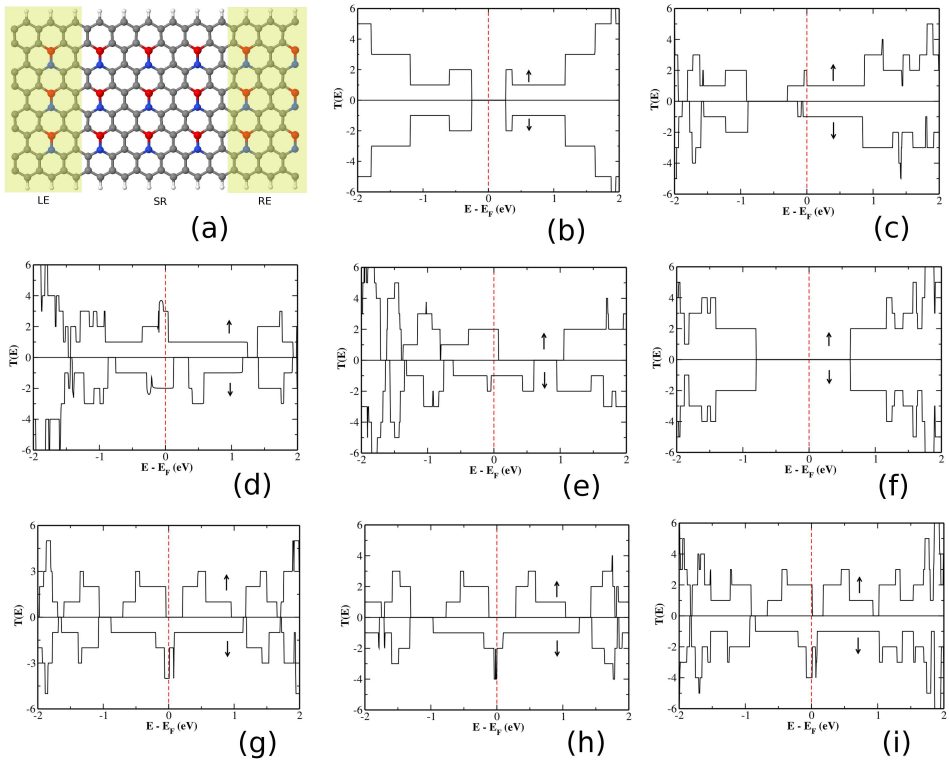

Figure 4.16: Schematic in (a) shows a view of two-probe electrical device modeled from 8-ZBNCNR system. Central scattering region (SR), left and right electrodes (LE and RE) are indicated. Panels in (b), (c), (d), (e), (f) and (g) show spin polarized transmission functions for pristine 8-ZGNR and 8-ZBNCNRs, respectively, with different edge states for the structures, as shown in Fig. 4.10. The spin polarized transmission functions for the 6-ZBNCNR and 10-ZBNCNR with the terminating H-passivated C-edges, are shown in panel (h) and (i), respectively. The Fermi level is set to zero.

for pure 8-ZGNR show step-like behavior with a spin-symmetric semiconducting gap at the E_F, which compares fairly well with the previous DFT and many-body studies [543, 544]. The T(E) also well corresponds to the electronic band structure calculated for 8-ZGNR, as shown in Fig. 4.11 (a). It is clear that the transmissions channel near to the E_F participate in electron conduction under an applied source-drain bias voltage (V_b). As also can be seen from the Fig. 4.16 (c), (d) and (e), the transmissions indicate conducting behaviors for structures with both edges terminated by either bare B or N or B and N atoms (see the structures in Fig. 4.10 (a), (b), (c)). Note that, there are certain sharp peaks and valleys near to the E_F in the calculated transmission functions for these structures, which result from the electron scattering by the bare edge hetero atoms as well as by the middle B and N atoms. The transmission functions shown in Fig. 4.16 (f) for H-passivated B- and N-edged 8-ZBNCNR shows spin-symmetric semiconducting properties as found for pristine 8-ZGNR. The T(E) corresponds to the calculated electronic band diagrams for this structure. More interestingly, we find a fully spin-polarized half-metallic state for H-passivated C-edged 8-ZBNCNR, where the minority spin channels show finite transmission functions, while there is no transmission functions for the majority spin channels at the E_F (see in Fig. 4.16 (g)). Also, note that, the number of sharp peak and valleys have been reduced for all the edge-passivated ZBNCNRs, in comparison to the ribbons with bare edges. Furthermore, it is important to investigate the effect of ribbon width on the calculated zero-bias transmission functions for this intrinsic half-metallic H-passivated C-edged ZBNCNR. Presumably,

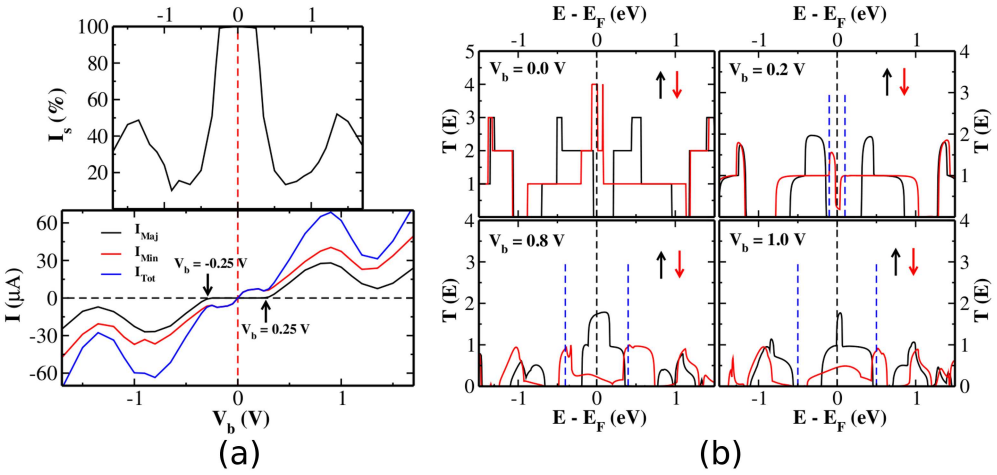

Figure 4.17: I-V characteristic and extent of spin polarization against the applied bias voltages for the 8-ZBNCNR with the terminating H-passivated C-edges (a). Pnael (b) represents spin-polarized transmission functions at different bias voltages. Black and blue dashed lines indicate the Fermi energy (E_F) and bias window, respectively.

we consider calculating transmission functions for two different widths ZB-NCNRs: one with smaller width, 6-ZBNCNR and other with larger width, 10-ZBNCNR. Our results show that the smaller width ribbon (6-ZBNCNR) exhibits strong half-metallic behavior while the larger width 10-ZBNCNR shows a metallic state. Thus, our findings based on calculated zero-bias transmission functions agree fairly well with the band structure calculations (see Fig. 4.11).

As, in practice, all the electronic devices function at finite bias-voltage, we also have calculated the I-V_b characteristics for the H-passivated C-edged 8-ZBNCNR, which is found to be a half-metal. We present the spin-polarized I-V_b curves in bottom panel of Fig. 4.17 (a). As can be seen from the Fig. 4.17 (a), the current carried by the minority spin channels increases with the applied bias voltage (V_b), whereas, the majority spin-current does not show

any finite current up to a critical bias voltage, $V_b^c = \pm 0.25$ V. As we increase the bias voltage V_b, the electric current carried by minority spin channel starts increasing up to a $V_b = 0.19V$, then show decreasing behavior till the bias voltage $V_b = 0.25$ V, reflecting a negative differential resistance (NDR) behavior. Beyond this applied V_b, we find finite currents carried by both the majority and minority spin channels which increase up to a bias-voltage, $V_b = \pm 0.9$ V. Beyond this V_b, the calculated currents show decreasing behavior up to a $V_b = \pm 1.35$ V, for both the spin components, reflecting again a NDR behaviors. When V_b further increases from 1.35 V to 1.8 V, the current starts increasing for both the spin channels. Our results show complete spin-polarized current up to a bias-voltage $V_b = \pm 0.25$ V. To quantify the extent of spin-polarized current, we have calculated spin polarization (I_s) using the euqation (4.5), as was defined earlier. As shown in top panel of Fig. 4.17 (a), we find spin-polarized current for the applied bias-voltage V_b, with 100% spin polarization up to a bias voltage $V_b = \pm 0.25$ V. After that, as the V_b increases, the spin polarization decreases to 13% for $V_b = \pm 0.65$ V, and then, starts increasing up to 50% for $V_b = \pm 1.35$ V, followed by a decrease in spin polarization at higher bias-voltages. Interestingly, we find a symmetric I-V_b characteristics and spin-polarized electric current for both the positive and negative applied bias voltages.

To understand the spin-polarized current and observed NDR behaviors, we analyze the T(E,V_b) calculated at different applied bias voltages ($V_b = 0.0$, 0.2, 0.8 and 1.0 V). We plot the transmission functions at these four V_b in Fig. 4.17 (b). Note that, the transmission coefficients, T(E,V_b), is the function of energy (E) and bias voltage V_b. Thus, the current calculated as an integral

over T(E,V_b), depends on the two factors: the magnitude of transmission coefficients and bias window. As shown in Fig. 4.9 (b) for the V_b = 0.0 V, the transmission coefficients show finite peak values for the minority spin channels, whereas, a gap exists for the majority spin channel. Also note that, there are two available channels above and below the E_F for the majority spin which may conduct the electric current under certain external V_b. When we increase V_b, the electric current first increases and then, starts decreasing at V_b = 0.19 V and continue to decrease up to V_b = 0.25 V, showing first NDR behavior as discussed above. When V_b = 0.2 V, the transmission peaks within the bias window, appear only for the majority spin channel with a decrease in magnitude than the lower V_b, causing NDR, and no transmission coefficients exist for the minority spin channel. An analysis of transmission peaks at V_b = 0.8 V shows that the majority spin channels enter into the bias window, and consequently, start conducting along with the minority spin channels, causing overall increase in the total electric current. A second NDR peak is found at V_b = 0.9 V as mentioned above. A comparison of calculated transmission functions at V_b = 0.8 and 1.0 V reveal that the available transmission peaks become narrower for the larger V_b compared to the smaller V_b (0.8 V), resulting in a significant decrease in the electric current. This explains the second NDR behavior found at higher bias voltage (at V_b = 0.9 V). The similar reasoning holds for the spin-polarized current and NDR found at negative bias-voltages also.

4.4 Conclusions

In summary, we have shown that, the patching of semiconducting and/or insulating B_xN_y nano-domains of various regular shapes and sizes with single-layer graphene can significantly tune the electronic and magnetic properties by modulating its carrier type and concentration and the potential experienced by them, using DFT calculations. Our results have shown that, all B_xN_y nano-domains substituted graphene (h-BN sheet) nano-hybrids are energetically stable compared to any irregular $B_xN_yC_z$ hybrids, and show intermediate structural stability in between that of pristine graphene and h-BN sheets. We have shown that the hybridization of B_xN_y nano-domains with graphene opens up a tunable band gap for electronic devices integration. The geometrical shapes and sizes of B_xN_y nano-domains have significant impact in modulating graphene's (h-BN sheet's) electronic and magnetic properties. Interestingly, the triangular B_xN_y embedded graphene is either an electron doped or a hole doped system depending on the excess of B or N content in the embedded nano-domain, whereas, all the other B_xN_y substituted graphene hybrids are the iso-electronic with graphene. Our findings have shown that all the hybrid $B_xN_yC_z$ systems, exhibit nonmagnetic semiconducting band structures except for the triangular shaped B_xN_y substituted graphene, which stabilizes in either non-magnetic or magnetic ground states depending on the triangular nano-domain geometries and sizes with finite magnetic moments for the later. We also found that the finite magnetic moment of these magnetic nano-hybrids mainly arises from the border C atoms due to the charge

redistribution induced by the charge transfer effects. This can also be accounted for the presence of partially occupied spin asymmetric mid-gap states in between valence and conduction bands originating due to the imbalance in A-B sublattice picture. Interestingly, we found that, all the T_a-B_xN_y substituted graphene nano-hybrids exhibit a conducting ground state because of the presence of mid-gap states which appear at the Fermi level. We also found a nonmagnetic metallic as well as nonmagnetic semiconducting states for smaller T_b-B_xN_y domains size and a spin-polarized metallic and half-metallic ground states with full control over the spin components for larger nano-domains size with B- and N-termination, respectively.

Moreover, the results obtained from the hybridized zigzag graphene and zigzag boron nitride nanoribbons have shown the tunable electronic states depending on the position of their components, zigzag C-C and B-N chains. We have found a robbust half-metal, for the 8-ZGNR-BN, *i.e.*, a zigzag edge graphene nanoribbon with the middle C-C zigzag chains substituted by isoelectronic B-N chains. Additionally, the calculations have also shown that, this nanoribbon structure can be used to fabricate an electrical device, which operates under the finite source-drain bias voltages. Most interestingly, this electrical device exhibits 100% spin-polarized currents within a small ($V_b = \pm 0.52$ V) range of bias voltages.

Further, we have demonstrated the interesting electronic structures of BN-fused polyacene zigzag graphene nanoribbons. Our results have shown that, depending on the edge atom types and passivation nature, the nanoribbons exhibit metallic, semiconducting and half-metallic behaviors. We have

also shown that, the half-metallic properties is robust under the small external cross-ribbon electric fields. Interestingly, our electrical transport calculations have revealed a spin-polarized electrical currents as well as negative differential resistance behaviors with the change in source-drain bias voltage.

The results discussed here, suggest a huge possibilities for spintronic device applications in these reduced dimensions. Moreover, given the recent progress on synthesizing phase separated $B_xN_yC_z$ nano-hybrid, we believe that, the possibilities presented here may become a part of the experimental development in the field of boron-carbon-nitrogen-based nanoelectronics.

Chapter 5

Decorating Graphene and Hexagonal Boron Nitride with Metals and Metal Clusters*

5.1 Introduction

Low-dimensional materials, such as two-dimensional (2D) graphene and its hexagonal boron nitride analogue (h-BN sheet) have garnered tremendous research interest due to their unsual mechanical, electronic and transport properties [182, 406, 475, 545]. Graphene and h-BN sheet are crystalline materials composed of sp^2 hybridized carbon, boron and nitrogen atoms, respectively, tightly packed into a honeycomb lattice. Exceptional electronic properties

*Work reported in this chapter is published in: (a) K. S. Subrahmanyam, Arun K. Manna, Swapan K. Pati and C. N. R. Rao, *Chem. Phys. Lett.* **497**, 70 (2010); (b) Arun K. Manna and Swapan K. Pati, *Book Chapter, World Scientific Publishing Co. Pte. Ltd. Singapore* **ISBN: 13-978-981-4329-35-4**, 59 (2011); (c) Arun K. Manna and Swapan K. Pati (submitted, 2013)

and their desired tunability made graphene a suitable candidate for the successful replacement of high-cost silicon based electronic devices [546, 547]. Since the single-layer graphene is a zero band gap semiconductor, *i.e.*, a semi-metal with vanishing density of states (DOS) at the charge neutrality point, and its isoelectronic boron nitride analogue, h-BN sheet, is a large band gap insulator, thus, both the candidates have limitations for direct applications in electronic devices [182, 548].

In order to utilize these graphitic materials for electronic applications, several methods have been proposed theoretically and a few of them have been successfully materialized by experimental methods [210, 213, 214, 249, 253, 254, 541, 549]. It has been demonstrated that a mixture of boron, carbon and nitrogen atoms with varying compositions could indeed open up a gap at the charge neutrality point whose magnitudes strongly depends on the position and amount of each species present in these hybrid materials, known as BCN [249, 253], as also discussed in chapter 4. Another very interesting way of engineering band gap is by creating some pore in these graphitic sheets, known as nanoporous carbon or antidot lattice, where the size and shape of the pores would determine the band gap values [525, 547]. On the other hand, one can move from 2D graphene and h-BN to their quasi-one-dimensional nanoribbon structures to design the band gap values.

All the methods mentioned above are eventually destructive in the sense that one cannot restore the parent materials, *i.e.* pristine graphene and h-BN sheet for the purpose of futuristic usage. Aiming in tailoring the electronic and magnetic properties of these 2D sheets, the researchers have demonstrated that, the surface adsorption of external species, which include various

gas molecules, metal atom and small metal nanoclusters, etc. has potential impact in tuning their electronic properties [477, 495, 550–555]. Along these lines, the surface adsorption of electron donor and acceptor molecules on these 2D sheets has been proved to be an effective way of modulating the electronic structure of graphene and h-BN sheets induced by the molecular charge transfer [402, 492, 493]. On the other hand, surface adsorption of various metal atoms and a few atom metal nanoclusters can hold a great promise in controlling electronic and magnetic properties of graphene and h-BN sheet. However, the consideration of transition metal and metal nanoclusters possessing vacant d-orbitals, adsorbed on graphene and h-BN sheets would be a promising approach in order to control both the charge and spin degrees of freedom in the composites. Earlier studies mainly considered the interaction of single or a few atoms transition metal nanoclusters deposited on these 2D sheets. However, the electronic and magnetic property of the 2D graphene and h-BN sheet, including both the pristine and porous sheets, strongly depends on the sizes of the adsorbed transition metal nanoclusters. So far, the consideration of larger cluster sizes was not undertaken in the previously reported studies. Even if there is no systematic study which could compare and unravel the interaction driven changes in electronic and magnetic properties of graphene and h-BN sheets in presence of different metals and metal clusters.

In this chapter, we have mainly described the effect of external metals and their clusters on the modification of electronic properties of a pure monolayer 2D graphene and a pristine h-BN sheet, using first-principles density functional theory calculations. We have chosen a few representative metals and

metal clusters from the first-row transition metals (Fe, Co, Ni) and the bulk non-transition metals and metal clusters (Pd, Ag, Pt and Au) consisting of 40 atoms embedded on graphitic surface for modeling the metal nanoclusters interactions. Additionally, we have also investigated the electronic properties of porous graphene and h-BN sheets. The present demonstration has also shown the effects of magnetic metal (Fe) impurity on these porous sheets properties. It is found that, the chemical nature of the embedded metals and metal clusters on graphene and h-BN sheets, plays a key role in changing their intriguing electronic structure. The study suggests a diverse electronic as well as magnetic properties for these sheets decorated with metals and metal clusters, depending on the chemical nature of the sheets, and the embedded metals and metal clusters.

5.2 Computational Methods

The first-principles calculations are carried out using the linear combination of atomic orbital density-functional theory (DFT) methods implemented in the SIESTA package [349, 350]. The generalized gradient approximation (GGA) in the Perdew-Burke-Ernzerhof (PBE) form [389] and double ζ polarized (DZP) basis set are chosen for the spin-polarized DFT calculations. The interaction between ionic cores and valence electrons is described by norm conserving pseudopotentials [390] in the fully non-local Kleinman-Bylander form [391]. All the structures are relaxed until the maximum atomic forces are smaller than 0.04 eV$\mathring{A}^{-1}$. A 400 Ry mesh cutoff is used and the Brillouin zone sampling is done using $10 \times 10 \times 1$ Monkhorst-Pack k-points.

We have considered (4 × 4) supercell containing 64 carbon (32 B and 32 N) atoms of pristine graphene (h-BN) sheet for modeling the single metal dopant adsorption on 2D graphene. For modeling the graphene and h-BN sheets decorated with the metal clusters, we have chosen a 8 × 8 supercell, which contains 128 atoms (128 C atoms of the graphene, while, 64 B and 64 N atoms for the h-BN sheet).

5.3 Results and Discussions

Possessing many exotic and interesting properties and the possibilities of their modulation in a controlled manner, the 2D graphene and h-BN sheets have been of great research interest in recent years. There are many potential modification routes to increase their device applicability. In this chapter, we have described the effect of metals, including both the transition metals and non-transition metals and their clusters (*i.e.*, embedding a few representative novel metals and metal clusters of Fe, Co, Ni and Pd, Ag, Pt and Au with sufficiently large number of atoms (40)) to explore its responses on the electronic structure and magnetic properties of these 2D sheets. Additionally, we have also discussed the intrinsic electronic structures of porous graphene and h-BN sheets and their modification by the presence of magnetic atom. Our results have suggested that, the magnetic ordering in these 2D sheets can be switched from low-spin to high-spin states or vice versa by simply varying the chemical nature of the substrate sheet. Moreover, the present inventigations have also suggested a few efficient routes to engineer band gaps in these two-dimensional sheets, which would open up new avenues for

optoelectronic device applications.

5.3.1 Transition Metals and Metal Clusters on Graphene and h-BN Sheets

Here we have described the electronic structures of transition metals (Fe, Co, Ni) and metal clusters (Fe_{40}, Co_{40}, Ni_{40}) decorated graphene and h-BN sheets using DFT. We have focused on the preferred adsorption site for the metal atom, adsorption energy and the modification of the sheet electronic structures. First, we will address the adsorption of each of these single transition metal atom on the two-dimensional sheets considered. To this end, we have considered 4×4 supercell of graphene and h-BN sheet with the presence of single metal atom. Note that, there are three possible adsorption sites in graphene for the metal atoms. They include hexagonal ring center (H), atom center top (T) and on top of a C-C bond, *i.e.*, bridge side. For the h-BN sheet, unlike all the identical C atoms in graphene, there are two different atoms (B and N) on the two different sublattice points. Consequently, metal atom can sit either on top of a B atom (T_B) or on top of a N atom (T_N). All possible adsorption sites are pictorially shown in Fig. 5.1.

To find the stable adsorption sites on these graphitic sheets, we have fully optimized the structures of graphene-metal complexes without any geometry constraint using spin-polarized DFT calculations. Further, to assess the stable adsorption sites, we have defined the adsorption energy (E_d), which is

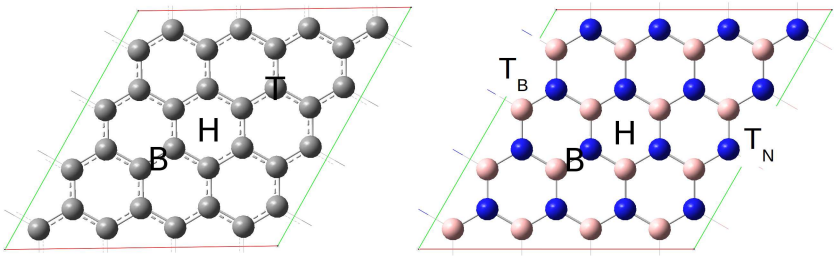

Figure 5.1: Possible adsorption sites for the metal atom doposited on graphene (left panel) and h-BN (right panel) surface. H, B, and T (T_N and T_B in h-BN) indicate the ring center hollow site, bridge site between the two bonded atoms and atom centered top site.

Table 5.1: Binding energies and magnetic moments of all graphene-M complexes for various adsorption sites of metal atoms.

Composites	E_d (eV)	μ_B	Composites	E_d (eV)	μ_B
Graphene@Fe	-2.11 (H), -2.10 (B), -0.10 (T)	2.38 (4.00)	h-BN@Fe	-0.21 (H), -1.05 (B), -1.18 (T_B), -1.18 (T_N)	4.00 (4.00)
Graphene@Co	-3.21 (H), -3.19 (B), -2.36 (T)	1.44 (3.00)	h-BN@Co	-2.17 (H), -1.91 (B), -2.17 (T_B), -1.91 (T_N)	3.00 (3.00)
Graphene@Ni	-2.98 (H), -2.95 (B), -2.38 (T)	0.00 (2.00)	h-BN@Ni	-1.63 (H), -2.18 (B), -1.57 (T_B), -2.20 (T_N)	0.00 (2.00)

estimated using the following relation:

$$E_d = E_{graphene@M/h-BN@M} - E_{graphene/h-BN} - E_M(M = Fe, Co, Ni) \quad (5.1)$$

where $E_{graphene@M/h-BN@M}$ and $E_{graphene/h-BN}$ are the total optimized energy of the metal decorated graphene/h-BN composite and of the isolated graphene/h-BN sheet, respectively. The E_M indicates the total single-point energy of an isolated metal (M) atom when present within the same supercell. All results are given in Table 5.1.

From the optimized structures and corresponding asdorption energy values, we have found that, each of the three transition metal finds graphene

hexagonal ring center hollow (H) position as the stable adosrption site. On the other hand, for the h-BN sheet, only Co finds hollow site as the minimum energy adsorption configuration, whereas, the Fe and Ni atoms reside on top of a N atom (T_N). The adsorption energy values corresponding to the stable position of the Fe, Co and Ni on graphene are -2.11 eV, -3.21 eV and -2.98 eV respectively. The E_d values are found to be -1.18 eV, -2.17 eV and -2.20 eV for Fe, Co and Ni adsorption on h-BN sheet for their minimum energy structures. Note that, large negative E_d value indicates strong adsorption of metal atoms. Our results show that, the adsorption strength is higher for the graphene than the h-BN sheet for these metal atoms considered. In graphene, each C atom possesses one unhybridized p_z electron. So, there are total six p_z electrons available in a hexagonal graphene ring. These six p_z orbitals of graphene strongly hybridize with the transition metal d-orbitals, making a η^6 coordination. This results in the large negative adsorbtion energy for the hollow site coordinations for these transition metals. However, for the h-BN sheet, the p_z eletrons delocalization is absent, and the electrons are completely localized on the B and N sites due to the p_π-p_π electron back donation. This also explains why the h-BN sheet is a strong insulator, while, its isoelectronic analogue, graphene is a semi-metal. Because of this electron localization and the large electronegativity of N atom, the transition metals (Fe and Ni) find N atom top (T_N) position as the stable adsorption sites. However, the Co finds hollow (H) position as the minimum energy adsorption site. It is also found that, Co shows the higher adsorption strength for the graphene, while, Ni exhibits more affinity for the h-BN sheet, among all the three metals. It is also clear from Table 5.1, the difference in adsorption

energy among three metal atoms on the h-BN sheet for their minimum energy configurations is small (∼30 meV). This suggests that, the h-BN sheet is less selective to these metal atoms than graphene. The distance of adsorbed metal atom from the plane of the graphene/h-BN sheet is found to be between ∼1.5 and ∼2.0 $\mathring{A}$, depending on the types of metals. The calculations have also shown that, the Fe and Co adsorption on graphene lead to the magnetic states, where the finite magnetic moments mainly come from the adsorbed metal d-orbitals. However, Ni adsorbed graphene composite predicts a nonmagnetic electronic state with zero magnetic moment. It is clear that, the magnetic moments decrease in these graphene-M complexes in comparison to the moments found for the bare metal atoms. This is because, the electron transfer from graphene to the metal partially reduces the number of available unpaired electrons on the metal d- orbitals, and thereby, decreasing their magnetic moments. Note that, the effect is very strong for the Ni adsorbed graphene, where the system exhibits zero magnetic moment. Our results agree well with the previous findings [556–558].

Next, we investigate the electronic band structures of the transition metal atom decorated graphene and h-BN sheets. For this, we have only considered the minimum energy structures as discussed above. The electronic band diagrams and the corresponding density of states (DOS) along with the projected density of density of states (pDOS) are shown in Fig. 5.2. As can be seen, the graphene with adsorbed Fe and Co show spin-polarized metallic state, whereas, a nonmagnetic zero band gap semi-metallic electronic state is found for the graphene-Ni system. However, all the h-BN with the adsorbed transition metals exhibit spin-polarized semiconducting state with varying

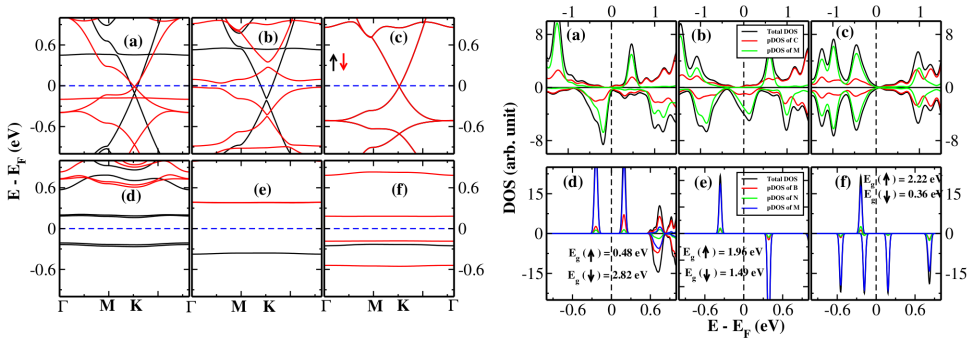

Figure 5.2: The electronic band structures (left panel) of graphene (top pannel) and h-BN (bottom panel) sheets with the adsorbed transition metal ad-atoms (Fe, Co, Ni). The corresponding electronic DOS (in right panel) of these composites. (a), (b) and (c) correspond the graphene-Fe, graphene-Co and graphene-Ni, while, (d), (e) and (f) indicate hBN-Fe, hBN-Co and hBN-Ni, respectively. The energy is scaled with respect to the Fermi Energy (E_F). The up and down arrows indicate the majority and minority spin channel, respectively.

band gaps for the two spin channels. As also can be seen from Fig. 5.2, there are a few flat bands near to the Fermi energy (E_F), which mainly arise from the adsorbed metal atom orbitals. The flat bands essentially indicate the localized electronic states, where, the electron possesses an infinite effective mass. The electronic conduction is greatly hindered by these localized states due to the electron back scattering. However, the presence of these massive electronic states below and above the Fermi energy, eventually, decreases the band gaps of the h-BN sheets, which is a wide band gap insulator. Thus, the transition metal decorated h-BN composiites may find applications in semiconductor devices.

In practice, during the experimental growth of graphene-metal composites, a number of metal atoms would have tendency to form small metal clusters of varying sizes. In particular, there are reports of various metal nanoparticles (metal cluster of nanometer dimensions) growth on graphene surface. Undoubtedly, it is of great importance to investigate the electronic structures and the magnetic properties of these metal cluster deposited graphene and h-BN sheets. Here, we have studied the structures and electronic properties of graphene and h-BN sheets decorated with sufficiently large metal clusters, *i.e.*, M_{40} (M = Fe, Co and Ni), which are possible to handle within our computational efforts. We have chosen the metal clusters, which were energy minimized using the Sutton-Chen 12-6 potentials [559] for the initial structural guess. Spin-polarized DFT, as implemented in SIESTA code is used to fully relax the cluster geometry. We have considered a 8×8 supercell of graphene and h-BN sheets with these metal clusters initially placed at about 3.0 $\mathring{A}$ above the sheet planes. All geometry optimizations and the electronic structure calculations of these graphene-M_{40} composites are performed using spin-polarized DFT methods. In order to study the adsorption strength, we have calculated the binding energy of the metal clusters on these 2D sheets using the following relation:

$$E_b = E_{graphene/h-BN@M_{40}} - E_{graphene/h-BN} - E_{M_{40}}(M = Fe, Co, Ni) \quad (5.2)$$

where $E_{graphene/h-BN@M_{40}}$, $E_{graphene/h-BN}$ and $E_{M_{40}}$ are the total energy corresponding to the optimized geometry of graphene/h-BN@M_{40} composite and isolated graphene/h-BN and M_{40}, respectively. As is clear from the above

Table 5.2: Binding energies, magnetic moments per metal and electron transfer (ET) of all graphene-M_{40} and h-BN@M_{40} complexes. In ET values, +ve (-ve) sign indicates the electron transfer from the sheet (metal cluster) to the metal cluster (sheet). $I.E_v$ ($I.E_a$) and $E.A_v$ ($E.A_a$) represent the vertical (adiabatic) ionization energy and electron affinity of bare M_{40} cluster in eV, respectively.

Composites	E_b (eV)	μ_B	ET	Composites	E_b (eV)	ET (e)	μ_B	$I.E_v$ ($I.E_a$)	$E.A_v$ ($E.A_a$)
Graphene@Fe_{40}	-5.22	2.85 (2.85)	2.65	h-BN@Fe_{40}	-2.22	0.73	2.85 (2.85)	4.70 (4.69)	-2.42 (-2.43)
Graphene@Co_{40}	-2.79	1.85 (1.85)	1.97	h-BN@Co_{40}	-1.35	0.68	1.85 (1.85)	5.16 (5.15)	-2.81 (-2.82)
Graphene@Ni_{40}	-0.96	0.86 (0.85)	-0.07	h-BN@Ni_{40}	-2.98	-0.20	0.85 (0.85)	4.31 (4.31)	-1.80 (-1.81)

relation, higher the negative binding energy value, greater is the stability for the complexes. All results are provided in Table 5.2.

As can be seen, Fe_{40} binds strongly with the graphene, while, Ni_{40} shows least binding affinity for the graphene sheet among the metal nanoclusters considered. The binding strength order follows as: $Fe_{40} > Co_{40} > Ni_{40}$. We have found a significant amount of electron transfer from the graphene to the Fe_{40} and Co_{40} clusters. This suggests, the importance of electrostatic interactions, among many other scales of interactions, such as van der Waals and multipoles, for the stability of these graphene-M_{40} complexes. However, the magnetic moments of these composites does not show any change with respect to the moments found for the bare metal nanoclusters. The Ni_{40} nanocluster, which has less binding affinity for the graphene, show greater binding strength for the h-BN sheet. However, other two graphene-M_{40} (M = Fe, Co) nanocomposites have moderate binding energy. Our results have also revealed that, there are small charge transfer interactions, as reflected from the small amount of electron transfer from the h-BN to Fe_{40} and Co_{40}. In fact, for Ni_{40}, the charge transfer is quite small (-0.20 e). This is also found

for the graphene decorated with Ni_{40}. Also, note that, for both the graphene and h-BN sheets, the direction of electron transfer is totally reversed for the Ni_{40} metal nanocluster (see Table 5.2). The direction and extent of electron transfer is consistent with the ionization energy and electron affinity values of the bare metal clusters (see Table 5.2). The electron transfer to these adsorbed metal nanoclusters suggests that, these metal nanoparticles adsorbed on graphene and h-BN sheets may possess some catalytic activity. In fact, the metal nanocluster deposited graphene hybrids were shown to have enhanced catalytic activity for many reactions occuring on the nanocluster surfaces [560–564].

To understand the changes in electronic structures of these 2D sheets, we have calculated the spin-polarized electronic density of states (DOS) for all these M_{40} nanoclusters complexed with graphene and h-BN sheets separately. We have provided the DOS and projected density of states (pDOS) of these complexes in Fig. 5.3. As shown in the figure, all the systems are found to be metals with large spin-polarization at the Fermi energy. The extent of spin-polarization is found large for the h-BN than the graphene, when decorated with the metal nanoclusters. The pDOS analysis reveals that, the electronic states at and near to the Fermi energy, mainly come from the metal d-orbitals. To note, the single-layer graphene is a zero band gap semiconductor, while, the mono-layer of h-BN is a wide band gap insulator. Also, both pristine graphene and h-BN sheets have zero net magnetic moments. However, the presence of these metal nanoparticles on these 2D substrates lead strong spin-polarized systems, which may find applications in memory devices.

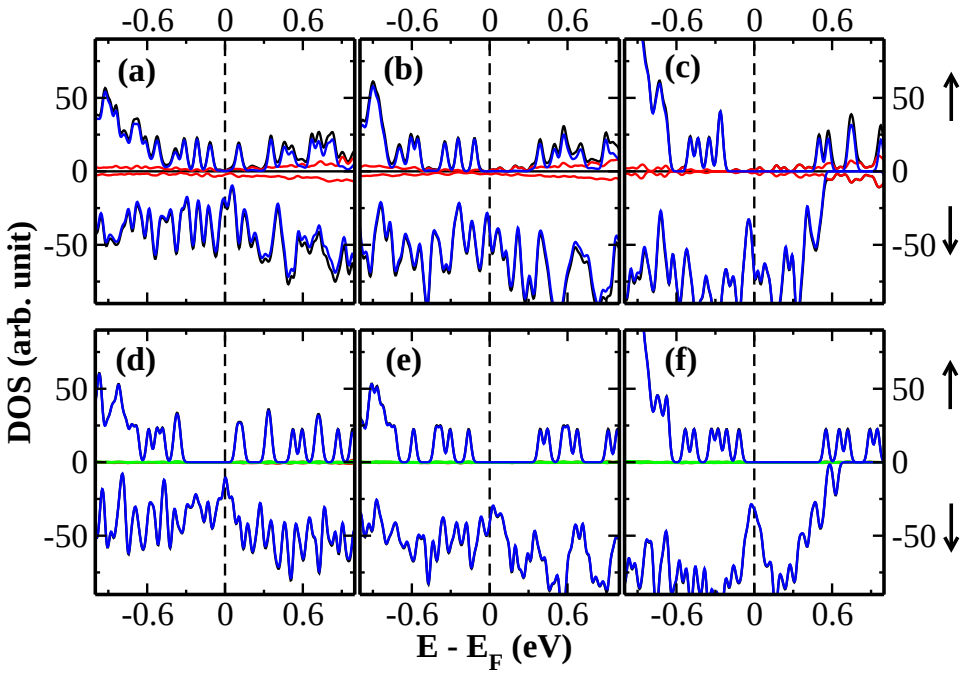

Figure 5.3: The electronic density of states (DOS) of graphene (top pannel) and h-BN (bottom panel) sheets with the adsorbed transition metal clusters M_{40} (M = Fe, Co, Ni). The black, red and blue color lines correspond to the total DOS and pDOS of graphene and adsorbed M_{40} (top panel). For the bottom panel, the black, red, green and blue lines indicate the total DOS and pDOS of B, N and M_{40}, respectively. The energy is scaled with respect to the Fermi Energy (E_F). The up and down arrows indicate the majority and minority spin channel, respectively.

Table 5.3: Binding energies and magnetic moments of all graphene@M and h-BN@M (M = Pd, Ag, Pt, Au) complexes for the different adsorption sites.

Composites	E_d (eV)	μ_B	Composites	E_d (eV)	μ_B
Graphene@Pd	-2.18 (H), -2.22 (B), -2.17 (T)	0.00 (0.00)	h-BN@Pd	-1.49 (H), -1.61 (B), -1.40 (T_B), -1.61 (T_N)	0.00 (0.00)
Graphene@Ag	-1.67 (H), -1.69 (B), -1.67 (T)	0.55 (1.00)	h-BN@Ag	-1.49 (H), -1.52 (B), -1.52 (T_B), -1.52 (T_N)	1.00 (1.00)
Graphene@Pt	-2.67 (H), -3.24 (B), -3.23 (T)	0.18 (0.00)	h-BN@Pt	-2.61 (H), -2.11 (B), -1.83 (T_B), -2.61 (T_N)	0.00 (0.00)
Graphene@Au	-1.01 (H), -1.32 (B), -1.37 (T)	1.24 (1.00)	h-BN@Au	-1.21 (H), -1.36 (B), -1.34 (T_B), -1.37 (T_N)	1.00 (1.00)

5.3.2 Non-Transition Metals and Metal Clusters on Graphene

In the previous section, we have discussed the effects of transition metals and metal clusters on the changes in electronic and magnetic properties of graphene as well as h-BN sheets. It would really be interesting to study the effects of non-transition metals, such as Pd, Ag, Pt and Au, and how these modify these sheets electronic structures. Thus, we have considered investigating the favourable adsorption site and electronic properties of the graphene and h-BN sheets in presence of these non-transition metals on the 2D surfaces. We have used spin-polarized DFT calculations as used for the studies discussed above. We have estimated the adsorption energy (E_d) for the graphene@M and h-BN@M composities using the relation already mentioned in the previous section, for understanding their stability and the preferred adsorption sites. The results are presented in Table 5.3.

As given in Table 5.3, the metal atoms find C-C bridge (B) position for the stable adsorption sites on graphene except for the Au, which is stabilized on the C atom top position (T). This is completely different from the preferred adsorption sites (H) found for the transition metal adsorption, as

already discussed in the previous section. To understand this difference in adsorption preferrence, we look at the sizes and valence electronic configuration of these metal atoms. Unlike the small transition metal atoms (Fe, Co, Ni) considered, the non-transition metals (Pd, Ag, Pt, Au) have large atomic radii. Moreover, the valence electrons of these non-transition metals are of "s" type, which is spherically symmetric. This is in contrast to the more diffused valence d-orbitals present in transition metals. Because of the larger sizes and the presence of outer most "s" orbitals, these non-transition metals (Pd, Ag and Pt) stabilize at the bridge center of a C-C bond in graphene. Moreover, we have found a small amount of electron transfer from the graphene to the adsorbed metal atoms. In contrast to this, Au, being more electropositive among the metals considered, a small amount of electron is transferred to the graphene from the Au atom. Our results have shown that, the Pt adsorbs strongly to the graphene surface, whereas, the less adsorption strength is found for the Au atom. This is because of the large charge transfer found for the Pt adsorbed graphene compared to the other graphene-metal complexes. For the h-BN, the most preferred adsorption site is found to be the N atom top (T_N) center for all the four metals considered. Interestingly, Pt shows large negative adsorption energy, indicating strong binding to the h-BN sheet, while, less negative adsorption energy is obtained for the Au. This is similar to the binding strength found for these metal atoms adsorption on graphene. Moreover, we have found that, Au shows similar adsorption energy for both graphene and h-BN sheet (see Table 5.3). All other metal atoms strongly bind to the graphene in comparison to the h-BN. The calculations have also shown that, the adsorption of

Ag and Au on graphene and h-BN sheets results in spin-polarized electronic states with small magnetic moments (0.55 μ_B for graphene-Ag and 1.24 μ_B for graphene-Au). Note that, both Ag and Au possess one unpaired electron in their valence "s" electronic shell. Adsorption of these metal atoms on graphene causes the redistribution of electronic charges on these metal atom orbitals as well as on the graphene C p_z orbitals. This results modify the magnetic moments. However, the charge transfer effect is negligible for the adsorption of these metal atoms on h-BN sheet. Therefore, the atomic spin moment (1 μ_B for Ag and Au) does not change for the Ag and Au decorated on h-BN (see Table 5.3).

Next, we have investigated the electronic structure of these non-transition metals decorated graphene and h-BN sheets. The spin resolved electronic band structures are given in Fig. 5.4. Our results predict a metallic state for the graphene adsorbed Ag ad-atom. On the other hand, we have found small band gaps for other three metals (Pd, Pt, Au) adsorption. This suggests a semimetal to semiconductor transition due to the strong adsorption of these metal atoms, which breaks the local structural symmetry. The induced band gap values are indicated in Fig. 5.4. However, the h-BN sheet decorated with all the four metals, separately, show semiconducting state with varying band gap values (see Fig. 5.4).

To understand the effects of large clusters consisting of non-transition metals, we have also considered clusters of 40 nuclearity (M_{40}) for investigating the graphene-M_{40} systems. Here, we have studied the two dimensional periodic arrays of metal clusters deposited on graphene. The initial structural guess for the metal clusters is modeled by Sutton-Chen 12-6 potentials [559].

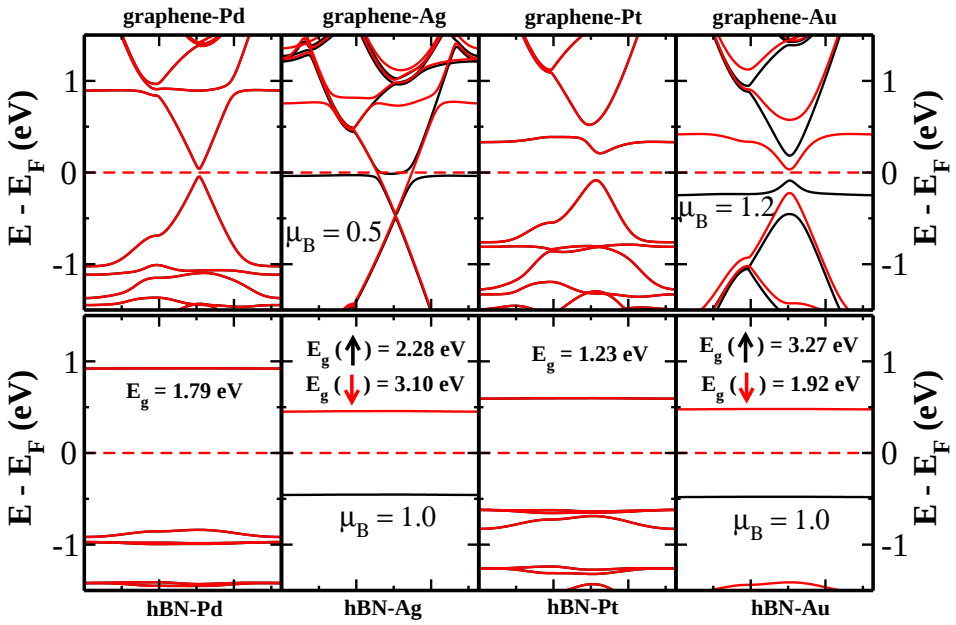

Figure 5.4: (Color online) The electronic band structures of graphene (top pannel) and h-BN (bottom panel) sheets with the adsorbed non-transition metal ad-atoms. The energy is scaled with respect to the Fermi Energy (E_F). The up and down arrows indicate the majority and minority spin channel, respectively.

Table 5.4: Summary of results for metal nanoclusters deposited on graphene. The +ve (-ve) sign indicates the electron transfer from graphene (metal cluster) to metal cluster (graphene). The R_{eq} and C.T represent the equilibrium distances of separation and amount of charge transfer, respectively. $I.E_v$ ($I.E_a$) and $E.A_v$ ($E.A_a$) represent the vertical (adiabatic) ionization energy and electron affinity of bare M_{40} cluster in eV, respectively.

Nanocomposites	R_{eq} (Å)	ΔE_{stab} (eV)	ΔE_{form} ($\Delta E_{form}{}^c$) (eV)	C.T (e)	$I.E_v$ ($I.E_a$)	$E.A_v$ ($E.A_a$)
Graphene@Pd_{40}	2.33	-4.74	-3.70 (-3.58)	3.62	5.78 (5.76)	-3.54 (-3.55)
Graphene@Ag_{40}	2.45	-2.19	-2.45 (-2.40)	2.00	4.68 (4.68)	-2.48 (-2.51)
Graphene@Pt_{40}	2.35	-2.86	-6.14 (-6.07)	2.41	6.82 (6.60)	-4.10 (-4.03)
Graphene@Au_{40}	2.83	-1.91	-4.13 (-4.03)	-0.17	4.10 (4.10)	-1.49 (-1.54)

The relative stability of the metal nanoclusters embedded on graphene surface (i.e., graphene@M_{40}) is determined by the stabilization energies (E_{stab}) or the so-called binding energy, calculated using equation (5.3). As is well known, the larger the stabilization energy, the stronger is the binding of the guest cluster to the graphene surface. The stabilization energy per deposited metal cluster is calculated by subtracting the energy of the optimized isolated cluster of nuclearity 40, E(M_{40}) and the optimized equilibrium energy of the graphene supercell, E(graphene), from the total energy of the optimized composite systems, E(graphene@M_{40}):

$$\Delta E_{stab} = E_{graphene@M_{40}} - E_{graphene} - E_{M_{40}} \tag{5.3}$$

A summary of the results for the optimized structures for all four complexes is provided in Table 5.4.

We too have calculated the formation energies (E_{form}) per metal atom defined in equation (5.4 and 5.5) of these metal nanoclusters in presence as well as in absence of graphene to focus on the feasibility of spontaneous formation of clustering from constitutional atomic metal moiety under suitable experimental conditions. Our results indicate that the formation energy is slightly increased in presence of graphene, acting as a catalyst, relative to the free metal clustering.

$$\Delta E_{form} = [E_{graphene@M_{40}} - E_{graphene} - 40 * E_{M_{40}}]/40 \tag{5.4}$$

$$\Delta E^{c}_{form} = [E_{M_{40}} - 40 * E_{M}]/40 \tag{5.5}$$

where the $E(M_{40})$ and E(M) are the energies of optimized metal nanocluster and of a single metal atom, respectively.

From the fully optimized geometries, we find that the shortest separation between a metal atom of the deposited metal cluster and the closest carbon atom of the graphene layer for the graphene@M_{40} complexes are between 2.3 $\mathring{A}$ and 2.8 $\mathring{A}$ (see Table 5.4). Also as given in Table 5.4, the relative stabilization energies are higher in magnitude for Pd, Ag, Pt clusters embedded graphene complexes compared to the Au_{40} cluster which clearly indicates a relatively weak interaction between the Au nanoparticles and the graphene in comparison to others. The relatively higher binding energies combined with smaller equilibrium distances of separation dictate that all three (Pd, Ag, Pt) metal clusters do eventually adsorbed strongly on the graphene surface, inducing local structural deformation. An analysis of the Mülliken population suggests that there is an effective charge transfer between the adsorbed metal

cluster and graphene. For the Pd, Ag, and Pt cluster deposition, the charge transfer occurs from graphene to metal cluster at their equilibrium distances of separation, while for Au nanoclusters, the direction of charge transfer is from metal cluster to graphene. It is also clear from Table 5.4 that the extent of charge transfer for Pd, Ag, Pt nanocluster is larger compared to that for the Au cluster with greater extent of charge transfer for Pd case, resulting in higher stabilization energy. To understand this, we have computed the vertical as well as adiabatic first ionization energy (I.E) and electron affinity (E.A) of individual metal clusters. Both the I. E and E. A values computed with the two different strategies follow the similar trend and can be analyzed to understand the extent of charge transfer. We find that the trend in extent of charge transfer which determines the overall stabilization energy of the complexes follow the same pattern in changes in either I. E or E. A of the metal clusters belonging to a particular period in the periodic table. In contrast to Pd, Ag, Pt clusters, the comparatively smaller magnitude of E. A. together with relatively lower value of I.E make the Au_{40} cluster to act as weak electron donor when adsorbed on graphene.

In order to understand the mechanism and the extent of charge transfer, we have calculated the energy and difference in charge densities of the composites by varying the distance between the ad metal nanoclusters and the graphene. The interaction energy is found to change inversely with the distance between metal cluster and graphene, clearly predicting that such interactions are mainly due to Coulombic forces as already observed for SWCNT interacting with Pt, Au nanoclusters [565] and for electron donor/acceptor

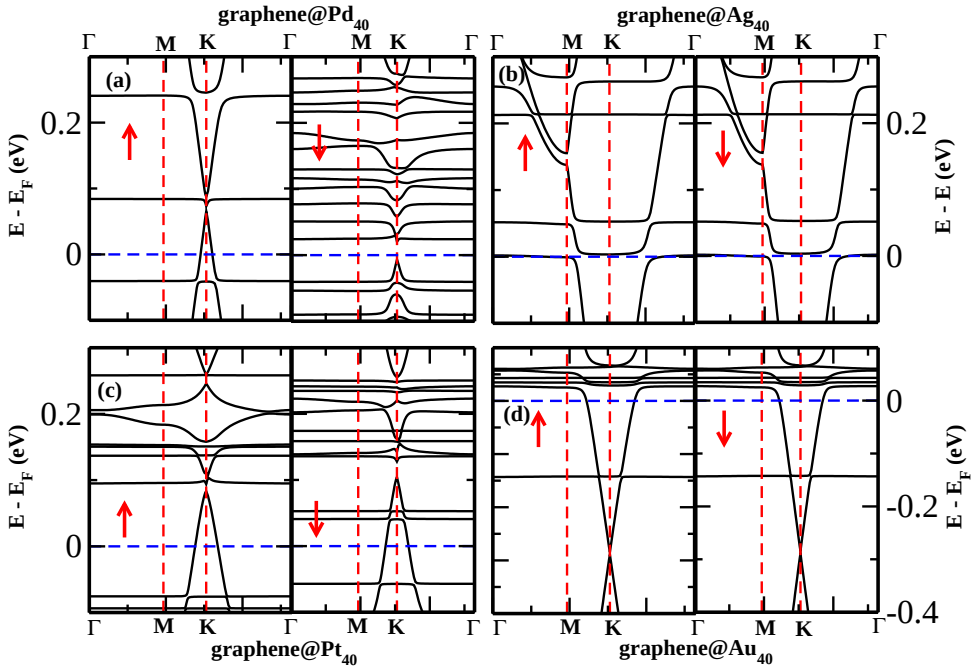

Figure 5.5: The electronic band structures of four metal nanoclusters (Pd_{40} (a), Ag_{40} (b), Pt_{40} (c) and Au_{40} (d)) embedded graphene nanocomposites. The energy is scaled with respect to the Fermi Energy (E_F). The up and down arrows indicate the majority and minority spin channel, respectively.

molecules adsorbed SWCNT [275] and graphene cases [493]. From the analysis of difference in charge density, we also find that the electron density at the outermost valence orbitals of Pd, Ag, and Pt increases while that at the orbitals of carbon in closer proximity to the metal cluster decreases. The situation is exactly reversed for the Au nanoparticle deposition on graphene as expected from the reverse directionality of charge transfer. Thus, our results predict that the changes in electronic properties of nanoclusters doped graphene is mainly due to direct charge transfer between the two.

We consider to focus on the changes in electronic band structures of

the metal nanocluster embedded graphene systems. From the fully relaxed configuration of all the nano composites, it is clear that the region of the graphene in close proximity to the metal cluster is slightly deformed for all the metal clusters deposition, which is capable of breaking the local A-B sublattice symmetry. Consequently, this can indeed cause an opening of band gap in the charge transfer complexes near the Fermi energy. Interestingly, we find that the band gap of a few meV opens near to the K-point, between the graphene-like bands which touches at the Dirac point in case of pure graphene, as can be seen from Fig. 5.5. The effect is very negligible for Au_{40} intercalated graphene as expected from small structural changes mentioned above. It is also to be noted that the energy-gap region is above (below) the Fermi energy due to electron transfer from the graphene (metal nanoclusters) to metal nanoclusters (graphene) for Pd, Ag, Pt (Au) and, therefore, the neutral systems are still metallic. The appropriate tuning of carrier concentrations can result in placing the Fermi energy in the gap region, and the resulting system would behave as semiconductor. However, all the bands for composite systems are essentially a superposition of the bands arising from isolated systems. Moreover, the flat bands near the Fermi level arise from the localized electronic states of the metal nanoclusters, whereas, the bands at the high symmetric K-points are entirely from graphene. The calculated density of states (DOS) and its projection on individual fragment present in nanocomposites show that the graphene is indeed still in its semimetallic state for the deposition of nanoclusters, Pd_{40} and Pt_{40}, while the same becomes metallic in presence of metal nanoclusters, Ag_{40} and Au_{40}. The relatively strong adsorption of Pd_{40} and Pt_{40} nanoclusters on graphene

induced by the larger extent of charge transfer result in a net spin polarization for the complexes. The spin-polarization of the two nanocomposite arises mainly from the adsorbed metal clusters. Interestingly, the graphene@Pd_{40} nanocomposite can act as perfect spin filter without any charge injection as can be seen from Fig. 5.5(a). This is because of the presence of metallic majority spin channel, whereas, the minority spin channel is semiconducting, i.e., typical half-metallic behavior. Therefore, the doping of appropriate metal cluster on 2D graphene shows a new inroad towards designing of new nanomaterials of tunable electronic properties including room temperature half-metallicity for advanced device applications.

5.3.3 Porous Graphene and h-BN Sheets with Magnetic Impurity

So far, we have discussed the electronic structures of pristine two-dimensional graphene and h-BN sheets with the adsorbed metals and metal nanoclusters. But, in practice, these 2D sheet structures acquire various defects during their experimental growth processes. Among different defects, such as Stone-Wales defect (5-7-5), topological line defect (5-8-5) etc. which are most likely to present in these 2D structures, the appearance of hexagonal pores with smooth edges have drawn much research interest. In fact, there are experimental bottom up demonstration for the successful materialization of porous graphene [566]. Moreover, a few theoretical studies have also been devoted in exploring these porous sheet properties [567–569].

In the present investigations, we have studied the electronic structures of

the 2D porous graphene and h-BN sheets within GGA/PBE level of theory using DFT methods. To model the porous sheet structures, we have considered a 3 × 3 supercell of graphene and h-BN sheets with a single pore, containing 18 atoms. Note that, the extended porous structures resemble to a 2D polymer of benzene (polyphenlyene) and borazene (BN analogue of polyphenlyene) units, where, each hexagonal ring is connected to the neighbouring rings via 1, 3, 5 positions. The optimized geometries are shown in Fig. 5.6. Our results have revealed that, the porous structures preserve the 2D planar geometries after full geometry relaxation. This is also confirmed from the geometries optimized using the 6 × 6 supercells (72 atoms). Moreover, the C-C bond distances in porous graphene are found to be ∼1.41 $\mathring{A}$, for all bonds within the hexagonal ring, whereas, ∼1.50 $\mathring{A}$ bond length is obtained for the C-C bonds, that connect the two hexagonal rings. Note that, the C-C bond distance in pristine graphene is found to be ∼1.41 $\mathring{A}$, obtained using the same level of theory. This clearly suggests the C-C bond elongation (∼0.09 $\mathring{A}$) along the joints of the two benzene rings for the porous graphene in comparison to the pristine graphene. This increase in C-C bond lengths slightly localizes the electrons on the hexagonal ring present in porous graphene. This may cause supressing the electronic conductions of the sheet. On the other hand, the B-N bond length in porous h-BN sheet is found to be ∼1.44 $\mathring{A}$ for the bonds within the borazene ring, while, the B-N bond distance between the two borazene rings is ∼1.49 $\mathring{A}$. For comparison, we have also extimated the B-N bond length in pristine h-BN, which is ∼1.45 $\mathring{A}$. This also clearly indicates the bond elongation along the lines connecting the two hexagonal rings in the porous h-BN sheet compared to the pristine

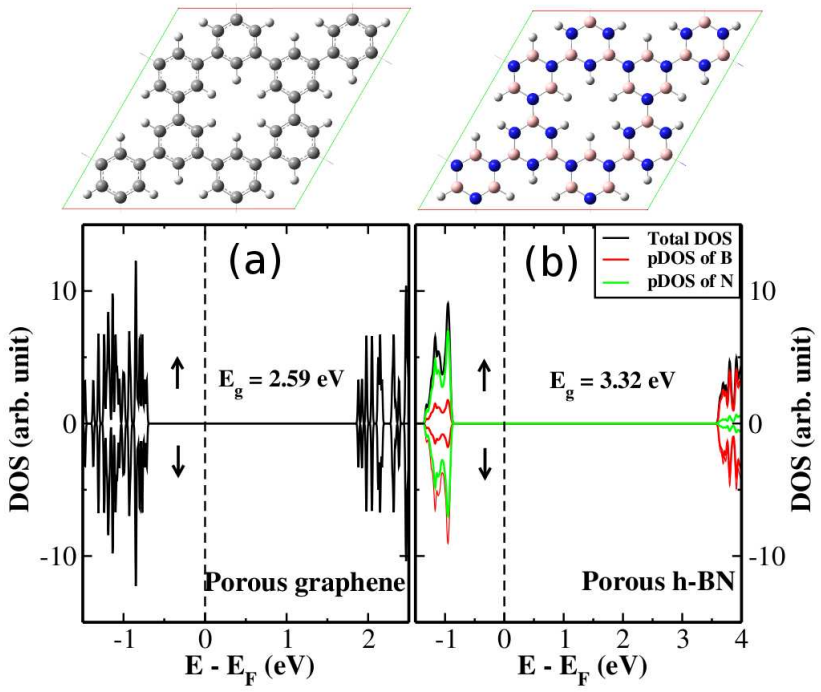

Figure 5.6: The optimized structures and the electronic DOS and pDOS for the porous graphene (a) and porous h-BN (b) single-layer sheets. The energy is scaled with respect to the Fermi Energy (E_F). The up and down arrows indicate the majority and minority spin channels, respectively. The semiconducting band gaps are also indicated.

h-BN. These findings are in good agreement with the previously reported results [567, 569].

To explore the electronic structures, in Fig. 5.6, we have shown the spin-polarized electronic density of states (DOS) and its projections (pDOS) on the different chemical species present in the sheets. Our results have shown that, both the porous sheets are nonmagnetic semiconductors. The band gap values are 2.59 eV and 3.32 eV, for the porous graphene and h-BN sheets, respectively. The creation of pores in graphene localizes the conduction electrons by introducing a potential barrier for its carriers, and thus, opening up

of a band gap. On the other hand, the presence of pores in the h-BN sheet reduces the large insulating band gap (∼4.65 eV using DFT-GGA/PBE) of h-BN sheet. This is because, the presence of pores causes some localized electronic states, which come from the edge atoms of the porous h-BN sheet. These states appear between the valence and conduction bands of h-BN sheet, and thus, showing reduced band gap. Moreover, as expected and also shown in Fig. 5.6, the valence bands are mainly comprised of N atomic orbitals, while, the conduction bands come from the B atomic orbitals.

Herein the main focus of our study is to investigate the effects of transition metal impurities on these porous sheets properties. To this end, we have consiered a 3 × 3 supercell of porous graphene and h-BN sheets with the two transition metal Fe atoms, adsorbed on the stable hexagonal ring centers. We have initially placed the Fe atoms ∼2.0 $\mathring{A}$ above the sheets plane, and optimized the geometries using spin-polarized DFT with two different spin configurations on the Fe atoms. The spins on the two Fe atoms can be aligned either parallel or antiparallel, and accordingly, the configuration is termed as high spin (HS) ferromagnetic (FM) or low spin (LS) antiferromagnetic (AFM) states, respectively. We have fully optimized the geometry considering both the spins configurations. And for a comparison, we have also carried out the calculations on pristine sheets. The calculations show that, an AFM state is preferred for the porous graphene adsorbed with the Fe atoms, while, the pristine graphene with the adsorbed Fe atoms stabilizes in a FM state. The energy difference between the AFM and FM state for the porous graphene with the Fe impurity is ∼ 34 meV, which is slightly larger than the room temperature energy (∼26 meV). Thus, it shows a weak AFM spin ordering of

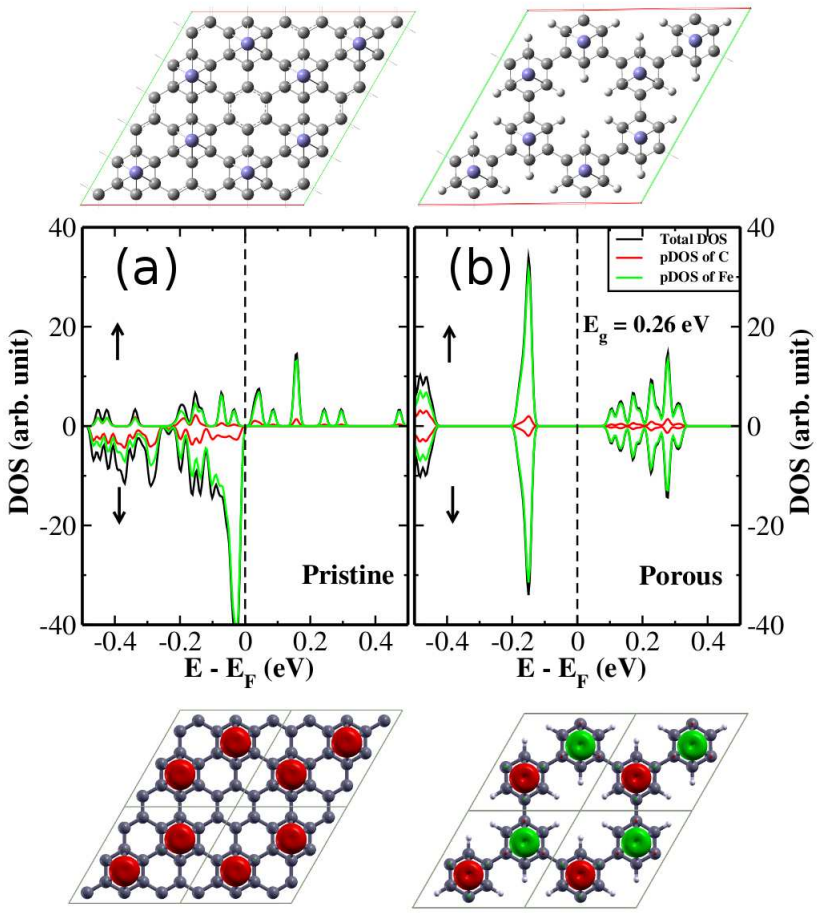

Figure 5.7: The optimized structures (top panel) and the electronic DOS and pDOS (middle panel) and spin density (bottom panel) for the pristine graphene (a) and porous graphene (b) sheets with adsorbed Fe atoms. The energy is scaled with respect to the Fermi Energy (E_F). The up and down arrows indicate the majority and minority spin channels, respectively. The semiconducting band gaps are also indicated.

these adsorbed Fe atoms over the porous graphene. However, the FM state is strongly preferred over AFM state by ∼134 meV for the Fe adsorbed pristine graphene. The Fe-Fe distances in pristine (h-BN) and porous graphene (h-BN) complexes, are 4.34 (4.37) $\mathring{A}$ and 4.43 (4.40) $\mathring{A}$, respectively. This slightly large distance between the adsorbed Fe atoms in porous sheets is due the bond lengths elongations of the connecting bonds between the phenylene rings.

Additionally, we have also analyzed the electronic DOS and pDOS to examine the changes in electronic structures of these 2D sheets. The results show that, the porous graphene with adsorbed Fe atoms in its AFM spin configurations ($i.e.$, stable state) is a spin symmetric semiconductor, with a band gap of ∼0.26 eV. However, its pristine analogue with the Fe ad-atoms, is a magnetic metal, with a ∼2.4 μ_B moments per Fe atom. The results predict a spin switching behaviors ($i.e.$, FM ↔ AFM), while going from Fe-graphene to Fe-porous graphene.

However, the strong FM and AFM states are found to be the stable structures for the Fe adsorbed porous h-BN and pristine h-BN sheets, respectively. Both the h-BN sheets with the adsorbed Fe atoms show spin-polarized semiconducting state with the moderate band gap values (see in Fig. 5.8). Note that, the electronic states near to the Fermi energy (E_F) mainly come from the Fe d-orbitals. Interestingly, we have found that, varying the sheets chemistry or introducing pores may be useful for changing the spin states on the transition metal ad-atoms. Our results have also revealed that, the porous graphene and h-BN sheets bind strongly to the Fe than their pristine analogues. The binding energy of Fe for the pristine and porous graphene is

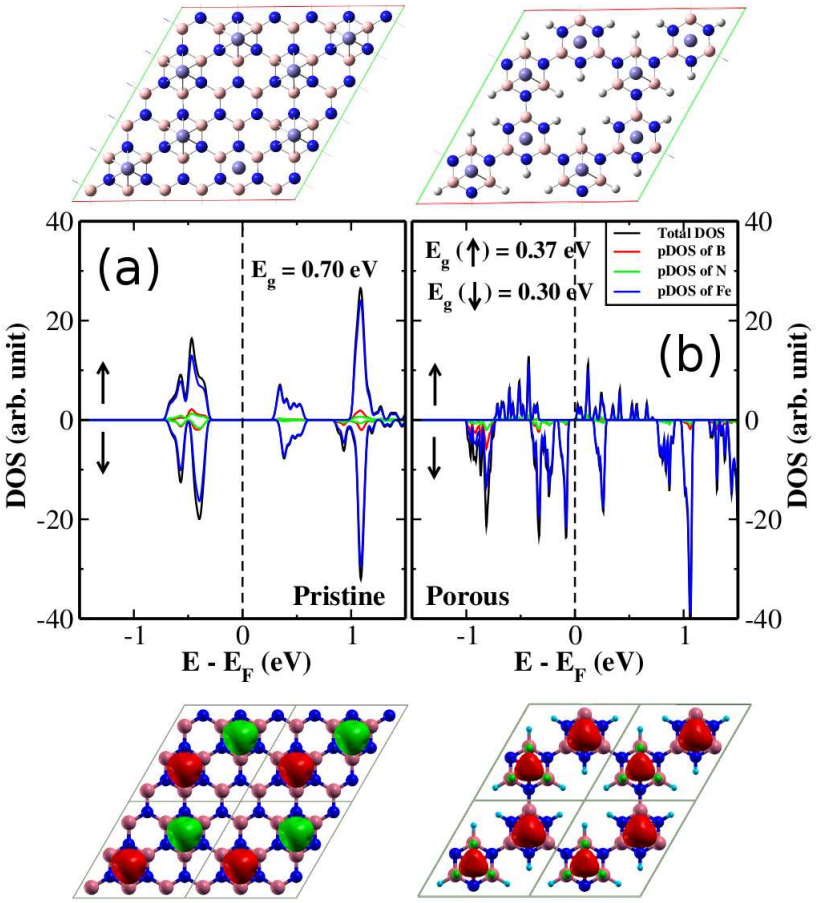

Figure 5.8: The optimized structures (top panel) and the electronic DOS and pDOS (middle panel) and spin density (bottom panel) for the pristine h-BN (a) and porous h-BN (b) sheets with adsorbed Fe atoms. The energy is scaled with respect to the Fermi Energy (E_F). The up and down arrows indicate the majority and minority spin channels, respectively. The semiconducting band gaps are also indicated.

found as ∼-2.82 eV and ∼-2.24 eV, respectively, per adsorbed Fe atom. Note that, negative binding energy values suggest favourable binding of Fe atoms to the sheets. For the pristine and porous h-BN sheets, the binding energy values are ∼-1.34 eV and ∼-1.58 eV, respectively, for the Fe adsorption. The increase in binding energy is due to the presence of electron localizations effects in these porous sheets, which stabilizes the Fe on the 2D porous surfaces than their pristine analogues. Moreover, the Fe interacts strongly (more negative binding energy) with the porous graphene in comparison to the porous h-BN sheet. These results clearly suggest their possible use in removing the Fe contaminants, that might present in various solutions or even in drinking water. In order to verify that, there is no clustering of these adsorbed Fe atoms on the 2D sheets, we have also performed the geometry optimizations considering a large 6 × 6 supercell containing 6 Fe atoms. The optimized structures with the minimum energy spin configurations show no clustering of the adsorbed Fe atoms.

Unprecedented research interests have been shown for varous organometallic sandwiched compounds. These include both 1D and 2D structures, with much attentions have been given to the 1D molecular wires, because of their predicted interesting electronic and spintronics properties. Here we present the results obtained from the first-principles DFT calculations on the two different 2D Fe sandwiched porous graphene and h-BN sheets structures. We have considered the two layers of porous graphene and h-BN sheets stacked on top of each other, and in the middle, a few Fe atoms are hexagonally arranged. Note that, the Fe atom is placed between the two phenylene rings of the two porous layers. To compare the results with the Fe sandwiched

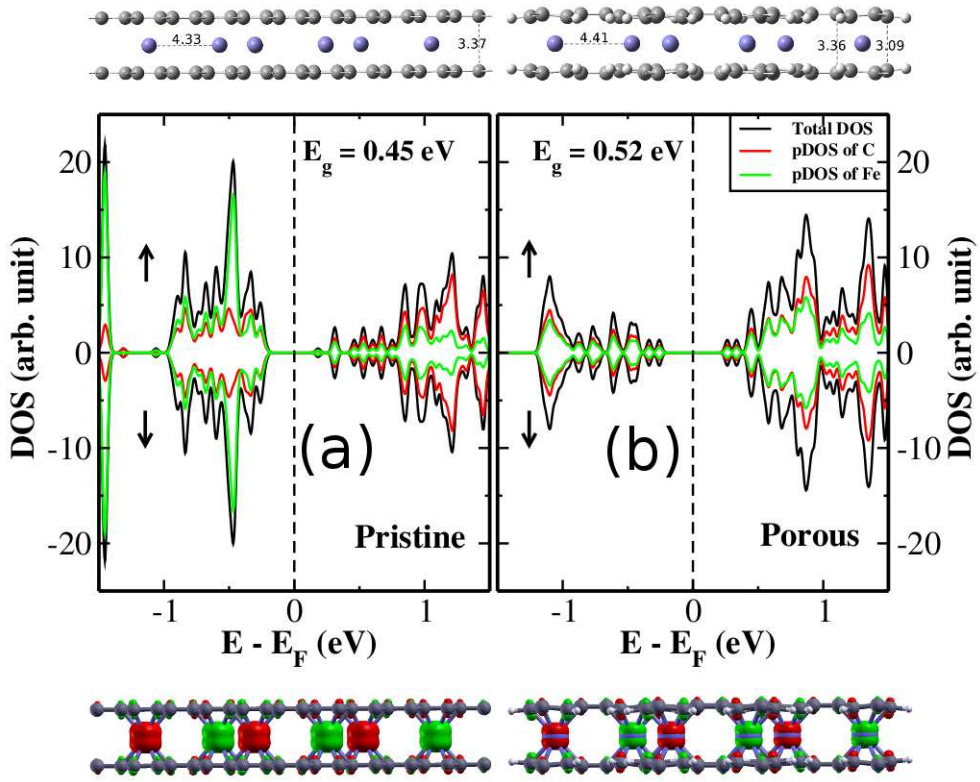

Figure 5.9: The optimized structures (top panel) and the electronic DOS and pDOS (middle panel) and spin density (bottom panel) for the bi-layer pristine graphene (a) and porous graphene (b) sheets with sandwiched Fe atoms. The numbers in top panel indicate the distances in $\mathring{A}$. The energy is scaled with respect to the Fermi Energy (E_F). The up and down arrows indicate the majority and minority spin channels, respectively. The semiconducting band gaps are also indicated.

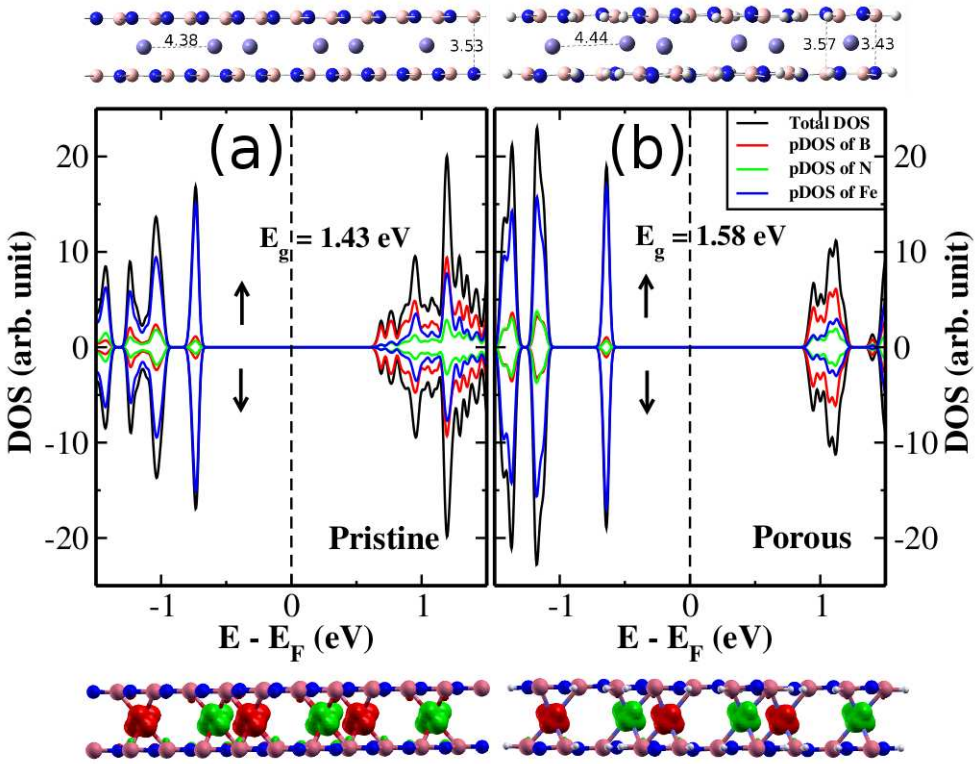

Figure 5.10: The optimized structures (top panel) and the electronic DOS and pDOS (middle panel) and spin density (bottom panel) for the bi-layer pristine h-BN (a) and porous h-BN (b) sheets with sandwiched Fe atoms. The numbers in top panel indicate the distances in $\mathring{A}$. The energy is scaled with respect to the Fermi Energy (E_F). The up and down arrows indicate the majority and minority spin channels, respectively. The semiconducting band gaps are also indicated.

pristine sheets, we have also considered studying their sandwiched pristine analogues.

The spin polarized results have shown that, the energy difference between the FM and AFM states is only ∼7 meV and ∼28 meV for the Fe sandwiched porous graphene and porous h-BN sheets, respectively, with slightly higher stability obtained for the AFM spins configurations on the intercalated Fe atoms. This suggests their paramagnetic behaviors at room temperature

(∼26 meV). However, the calculations on their pristine sandwiched complexes show that, the AFM state is stabler for the graphene with energy difference between AFM and FM being ∼78 meV, while, the Fe sandwiched pristine h-BN complex preserves the paramagnetic spin configurations, as reflected from the small energy (∼4 meV) difference between the AFM and FM states. Moreover, the spin-density is found to be mainly localized on the Fe atoms for both the graphene as well as h-BN sheets sandwiched complexes. The binding energy values are ∼-5.67 eV and ∼-3.42 eV per sandwiched Fe atoms for the porous graphene and porous h-BN sheets, respectively. However, the binding energy values obtained for their pristine analogues, are ∼-4.90 eV (graphene) and ∼-2.70 eV (h-BN). This clearly suggests that, the Fe has strong preference for producing these porous sandwiched compounds than their pristine structures.

Additionally, from the optimized geometries, as shown in Fig 5.9 and Fig. 5.10, it is clear that, there is a significant structural distorsions for the porpous graphene and h-BN sheets. The planarity of the porous sheets are destroyed in these complexes. As can be seen from the Fig. 5.9, the inter-layer distances for the two consecutive C atoms are ∼3.36 $\mathring{A}$ and ∼3.09 $\mathring{A}$, which differ by ∼0.27 $\mathring{A}$. For the porous h-BN sandwiched complex, the inter-layer distances are ∼3.57 $\mathring{A}$ and ∼3.43 $\mathring{A}$ for the two consecutive atoms, which differ by ∼0.14 $\mathring{A}$. Thus, the structural distorsions is more for the porous graphene complex than the porous h-BN complex. Note that, the distance between the two layers for the Fe sandwiched pristine graphene and pristine h-BN complexes is almost uniform throughout the plane, and the values are ∼3.37 $\mathring{A}$ and ∼3.53 $\mathring{A}$, respectively. Moreover, we have not found

any noticeable change in the planar geometry for the sandwiched complexes of pristine sheets.

Next, we have investigated the electronic structures by calculating the electronic DOS of these bi-layer sandwiched complexes for the minimum energy spins configurations. As shown in Fig. 5.9 and Fig. 5.10, both the pristine and porous Fe sandwiched compounds show semiconducting band gaps. The gap values are ∼0.45 eV and ∼0.52 eV, respectively, for the Fe sandwiched pristine and porous graphene complexes. However, as expected, the semiconducting band gaps for the Fe sandwiched pristine and porous h-BN complexes are found comparatively large, with the calculated gap values ∼1.43 eV and ∼1.58 eV, respectively. The results suggest their applications in semiconductor devices. Additionally, we have also analyzed the pDOS for these Fe sandwiched graphitic complexes to understand the orbitals contribution to the valence and conduction bands electronic states. The analysis have shown that, both the Fe d orbitals and C p_z orbitals mainly contribute to the valence and conduction bands states for the bi-lyaer graphene complex. In case of h-BN complexes, we have found that, the valence bands mainly comprise of Fe d orbitals, while, the major contribution to the conduction band come from the B p_z orbitals of the h-BN sheets.

5.4 Conclusions

In summary, we have presented results on the modification of the intrinsic electronic structure of pristine two-dimensional graphene and h-BN sheets in response to the external perturbations introduced by a few metals and their

clusters, using first-principles density functional theory calculations. Our results have shown that, the nature of the external metals (metal clusters) have significant impact in tuning the electronic structures of these 2D sheets. Depending on the types (metals and metal clusters), the spin-polarized semiconducting and metallic states can be realized. However, the presence of Ni atom adsorbed on graphene and h-BN sheets provides a nonmagnetic structure. The large extent of spin polarization is found for the deposition of magnetic clusters (Fe_{40}, Co_{40} and Ni_{40}), which mainly comes from the embedded clusters. This suggests that, these composites may find potential applications in spin selective electronic devices. The presence of nonmagnetic metals (Pd, Ag, Pt and Au) opens up a small band gap between the valence and conduction bands in graphene, and thus offers a possibile semimetal to perfectly semiconductor metallic transition. Interestingly, we find typical half-metallic behavior for graphene@Pd_{40} nanocomposite, which has potential applications in spintronic device fabrication. The electronic band structures calculations on porous graphene and h-BN sheets have revealed moderate band gap values ($\sim$2.59 eV and $\sim$3.32 eV for porous graphene and porous h-BN, respectively), which is between the band gaps found for the pristine graphene (zero band gap) and h-BN sheets (large band gap, $\sim$4.56 eV using GGA-PBE). This suggests their possible applications in semiconductor devices. The presence of Fe impurities hexagonally distributed on these porous sheets results in larger extent of adsorption energy in comparison to the results found for their pristine analogues. This is also true for Fe sandwiched between the two porous sheets. This can be understood as follows: the presence of the pores causes electrons to be localized, and hence,

are available for interacting with the metal orbitals to a greater extent compared to the delocalized electrons present in pristine sheets. The higher extent of adsorption energy suggests the possible applications of these porous mono-layer and bi-layer sheets for the effective traping of Fe contaminants in solutions. Interestingly, we have found that, the presence of Fe on these 2D sheets show spin-switching behaviors between the high-spin ferromagnetic and the low-spin antiferromagnetic states with the change in sheets structure (*i.e.*, pristine $\leftrightarrow$ porous). We have attributed these distinct spin-switching behaviors to the different coupling strengths among the adsorbed Fe metals, mediated via 2D sheet electrons. Because of these interesting electronic and magnetic properties, the different metals and metal clusters decorated 2D sheets may find applications in electronic and spintronic devices.

Chapter 6

Molecular Charge Transfer Effect on Graphene and Single-Walled Carbon Nanotubes*

6.1 Introduction

Low dimensional carbon nanomaterials, like fullerenes, nanotubes and graphene have been of extensive research interest in condensed-matter physics and in materials sciences because of their interesting electronic, mechanical and

*Work reported in this chapter is published in: (a) Arun K. Manna and Swapan K. Pati, *Chem. Asian J.* **4**, 855 (2009); (b) Arun K. Manna and Swapan K. Pati, *Nanoscale* **2**, 1190 (2010); (c) Arun K. Manna and Swapan K. Pati, *Book Chapter, World Scientific Publishing Co. Pte. Ltd. Singapore* **ISBN: 13-978-981-4329-35-4**, 59 (2011)

optical properties [130, 137, 260, 261, 406, 570]. In fact, the diverse electronic properties of carbon nanomaterials strongly depend on their dimensionalities. The electronic confinement in these reduced dimensions give rise to many exotic phenomena that have been of potential scientific interests over the decades [261, 571–578]. The recent experimental realization of one-dimensional (1D) and two-dimensional (2D) nanosystems have drawn a major attention of a large number of scientific communities for their possible applications in nanoelectronics [129–131].

Among low-dimensional carbon systems, 2D graphene and quasi-1D carbon nanotubes have become promising materials because of their unique structural and electronic properties, and hold good promise for designing of next generation electronic devices [178, 193, 194, 260, 406, 475–477]. Single-layer pristine graphene is a zero-gap material, whereas single-walled carbon nanotubes (SWCNTs) can be conducting or semiconducting depending on the nanotube's chiralities. However, in practice, their intrinsic properties may not be suitable for direct device integration, and hence, the developement of novel means to achieve controllable properties will be extremely valuable for device applications. In fact, tunable electronic properties of graphene and SWCNTs have practical applications in nanoscience and nanotechnology [129, 579].

In general, electronic properties of materials in reduced dimensions are mainly governed by their size, geometry, boundary conditions and more importantly by the nature of electronic correlations [487, 570]. In addition to these, the carrier type and its concentration play an important role in controlling the novel optoelectronic and transport properties. The *massless* Dirac

fermions describe the low-energy electronic structure of graphene, which in effect results in very high carrier mobilities. Moreover, the carrier (electron or hole) mobilities can be tuned by controlling the external electric field in graphene and nanotubes' based field effect devices [129,579]. Futhermore, the possible utilization of spin components in graphene-based electronic devices depends on the extent of spin polarization [482,483]. In this respect, the half-metallic materials, as discussed in previous chapters, result in spin-polarized current [249, 484, 486, 488, 489, 580, 580].

In fact, appropriate controlling and/or tuning of the electronic structure of graphene and SWCNTs have numerous applications in advanced device fabrications. The significant changes in properties, in particular of phonon frequency and electronic structure, are reported to occur when electrons or holes are added by electrochemical means [490]. It is indeed possible to achieve a high level of doping through electrochemical top-gating [490, 581, 582]. Apart from this, the other possible way of tuning the carrier type and its concentrations is by the incorporation of appropriate external electron donor or acceptor guests into the host carbon nanostructures. To achieve this, the boron and nitrogen atoms implantation [237, 246, 249, 583], chemical functionalization [584, 585], doping with various metals and metal clusters [403, 586], and surface adsorption of selective donor and acceptor molecules [198,275,457,492,493,587] into graphene and SWCNTs, have been successfully considered to be the effective routes among others. It is commonly known that, charge transfer occurs in molecular donor-acceptor systems. However, this can be achieved in two different pathways, namely, intramolecular and intermolecular charge transfer processes. To achieve the

intramolecular pathway, one has to form a new chemical bond between the electron donor and acceptor host-guest systems. As a result, it would possibly destroy the characteristic sp^2-bonding framework and the intriguing electronic structure, because of the substantial structural deformation introduced by the formation of new chemical bonds. In sharp contrast to this, intermolecular pathways are more effective, where, either electrons or holes are added through charge transfer processes by non-covalently adsorbing various selective electron donor or acceptor molecules on the graphene and nanotube surfaces. Such controlled adsorption of donor or acceptor molecules induce charge transfer, which in turn greatly change the optoelectronic properties of 2D graphene and quasi-1D SWCNTs, in particular the characteristic Raman spectra of these graphitic materials [198, 275, 457, 492, 493, 587].

In this chapter, we have mainly investigated the effects of external molecular dopants, namely, the electron donor and acceptor molecules on the modification of electronic properties of a pristine single layer 2D graphene and quasi-1D single-walled carbon nanotubes (SWCNTs), using first-principles density functional theory calculations. The charge transfer is carried out by adsorbing selective electron donor and acceptor molecules on the graphene and nanotubes surfaces [275, 493]. For this, we have considered a few representative donor and acceptor molecules with the varying affinities for the electron. Tetracyanoethylene (TCNE) and tetracyanoquinodimethane (TCNQ) have been chosen as the electron acceptors, and tetrathiafulvalene (TTF) as the electron donor. The study shows that, the chemical nature of the dopant molecules (electron donor/acceptor molecules) on graphene and SWCNTs has significant impacts in changing their intriguing electronic structure. Our

theoretical findings [275, 493] compare fairly well with the recently reported experimental results [198, 492].

6.2 Computational Methods

The first-principle calculations are carried out using the linear combination of atomic orbital density-functional theory (DFT) methods, as implemented in the SIESTA package [349, 350]. The generalized gradient approximation (GGA) in the Perdew-Burke-Ernzerhof (PBE) form [389] and double ζ polarized (DZP) basis set are chosen for the spin-polarized DFT calculations. The interaction between ionic cores and valence electrons is described by norm conserving pseudopotentials [390] in the fully non-local Kleinman-Bylander form [391]. The pseudopotentials are constructed from 1, 4, 5, and 6 valence electrons for the H, C, N and S atoms, respectively. A reasonable mesh cut-off of 400 Ry for the grid integration is utilized to represent the charge density.

We have considered (8×8) supercell containing 128 carbon atoms of graphene for modeling the doping of 2D graphene. Periodic boundary conditions and a supercell approximation with a lateral separation of 12 $\mathring{A}$ between the adsorbed molecules are used to ensure that the interactions between molecule and their periodic images are negligible. On the other hand, the supercell ($1 \times 1 \times 5$) and ($1 \times 1 \times 6$) containing 160 carbon atoms of a semiconducting (8,0) SWCNT and 120 carbon atoms of a metallic (5,5) SWCNT are used for the modeling of SWCNTs doping. It is necessary to ensure that the x-and y-axes of the periodic supercells are large enough, so that, there

is negligible interaction between adsorbed molecule with adjacent supercell. A distance of 20 $\mathring{A}$ along the x-and y-axes is found to be sufficient to ensure the energy convergence. The presence of large curved surface area and the negligibly small decrease in adsorption energy while going from one to two number of adsorbate molecules lead us to consider two molecules adsorbed oppositly to the nanotube surface per supercell.

The geometry optimization and all electronic structcures calculations, are carried out using $10 \times 10 \times 1$ Monkhorst K-points for sampling the 2D brillouin zone of graphene. For full relaxation of all SWCNTs systems, we have sampled the Brilliouin zone by $1 \times 1 \times 40$ k-points using the Monkhorst-Pack scheme, whereas, for electronic properties calculations, the Brilliouin zone is sampled by $1 \times 1 \times 80$ k-points. The optimal atomic positions are determined until the magnitude of the forces acting on all atoms is less than 0.04 eV$\mathring{A}^{-1}$. Charge transfer and chemical bonds are, in most cases, can be described within DFT with the generalized gradient approximation (GGA) to account for the exchange and correlation energy of the electrons [588]. In addition to that, GGA approximation takes into account the semi-local exchange correlations, which have significant impact on low-dimensional spin systems like graphene and carbon nanotubes. Since local density approximation overestimates the adsorption energy for these weakly bound systems, [589] we have considered GGA to be an appropriate choice for describing interaction of either donor or acceptor with the large sp^2 π surface of SWCNTs.

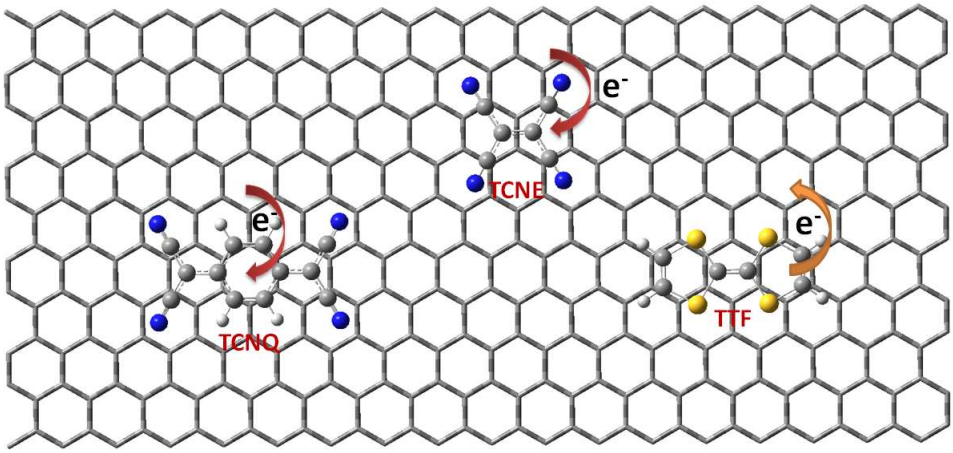

Figure 6.1: Schematic representation of charge transfer process between graphene and electron donor, TTF and electron acceptor, TCNQ and TCNE molecules. The yellow, blue, grey, and white color atoms correspond to sulfur, nitrogen, carbon and hydrogen, respectively.

6.3 Results and Discussions

Here, we have discussed the effects of molecular doping on the graphene and single-walled carbon nanotubes electronic structures. We first present the results obtained from the molecular doping of graphene. Then, we have discussed the doping of various SWCNTs by the surface adsorption of different electron donor and acceptor molecules. In both the cases, we have addressed the charge transfer effects on the electronic properties of these complexes (Graphene-Donor/Acceptor molecules and SWCNTs-Donor/Acceptor molecules) molecule).

6.3.1 Molecular Doping of Graphene

In this section, we have discussed the changes in electronic properties of 2D graphene induced by molecular charge transfer [493]. To achieve the goal, we

have considered a few representative organic donor and acceptor molecules. The schematic diagram of the charge transfer processess, which includes these dopants molecules, is shown in Fig. 6.1.

To understand the relative stability of the molecules adsorbed graphene complexes, we have calculated the adsorption energy (E_{ad}), using the following relation:

$$E_{ad} = E_{graphene-molecule} - E_{graphene} - E_{molecule} \tag{6.1}$$

where, $E_{graphene-molecule}$, $E_{graphene}$ and $E_{molecule}$ are the total optimized energy of graphene-molecule complex, and the optimized energy of isolated graphene and molecule, respectively.

From the relaxed geometries, we have found that all the sorbed molecules surface adsorbed above the graphene at about 3.0 Å [493]. Moreover, the calculated adsorption energies that essentially examine the relative stability of adsorbate-graphene complexes are within a few kcal mol^{-1} ($\sim$31 - $\sim$47 kcal mol^{-1}), suggesting a physisorption process [493] with larger adsorption energy for TCNQ adsorbed complex. An analysis of the Mülliken population suggests that, there is an effective charge transfer between the adsorbed molecule and graphene. For both TCNE and TCNQ adsorption, the amount of electron transfer from graphene to adsorbed molecule is found to be $\sim$ 0.31 e and $\sim$ 0.39 e, respectively, consistent with their nature of electron-withdrawing tendency [493]. For electron donor, TTF, electron transfer of $\sim$ 0.11 e is found from the molecule to graphene. The large value of adsorption energy for TCNQ on graphene compared to the others can be attributed

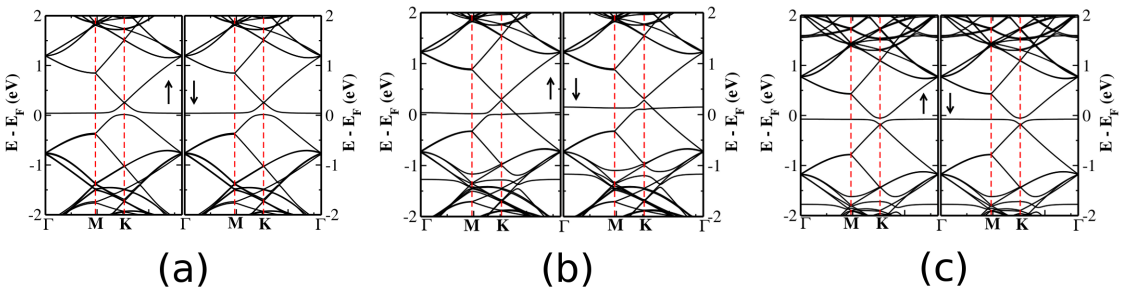

Figure 6.2: The electronic band structures for (a) Graphene-TCNE, (b) Graphene-TCNQ and (c) Graphene-TTF. The up (down) arrows corresponds to the majority and minority spins respectively. The Fermi level is set to zero.

to the fact that, for TCNQ, the benzenoid structure provides a significant π surface for adsorption on graphene with a significant amount of charge transfer, and hence, gains stability through electrostatic forces as well as π-π stacking interactions. Incidentally, the charge transfer between graphene and adsorbed molecule results in electrostatic attraction and thereby, formation of a charge-transfer complex, in agreement with the UV/Vis spectrum reported by Rao and co-workers [198, 492]. Furthermore, it is also indentified conclusively that, the charge transfer occurs through Coulombic forces, as was the case for the interaction of carbon nanotubes with metal nanoparticles [565] and with donor and/or acceptor molecules [275], and various metal and metal oxide nanocluster-graphene complexes studied [402, 403].

To understand the effects of charge transfer interactions on electronic structure, we plot band diagrams and corresponding DOS in Fig. 6.2. The band structures around the Dirac point are significantly affected by molecular adsorption in graphene. For pristine 2D graphene, it was shown that, the spin-polarized electronic DOS vanishes exactly at the Fermi level due to the presence of *massless* Dirac fermions and there is no net spin-polarization.

The electronic band structures of graphene in presence of donor and acceptor molecules clearly show the presence of discrete molecular levels around the Fermi energy (see Fig. 6.2). The flat molecular levels of TCNE and TCNQ in charge-transfer physisorbed systems appear slightly above the Fermi energy, which cause depletion of electrons from the uppermost valence bands, and thereby, shifting the Fermi level down. In case of TTF adsorbed graphene, a flat band slightly below the Fermi level results an accumulation of electrons, causing the upward shifting of the Fermi level. Note that, the flat bands essentially indicates the localized electronic states, suggesting the presence of massive electrons. However, the presence of these flat bands give rise to finite DOS close to the Fermi level [493]. Moreover, all the systems are found to be metal because of the presence of finite DOS at the Fermi energy.

Also note that, in all three molecule-graphene complexes, breaking of the A-B sublattice symmetry induced by the local structural deformation creates a small band-gap. Injecting either electrons or holes can indeed change the electronic state from semi-metallic to metallic and even to a semiconducting state by tuning the Fermi level position in between the gap region. Note that, in a strict sense, the Dirac cone picture of graphene is absent in the graphene-molecule complexes. Instead, as shown in Fig. 6.2, the mixing of graphene band and discrete molecular level results in disappearance of cone picture for the valance band for TCNE and TCNQ and the conduction band for TTF. Interestingly, for electrochemical top-gating study, the linear dispersion near the Fermi level (cone picture) remains true even after doping to a high level [581, 582, 590]. In our case [493], as has been mentioned, the charge-transfer is molecular in nature, unlike the electrochemical gating.

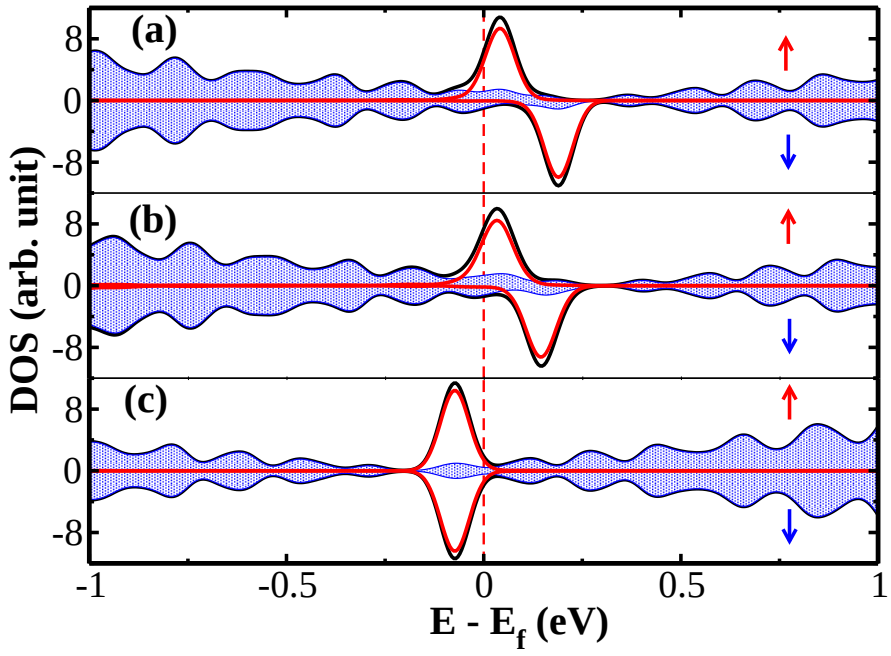

Figure 6.3: The density of states (DOS) for (a) Graphene-TCNE, (b) Graphene-TCNQ and (c) Graphene-TTF in the 8×8 supercell. The Fermi level is set to zero. The black, red and filled blue dotted area correspond to total DOS, molecule pDOS and graphene pDOS respectively. The DOS lines are broadened with Gaussian functions of width 0.05 eV.

From the pDOS analysis (see the Fig. 6.3), it is clear that the DOS at/near the Fermi level mainly comes from the adsorbed molecules. In fact, the graphene in graphene-molecule complex contributes only a little to the overall DOS at the Fermi energy. Note that, for pure graphene, there are no electronic states at the Fermi energy for transport process. It is also clear from Fig. 6.3 that, at Fermi energy, a finite spin polarization exists for TCNE and TCNQ complexes with graphene, while, for TTF adsorbed graphene, such a spin polarization is absent.

Further, we have also discussed about the Raman active G bands of graphene and graphene-molecule complexes for a direct comparison and detailed understanding of the experimental results recently reported by Rao *et al*. [198, 492]. Experimentally, it was shown that G-band softens and stiffens with increasing concentration of TTF and TCNE, respectively, with enhancement of the intensity ratio of D- to G-band [492]. In our calculations [493], we have obtained qualitatively similar results. For pure 2D graphene, our calculations yield the optical phonon frequency at Brillouin zone center Γ-point corresponding to the Raman active G-band at around 1579 cm^{-1}. This Raman G-band arises from the in-plane degenarate E_{2g} vibrational modes. However, in presence of electron acceptors (TCNE and TCNQ), we have found that the G-band frequency is shifted to a higher value ($\sim$ 1599 cm^{-1} and $\sim$ 1596 cm^{-1} for TCNE- and TCNQ-adsorbed graphene, respectively) because of the nonadiabatic removal of Kohn anomaly at Γ-point, while for the electron donor (TTF), it goes to a lower frequency region at about 1565 cm^{-1}, corroborating the experimental findings [198, 492]. It is

important to note that, the nature of the G-band shifts found for the molecular doping, is different from the electro-chemical doping of graphene studied using Raman spectroscopy [590]. This is becuase, the presence of surface adsorbed molecules causes substantial local structural distortions, which is probably absent in case of electro-chemical doping. However, the results discussed here, qualitatively agree well with previous calculations [591,592] and reported experimental results [198,492,593].

6.3.2 Molecular Doping of Single-Walled Carbon Nanotubes

In the previous section, we have demonstrated the effects of molecular doping on the electronic structures of graphene. However, it would be interesting to explore the changes in electronic properties of different SWCNTs modified by the surface adosorbed electron donor and acceptor molecules. In fact, there exists experimental evidences of molecular charge transfer effects on the SWCNTs properties by Raman spectroscopic studies [198,457,492].

Similar to the study of molecular doping of graphene, here, we have chosen TCNE and TCNQ, as the electron acceptors, while, TTF is selected, as the donor molecules. We have considered the two different SWCNTs, metallic, (5,5) SWCNT and semiconducting, (8,0) SWCNT, bearing almost same diameter (~ 6.8 $\mathring{A}$).

The relative stability of adsorbate-nanotube systems is determined by the adsorption energies. As it is well known, larger the adsorption energy,

Table 6.1: Adsorption energies (E_{ad}), equilibrium distance (D) and electron transfer (ET) for all SWCNT-molecule complexes. The +ve (-ve) ET value indicates the electron transfer from the nanotube (molecule) to the molecule (nanotube).

SWCNT	Molecule	E_{ad} (kcal mol^{-1})	D ($\AA$)	ET (e)
(5,5)SWCNT	TCNE	-27.08	2.96	0.35
(5,5)SWCNT	TCNQ	-38.68	3.06	0.41
(5,5)SWCNT	TTF	-27.31	3.09	-0.08
(8,0)SWCNT	TCNE	-25.54	2.82	0.26
(8,0)SWCNT	TCNQ	-31.32	3.11	0.33
(8,0)SWCNT	F_4-TCNQ	-36.22	3.08	0.39
(8,0)SWCNT	TTF	-29.61	2.95	-0.17

stronger is the binding of the adsorbate to the nanotube surface. The adsorption energy (E_{ad}) per adsorbate molecule is calculated by subtracting the energy of the optimized isolated molecule, $E_{molecule}$ and the optimized equilibrium energy of the adsorbent, $E_{(n,m)SWCNT}$, from the total energy of the optimized molecule-(n,m) SWCNT system, $E_{molecule+(n,m)SWCNT}$, i.e.,

$$E_{ad} = [E_{molecule+(n,m)SWCNT} - E_{(n,m)SWCNT} - 2 * E_{molecule}]/2 \qquad (6.2)$$

A summary of the results for the fully optimized structures for all the systems are provided in Table 6.1. As can be seen, the distance between SWCNT and the adsorbed molecule remain at about 2.8-3.1 $\AA$. The equilibrium adsorption distances are measured as the shortest distance between nanotube and adsorbed molecule. It can easily be seen from the Table 6.1 that for

adsorption of TCNE on both nanotubes, the distances are relatively shorter as expected from its smaller molecular size with significant amount of charge transfer. It is also clear that the equilibrium adsorption distances are comparatively smaller than that observed for molecules adsorbed on graphene surface [493]. Moreover, the adsorption energies are comparatively smaller than those obtained for same molecules adsorption onto graphene surface [493]. The reason of having lesser values of adsorption energy is due to the curved surface of SWCNTs compared to flat planar graphene surface. The stability of these physisorbed SWCNT-molecule complexes are due to the interactions of various length scales, including Coulombic as evidenced from finite charge transfer. Also, as can be seen, for all the cases, the interaction is weak in agreement with moderate values of adsorption energy (see Table 6.1). The relatively larger value of adsorption energy for TCNQ compared to TCNE, is attributed to the fact that for TCNQ, the benzenoid structure provides a significant π surface for adsorption on SWCNTs. This increases the extent of charge-transfer which in turn leads to gain the stability through electrostatic forces. Notably, the change in bond length alteration (BLA) reveals that the quinonoid form of TCNQ in its pure free gaseous state transform into benzenoid form on interacting with nanotubes. In comparison to TCNQ, the absence of large conjugated π surface with lesser amount of charge-transfer indicates that, both electrostatic as well as van der Walls forces are, however, comparatively small for TTF molecule adsorbed on SWCNTs. Interestingly, electron withdrawing adsorbates interact more specifically with metallic (5,5) SWCNT compared to the semiconducting (8,0) SWCNT with greater amount

of charge transfer, resulting in larger values of adsorption energy. On the contrary, in case of electron-donating molecules, the results are exactly opposite with comparatively larger adsorption energy for the semiconducting SWCNTs. These findings are well consistent with the recent experimental results obtained by Rao *et al*. [457].

An analysis of M*ü*lliken population suggests that, there is an effective charge transfer between adsorbed molecule and SWCNT. For both TCNE and TCNQ adsorbed onto metallic (5,5) SWCNT, the extent of electron transfer from nanotube to adsorbed molecules are found to be $\sim$ 0.35 e and $\sim$ 0.41 e, respectively, while for the adsorption on semiconducting (8,0) SWCNT, the values are $\sim$ 0.26 e, and $\sim$ 0.33 e, respectively, per sorbed molecule, per supercell. This is consistent with the nature of electron-withdrawing tendency of these molecules. For electron donor TTF, electron transfer of $\sim$ 0.08 e and $\sim$ 0.17 e are found from molecule TTF to (5,5) SWCNT and (8,0) SWCNT, respectively, per sorbed molecule, per supercell. To understand, whether the charge transfer accompanies spin moments, we have calculated the difference in spin-density (i.e. up-spin - down-spin densities). Interestingly, we find that for TCNQ molecule adsorbed on semiconducting (8,0) SWCNTs, there is accumulation of small but finite magnetic moment in nanotubes. For TCNE, however, there is a finite spin density in the molecule although nanotube remains nonmagnetic. In case of TTF, the hole carries no magnetic moment and both nanotube and the molecule remain nonmagnetic. Note that, for electron acceptor molecules (TCNE and TCNQ) adsorbed on SWCNTs, the interaction is mainly electrostatic

in nature as found from significant charge-transfer with definite spin moments. In fact, TCNQ, being the stronger electron acceptor in comparison to TCNE, the effect is more, similar to its adsorption on a Ag(100) and graphene surface [493, 594]. Incidentally, the charge transfer between nanotube and adsorbed molecule results in electrostatic attraction and thereby formation of a charge-transfer complex, in agreement with recent experimental results [457,587]. The majority spin density is mainly localized on the sp^2 carbon and nitrogen atoms for both TCNE and TCNQ adsorbed SWCNTs, while the minority-spin density is localized on the "sp" carbon atomic hybrid orbitals of cyano groups present in acceptor molecules. Because of weak interactions through p_z orbitals of TCNQ and its strong hole doping nature compared to TCNE with SWCNTs, the latter contributes less to the overall spin, as noted earlier. Moreover, the excess transfered charge is mainly localized on the N atoms of the electron-withdrawing cyano group of both TCNE and TCNQ molecules, while for TTF adsorption, the relatively lesser extent of charge depletion from S atoms gives rise to moderate values of adsorption energy. We, however, would like to mention that, our results on the amount of charge-transfer obtained through M*ü*lliken population analysis are probably qualitatively correct, as the SIESTA code used in the present study, does not include van der Waals interaction properly.

To understand the effects of molecular interactions on the nanotubes electronic structures, we plot band diagrams in Fig. 6.4 and Fig. 6.5, for the metallic (5,5) SWCNT and semiconducting (8,0) SWCNT, respectively. The band structures around the Fermi energy are significantly affected by molecular adsorption in both types SWCNTs. For pure quasi-1D metallic (5,5)

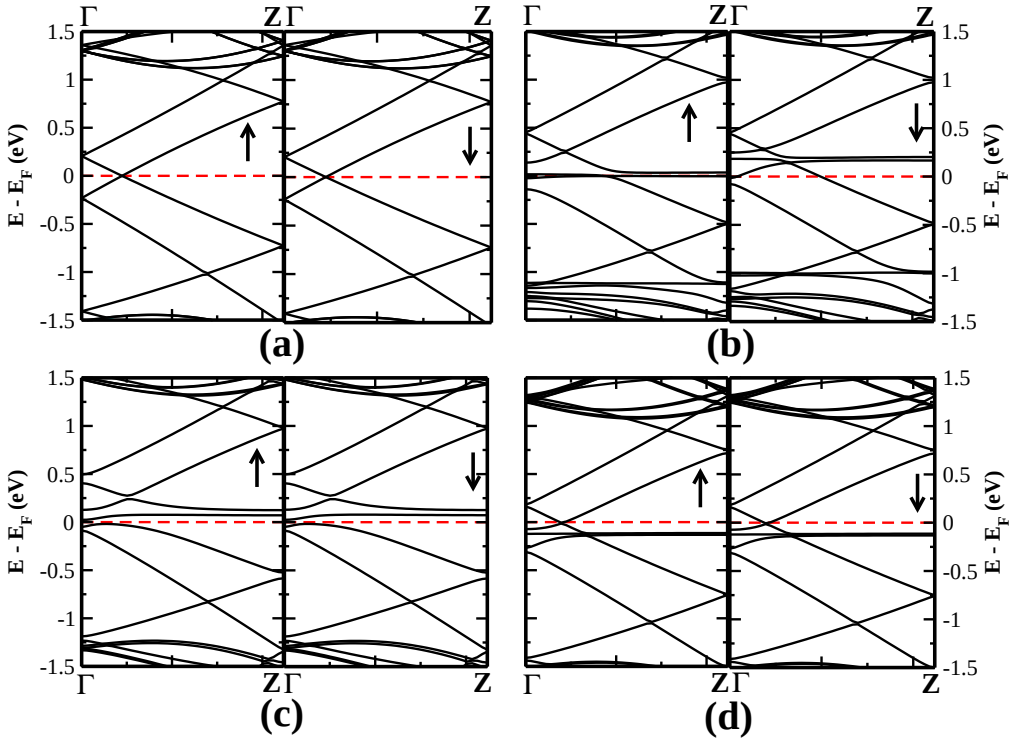

Figure 6.4: The spins resolved electronic band structures for pure (5,5) SWCNT (a), (5,5) SWCNT-TCNE (b), (5,5)SWCNT-TCNQ and (5,5) SWCNT-TTF (d). The Fermi level is set to zero. The up and down arrows indicate the majority and minority spin channel, respectively.

SWCNT, spins symmetric electronic states appear at the Fermi level, resembling the metallic behavior (see Fig. 6.4)). In case of pure quasi-1D (8,0) SWCNT, a semiconducting band gap of ∼0.55 eV appears at the Fermi energy. Moreover, (5,5) SWCNT also shows spins symmetirc electronic states, indicating zero spin polarization. The presence of donor and acceptor adsorbates creates the discrete molecular levels around the Fermi energy, as indicative from the flat bands near the Fermi energy for all SWCNT-molecule complexes. The presence of flat molecular levels of TCNE and TCNQ in charge-transfer physisorbed systems at slightly above the Fermi level give rise to finite DOS for the molecule-nanotube complexes. In case of TTF adsorbed SWCNTs, a flat band arises slightly below the Fermi level, resulting in finite DOS for the composites. In the later case, both majority and minority spins are affected in exactly same manner with negligible amount of molecular charge-transfer. Also note that, in all the six molecule-SWCNT complexes, the Fermi level shifts from its original position *i.e.* from its pure states (see Fig. 6.4 and Fig. 6.5). Interestingly, however, we have found that, in case of TCNE and TCNQ adsorbates, the electrons are removed from the SWCNTs, depleting electron cloud from the uppermost valence bands of the later, with Fermi energy shifting towards the valance band. The effect is more pronounced for metallic (5,5) SWCNT, compared to the semiconducting (8,0) SWCNT, as the former has more carriers than the later. On the other hand, the accumulation of electrons cause shifting of the Fermi level towards the conduction band for TTF intercalated SWCNTs. Note that, in a strict sense, the completely pure band picture of SWCNTs near to the Fermi level is absent in SWCNT-molecule complexes. Instead, as shown in Fig. 6.4

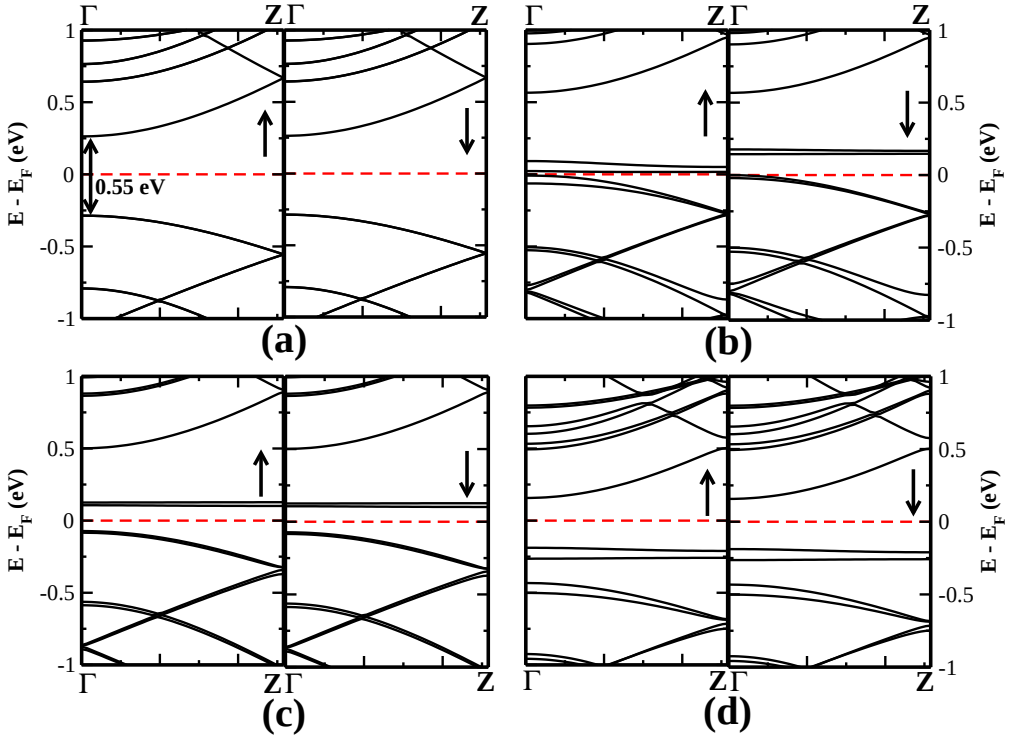

Figure 6.5: The spins resolved electronic band structures for pristine (8,0) SWCNT (a), (8,0) SWCNT-TCNE (b), (8,0) SWCNT-TCNQ (c) and (8,0) SWCNT-TTF (d). The Fermi level is set to zero. The up and down arrows indicate the majority and minority spin channel, respectively.

and 6.5, the hybridization of SWCNT bands and the discrete molecular level results in disappearance of pure band picture for the charge-transfer complexes.

Interestingly, for electrochemical top-gating study, the pure dispersive bands near the Fermi level remains unaltered even after doping to a high level as observed in case of graphene [581, 582, 590]. In our case, doping is done by means of electron-donor and -acceptor molecules, which causes the appearance of discrete localized molecular level resulting in re-hybridization of bands. Moreover, as has been mentioned, the molecular charge-transfer

is fractional unlike the electrochemical gating. Interestingly, for the TCNE adsorption on (5,5) SWCNT, a small band gap $\sim$ 50 meV opens at the Fermi level (see Fig. 6.6), showing the possibility of apparent metal-semiconductor transition whose signature was found in characteristic Raman spectroscopy, thus corroborating with the experimental findings [457]. On the other hand, the interaction of semiconducting (8,0) SWCNT with TCNQ closes up the minority spin gap completely, whereas, a small $\sim$ 8 meV gap present in the majority spin channel, which is negligibly small than the room temperature energy ($\sim$26 meV), opening up a strong possibility of semiconductor-metal transition. Moreover, the semiconducting gap of $\sim$0.55 eV for (8,0) SWCNT reduces to $\sim$0.21 eV and $\sim$0.35 eV for the interactions with TCNE and TTF adsorbates, respectively.

To verify the consistency of our results, we also consider a distinct metallic (9,0) SWCNT which has different diameter and chirality from the previous one. Although the pure (9,0) SWCNT has a pseudo gap exactly at the Fermi energy, after interaction with TCNE, it opens up the band gap supporting our findings as a general case. Furthermore, since the TCNQ, a strong electron acceptor, on interaction with semiconducting (8,0) SWCNT closes up the gap as discussed earlier, we too have thought to consider a better and stronger electron-withdrawing adsorbate molecule, a fluorinated derivative of TCNQ *i.e.*, tetrafluro quinodimethane (F_4-TCNQ), and find similar semiconductor-metal transition.

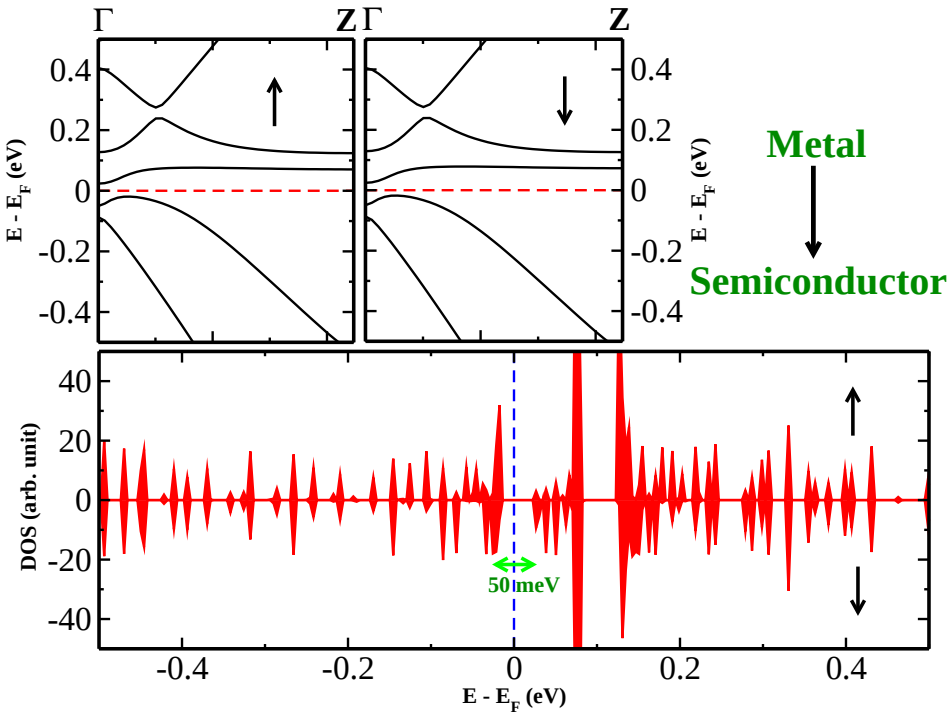

Figure 6.6: The spin-polarized electronic band structures and density of states (DOS) for (5,5) SWCNT-TCNE complex, showing metal to semiconductor transition. The Fermi level is set to zero. The up and down arrows indicate the majority and minority spin channel, respectively.

6.4 Conclusions

In this chapter, we have discussed the fascinating effects of molecular doping on the modification of the intriguing electronic structure of pristine 2D graphene and various SWCNTs, using first-principles density functional theory level of calculations. Our results have shown that the nature of the external dopants molecules has a significant impact for modifying electronic structures of graphene and carbon nanotubes through charge transfer mechanisms. We have also shown that, the presence of organic donor or acceptor molecules on graphene can significantly change the electronic properties, in particular, the characteristic Raman spectra of graphene. For all cases, the magnitude of adsorption energies are found to be moderate, suggesting physisorption process. The adsorption is mainly governed by the charge transfer interactions, the signature of which is found experimentally in UV-visible spectra. We have found a downward shift of Fermi level relative to the Dirac point for TCNE and TCNQ adsorbed graphene, whereas, the Fermi level shifts upward from the Dirac point for TTF intercalated graphene. Moreover, we have also found that a small band gap opens up in between the valence and conduction bands, and thus, tuning of carrier concentrations indeed can change the graphene electronic structure from semi-metallic to perfect metallic through semiconducting behavior. Interestingly, we find that the molecular charge-transfer results in stiffening and softening of Raman active G-band frequency, depending on the nature of the dopant molecule, as found experimentally. Thus, the Raman spectra can be used as a finger print for understanding the molecular charge-transfer interactions in graphene-adsorbate complexes.

Additionally, the results obtained from the molecular doping of SWCNTs, have revealed that, the electron acceptor molecules strongly adsorb on both the nanotubes in comparison to the electron donor moleucles, with the greater adsorption affinity found for the metallic SWCNTs. Interestingly, the calculations have also shown that, TCNE causes metal $\rightarrow$ semiconductor transition in (5,5)SWCNT, while, the semiconducting (8,0)SWCNT transforms to a metal in presence of surface adsorbed strong electron acceptors, TCNQ and F_4-TCNQ. Moreover, the presence of TCNQ and F_4-TCNQ on (8,0)SWCNT results in spin-polarization on the nanotube.

Since adsorption of donor or acceptor dopants gives rise to tuning of band-gap as well as carrier type in graphene and SWCNTs, we have suggested that, it is possible to fabricate the graphene and nanotubes based electronic devices through simple means, possibly even a p-n junction using both donor and acceptor molecules.

Bibliography

[1] J. D. Watson and F. H. Crick, Nature **171**, 737 (1953).

[2] R. D. Wells, R. Dere, M. L. Hebert, M. Napierala, and L. S. Son, Nucleic Acids Res. **33**, 3785 (2005).

[3] J. Zhao, A. Bacolla, G. Wang, and K. M. Vasquez, Cell. Mol. Life Sci. **67**, 43 (2010).

[4] G. Wang and K. M. Vasquez, Mutat. Res. **598**, 103 (2006).

[5] A. Bacolla and R. D. Wells, Mol. Carcinog **48**, 273 (2009).

[6] J. Y. Lee, B. Okumus, D. S. Kim, and T. Ha, Proc. Natl. Acad. Sci. U.S.A **102**, 18938 (2005).

[7] Z. Du, Y. Zhao, and N. Li, Genome Res. **18**, 233 (2008).

[8] L. Organesian and T. M. Bryan, Bioessays **29**, 155 (2007).

[9] D. J. Patel, A. T. Phan, and V. Kuryavyi, Nucleic Acids Res. **35**, 7429 (2007).

[10] J. T. Davis and G. P. Spada, Chem. Soc. Rev. **36**, 296 (2007).

[11] A. Calzonari, R. D. Felice, and E. Molinari, Solid State Commun. **131**, 557 (2004).

[12] A.-M. Guo and S.-J. Xiong, Phys. Rev. B **80**, 035115 (2009).

[13] M. F. Crommie, C. P. Lutz, and D. M. Eigler, Science **262**, 218 (1993).

[14] G. D. Stucky and J. E. Macdougall, Science **247**, 669 (1990).

[15] T. Takagahara and K. Takeda, Phys. Rev. B **46**, 15578 (1992).

[16] B. Delley and E. F. Steigmeier, Phys. Rev. B **47**, 1397 (1993).

[17] G. W. Bryant, Phys. Rev. B **37**, 8763 (1988).

[18] M. V. R. Krishna and R. A. Friesner, J. Chem. Phys. **95**, 8309 (1991).

[19] G. T. Einevoll, Phys. Rev. B **45**, 3410 (1992).

[20] P. B. Wiegmann, Phys. Rev. Lett. **60**, 821 (1988).

[21] Q. M. Si, S. Rabello, K. Ingersent, and J. L. Smith, Nature **413**, 804 (2001).

[22] E. Dagotto, Science **309**, 257 (2005).

[23] M. Capone, M. Fabrizio, C. Castellani, and E. Tosatti, Science **296**, 2364 (2002).

[24] S. Chakravarty, M. P. Gelfand, and S. Kivelson, Science **254**, 970 (1991).

[25] C. D. Dimitrakopoulos and P. R. L. Malenfant, Adv. Mater. **14**, 99 (2002).

[26] J. S. Moodera, L. R. Kinder, T. M. Wong, and R. Meservey, Phys. Rev. Lett. **74**, 3273 (1995).

[27] R. Venkatasubramanian, E. Siivola, T. Colpitts, and B. O'Quinn, Nature **413**, 597 (2001).

[28] Z. Bao, A. Dodabalapur, and A. J. Lovinger, Appl. Phys. Lett. **69**, 4108 (1996).

[29] R. L. Hoffman, B. J. Norris, and J. F. Wager, Appl. Phys. Lett. **82**, 733 (2003).

[30] M. Dawber, K. M. Rabe, and J. F. Scott, Rev. Mod. Phys. **77**, 1083 (2005).

[31] A. R. Murphy and J. M. J. Frechet, Chem. Rev. **107**, 1066 (2007).

[32] D. H. Lowndes, D. B. Geohegan, A. A. Puretzky, D. P. Norton, and C. M. Rouleau, Science **273**, 898 (1996).

[33] J. Moreland and J. W. Ekin, J. Appl. Phys. **58**, 3888 (1985).

[34] C. Zhou, C. J. Muller, M. R. Deshpande, J. W. Sleight, and M. A. Reed, Appl. Phys. Lett. **67**, 1160 (1995).

[35] J. J. Parks, A. R. Champagne, G. R. Hutchison, S. Flores-Torres, H. D. Abruna, and D. C. Ralph, Phys. Rev. Lett. **99**, 026601 (2007).

[36] L. Fernandez-Seivane, V. M. Garcia-Suarez, and J. Ferrer, Phys. Rev. B **75**, 075415 (2007).

[37] G. Binnig, H. Rohrer, C. Gerber, and E. Weibel, Appl. Phys. Lett. **40**, 178 (1981).

[38] I. W. Lyo and P. Avouris, Science **253**, 173 (1991).

[39] A. A. Dhirani, R. W. Zehner, R. P. Hsung, P. Guyotsionnest, and L. R. Sita, J. Am. Chem. Soc. **118**, 3319 (1996).

[40] T. A. Jung, R. R. Schlittler, and J. K. Gimzewski, Nature **386**, 696 (1997).

[41] M. T. Reetz, W. Helbig, S. A. Quaiser, U. Stimming, N. Breuer, and R. Vogel, Science **267**, 367 (1995).

[42] Z. L. Wang, J. Phys. Chem. B **104**, 1153 (2000).

[43] W. Coene, G. Janssen, M. O. Debeeck, and D. Vandyck, Phys. Rev. Lett. **69**, 3743 (1992).

[44] G. Binnig, H. Rohrer, C. Gerber, and E. Weibel, Phys. Rev. Lett. **56**, 930 (1986).

[45] F. J. Giessibl, Science **267**, 68 (1995).

[46] M. Rief, F. Oesterhelt, B. Heymann, and H. E. Gaub, Science **275**, 1295 (1997).

[47] G. Meyer and N. M. Amer, Appl. Phys. Lett. **53**, 1045 (1988).

[48] R. W. Carpick and M. Salmeron, Chem. Rev. **97**, 1163 (1997).

[49] D. Rugar and P. Hansma, Phys. Today **43**, 23 (1990).

[50] J. R. Schrieffer and A. P. Kampf, J. Phys. Chem. Solids **56**, 1673 (1995).

[51] C. G. Olson, R. Liu, A. B. Yang, D. W. Lynch, A. J. Arko, R. S. List, B. W. Veal, Y. C. Chang, P. Z. Jiang, and A. P. Paulikas, Science **245**, 731 (1989).

[52] N. P. Armitage, F. Ronning, D. H. Lu, C. Kim, A. Damascelli, K. M. Shen, D. L. Feng, H. Eisaki, Z. X. Shen, P. K. Mang, *et al.*, Phys. Rev. Lett. **88**, 257001 (2002).

[53] T. Ohta, A. Bostwick, J. L. McChesney, T. Seyller, K. Horn, and E. Rotenberg, Phys. Rev. Lett. **98**, 206802 (2007).

[54] T. Kondo, A. F. Santander-Syro, O. Copie, C. Liu, M. E. Tillman, E. D. Mun, J. Schmalian, S. L. Bud'ko, M. A. Tanatar, P. C. Canfield, *et al.*, Phys. Rev. Lett. **101**, 147003 (2008).

[55] O. Avery, C. Macleod, and M. McCarty, J. Expt. Med. **79**, 137 (1944).

[56] A. D. Hershey and M. C. Avery, J. Gen. Phyysiol. **36**, 39 (1952).

[57] R. E. Franklin and R. G. Gosling, Nature **171**, 740 (1953).

[58] M. H. F. Wilkins, A. R. Stokes, and H. R. Wilson, Nature **171**, 738 (1953).

[59] E. Chargaff, Experientia **6**, 201 (1950).

[60] R. Wing, H. Drew, T. Takano, C. Broka, S. Tanaka, K. Itakura, and R. E. Dickerson, Nature **287**, 755 (1980).

[61] A. Ghosh and M. Bansal, Acta Cryst. D **59**, 620 (2003).

[62] R. R. Sinden, DNA Structure and Function; Academic Press, San Diego (1994).

[63] A. Rich, A. Nordheim, and A. H. Wang, Annu. Rev. Biochem. **53**, 791 (1984).

[64] E. Henderson, C. C. Hardin, S. K. Walk, I. Tinoco, and E. H. Balckburn, Cell (Cambridge, Mass.) **51**, 899 (1987).

[65] J. R. Williamson, M. K. Raghuraman, and T. R. Cech, Cell (Cambridge, Mass.) **59**, 871 (1989).

[66] A. M. Zahler, J. R. Williamson, T. R. Cech, and D. M. Prescott, Nature **350**, 718 (1991).

[67] D. M. Tasset, M. F. Kubik, and W. Steiner, J. Mol. Bio. **272**, 688 (1997).

[68] T. Simonsson, Biol. Chem. **382**, 621 (2001).

[69] W. U. Dittmer, A. Reuter, and F. C. Simmel, Angew. Chem., Int. Ed. **43**, 3550 (2004).

[70] D. Miyoshi, M. Inoue, and N. Sugimoto, Angew. Chem., Int. Ed. **45**, 7716 (2006).

[71] K. Dutta, T. Fujimoto, M. Inoue, D. Miyoshi, and N. Sugimoto, Chem. Commun. **46**, 7772 (2010).

[72] K. L. Wang, M. X. You, Y. Chen, D. Han, Z. Zhu, J. Huang, K. Williams, C. J. Yang, and W. H. Tan, Angew. Chem., Int. Ed. **50**, 6098 (2011).

[73] D. Miyoshi and N. Sugimoto, DNA Nanotechnology Methods and Protocols, ed. G. Zuccheri and B. Samori, Humana Press, New York **7**, 93 (2011).

[74] V. M. Marathias and P. H. Bolton, Biochemistry **38**, 4355 (1999).

[75] Y. Wang and D. J. Patel, Structure **2**, 1141 (1994).

[76] S. Burge, G. N. Parkinson, P. Hazel, A. K. Todd, and S. Neidle, Nucleic Acids Res. **34**, 5402 (2006).

[77] G. Laughlan, A. I. H. Murchie, D. G. Norman, M. H. Moore, P. C. E. Moody, D. M. J. Lilley, and B. Luisi, Science **265**, 520 (1994).

[78] K. Phillips, Z. Dauter, A. H. I. Murchie, D. M. J. Lilley, and B. Luisi, J. Mol. Biol. **273**, 171 (1997).

[79] G. N. Parkinson, M. P. Lee, and S. Neidle, Nature (Lond.) **417**, 876 (2002).

[80] M. Gellert, M. N. Lipsett, and D. R. Davies, Proc. Natl. Acad. Sci. U. S. A. **48**, 2013 (1962).

[81] J. Choi and T. Majima, Chem. Soc. Rev. **40**, 5893 (2011).

[82] K. Fujita and H. Ohno, Chem. Commun. **48**, 5751 (2012).

[83] J. Novotný, P. Kulhánek, and R. Marek, J. Phys. Chem. Lett. **3**, 1788 (2012).

[84] M. Nikan, B. O. Patrick, and J. C. Sherman, ChemBioChem **13**, 1413 (2012).

[85] R. K. Moyzis, J. M. Buckingham, L. S. Cram, M. Dani, L. L. Deaven, M. D. Jones, J. Meyne, R. L. Ratliff, and J. R. Wu, Proc. Natl. Acad. Sci. U. S. A. **85**, 6622 (1988).

[86] S. R. Kerwin, Curr. Pharmaceutic. Design **6**, 441 (2000).

[87] B. Corry and N. M. Smith, Chem. Commun. **48**, 8958 (2012).

[88] D. Y. Sun, B. Thompson, B. E. Cathers, M. Salazar, S. M. Kerwin, J. O. Trent, T. C. Jenkins, S. Neidle, and L. H. Hurley, J. Med. Chem. **40**, 2113 (1997).

[89] I. Haq, J. O. Trent, B. Z. Chowdhry, and T. C. Jenkins, J. Am. Chem. Soc. **121**, 1768 (1999).

[90] S. Neidle, Curr. Opin. Struct. Biol. **19**, 239 (2009).

[91] R. T. Wheelhouse, D. K. Sun, H. Y. Han, F. X. G. Han, and L. H. Hurley, J. Am. Chem. Soc. **120**, 3261 (1998).

[92] H. Yaku, T. Fujimoto, T. Murashima, D. Miyoshi, and N. Sugimoto, Chem. Commun. **48**, 6203 (2012).

[93] D. Sen and W. Gilbert, Methods Enzymol. **211**, 191 (1992).

[94] A.-M. Guo and S.-J. Xiong, Phys. Rev. B **80**, 035115 (2009).

[95] M. Cavallari, A. Calzolari, A. Garbesi, and R. D. Felice, J. Phys. Chem. B **110**, 26337 (2006).

[96] G. W. Collie, S. M. Haider, S. Neidle, and G. N. Parkinson, Nucleic Acids Res. **259**, 1 (2010).

[97] J. Deng, Y. Xiong, and M. Sundaralingam, Proc. Natl. Acad. Sci. **98**, 13665 (2001).

[98] C. Cheong and P. B. Moore, Biochemistry **31**, 8406 (1992).

[99] H. Martadinata, B. Heddi, K. W. Lim, and A. T. Phan, Biochemistry **50**, 6455 (2011).

[100] B. Datta, M. E. Bier, S. Roy, and B. A. Armitage, J. Am. Chem. Soc. **127**, 4199 (2005).

[101] Y. Krishnan-Ghosh, E. Stephens, and S. Balasubramanian, J. Am. Chem. Soc. **126**, 5944 (2004).

[102] N. K. Sharma and K. N. Ganesh, Org. Biomol. Chem. **9**, 725 (2011).

[103] S. Saha, J. Cai, D. Eiler, and A. D. Hamilton, Chem. Commun. **46**, 1685 (2010).

[104] V. Esposito, A. Randazzo, A. Messere, A. Galeone, L. Petraccone, C. Giancola, G. Piccialli, and L. Mayol, Eur. J. Org. Chem. p. 3364 (2003).

[105] B. Datta, C. Schmitt, and B. A. Armitage, J. Am. Chem. Soc. **125**, 4111 (2003).

[106] B. Datta and B. A. Armitage, J. Am. Chem. Soc. **123**, 9612 (2001).

[107] P. Peumans, A. Yakimov, and S. R. Forrest, J. Appl. Phys. **93**, 3693 (2003).

[108] J. Britt and C. Ferekides, Appl. Phys. Lett. **62**, 2851 (1993).

[109] S. Yoo, B. Domercq, and B. Kippelen, Appl. Phys. Lett. **85**, 5427 (2004).

[110] R. W. Birkmire and E. Eser, Annual Rev. Mater. Sci. **27**, 625 (1997).

[111] T. L. Chu and S. S. Chu, Solid-State Electronics **38**, 533 (1995).

[112] Z. Bao, A. Dodabalapur, and A. J. Lovinger, Appl. Phys. Lett. **69**, 4108 (1996).

[113] K. Nomura, H. Ohta, A. Takagi, T. Kamiya, M. Hirano, and H. Hosono, Nature **432**, 488 (2004).

[114] F. Garnier, G. Horowitz, X. H. Peng, and D. Fichou, Adv. Mater. **2**, 592 (1990).

[115] K. Nomura, H. Ohta, K. Ueda, T. Kamiya, M. Hirano, and H. Hosono, Science **300**, 1269 (2003).

[116] C. R. Kagan, D. B. Mitzi, and C. D. Dimitrakopoulos, Science **286**, 945 (1999).

[117] H. E. Katz, J. Mater. Chem. **7**, 369 (1997).

[118] J. Y. Ouyang, C. W. Chu, C. R. Szmanda, L. P. Ma, and Y. Yang, Nat. Mater. **3**, 918 (2004).

[119] A. V. Rozhkov, G. Giavaras, Y. P. Bliokh, V. Freilikher, and F. Nori, Phys. Rep. **503**, 77 (2011).

[120] H. W. Kroto, J. R. Heath, S. C. O'Brien, R. F. Curl, and R. E. Smalley, Nature **318**, 162 (1985).

[121] S. Iijima, Nature **354**, 56 (1991).

[122] S. Iijima and T. Ichihashi, Nature **363**, 603 (1993).

[123] T. W. Ebbesen and P. M. Ajayan, Nature **358**, 220 (1992).

[124] R. E. Peierls, Helv. Phys. Acta **7**, 81 (1934).

[125] R. E. Peierls, Ann. Inst. Henri Poincare **5**, 177 (1935).

[126] L. D. Landau, Phys. Z. Sowjetunion **11**, 26 (1937).

[127] L. D. Landau and E. M. Lifshitz, Statistical Physics Part I, Sections 137 and 138 (Pergamon, Oxford, (1980)) .

[128] N. D. Mermin, Phys. Rev. **176**, 250 (1968).

[129] K. S. Novoselov, A. K. Geim, S. V. Morozov, D. Jiang, Y. Zhang, S. V. Dubonos, I. V. Grigorieva, and A. A. Firsov, Science **306**, 666 (2004).

[130] K. S. Novoselov, D. Jiang, F. Schedin, T. J. Booth, W. Khotkevich, S. V. Morozov, and A. K. Geim, Proc. Natl. Acd. Sci. **102**, 10451 (2005).

[131] K. S. Novoselov, A. K. Geim, S. V. Morozov, D. Jiang, M. I. Katsnelson, I. V. Grigorieva, S. V. Dubonos, and A. A. Firsov, Nature **438**, 197 (2005).

[132] K. S. Subrahmanyam, L. S. Panchakarla, A. Govindaraj, and C. N. R. Rao, J. Phys. Chem. C **113**, 4257 (2009).

[133] J. C. Meyer, A. K. Geim, M. I. Katsnelson, K. S. Novoselov, T. J. Booth, and S. Roth, Nature **446**, 60 (2007).

[134] A. Fasolino, J. H. Los, and M. I. Katsnelson, Nat. Mater. **6**, 858 (2007).

[135] E. H. Lieb, Phys. Rev. Lett. **62**, 1201 (1989).

[136] D. A. Areshkin, D. Gunlycke, and C. T. White, Nano. Lett. **7**, 204 (2007).

[137] Y. B. Zhang, Y. W. Tan, H. L. Stormer, and P. Kim, Nature **438**, 201 (2005).

[138] K. S. Novoselov, E. McCann, S. V. Morozov, V. I. Falko, M. I. Katsnelson, U. Zeitler, D. Jiang, F. Schedin, and A. K. Geim, Nat. Phys. **2**, 177 (2006).

[139] V. P. Gusynin and S. G. Sharapov, Phys. Rev. Lett. **95**, 146801 (2005).

[140] C. L. Kane and E. J. Mele, Phys. Rev. Lett. **95**, 226801 (2005).

[141] K. S. Novoselov, Z. Jiang, Y. Zhang, S. V. Morozov, H. L. Stormer, U. Zeitler, J. C. Mann, G. S. Boebinger, P. Kim, and A. K. Geim, Science **315**, 1379 (2007).

[142] K. Nomura and A. H. MacDonald, Phys. Rev. Lett. **96**, 256602 (2006).

[143] C. L. Kane and E. J. Mele, Phys. Rev. Lett. **95**, 146802 (2005).

[144] D. A. Abanin, P. A. Lee, and L. S. Levitov, Phys. Rev. Lett. **96**, 176803 (2006).

[145] J. Alicea and M. P. A. Fisher, Phys. Rev. B **74**, 075422 (2006).

[146] D. A. Abanin, K. S. Novoselov, U. Zeitler, P. A. Lee, A. K. Geim, and L. S. Levitov, Phys. Rev. Lett. **98**, 196806 (2007).

[147] Z. Jiang, Y. Zhang, H. L. Stormer, and P. Kim, Phys. Rev. Lett. **99**, 106802 (2007).

[148] L. Brey and H. A. Fertig, Phys. Rev. B **73**, 195408 (2006).

[149] A. H. C. Neto, F. Guinea, and N. M. R. Peres, Phys. Rev. B **73**, 205408 (2006).

[150] I. F. Herbut, Phys. Rev. B **75**, 165411 (2007).

[151] L. Sheng, D. N. Sheng, F. D. M. Haldane, and L. Balents, Phys. Rev. Lett. **99**, 196802 (2007).

[152] Y. Hasegawa and M. Kohmoto, Phys. Rev. B **74**, 155415 (2006).

[153] F. Guinea, M. I. Katsnelson, and A. K. Geim, Nat. Phys. **6**, 30 (2010).

[154] S. Pisana, M. Lazzeri, C. Casiraghi, K. S. Novoselov, A. K. Geim, A. C. Ferrari, and F. Mauri, Nat. Mater. **6**, 198 (2007).

[155] M. I. Katsnelson, K. S. Novoselov, and A. K. Geim, Nat. Phys. **2**, 620 (2006).

[156] C. W. J. Beenakker, Rev. Mod. Phys. **80**, 1337 (2008).

[157] N. Stander, B. Huard, and D. Goldhaber-Gordon, Phys. Rev. Lett. **102**, 026807 (2009).

[158] A. F. Young and P. Kim, Nat. Phys. **5**, 222 (2009).

[159] G. Csanyi, P. B. Littlewood, A. H. Nevidomskyy, C. J. Pickard, and B. D. Simons, Nat. Phys. **1**, 42 (2005).

[160] B. Uchoa and A. H. C. Neto, Phys. Rev. Lett. **98**, 146801 (2007).

[161] Y. J. Jiang, D. X. Yao, E. W. Carlson, H. D. Chen, and J. P. Hu, Phys. Rev. B **77**, 235420 (2008).

[162] J. Gonzalez and E. Perfetto, Phys. Rev. B **76**, 155404 (2007).

[163] H. B. Heersche, P. Jarillo-Herrero, J. B. Oostinga, L. M. K. Vandersypen, and A. Morpurgo, Nature **446**, 56 (2007).

[164] O. V. Yazyev and L. Helm, Phys. Rev. B **75**, 125408 (2007).

[165] L. R. Radovic and B. Bockrath, J. Am. Chem. Soc. **127**, 5917 (2005).

[166] K. Harigaya, J. Phys.: Condens. Matter **13**, 1295 (2001).

[167] J. J. Palacios, J. Fernandez-Rossier, and L. Brey, Phys. Rev. B **77**, 195428 (2008).

[168] K. Harigaya and T. Enoki, Chem. Phys. Lett. **351**, 128 (2002).

[169] O. V. Yazyev, Phys. Rev. Lett. **101**, 037203 (2008).

[170] H. Kumazaki and D. S. Hirashima, J. Phys. Soc. Jpn. **76**, 064713 (2007).

[171] H. Min, G. Borghi, M. Polini, and A. H. MacDonald, Phys. Rev. B **77**, 041407 (2008).

[172] K. I. Sasaki and R. Saito, J. Phys. Soc. Jpn. **77**, 054703 (2008).

[173] J. Jung and A. H. MacDonald, Phys. Rev. B **79**, 235433 (2009).

[174] J. Jung, T. Pereg-Bernea, and A. H. MacDonald, Phys. Rev. Lett. **102**, 227205 (2009).

[175] W. F. Li, M. W. Zhao, Y. Y. Xia, R. Q. Zhang, and Y. G. Mu, J. Mater. Chem. **19**, 9274 (2009).

[176] V. V. Cheianov and V. I. Fal'ko, Phys. Rev. B **74**, 041403 (2006).

[177] V. V. Cheianov, V. I. Fal'ko, and B. L. Altshuler, Science **315**, 1252 (2007).

[178] B. Huard, J. A. Sulpizio, N. Stander, K. Todd, B. Yang, and D. Goldhaber-Gordon, Phys. Rev. Lett. **98**, 236803 (2007).

[179] J. R. Williams, L. DiCarlo, and C. M. Marcus, Science **317**, 638 (2007).

[180] L. M. Zhang and M. M. Fogler, Phys. Rev. Lett. **100**, 116804 (2008).

[181] A. K. Geim and K. S. Novoselov, Nat. Mater. **6**, 183 (2007).

[182] A. H. C. Neto, F. Guinea, N. M. R. Peres, K. S. Novoselov, and A. K. Geim, Rev. Mod. Phys. **81**, 109 (2009).

[183] D. Pacilé, J. Meyer, C. Ö. Girit, and A. Zettl, Appl. Phys. Lett. **92**, 133107 (2008).

[184] Y. Shi, C. Hamsen, X. Jia, K. K. Kim, A. Reina, M. Hofman, A. L. Hsu, K. Zhang, H. Li, Z. Y. Juang, *et al.*, Nano Lett. **10**, 4134 (2010).

[185] L. Song, L. Ci, H. Lu, P. B. Sorokin, C. Jin, J. Ni, A. G. Kvashnin, D. G. Kvashnin, J. Lou, B. I. Yakobson, *et al.*, Nano Lett. **10**, 3209 (2010).

[186] A. Ismach, H. Chou, D. A. Ferrer, Y. Wu, S. McDonnell, H. C. Floresca, A. Covacevich, C. Pope, R. Piner, M. J. Kim, *et al.*, ACS Nano **6**, 6378 (2012).

[187] K. K. Kim, A. Hsu, X. Jia, S. M. Kim, Y. Shi, M. Hofmann, D. Nezich, J. F. Rodriguez-Nieva, M. Dresselhaus, T. Palacios, *et al.*, Nano Lett. **12**, 161 (2012).

[188] W. Q. Han, L. Wu, Y. Zhu, K. Watanabe, and T. Taniguchi, Appl. Phys. Lett. **93**, 223103 (2008).

[189] C. Jin, F. Lin, K. Suenaga, and S. Iijima, Phys. Rev. Lett. **102**, 195505 (2009).

[190] X. Blase, A. Rubio, S. G. Louie, and M. L. Cohen, Phys. Rev. B **51**, 6868 (1995).

[191] K. Watanabe, T. Taniguchi, and H. Kanda, Nat. Mater. **3**, 404 (2004).

[192] B. Arnaud, S. Lebegue, P. Rabiller, and M. Alouani, Phys. Rev. Lett. **96**, 026402 (2006).

[193] A. H. C. Neto, F. Guinea, N. M. R. Peres, K. S. Novoselov, and A. K. Geim, Rev. Mod. Phys. **81**, 109 (2009).

[194] M. I. Katsnelson, Mater. Today **10**, 20 (2007).

[195] T. Enoki, Y. Kobayashi, and K. I. Fukui, Int. Rev. Phys. Chem. **26**, 609 (2007).

[196] M. J. Allen, V. C. Tung, and R. B. Kaner, Chem. Rev. **110**, 132 (2010).

[197] C. N. R. Rao, A. K. Sood, R. Voggu, and K. S. Subrahmanyam, J. Phys. Chem. Lett. **1**, 572 (2010).

[198] C. N. R. Rao, A. K. Sood, K. S. Subrahmanyam, and A. Govindaraj, Angew. Chem. Int. Ed. **48**, 7752 (2009).

[199] S. M. M. Dubois, Z. Zanolli, X. Declerck, and J. C. Charlier, Eur. Phys. J. B. **72**, 1 (2009).

[200] M. H. Liang, B. Luo, and L. J. Zhi, Int. J. Ener. Res. **33**, 1161 (2009).

[201] D. W. Boukhvalov and M. I. Katsnelson, J. Phys.: Condens. Matter **21**, 344205 (2009).

[202] H. K. M. Burghard and K. Kern, Adv. Mater. **21**, 2586 (2009).

[203] N. M. R. Peres, J. Phys.: Condens. Matter. **21**, 323201 (2009).

[204] A. K. Geim, Science **324**, 1530 (2009).

[205] P. Avouris, Z. H. Chen, and V. Perebeinos, Nat. Nanotech. **2**, 605 (2007).

[206] Y.-W. Son, M. L. Cohen, and S. G. Louie, Nature **444**, 347 (2006).

[207] H. Raza and E. C. Kan, Phys. Rev. B **77**, 245434 (2008).

[208] S. Dutta and S. K. Pati, J. Phys. Chem. B **112**, 1333 (2008).

[209] S. Dutta, A. K. Manna, and S. K. Pati, Phys. Rev. Lett. **102**, 096601 (2009).

[210] S. Dutta and S. K. Pati, Carbon **48**, 4409 (2010).

[211] Z. Yu, M. L. Hu, C. X. Zhang, C. Y. He, L. Z. Sun, and J. Zhong, J. Phys. Chem. C **115**, 10836 (2011).

[212] Y. Liu, X. Wu, Y. Zhao, X. C. Zeng, and J. Yang, J. Phys. Chem. C **115**, 9442 (2011).

[213] E. A. Basheer, P. Parida, and S. K. Pati, New. J. Phys. **13**, 053008 (2011).

[214] S. Dutta and S. K. Pati, J. Mater. Chem. **20**, 8207 (2010).

[215] C. H. Park and S. G. Louie, Nano Lett. **8**, 2200 (2008).

[216] R. B. Chen, C. P. Chang, F. L. Shyu, and M. F. Lin, Solid State Commun. **123**, 365 (2002).

[217] V. Barone and J. E. Peralta, Nano Lett. **8**, 2210 (2008).

[218] F. Zheng, G. Zhou, Z. Liu, J. Wu, W. Duan, B.-L. Gu, and S. B. Zhang, Phys. Rev. B **78**, 205415 (2008).

[219] Y. W. Son, M. L. Cohen, and S. G. Louie, Phys. Rev. Lett. **97**, 216803 (2006).

[220] X. Y. Yang, X. Dou, A. Rouhanipour, L. J. Zhi, H. J. Rader, and K. Mullen, J. Am. Chem. Soc. **130**, 4216 (2008).

[221] L. J. Zhi and K. Mullen, J. Mater. Chem. **18**, 1472 (2008).

[222] S. Muller and K. Mullen, Phil. Trans. R. Soc. A **365**, 1453 (2007).

[223] J. S. Wu, W. Pisula, and K. Mullen, Chem. Rev. **107**, 718 (2007).

[224] L. Tapaszto, G. Dobrik, P. Lambin, and L. P. Biro, Nat. Nanotech. **3**, 397 (2008).

[225] C. Berger, Z. M. Song, X. B. Li, X. S. Wu, N. Brown, C. Naud, D. Mayou, T. B. Li, J. Hass, A. N. Marchenkov, *et al.*, Science **312**, 1191 (2006).

[226] C. Berger, Z. M. Song, T. B. Li, X. B. Li, A. Y. Ogbazghi, R. Feng, Z. T. Dai, A. N. Marchenkov, E. H. Conrad, P. N. First, *et al.*, J. Phys. Chem. B **108**, 19912 (2004).

[227] W. A. de Heer, C. Berger, X. S. Wu, P. N. First, E. H. Conrad, X. B. Li, T. B. Li, M. Sprinkle, J. Hass, M. L. Sadowski, *et al.*, Solid State Comm. **143**, 92 (2007).

[228] E. Bekyarova, M. E. Itkis, P. Ramesh, C. Berger, M. Sprinkle, W. A. de Heer, and R. C. Haddon, J. Am. Chem. Soc. **131**, 1336 (2009).

[229] S. S. Datta, D. R. Strachan, S. M. Khamis, and A. T. C. Johnson, Nano Lett. **8**, 1912 (2008).

[230] X. L. Li, X. R. Wang, L. Zhang, S. W. Lee, and H. J. Dai, Science **319**, 1229 (2008).

[231] X. R. Wang, Y. J. Ouyang, X. L. Li, H. L. Wang, J. Guo, and H. J. Dai, Phys. Rev. Lett. **100**, 206803 (2008).

[232] Z. Li, W. Zhang, Y. Luo, J. Yang, and J. G. Hou, J. Am. Chem. Soc. **131**, 6320 (2009).

[233] D. V. Kosynkin, A. L. Higginbotham, A. Sinitskii, J. R. Lomeda, A. Dimiev, B. K. Price, and J. M. Tour, Nature **458**, 872 (2009).

[234] N. L. Rangel, J. C. Sotelo, and J. M. Seminario, J. Chem. Phys. **131**, 031105 (2009).

[235] L. Y. Jiao, L. Zhang, X. R. Wang, G. Diankov, and H. J. Dai, Nature **458**, 877 (2009).

[236] A. Hirsch, Angew. Chem. Int. Ed. **48**, 6594 (2009).

[237] L. Ci, L. Song, C. H. Jin, D. Jariwala, D. X. Wu, Y. J. Li, A. Srivastava, Z. F. Wang, K. Storr, L. Balicas, *et al.*, Nat. Mater. **9**, 430 (2010).

[238] I. Caretti, R. Torres, R. Gago, A. R. Landa-Canovas, and I. Jimenez, Chem. Mater. **22**, 1949 (2010).

[239] K. Raidongia, D. Jagadeesan, M. Upadhyay-Kahaly, U. V. Waghmare, S. K. Pati, M. Eswaramoorthy, and C. N. R. Rao, J. Mater. Chem. **18**, 83 (2008).

[240] J. Yu, J. Ahn, S. Yoon, Q. Zhang, B. Gan, K. Chew, M. Yu, X. Bai, and E. Wang, Appl. Phys. Lett. **77**, 1949 (2000).

[241] R. Arenal, X. Blase, and A. Loiseau, Adv. Phys. **59**, 101 (2010).

[242] O. Stephan, P. M. Ajayan, C. Colliex, P. Redlich, J. M. Lambert, P. Bernier, and P. Lefin, Science **266**, 1683 (1994).

[243] E. J. Kan, X. Wu, Z. Li, X. C. Zeng, J. Yang, and J. Hou, J. Chem. Phys. **129**, 084712 (2008).

[244] Y. Liu, X. Wu, Y. Zhao, X. C. Zeng, and J. Yang, J. Phys. Chem. C **000**, 000 (2011).

[245] S. Tang and Z. Cao, Phys. Chem. Chem. Phys **12**, 2313 (2010).

[246] S. Dutta, A. K. Manna, and S. K. Pati, Phys. Rev. Lett. **102**, 096601 (2009).

[247] Y. Ding, Y. Wang, and J. Ni, Appl. Phys. Lett. **95**, 123105 (2009).

[248] T. Hatakeyama, S. Hashimoto, S. Seki, and M. Nakamura, J. Am. Chem. Soc. **133**, 18614 (2011).

[249] A. K. Manna and S. K. Pati, J. Phys. Chem. C **115**, 10842 (2011).

[250] S. Kumar, N. Kamaraju, K. S. Vasu, A. Nag, A. K. Sood, and C. N. R. Rao, Chem. Phys. Lett. **499**, 152 (2010).

[251] K. Raidongia, D. Jagadeesan, M. Upadhyay-Kahaly, U. V. Waghmare, S. K. Pati, M. Eswaramoorthy, and C. N. R. Rao, J. Mater. Chem. **18**, 83 (2008).

[252] L. S. Panchakarla, K. S. Subrahmanyam, S. K. Saha, A. Govindaraj, H. R. Krishnamurthy, U. V. Waghmare, and C. N. R. Rao, Adv. Mater. **21**, 4726 (2009).

[253] A. Nag, K. Raidongia, K. P. S. S. Hembram, R. Datta, U. V. Waghmare, and C. Rao, ACS Nano **4**, 1539 (2010).

[254] K. Venu, S. Kanuri, K. Raidongia, K. P. S. S. Hembram, U. V. Waghmare, and R. Datta, Solid State Commun. **150**, 2262 (2010).

[255] J. Yu and J. Rafique, Int. J. Nanotech. **4**, 32 (2007).

[256] M. Hubáček and T. Sato, J. Solid State Chem. **114**, 258 (1995).

[257] J. D. R. Martins and H. Chacham, ACS Nano **5**, 385 (2011).

[258] J. Jung, Z. Qiau, Q. Niu, and A. H. MacDonald, Nano Lett. **12**, 2936 (2012).

[259] M. Noei, M. Fathipour, and M. Pourfath, Jpn. J. Appl. Phys. **51**, 035101 (2012).

[260] K. S. Novoselov, A. K. .Geim, S. V. Morozov, D. Jiang, Y. Dubonos, S. V. Grigorieva, I. V., and A. A. Firsov, Science **306**, 666 (2004).

[261] M. S. Dresselhaus, G. Dresselhaus, and P. C. Eklund, Science of Fullerenes and Carbon Nanotubes: Their Properties and Applications, Academic Press, New York (1996).

[262] J. M. Marulanda, Electronic Properties of Carbon Nanotubes **DOI:10.5772/980**, ISBN 978 (2011).

[263] F. J. Owens, Mater. Lett. **61**, 1997 (2007).

[264] X. Blase, J. C. Charlier, A. D. Vita, and R. Car, Appl. Phys. Lett. **70**, 197 (1997).

[265] Y. L. Mao, X. H. Yan, Y. Xiao, J. X. Cao, and J. Xiang, Int. J. Mod. Phys. C **16**, 1363 (2005).

[266] C. S. Yeung, Y. K. Chen, and Y. A. Wang, Carbon Nanotubes - Growth and Applications **DOI: 10.5772/19139**, ISBN: 978 (2011).

[267] M. Mananghaya, E. Rodulfo, G. N. Santos, A. R. Villagracia, and A. N. Ladines, J. Nanomater. **2012**, 104891 (2012).

[268] F. Ding, Phys. Rev. B **72**, 205409 (2005).

[269] S. L. Mielke, D. Troya, S. Zhang, J. L. Li, S. Xiao, R. Car, R. S. Ruoff, G. C. Schatz, and T. Belytschko, Chem. Phys. Lett. **390**, 413 (2004).

[270] S. Zhang, S. L. Mielke, R. Khare, D. Troya, R. S. Ruoff, G. C. Schatz, and T. Belytschko, Phys. Rev. B **71**, 115403 (2005).

[271] M. Grujicic, G. Cao, and R. Singh, Appl. Sur. Sci. **211**, 166 (2003).

[272] J. Kotakoski, A. V. Krasheninnikov, and K. Nordlund, Phys. Rev. B **74**, 245420 (2006).

[273] B. Huang, Y. W. Son, G. Kim, W. Duan, and J. Ihm, J. Am. Chem. Soc. **131**, 17919 (2009).

[274] C. Wang, G. Zhou, H. Liu, J. Wu, Y. Qiu, B. L. Gu, and W. Duan, J. Phys. Chem. B **110**, 10266 (2006).

[275] A. K. Manna and S. K. Pati, Nanoscale **2**, 1190 (2010).

[276] J. P. Lu, J. Han, and C. K. Yang, Appl. Phys. Lett. **82**, 3746 (2003).

[277] J. Zhao, Z. Chen, Z. Zhou, H. Park, P. von R. Schleyer, and J. P. Lu, ChemPhysChem **6**, 598 (2005).

[278] V. N. Khabashesku, W. E. Billups, and J. L. Margrave, Acc. Chem. Res. **35**, 1087 (2002).

[279] Y. P. Sun, K. Fu, Y. Lin, and W. Huang, Acc. Chem. Res. **35**, 1096 (2002).

[280] V. Georgakilas, K. Kordatos, M. Prato, D. M. Guldi, M. Holzinger, and A. Hirsch, J. Am. Chem. Soc. **124**, 760 (2002).

[281] H. Kuzmany, A. Kukovecz, F. Simon, M. Holzweber, C. Kramberger, and T. Pichler, Synth. Metals **141**, 113 (2004).

[282] S. B. Fagan, A. J. R. da Silva, R. Mota, R. J. Baierle, and A. Fazzio, Phys. Rev. B **67**, 2003 (2003).

[283] K. V. Singh, R. R. Pandey, X. Wang, R. Lake, C. S. Ozkan, K. Wang, and M. Ozkan, Carbon **44**, 1730 (2006).

[284] J. H. Burroughes, D. D. C. Bradley, A. R. Brown, R. N. Marks, K. Mackey, R. H. Friend, P. L. Burns, and A. B. Holmes, Nature **347**, 539 (1990).

[285] R. H. Friend, R. W. Gymer, A. B. Holmes, J. H. Burroughes, R. N. Marks, C. Taliani, D. D. C. Bradley, D. A. dos Santos, J. L. Bredas, M. Logdlund, *et al.*, Nature **397**, 121 (1999).

[286] H. Sirringhaus, P. J. Brown, R. H. Friend, R. N. Nielsen, K. Bechgaard, B. M. W. Langeveld-Voss, R. A. J. Spiering, A. J. H.and Janssen, E. W. Meijer, P. Herwig, and D. W. de Leeuw, Nature **401**, 685 (1999).

[287] J. L. Bredas, D. Beljonne, V. Coropceanu, and J. Cornil, Chem. Rev. **104**, 4971 (2004).

[288] V. Coropceanu, J. Cornil, D. A. da Silvo Filho, Y. Olivier, R. Silbey, and J. L. Bredas, Chem. Rev. **107**, 926 (2007).

[289] J. L. Bredas, J. P. Calbert, D. A. da Silva Filho, and J. Cornil, PNAS **99**, 5804 (2002).

[290] A. Datta, S. Mohakud, and S. K. Pati, J. Mater. Chem. **17**, 1933 (2007).

[291] A. Datta, S. Mohakud, and S. K. Pati, J. Chem. Phys. **126**, 144710 (2007).

[292] S. Mohakud and S. K. Pati, J. Mater. Chem. **19**, 4356 (2009).

[293] R. G. Kepler, P. E. Bierstedt, and R. E. Merrifeld, Phys. Rev. Lett. **5**, 503 (1960).

[294] O. H. LeBlanc Jr., in Physics and Chemistry of the Organic Solid State, edited by M. M. Labes, D. Fox and A. Weissberger (Interscience, New York, (1957), p.133) .

[295] G. Horowitz, Adv. Mater. **10**, 365 (1998).

[296] G. Horowitz, J. Mater. Res **19**, 1946 (2004).

[297] A. Dodabalapur, L. Torsi, and H. E. Katz, Science **268**, 270 (1995).

[298] P. W. M. Blom, M. J. M. deJong, and J. J. M. Vleggaar, Appl. Phys. Lett. **68**, 3308 (1996).

[299] D. Fichou, Handbook of Oligo- and Polythiophenes; Wiley-VCH: Weinheim: New York, 1999. .

[300] A. M. van de Craats and J. M. Warman, Adv. Mater. **13**, 130 (2001).

[301] J. M. Warman, M. P. de Haas, G. Dicker, F. C. Grozema, J. Piris, and M. G. Debije, Chem. Mater. **16**, 4600 (2004).

[302] P. Prins, L. P. Candeias, A. J. J. M. van Breemen, J. Sweelssen, P. T. Herwig, H. F. M. Schoo, and L. D. A. Siebbeles, Adv. Mater. **17**, 718 (2005).

[303] R. J. O. M. Hoofman, M. P. de Haas, L. D. A. Siebbeles, and J. M. Warman, Nature **392**, 54 (1998).

[304] T. Holstein, Ann. Phys. (N. Y.) **8**, 325 (1959).

[305] T. Holstein, Ann. Phys. (N. Y.) **8**, 343 (1959).

[306] G. Nan, X. Yang, L. Wang, Z. Shuai, and Y. Zhao, Phy. Rev. B **79**, 115203 (2009).

[307] A. Troisi and G. Orlandi, Phys. Rev. Lett. **96**, 086601 (2006).

[308] A. Troisi and G. Orlandi, J. Phys. Chem. A **110**, 4065 (2006).

[309] A. Troisi, Adv. Mater. **19**, 2000 (2007).

[310] R. A. Marcus, Rev. Mod. Phys. **65**, 599 (1993).

[311] R. A. Marcus, J. Chem. Phys. **24**, 966 (1956).

[312] N. S. Hush, J. Chem. Phys. **28**, 962 (1958).

[313] K. Senthilkumar, F. C. Grozema, F. M. Bickelhaupt, and L. D. A. Siebbels, J. Chem. Phys. **119**, 9809 (2003).

[314] K. Senthilkumar, F. C. Grozema, C. F. Guerra, F. M. Bickelhaupt, F. D. Lewis, B. Y. A., M. A. Ratner, and L. D. A. Siebbeles, J. Am. Chem. Soc. **127**, 14894 (2005).

[315] B. C. Lin, C. P. Cheng, Z. Q. You, and C. P. Hsu, J. Am. Chem. Soc. **127**, 66 (2005).

[316] I. Newton, Philosophi naturalis principia mathematica; London (1687).

[317] R. W. Hockney, S. P. Goel, and J. W. Eastwood, J. Comput. Phys. **14**, 148 (1974).

[318] L. Verlet, Phys. Rev. **159**, 98 (1967).

[319] W. C. Swope, H. C. Andersen, P. H. Berens, and K. R. Wilson, J. Chem. Phys. **76**, 637 (1982).

[320] H. J. C. Berendsen, J. P. M. Postma, W. F. V. Gunsteren, A. Dinola, and J. R. Haak, J. Chem. Phys. **81**, 3684 (1984).

[321] B. Hess, C. Kutzner, D. van der Spoel, and E. Lindahl, J. Chem. Theor. Comput. **4**, 345 (2008).

[322] D. A. Pearlman, D. A. Case, J. W. Caldwell, W. S. Ross, T. E. C. III, S. Debolt, D. Ferguson, S. Seibel, and P. Kollman, Comp. Phys. Comm. **91**, 1 (1995).

[323] M. Parrinello and A. Rahman, J. Appl. Phys. **52**, 7182 (1981).

[324] J. Ryckaert, G. Ciccotti, and H. Berendsen, J. Comput. Phys. **23**, 327 (1977).

[325] B. Hess, H. Bekker, H. Berendsen, and J. Fraaije, J. Comput. Chem. **18**, 1463 (1997).

[326] P. P. Ewald, Annalen der Physik **369**, 253 (1921).

[327] D. van der Spoel, E. Lindahl, B. Hess, A. R. Buuren, E. Apol, P. Meulenhoff, D. P. Tieleman, A. L. T. M. Sijbers, K. A. Feenstra, R. van Drunen, *et al.*, Gromacs User Manual version 4.5.4 (2010).

[328] T. Darden, D. York, and L. Pedersen, J. Chem. Phys. **98**, 10089 (1993).

[329] U. Essmann, L. Perera, M. L. Berkowitz, T. Darden, H. Lee, and L. G. Pedersen, J. Chem. Phys. **103**, 8577 (1995).

[330] W. Kohn and L. J. Sham, Phys. Rev. **140**, A1133 (1965).

[331] P. Hohenberg and W. Kohn, Phys. Rev. **136**, B864 (1964).

[332] D. M. Ceperley and B. J. Alder, Phys. Rev. Lett. **45**, 566 (1980).

[333] J. P. Perdew, K. Burke, and M. Ernzerhof, Phys. Rev. Lett. **77**, 3865 (1996).

[334] J. P. Perdew, K. Burke, and M. Ernzerhof, Phys. Rev. Lett. **78**, 1396 (1997).

[335] J. P. Perdew and Y. Wang, Phys. Rev. B **45**, 13244 (1992).

[336] J. P. Perdew, J. A. Chevary, S. H. Vosko, K. A. Jackson, M. R. Pederson, D. J. Singh, and C. Fiolhais, Phys. Rev. B **46**, 6671 (1992).

[337] A. D. Becke, Phys. Rev. A **38**, 3098 (1988).

[338] C. Lee, W. Yang, and R. G. Parr, Phys. Rev. B **37**, 785 (1988).

[339] F. A. Hamprecht, A. J. Cohen, D. J. Tozer, and N. C. Handy, J. Chem. Phys. **109**, 6264 (1998).

[340] A. D. Boese, N. L. Doltsinis, N. C. Handy, and M. Sprik, J. Chem. Phys. **112**, 1670 (2000).

[341] W. A. Harrison, in Pseudopotentials in the Theory of Metals (W. A. Benjamin, New York (1966)) .

[342] H. Ehrenreich, F. Seitz, and D. Turnbull, Solid State Physics (Academic Press, New York (1970)) .

[343] G. B. Bachelet, D. R. Hamaaa, and M. Schluter, Phys. Rev. B **26**, 4199 (1982).

[344] D. Vanderbilt, Phys. Rev. B **41**, 7892 (1990).

[345] M. J. Frisch et al., Gaussian 09, revision A.02; Gaussian, Inc., Wallingford (2010) .

[346] M. W. Schmidt et al., J. Comput. Chem. **14**, 1347 (1993).

[347] F. M. Bickelhaupt and E. J. Baerends, Reviews on Computational Chemistry **15**, 1 (2000).

[348] G. Te Velde et al., J. Comput. Chem. **22**, 931 (2001).

[349] J. M. Soler, E. Artacho, J. D. Gale, A. Garca, J. Junquera, P. Ordejn, and D. Snchez-Portal, J. Phys.: Condens. Matt. **14**, 2745 (2002).

[350] P. Ordejon, E. Artacho, and J. M. Soler, Phys. Rev. B **53**, R10441 (1996).

[351] G. Kresse and J. Joubert, Phys. Rev. B **59**, 1758 (1999).

[352] P. E. Blochl, Phys. Rev. B **50**, 17953 (1994).

[353] G. Kresse and J. Furthmuller, Comput. Mater. Sci. **6**, 15 (1996).

[354] G. Kresse and J. Furthmuller, Phys. Rev. B **54**, 11169 (1996).

[355] J. Eddy and N. Maizels, Nucleic Acids Res. **34**, 3887 (2006).

[356] Z. Y. Kan, Y. Lin, F. Wang, X. V. Zhuang, Y. Zhao, D. W. Pang, Y. H. Hao, and Z. Tan, Nucleic Acids Res. **35**, 3646 (2007).

[357] R. D. Felice and A. Calzolari, Modern Methods for Theoretical Physical Chemistry of Biopolymers; Elsevier **20**, 485 (2006).

[358] A. Calzolari, R. D. Felice, E. Molinari, and A. Garbesi, J. Phys. Chem. B **108**, 2509 (2004).

[359] A. Calzolari, R. D. Felice, E. Molinari, and A. Garbesi, Appl. Phys. Lett. **80**, 3331 (2002).

[360] A. Calzolari, R. D. Felice, and E. Molinari, Solid State Commun. **131**, 557 (2004).

[361] R. D. Felice, A. Calzolari, A. G. S. S. Alexandre, and J. M. Soler, J. Phys. Chem. B **109**, 22301 (2005).

[362] W. D. Cornell, P. Cieplak, C. I. Bayly, I. R. Gould, K. M. Merz, D. M. Ferguson, D. C. S. T. Fox, J. W. Caldwell, and P. A. Kollman, J. Am. Chem. Soc. **117**, 5179 (1995).

[363] P. K. Samanta, A. K. Manna, and S. K. Pati, J. Phys. Chem. B **116**, 7618 (2012).

[364] S. Grimme, J. Comput. Chem. **27**, 1787 (2006).

[365] J. D. Chai and M. Head-Gordon, Phys. Chem. Chem. Phys. **10**, 6615 (2008).

[366] C. F. Guerra, H. Zijlstra, G. Paragi, and F. M. Bickelhaupt, Chem. Eur. J. **17**, 12612 (2011).

[367] J. Ŝponer, P. Jurečka, and P. Hobza, J. Am. Chem. Soc. **126**, 10142 (2004).

[368] S. S. Mallajosyula and S. K. Pati, J. Phys. Chem. B **111**, 11614 (2007).

[369] P. K. Samanta, A. K. Manna, and S. K. Pati, Chem. Asian J. **7**, 2718 (2012).

[370] R. Improta and V. Barone, Theor. Chem. Acc. **120**, 491 (2008).

[371] D. Onidas, D. Markovitsi, S. Marguet, A. Sharonov, and T. Gustavsson, J. Phys. Chem. B **106**, 11367 (2002).

[372] E. Livshits and R. Baer, Phys. Chem. Chem. Phys. **9**, 2932 (2007).

[373] T. Stein, L. Kronik, and R. Baer, J. Chem. Phys. **131**, 244119 (2009).

[374] A. Karolewski, L. Kronik, and S. Kummel, J. Chem. Phys. **138**, 204115 (2013).

[375] A. K. Jissy, U. P. M. Ashik, and A. Datta, J. Phys. Chem. C **115**, 12530 (2010).

[376] J. T. Davis, Angew. Chem. Int. Ed. **43**, 668 (2004).

[377] J. Gu, J. Leszczynski, and M. Bansal, Chem. Phys. Lett. **311**, 209 (1999).

[378] M. Meyer, M. Brandl, and J. Sühnel, J. Phys. Chem. A **105**, 8223 (2001).

[379] T. V. Mourik, J. Chem. Phys. **125**, 191101 (2006).

[380] N. Spackova, I. Berger, and J. Sponer, J. Am. Chem. Soc. **121**, 5519 (1999).

[381] N. Spackova, I. Berger, and J. Sponer, J. Am. Chem. Soc. **123**, 3295 (2001).

[382] E. Fadrna, N. Spackova, R. Stefl, J. Koca, T. C. III, and J. Sponer, Biophys. J. **87**, 227 (2004).

[383] A. B. Kotlyar, N. Borovok, T. Molotsky, H. Cohen, E. Shapir, and D. Porath, Adv. Mater. **17**, 1901 (2005).

[384] N. Borovok, T. Motlsky, J. Ghabboun, D. Porath, and A. Kotlyar, Anal. Biochem. **374**, 71 (2008).

[385] E. Hatcher, A. Balaeff, S. Keinan, R. Venkatramani, and D. N. Beratan, J. Am. Chem. Soc. **130**, 11752 (2008).

[386] A. Virgilio, V. Esposito, G. Citarella, L. Mayol, and A. Galeone, Chem. Bio. Chem. (2012).

[387] M. Tomaško, M. Vorličková, and J. Sagi, Biochimiie **91**, 171 (2009).

[388] C. F. Guerra, T. van der Wijst, J. Poater, M. Swart, and F. M. Bickelhaupt, Theor. Chem. Acc. **125**, 245 (2010).

[389] K. Burke, J. P. Perdew, and M. Ernzerhof, Int. J. Quantum Chem. **61**, 287 (1997).

[390] N. Troullier and J. L. Martins, Phys. Rev. B **43**, 1993 (1991).

[391] L. Kleinman and D. M. Bylander, Phys. Rev. Lett. **48**, 1425 (1982).

[392] S. S. Mallajosyula and S. K. Pati, Angew. Chem. Int. Ed. **48**, 4977 (2009).

[393] M. Cavallari, A. Garbesi, and R. D. Felice, J. Phys. Chem. B **113**, 13152 (2009).

[394] C. D. M. Churchill and S. D. Wetmore, Phys. Chem. Chem. Phys. **13**, 16373 (2011).

[395] D. Kosenko, L. Gor, O. V. Shishkin, J. Sponer, and J. Leszczynski, J. Phys. Chem. B **112**, 150 (2008).

[396] P. Schyman, L. A. Eriksson, and A. Laaksonen, J. Phys. Chem. B **113**, 6574 (2009).

[397] B. Xerri, C. Morell, A. Grand, J. Cadet, P. Cimino, and V. Barone, Org. Biomol. Chem. **4**, 3986 (2006).

[398] S. D. W. A. L. Millen, R. A. Manderville, J. Phys. Chem. B **114**, 4373 (2010).

[399] A. Cerf, T. Alava, R. A. Barton, and H. G. Craighead, Nano Lett. **11**, 4232 (2011).

[400] J. Shendure and H. Ji, Nat. Biotech. **26**, 1135 (2008).

[401] C. H. Lu, H. H. Yang, C. L. Zhu, X. Chen, and G. N. Chen, Angew. Chem. Int. Ed. **48**, 4785 (2009).

[402] B. Das, R. Voggu, C. S. Rout, and C. N. R. Rao, Chem. Comm. **41**, 5155 (2008).

[403] K. S. Subrahmanyam, A. K. Manna, S. K.Pati, and C. N. R. Rao, Chem. Phys. Lett. **497**, 70 (2010).

[404] X. D. Wen, L.Hand, V. Labet, T. Yang, R. Hoffmann, N. Ashcroft, A. R. Oganov, and A. O. Lyakhov, Proc. Natl. Acad. Sci. **108**, 6833 (2011).

[405] J. H. Seol, I. Jo, A. L. Moore, L. Lindsay, Z. H. Aitken, M. T. Pettes, X. Li, Z. Yao, R. Huang, D. Broido, *et al.*, Science **328**, 213 (2010).

[406] A. K. Geim and K. S. Novoselov, Nat. Mater. **6**, 183 (2007).

[407] Z. Liu, S. M. Tabakman, K. Jiang, S. Fan, and H. Dai, J. Am. Chem. Soc. **130**, 13540 (2008).

[408] Y. Chen, H. Liu, T. Ye, J. Kim, and C. Mao, J. Am. Chem. Soc. **129**, 8696 (2007).

[409] D. A. Heller, H. Jin, B. M. Martinez, D. Patel, B. Miller, T.-K. Yeung, P. V. Jena, C. Hobartner, T. Ha, S. K. Silverman, *et al.*, Nat. Nanotech. **4**, 114 (2009).

[410] L. Cao, X. Wang, M. J. Meziani, F. Lu, H. Wang, P. Luo, Y. Lin, B. A. Harruff, L. M. Veca, D. Murray, *et al.*, J. Am. Chem. Soc. **129**, 11318 (2007).

[411] C. C. Fu, H. Y. Lee, K. Chen, T. S. Lim, H. Y.Wu, P. Lin, P. K. Wei, P. H. Tsaon, H. C. Chang, and W. Fann, Proc. Natl. Acad. Sci. **104**, 727 (2007).

[412] C. Hao, L. Ding, X. Zhang, and H. Ju, Anal. Chem. **79**, 4442 (2007).

[413] R. Yang, J. Jin, Y. Chen, N. Shao, H. Kang, Z. Xiao, Z. Tang, Y. Wu, Z. Zhu, and W. Tan, J. Am. Chem. Soc. **130**, 8351 (2008).

[414] Z. Zhu, Z. Tang, J. A. Phillips, R. Yang, H. Wang, and W. Tan, J. Am. Chem. Soc. **130**, 10856 (130).

[415] M. Zheng, A. Jagota, E. D. Semke, B. A. Diner, R. S. McLean, S. R. Lustig, R. E. Richardson, and N. G. Tassi, Nat. Mater. **2**, 338 (2003).

[416] K. A. Williams, P. T. M. Veenhuizen, B. G. de la Torre, R. Eritja, and C. Dekker, Nature **420**, 761 (2002).

[417] D. Pantarotto, R. Singh, D. McCarthy, M. Erhardt, J. P. Briand, M. Prato, K. Kostarelos, and A. Bianco, Angew. Chem. Int. Ed. **116**, 5354. (2004).

[418] R. Singh, D. Pantarotto, D. McCarthy, O. Chaloin, J. Hoebeke, D. Charalambos, J. P. Briand, M. Prato, A. Bianco, and K. Kostarelos, J. Am. Chem. Soc. **127**, 4388 (2005).

[419] N. Nakashima, S. Okuzono, H. Murakami, T. Nakai, and K. Yoshikawa, Chem. Lett. **32**, 456 (2003).

[420] C. Staii, A. T. J. Jr, M. Chen, and A. Gelperin, Nano Lett. **5**, 1774. (2005).

[421] C. Dwyer, M. Guthold, M. Falvo, S. Washburn, R. Superfine, and D. Erie, Nanotechnology **13**, 601. (2002).

[422] H. Gao, Y. Kong, D. Cui, and C. S. Ozkan, Nano Lett. **3**, 471 (2003).

[423] D. A. Heller, E. S. Jeng, T. K. Yeung, B. M. M. Martinez, A. E. Moll, J. B. Gastala, and M. S. Strano, Science **311**, 508 (2006).

[424] S. E. Baker, W. Cai, T. L. Lasseter, K. P. Weidkamp, and R. J. Hamers, Nano Lett. **2**, 1413 (2002).

[425] X. Tu, S. Manohar, A. Jagota, and M. Zheng, Nature **460**, 250 (2009).

[426] M. S. Strano, M. Zhen, A.Jagota, G. B. Onoa, D. A. Heller, P. W. Barone, and M. L. Usrey, Nano Lett. **4**, 543 (2004).

[427] M. Zheng, A. Jagota, M. S. Strano, A. P. Santos, P. Barone, S. G. Chou, B. A. Diner, M. S. Dresselhaus, R. S. M. Mclean, and G. B. Onoa, Science **302**, 1545 (2003).

[428] S. Daniel, T. P. Rao, K. S. Rao, S. U. Rani, and T. G. Naidu; Lee, H. Y.; Kawai, Sensors and Actuators B: Chemical **122**, 672 (2007).

[429] S. Li, P. He, J. Dong, Z. Guo, and L. Dai, J. Am. Chem. Soc. **127**, 14 (2005).

[430] A. Bianco, K. Kostarelos, and M. Prato, Current opinion in chemical biology **9**, 674 (2005).

[431] S. Wang, R. Wang, P. Sellin, and Q. Zhang, Biochemical and biophysical research communications **325**, 1433 (2004).

[432] X. Zhao and J. K. Johnson, J. Am. Chem. Soc. **129**, 10438 (2007).

[433] H. Gao and Y. Annu.Kong, Rev. Mater. Res. **34**, 123 (2004).

[434] W. Martin, W. Zhu, and G. Krilov, J. Phys. Chem. B **112**, 16076 (2008).

[435] R. R. Johnson, A. T. C.Johnson, and M. L. Klein, Nano Lett. **8**, 69 (2008).

[436] R. R. Johnson, A. K. A. T. C. Johnson, and M. L. Klein, Nano Lett. **9**, 537 (2009).

[437] B. Gigliotti, B. Sakizzie, D. S. Bethune, R. M. Shelby, and J. N. Cha, Nano Lett. **6**, 159 (2006).

[438] S. Manohar, T. Tang, and A. Jagota, J. Phys. Chem. C **111**, 17835 (2007).

[439] G. Lu, P. Maragakis, and E. Kaxiras, Nano Lett. **5**, 897 (2005).

[440] Y. Wu, J. A. Phillips, H. Liu, R. Yang, and W. Tan, ACS Nano. **2**, 2023 (2008).

[441] S. Akca, A. Foroughi, D. Frochtzwajg, and H. W. C. Postma, PLoSONE **6**, e18442 (2011).

[442] X. Zhao, J. Phy. Chem. C **115**, 6181 (2011).

[443] J. M. Thomas and A. C. David, In Molecular Modeling of Nucleic Acids American Chemical Society **682**, 379 (1997).

[444] T. A. D. D. A. D. Case, T. E. Cheatham, C. L. Simmerling, J. Wang, R. E. Duke, R. Luo, R. C. Walker, W. Zhang, K. M. Merz, B. Roberts, *et al.*, AMBER 11, University of California, San Francisco p. 2010.

[445] J. Zou, B. Ji, X. Q. Feng, and H. Gao, Nano Lett. **6**, 430 (2006).

[446] G. Hummer, J. C. Rasaiah, and J. P. Noworyta, Nature **414**, 188 (2001).

[447] W. L. Jorgensen, J. Am. Chem. Soc. **129**, 10438 (2007).

[448] C. L. Cheng and G. J. Zhao, Nanoscale **4**, 2301 (2012).

[449] W. L. Jorgensen, J. Am. CheM. Soc. **103**, 335 (1981).

[450] B. Hess, C. Kutzner, D. van der Spoel, and E. Lindahl, J. Chem. Theo. and Comput. **4**, 435 (2008).

[451] W. Humphrey, A. Dalke, and K. Schulten, J. Mol. Graphics **14**, 33 (1996).

[452] Chipot, Springer Verlag, Berlin **10**, 978 (2007).

[453] R. R. Johnson, A. Johnson, and M. L. Klein, Small **6**, 31 (2010).

[454] P. K.Samanta, G. Periyasamy, A. K. Manna, and S. K. Pati, J. Mater. Chem. **22**, 6774 (2012).

[455] S. Gowtham, R. H. Scheicher, R. Ahuja, R. Pandey, and S. P. Karna, Phys. Rev. B **76**, 033401 (2007).

[456] J. Antony and S. Antony, Phys. Chem. Chem. Phys. **10**, 2722 (2008).

[457] N. Varghese, U. Mogera, A.Govindaraj, A. Das, P. K. Maiti, A. K. Sood, and C. N. R. Rao, Chem. Phys. Chem. **10**, 206 (2009).

[458] S. Manohar, A. R. Mantz, K. E. Bancroft, C. Y. Hui, A. Jagota, and D. V. Vezenov, Nano Lett. **8**, 4365 (2008).

[459] T. van der Wijst, B. Lippert, M. Swart, C. F. Guerra, and F. M. Bickelhaupt, J. Biol. Inorg. Chem. **15**, 387 (2010).

[460] P. Sket and J. Plavec, J. Am. Chem. Soc. **132**, 12724 (2010).

[461] L. Joly, F. Rosu, M. Swart, and V. Gabelica, Chem. Commun. **48**, 8386 (2012).

[462] M. Meyer, C. Schneider, M. Brandl, and J. S*ü*hnel, J. Phys. Chem. A **105**, 11560 (2001).

[463] N. D. Mermin, Phys. Rev. **176**, 250 (1968).

[464] A. Fasolino, J. H. Los, and M. I. Katsnelson, Nat. Mater. **6**, 858 (2007).

[465] W. Saenger, Principles of nucleic acid structure 1984.: New York (1984).

[466] P. Maragakis, R. L. Barnett, E. Kaxiras, M. Elstner, and T. Frauenheim, Phys. Rev. B **66**, 241104 (2002).

[467] Y. Zhang, Y. W. Tan, H. L. Stormer, and P. Kim, Nature (London) **438**, 201 (2005).

[468] Y. Zhang, V. W. Brar, C. Girit, A. Zettl, and A. F. Crommie, Nat. Phys. **5**, 722 (2009).

[469] C. O. Girit, J. C. Meyer, R. Erni, M. D. Rossell, C. Kisielowski, L. Yang, C. Park, M. F. Crommie, M. L. Cohen, S. G. Louie, *et al.*, Science **323**, 1705 (2009).

[470] Y. Zhang, T. T. Tang, C. Girit, Z. Hao, M. C. Martin, A. Zettl, M. F. Crommie, Y. R. Shen, and F. Wang, Nature **459**, 820 (2009).

[471] K. Kim, Z. Lee, W. Regan, C. Kisielowski, M. F. Crommie, and A. Zettl, ACS Nano **5**, 2142 (2011).

[472] W. Regan, N. Alem, B. Aleman, B. Geng, C. Girit, L. Maserati, F. Wang, M. Crommie, and A. Zettl, Appl. Phys. Lett. **96**, 113102 (2010).

[473] M. L. Cohen and A. Zettl, Phys. Today p. 34 (2010).

[474] A. K. Singh, E. S. Penev, and B. I. Yakobson, ACS Nano **4**, 3510 (2010).

[475] C. Berger, Z. Song, X. Li, X. Wu, N. Brown, C. Naud, D. Mayou, T. Li, J. Hass, A. N. Marchenkov, *et al.*, Science **312**, 1191 (2006).

[476] M. Y. Han, B. Özyilmaz, Y. Zhang, and P. Kim, Phys. Rev. Lett. **98**, 206805 (2007).

[477] F. Schedin, A. K. Geim, S. V. Morozov, E. W. Hill, P. Blake, M. I. Katsnelson, and K. S. Novoselov, Nat. Mater. **6**, 652 (2007).

[478] B. Huard, J. A. Sulpizio, N. Stander, K. Todd, B. Yang, and D. Goldhaber-Gordon, Phys. Rev. Lett. **98**, 236803 (2007).

[479] H. Zeng, C. Zhi, Z. Zhang, X. Wei, X. Wang, W. Guo, Y. Bando, and D. Golberg, Nano Lett. **10**, 5049 (2010).

[480] D. Golberg, Y. Bando, Y. Huang, T. Terao, M. Mitome, C. Tang, and C. Zhi, ACS Nano **4**, 2979 (2010).

[481] N. Alem, R. Erni, C. Kisielowski, M. D. Rossell, W. Gannett, and A. Zettl, Phys. Rev. B **80**, 155425 (2009).

[482] W. Y. Kim, Y. C. Choi, and K. S. Kim, J. Mater. Chem. **18**, 4510 (2008).

[483] W. Y. Kim and K. S. Kim, J. Comput. Chem. **29**, 1073 (2008).

[484] S. M. Sairam, P. Parida, and S. K. Pati, J. Mater. Chem. **19**, 1761 (2009).

[485] S. K. Saha, M. Baskey, and D. Majumdar, Adv. Mater. **22**, 5531 (2010).

[486] W. Y. Kim and K. S. Kim, Nat. Nanotechnol. **3**, 408 (2008).

[487] S. Dutta, S. Lakshmi, and S. K. Pati, Phys. Rev. B **77**, 073412 (2008).

[488] 2936Dutta and S. K. Pati, J. Phys. Chem. B **112**, 1333 (2008).

[489] S. Dutta, A. K. Manna, and S. K. Pati, Phys. Rev. Lett. **102**, 096601 (2009).

[490] A. Das, S. Pisana, B. Chakraborty, S. Piscanec, S. K. Saha, U. V. Waghmare, K. S. Novoselov, H. R. Krishnamurthy, A. K. Geim, A. C. Ferrari, *et al.*, Nat. Nanotechnol. **3**, 210 (2008).

[491] B. Das, R. Voggu, C. S. Rout, and C. N. R. Rao, Chem. Commun. **41**, 5155 (2008).

[492] R. Voggu, B. Das, C. S. Rout, and C. N. R. Rao, J. Phys.: Condens. Matter. **20**, 472204 (2008).

[493] A. K. Manna and S. K. Pati, Chem.Asian J. **4**, 855 (2009).

[494] K. S. Subrahmanyam, A. K. Manna, S. K. Pati, and C. N. R. Rao, Chem. Phys. Lett. **497**, 70 (2010).

[495] H. Pinto, R. Jones, J. P. Goss, and P. R. Briddon, Phys. Status Solidi A **207**, 2131 (2010).

[496] J. Meyer, C. O. Girit, M. F. Crommie, and A. Zettl, Nature **454**, 319 (2008).

[497] R. Erni, M. D. Rossell, P. Hartel, N. Alem, K. Erickson, W. Gannett, and A. Zettl, Phys. Rev. B **82**, 165443 (2010).

[498] M. Kawaguchi, T. Kawashima, and T. Nakajima, Chem. Mater. **8**, 1197 (1996).

[499] M. O. Wanatabe, S. Itoh, K. Mizushima, and T. Sasaki, J. Appl. Phys. **78**, 2880 (1995).

[500] J. Wu, W. Q. Han, W. Walukiewicz, J. W. Ager, W. Shan, E. E. Haller, and A. Zettl, Nano Lett. **4**, 647 (2004).

[501] D. Pacile, J. C. Meyer, C. O. Girit, and A. Zettl, Appl. Phys. Lett. **92**, 133107 (2008).

[502] Z. Weng-Sieh, K. Cherrey, N. S. Chopra, A. Zettl, R. Gronsky, X. Blase, Y. Miyamoto, A. Rubio, S. G. Louie, and M. L. Cohen, Phys. Rev. B **51**, 11229 (1995).

[503] A. Y. Liu, R. M. Wentzcovitch, and M. L. Cohen, Phys. Rev. B **39**, 1760 (1989).

[504] B. Xu, Y. H. Lu, Y. P. Feng, and J. Y. Lin, J. Appl. Phys. **108**, 073711 (2010).

[505] K. Yuge, Phys. Rev. B **79**, 144109 (2009).

[506] C. W. Chang, W. Q. Han, and A. Zettl, J. Vac. Sci. Technol. B **23**, 1883 (2005).

[507] Y. Miyamoto, M. L. Cohen, and S. G. Louie, Solid State Commun. **102**, 605 (1997).

[508] Y. Miyamoto, M. L. Cohen, and S. G. Louie, Phys. Rev. B **52**, 14971 (1995).

[509] D. Tomanek, R. M. Wentzcovitch, S. G. Louie, and M. L. Cohen, Phys. Rev. B **37**, 3134 (1988).

[510] R. M. Wentzcovitch, M. L. Cohen, and S. G. L. S. G., Phys. Lett. A **131**, 457 (1988).

[511] Y. Miyamoto, A. Rubio, M. L. Cohen, and S. G. Louie, Phys. Rev. B **50**, 4976 (1994).

[512] Y. Miyamoto, A. Rubio, S. G. Louie, and M. L. Cohen, Phys. Rev. B **50**, 18360 (1994).

[513] H. Sun, S. H. Jhi, D. Roundy, M. L. Cohen, and S. G. Louie, Phys. Rev. B **64**, 094108 (2001).

[514] A. Rubio, Nat. Mater. **9**, 379 (2010).

[515] S. Y. Zhou, G. H. Gweon, A. V. Fedorov, P. N. First, W. A. de Heer, D. H. Lee, F. Guinea, A. H. C. Neto, and A. Lanzara, Nat. Mater. **6**, 770 (2007).

[516] L. Liu and Z. Shen, Appl. Phys. Lett. **95**, 252104 (2009).

[517] L. Chen, C. Bourbonnais, T. Li, and A. M. S. Tremblay, Phys. Rev. Lett. **66**, 369 (1991).

[518] D. K. Samarakoon and X. Q. Wang, ACS Nano **4**, 4126 (2010).

[519] D. Haberer, D. V. Vyalikh, S. Taioli, B. Dora, M. Farjam, J. Fink, D. Marchenko, T. Pichler, K. Ziegler, S. Simonucci, *et al.*, Nano Lett. **10**, 3360 (2010).

[520] F. Yavari, C. Kritzinger, C. Gaire, L. Song, H. Gullapalli, T. Borca-Tasciuc, P. M. Ajayan, and N. Koratkar, Small **6**, 2535 (2010).

[521] W. Liu, Z. F. Wang, Q. W. Shi, J. Yang, and F. Liu, Phys. Rev. B **80**, 233405 (2009).

[522] J. A. F*ü*rst, T. G. Pedersen, M. Brandbyge, and A. P. Jauho, Phys. Rev. B **80**, 115117 (2009).

[523] S. Blankenburg, M. Bieri1, R. Fasel, K. M*ü*llen, C. A. Pignedoli, and D. Passerone, Small **6** (2010).

[524] M. Bieri, M. Treier, J. Cai, K. A*ï*t-Mansour, P. Ruffieux, O. Gr*ö*ning, P. Gr*ö*ning, M. Kastler, R. Rieger, X. Feng, *et al.*, Chem. Commun. p. 6919 (2009).

[525] T. G. Pedersen, C. Flindt, J. Pedersen, N. A. Mortensen, A. P. Jauho, and K. Pedersen, Phys. Rev. Lett. **100**, 136804 (2008).

[526] A. Du, Y. Chen, Z. Zhu, R. Amal, G. Q. Lu, and S. C. Smith, J. Am. Chem. Soc. **131**, 17354 (2009).

[527] N. Ooi, A. Rairkar, L. Lindsley, and J. B. Adams, J. Phys.: Condens. Matter **18**, 97 (2006).

[528] M. Brandbyge, J.-L. Mozos, P. Ordejon, J. Taylor, and K. Stokbro, Phys. Rev. B **65**, 165401 (2002).

[529] S. Azevedo, M. S. C. Mazzoni, R. W. Nunes, and H. Chacham, Phys. Rev. B **70**, 205412 (2004).

[530] S. Azevedo, Phys. Lett. A **351**, 109 (2006).

[531] S. Azevedo, R. de Paiva R., and J. R. Kaschny, J. Phys.: Condens. Matter. **18**, 10871 (2006).

[532] S. Azevedo and R. de Paiva, Europhys. Lett. **75**, 126 (2006).

[533] S. S. Alexandre, H. Chacham, and R. W. Nunes, Phys. Rev. B **63**, 045402 (2001).

[534] S. V. Morozov, K. S. Novoselov, and A. K. Geim, Phys.-Usp. **51**, 744 (2008).

[535] M. Inui, S. A. Trugman, and E. Abrahams, Phys. Rev. B **49**, 3190 (1994).

[536] G. Kresse and J. Joubert, Phys. Rev. B **59**, 1758 (1999).

[537] P. E. Blöchl, Phys. Rev. B **50**, 17953 (1994).

[538] G. Kresse and J. Furthmüller, Comput. Mater. Sci. **6**, 15 (1996).

[539] G. Kresse and J. Furthmüller, Phys. Rev. B **54**, 11169 (1996).

[540] Y. W. Son, M. L. Cohen, and S. G. Louie, Nature (London) **444**, 347 (2006).

[541] S. Dutta and S. K. Pati, J. Phys. Chem. B **112**, 1333 (2008).

[542] L. Ci, L. Song, C. Jin, D. Jariwala, D. Wu, Y. Li, A. Srivastava, Z. F. Wang, K. Storr, L. Balicas, *et al.*, Nat. Mater. **9**, 430 (2010).

[543] D. A. Areshkin and B. K. Nikolić, Phys. Rev. B **79**, 205430 (2009).

[544] S. M. M. Dubois, Z. Zanolli, X. Declerck, and J. C. Charlier, The European Physical Journal B-Condensed Matter and Complex Systems **72**, 1 (2009).

[545] M. Orlita, C. Faugeras, P. Plochocka, P. Neugebauer, G. Martinez, D. K. Maude, A. L. Barra, M. Sprinkle, C. Berger, W. A. de Heer, *et al.*, Phys. Rev. Lett. **101**, 267601 (2008).

[546] R. V. Noorden, Nature **442**, 228 (2006).

[547] J. Wu, W. Pisula, and K. M*ü*llen, Chem. Rev. **107**, 718 (2007).

[548] D. S. L. Abergel, V. Apalkov, J. Berashevich, K. Ziegler, and T. Chakraborty, Adv. Phys. **59**, 261 (2010).

[549] A. K. Manna and S. K. Pati, Chem. Asian. J. **4**, 855 (2009).

[550] T. O. Wehling, K. S. Novoselov, S. V. Morozov, E. E. Vdovin, M. I. Katsnelson, A. K. Geim, and A. I. Lichtenstein, Nano Lett. **8**, 173 (2008).

[551] T. O. Wehling, A. I. Lichtenstein, and M. I. Katsnelson, Appl. Phys. Lett. **93**, 202110 (2008).

[552] C. Casiraghi, S. Pisana, K. S. Novoselov, A. K. Geim, and A. C. Ferrari, Appl. Phys. Lett. **91**, 233108 (2007).

[553] O. Leenaerts, B. Partoens, and F. Peeters, Phys. Rev. B **77**, 125416 (2008).

[554] J. Zhou, Q. Wang, Q. Sun, and P. Jena, Phys. Rev. B **81**, 085442 (2010).

[555] H. Dil, J. Lobo-Checa, R. Laskowski, P. Blaha, S. Berner, J. Osterwalder, and T. Greber, Science **319**, 1824 (2008).

[556] Y. G. Zhou, J. Xiao-Dong, Z. G. Wang, H. Y. Xiao, F. Gao, and X. T. Zu, Phys. Chem. Chem. Phys. **12**, 7588 (2010).

[557] C. Ataca and S. Ciraci, Phys. Rev. B **82**, 165402 (2010).

[558] D. Ma, Z. Lu, W. Ju, and Y. Tang, J. Phys. Condens. Mater. **24**, 145501 (2012).

[559] J. P. K. Doye and D. J. Wales, New. J. Chem. **22**, 733 (1998).

[560] M. Zhou, A. Zhang, Z. Dai, Y. P. Feng, and C. Zhang, J. Phys. Chem. C **114**, 16541 (2010).

[561] M. Zhou, A. Zhang, Z. Dai, C. Zhang, and Y. P. Feng, J. Chem. Phys. **132**, 194704 (2010).

[562] Y. Tang, Z. Yang, and X. Dai, Phys. Chem. Chem. Phys. **DOI: 10.1039/C2CP41441D** (2012).

[563] Y. H. Lu, M. Zhou, C. Zhang, and Y. P. Feng, J. Phys. Chem. C **113**, 20156 (2009).

[564] E. J. Yoo, T. Okata, T. Akita, M. Kohyama, J. Nakamura, and I. Honma, Nano Lett. **9**, 2255 (2009).

[565] R. Voggu, S. Paul, S. K. Pati, and C. N. R. Rao, J. Phys. : Cond. Matt. **20**, 215211 (2008).

[566] M. Bieri, M. Treier, J. Cai, K. A. Mansour, P. Ruffieux, O. Gröning, P. Gröning, M. Kastler, R. Rieger, X. Feng, *et al.*, Chem. Commun. p. 6919 (2009).

[567] Y. Ding, Y. Wang, S. Shi, and W. Tang, J. Phys. Chem. C **115**, 5334 (2011).

[568] E. Khan, W. Hu, C. Xiao, R. Lu, K. Deng, J. Yang, and H. Su, J. Am. Chem. Soc. **134**, 5718 (2012).

[569] Y. Li, Z. Zhou, P. Shen, and Z. Chen, Chem. Commun. **46**, 3672 (2010).

[570] S. Lakshmi, S. Roche, and G. Cuniberti, Phys. Rev. B **80**, 193404 (2009).

[571] R. Saito, G. Dresselhaus, and M. S. Dresselhaus, Physical Properties of Carbon Nanotubes, Imperial College Press, London (1998).

[572] P. M. Ajayan, Chem. Rev. **99**, 1787 (1999).

[573] M. S. Dresselhaus, Carbon **33**, 871 (1995).

[574] T. W. Ebbesen, Annul Rev. of Materials Sci. **24**, 235 (1994).

[575] R. S. Baughman, A. A. ZAkhizov, and W. A. de Heer, Science **297**, 787 (2002).

[576] S. J. Tans, A. R. M. Verschueren, and C. Deeker, Nature **393**, 49 (1998).

[577] D. M. Guldi and M. Prato, Acc. Chem. Res. **33**, 695 (2000).

[578] M. Prato, J. Mater. Chem. **7**, 1097 (1997).

[579] B. B. L. Allen, P. D. Kichambare, and A. Star, Adv. Mater. **19**, 1439 (2007).

[580] S. M. Sairam and S. K. Pati, J. Phys. Chem. B **112**, 16982 (2008).

[581] L. D. M. Kalbac, L. Kavan and M. S. Dresselhaus, Nano Lett. **8**, 1257 (2008).

[582] M. A. Pimenta, G. Dresselhaus, M. S. Dresselhaus, L. G. Cancado, A. Jorio, and R. Saito, Phys. Chem. Chem. Phys. **9**, 1276 (2007).

[583] J. Kotakoski, A. V. Krasheninnikov, Y. Ma, A. S. Foster, K. Nordlund, and R. M. Nieminen, Phys. Rev. B **71**, 205408 (2005).

[584] J. Jhou, Q. Wan, Q. Sun, X. S. Chen, Y. Kawazoe, and P. Jena, Nano Lett. **9**, 3867 (2009).

[585] E. J. Kan, Z. Li, J. Yang, and J. G. Hou, J. Am. Chem. Soc. **130**, 4224 (2008).

[586] B. Das, B. Choudhury, A. Gomathi, A. K. Manna, S. K. Pati, and C. N. R. Rao, Chem. Phys. Chem. **12**, 937 (2011).

[587] R. Voggu, C. S. Rout, A. D. Franklin, T. S. Fisher, and C. N. R. Rao, J. Phys. Chem. C **112**, 13053 (2008).

[588] F. Ortmann, W. G. Schmidt, and F. Bechstedt, Phys. Rev. Lett. **95**, 186101 (2005).

[589] D. R. Salahub, Adv. Chem. Phys. **69**, 447 (1987).

[590] A. Das, S. Pisana, B. Chakraborty, S. Piscanec, S. K. Saha, U. V. Waghmare, K. S. Novoselov, H. R. Krishnamurthy, A. K. Geim, A. C. Ferrari, *et al.*, Nat. Nanotech. **3**, 210 (2008).

[591] O. Dubay and G. Kresse, Phys. Rev. B **67**, 035401 (2003).

[592] K. V. Christ and H. R. Sadeghpour, Phys. Rev. B **75**, 195418 (2007).

[593] D. Sanchez-Portal, E. Artacho, J. M. Soler, A. Rubio, and P. Ordejon, Phys. Rev. B **59**, 12678 (1999).

[594] D. Wegner, R. Yamachika, Y. Wang, V. W. Brar, B. M. Bartlett, J. R. Long, and M. F. Crommie, Nano Lett. **8**, 131 (2008).